Advancing Graph-Theoretic Techniques for Microstructure Reconstructions, Evolutions, and Property Evaluations

by

Iman Javaheri

A dissertation submitted in partial fulfillment
of the requirements for the degree of
Doctor of Philosophy
(Aerospace Engineering and Scientific Computing)
in the University of Michigan
2023

Doctoral Committee:

        Professor Veera Sundararaghavan, Chair
        Professor Daniel J. Inman
        Associate Professor Raj Rao Nadakuditi
        Dr. John A. Newman, NASA Langley Research Center
        Professor Anthony M. Waas

"I seem to have been only like a boy playing on the sea-shore, and diverting myself in now and then finding a smoother pebble or a prettier shell than ordinary, whilst the great ocean of truth lay all undiscovered before me." – Isaac Newton

Iman Javaheri

imanajv@umich.edu

ORCID iD: 0000-0001-6071-2817

To my beloved family, for paving the way

ACKNOWLEDGEMENTS

This dissertation would not have been possible without the support and guidance of so many. First and foremost, heartfelt gratitude is expressed to my advisor, Professor Veera Sundararaghavan, for his constant support, motivation, and guidance in my journey at the University of Michigan. His invaluable advisory in both professional and personal affairs, along with his persistent inspiration and positive attitude, have cheered up my research experience in many ways, for which I will be forever thankful. Also, a special thank you to Professors Anthony M. Waas, Daniel J. Inman, Raj Rao Nadakuditi, and Dr. John A. Newman for serving on my committee and providing valuable feedback on my dissertation. My co-authors deserve tremendous gratitude for their contributions in shaping and validating the data-driven frameworks described in this work as well. So a special appreciation is expressed to Professors Pınar Acar (from Virginia Tech), Marc DeGraef (from Carnegie Mellon University), Mohsen Taheri Andani (from Texas A&M), and Doctors Aaditya Lakshmanan, Siddhartha Srivastava, Jiangyi Luo, Sriram Ganesan, and Arulmurugan Senthilnathan (from Virginia Tech).

I feel very fortunate to be recruited as a part of the National Aeronautics and Space Administration (NASA) Pathways Program at Langley Research Center in Durability, Damage Tolerance, and Reliability (DDTR) Branch, which has immensely enhanced my academic research experience over the last four years by providing opportunities to attend many national/international conferences, technical workshops, leadership/-

Last but not least, I would not be writing this acknowledgment were it not for the

sacrifice and unconditional support of the loved ones in my life, who bestowed upon me the discipline and confidence to pursue my dreams, provided solace in times of need and distress, and taught me life lessons that I cannot begin to articulate here. I am deeply indebted to my parents, Mahnaz and Mojtaba, my siblings, Elham and Amir, and my aunt, Mitra – thank you for all you have done for me.

TABLE OF CONTENTS

LIST OF FIGURES

Figure

LIST OF TABLES

LIST OF APPENDICES

Appendix

LIST OF ABBREVIATIONS

1D   one-dimensional

2D   two-dimensional

3D   three-dimensional

ADRS   adaptive dynamic relaxation scheme

AM   additively-manufactured

BC   boundary condition

BD   building direction

BVP   boundary value problem

CAD   computer-aided design

CDF   cumulative distribution function

CFL   Courant-Friedrichs-Lewy

CI   confidence index

CP   crystal plasticity

CPD   conditional probability density

CPFEM   crystal plasticity finite element method

CPPD   crystal plasticity peridynamics

CT   computed tomography

CW   continuous wave

DCT	diffraction contrast tomography
DED	direct energy deposition
DFT	density functional theory
DIC	digital image correlation
EBSD	electron backscatter diffraction
FCC	face-centered cubic
FE	finite element
FEM	finite element method
GB	grain boundary
GUI	graphical user interface
HAGB	high-angle grain boundary
HEDM	high-energy X-ray diffraction microscopy
HOS	higher-order stabilization
ICME	integrated computational materials engineering
LAGB	low-angle grain boundary
LEGOMAT	locally-extracted globally-organized microstructural model
LENS	laser engineered net shaping
LPBF	laser powder-bed fusion
MRF	Markov random field
NOSBPD	non-ordinary state-based peridynamics
ODF	orientation distribution function
PBF	powder-bed fusion
PD	peridynamics
PDE	partial differential equation
PDF	probability density function

PPM	pixels per micrometer
RGB	red-green-blue
RVE	representative volume element
SD	scanning direction
SEM	scanning electron microscopy
SLM	selective laser melting
TD	transverse direction
VMM	variational multiscale method
X-FEM	extended-FEM

ABSTRACT

Complex applications in modern aerospace technology urgently call for advanced structural materials that are high-strength, lightweight, and yet tolerant to damage from loading conditions, extreme temperature, particle radiation, or environmental exposure. To swiftly fulfill these emerging material requirements, a multi-scale understanding of the relationships between processing, microstructure, and properties of metallic materials needs to be developed. Toward these goals, this dissertation presents computational models and software for (i) building three-dimensional (3D) microstructural maps of materials through Markovian inference from a set of three orthogonal two-dimensional (2D) experimental measurements, (ii) insertion of microstructural information into a geometrical grid at the component-scale level with iterative refinement using experimental measurements at locations of maximum uncertainty, (iii) implementation of Cauchy-Crofton technique as a post-processing step to minimize surface energies for the purposes of physics-based segmentation and texture evolution of microstructural aggregates, and (iv) development of crystal plasticity peridynamics (CPPD) technique for predicting fine-scale stress/strain localizations at micro-scale level. These numerical efforts serve as multi-scale modeling tools for the reconstruction of surrogate models to proactively simulate structural performance and quantify/reduce the uncertainty in computational materials prognosis, involving the complex nature of polycrystalline formation and texture simulation.

Traditionally, the underlying 3D microstructural information of polycrystalline struc-

tures has been digitized through experimental acquisition techniques, such as tomography or serial sectioning. These methods, however, only provide images over relatively small volumes of material. Furthermore, due to the stochasticity of material formation, a single snapshot of a microstructure does not adequately capture the property distributions in a component. In addition, currently-available numerical methods for microstructure synthesis, such as geometry-based (e.g., Voronoi tessellation), physics-based (e.g., phase-field, kinetic Monte Carlo), or feature-based (e.g., simulated annealing) techniques, run into various difficulties when modeling microstructural complexities including non-equilibrium grain structures, non-convex morphologies, multi-phase features, twins, and cell structures that naturally arise from material processing. These features, however, play an important role in the properties and performance of modern structural materials.

Therefore, this dissertation attempts to create a suite of data-driven computational models based on graph theoretic techniques to rapidly synthesize complex 3D polycrystalline microstructures with validated features that are extremely critical for microstructure quantification, property analysis, and materials design. The efficacy of this new procedure for the 3D characterization of microstructural components is demonstrated for a wide range of microstructures fabricated by conventional and additive manufacturing processes, along with quantitative comparisons against published experimental/analytical/simulated data in the literature. This approach is consistent with the goals of the integrated computational materials engineering (ICME) and Materials Genome Initiative for Global Competitiveness, which aims to deploy advanced materials more expeditiously.

CHAPTER I

Introduction

With emerging paradigm of integrated computational materials engineering (ICME) [1], multi-scale design optimization approaches for tailoring engineering properties through controlled processing parameters [2, 3, 4, 5, 6, 7] are of great interest to the design and manufacturing communities. Such simulations often involve solving microstructure-dependent properties, which require models beyond the grain-scale level that can accurately capture the underlying morphology and textural information of the materials [8, 9, 10]. The two-dimensional (2D) microstructures are convention-ally characterized through experimental instrumentations [11, 12, 13, 14]. However, sectional information obtained from 2D empirical characterization techniques is gen-erally insufficient for defining inherent microstructural parameters (e.g., neighbor con-nectivity, grain size, shape, boundary networks, etc.) [15, 16, 17, 18]. Nevertheless, these parameters are a critical aspect of the materials design and can strongly affect the capability of the structural systems to perform in their respective loading envi-ronments [19, 20, 21]. As a result, there has been a growing desire to develop accurate measurements, allowing for the direct acquisition of full-field three-dimensional (3D) microstructural information [22, 23, 24, 25, 26, 27, 28]. Hence, a comprehensive review of the existing 3D experimental acquisition techniques and numerical reconstruction frameworks, along with their limitations, are described next in Section 1.1. This

follows by introducing undirected graphical models and their applications for reconstructions of validated microstructural models, from the microscale level to part-scale geometries, respectively, in Sections 1.2 and 1.3. Thereafter, Sections 1.4-1.5 provide a brief background on the Cauchy-Crofton and peridynamics (PD) models that make the backbone of computational frameworks for modeling microstructural evolution and performance evaluations in this dissertation.

1.1 Overview of Microstructural Characterizations and Numerical Reconstruction Techniques

The need to precisely characterize 3D microstructures has led to the development of several experimental methods, which are mainly variants of two major procedures: serial sectioning [24, 25, 29, 30, 31, 32] and high-energy diffraction microscopy (HEDM) [33, 34, 35, 36, 37, 38, 39, 40, 41, 42, 43, 44]. Serial sectioning is a destructive approach in which layers of controlled thickness are sequentially polished away with high accuracy. This process enables metallographic etching and captures sectional images of a material's microstructure. Post-processing follows to render these 2D images into a solid 3D model. Contrary to serial sectioning, HEDM is a non-destructive technique that uses high-energy X-rays to probe a relatively bulk specimen. The diffraction pattern in this approach determines the crystallographic orientations of the microstructure. Acquiring 3D microstructures with the above experimental techniques is generally a prodigious process and requires the aid of expensive empirical scanning devices. Additionally, such procedures uncover microstructural information over a relatively small volume of materials. Therefore, a large number of specimens must be scanned and seamlessly merged to generate a component-scale computer-aided design (CAD) model. Such limitations reduce the general applicability of the experimental procedures, urging the development of robust computational reconstruc-

tion strategies from cheaper and faster 2D scanning techniques [45, 46, 47, 48, 49, 50]. As a result, recent developments towards generations of numerical methods to instantiate a virtual representation of solid 3D microstructures are described in detail in the following two paragraphs.

Numerical microstructure reconstruction is fast becoming an important topic of interest in the fields of materials modeling, simulation, and design [51]. Voronoi diagram (also known as Dirichlet tessellation or Thiessen tessellation) is a popular tool for constructing polycrystalline aggregates of metallic alloys [20, 52, 53]. A historical perspective for the development of the Voronoi diagram, including its implementations in crystallography and applications in a wide variety of scientific fields, is provided in Okabe [54]. Voronoi tessellation essentially consists of partitioning a plane into polygons whose boundaries are defined based on a set of nodes called generator points. Given these generators, the Voronoi polygons can then be synthesized using the algorithm described in Evans and Jones [55] to represent the underlying polycrystalline structures in metals. However, such representations largely provide an idealization of the microstructure and do not account for the complexities such as non-convex grain structures [56, 57, 58]. Alternatively, modern feature-matching reconstruction algorithms [20, 50, 59, 60, 61, 62, 63, 64, 65, 66, 67] can simulate various microstructural snapshots based on common sets of underlying features. Some of these features include marginal histograms [59], multi-resolution filter outputs (e.g., Gaussian and wavelet filters) [60, 61, 68], and point probability functions (e.g., auto-correlation function) [48, 62, 63, 64, 65, 66, 67]. Although these methods are efficient at modeling the global features of the microstructure, they usually fail at capturing the localized information in the form of per-pixel data, especially when reconstructing polycrystalline structures [61].

In addition, a popular geometry-based tool for 3D reconstructions of microstructures

is Dream.3D [69, 70, 71]. Dream.3D extracts statistical information (e.g., grain sizes, aspect ratios, and/or orientational features) and instantiates a full 3D representation that captures the overall crystallographic texture. However, the super-ellipsoidal approach associated with the Dream.3D reconstruction often tends to idealize the crystalline morphology [72] when modeling complexities such as non-equilibrium grain structures, non-convex shapes, twins, second phases, precipitates, and cell structures [53, 73]. These features naturally arise from manufacturing processes, playing an important role in the material's mechanical properties and performance. As a result, the particular problem of interest in this dissertation is to develop robust data-driven numerical models based on graph theoretic techniques to instantiate representative 3D microstructural datasets directly from 2D experimental images. To that extent, a comprehensive overview of the proposed image-based microstructural sampling and reconstruction strategy is outlined next.

1.2 Markov Random Fields for Microstructure Synthesis

It is experimentally observed that sufficiently-large windows from 2D micrographs or slices along a particular direction taken from a solid 3D microstructure generally 'look' alike [50, 51, 74, 75, 76]. Such an observation gives evidence to the notion of the stationary probability distribution underlying microstructural formations [46, 77, 78, 79, 80]. Accordingly, to reconstruct statistically-equivalent 2D microstructural images, one could start by sampling the conditional probability density (CPD) for the state of a pixel, given the known states of its neighbors, using reference 2D experimental images [81, 82, 83]. Here, during the sampling procedure, if only the nearest neighbors are deployed, the reconstruction strategy amounts to an Ising-type model [84, 85]. However, for general polycrystalline microstructures, the correlation lengths often span several pixels, and so a larger sampling window is usually required [86]. This approach is consistent with those proposed in the computer graphics com-

munity based on the Markov random field (MRF) technique [87, 88, 89] and texture reconstructions for materials modeling and design [50, 77, 78, 90, 91, 92, 93].

Furthermore, 3D microstructural information is crucial for understanding the relationships between the material structure and its properties. However, the 3D reference microstructures experimentally characterized by serial sectioning or X-ray computed tomography are expensive for routine applications due to the time and effort involved. On the contrary, the direct problem of measuring 2D surface images using optical or micro-diffraction methods is relatively easier. Using these 2D experimental images, inverse numerical models could be developed that would allow for the generations of full-field 3D microstructural maps of materials. Hence, the inverse problem of synthesizing 3D polycrystalline structures from 2D sectional images taken along orthogonal x, y, and z directions is of specific interest in this thesis. Generally, the sectional microstructural images obtained from empirical characterization techniques are in the form of pixels that contain red-green-blue (RGB) color channels, representing either scalars (e.g., phases, chemical composition), vectors (e.g., crystal orientations), or tensor states (e.g., stress, strain fields). The outcome of the inverse problem is a 3D solid model made of *voxels* (i.e., volumetric pixels) that are colored consistently with the 2D orthogonal experimental images, such that any arbitrary x, y, or z slice taken from the 3D solid model is 'similar' to its respective 2D exemplar. The measurement of similarities between the cross-sectional slices of the synthesized 3D microstructure and experimental 2D exemplars is based on a least-square distance (i.e., Euclidean-norm) cost function. Works in 3D microstructure reconstruction using MRF, as presented in Chapter II, have shown that such an approach can effectively capture global features (e.g., grain size, texture distribution, and grain neighborhood correlations) as well as localized information (e.g., precipitates and grain boundary networks) that closely consistent with the experimental images [91, 92, 93].

Moreover, it is possible to extend the data-driven reconstruction methodology in order to generate real-time descriptions of microstructural distributions at the part-scale geometry. Fundamental steps, as illustrated in Figure 1.1, include: (*i*) experimental acquisition of orthogonal scans of 2D microstructures, (*ii*) MRF for 3D reconstruction of the microstructural unit cell, and (*iii*) embedding the realized 3D microstructure into a virtual CAD geometry (i.e., a *digital twin*). This approach facilitates the rapid visualization of 3D maps of microstructural models at the component-scale level, enabling various user-defined processing modalities for customizable materials modeling and design. Next, an overview of prior microstructure reconstruction frameworks based on the MRF technique is discussed.

(a) Experimental image (polarized light microscopy, AA3002 alloy, 0.6x0.6 mm^2)

(b) 3D MRF reconstruction (0.6x0.6x0.6 mm^3)

(c) Virtual specimen at component-scale level

Characterization

Synthesis

Multi-scale representation
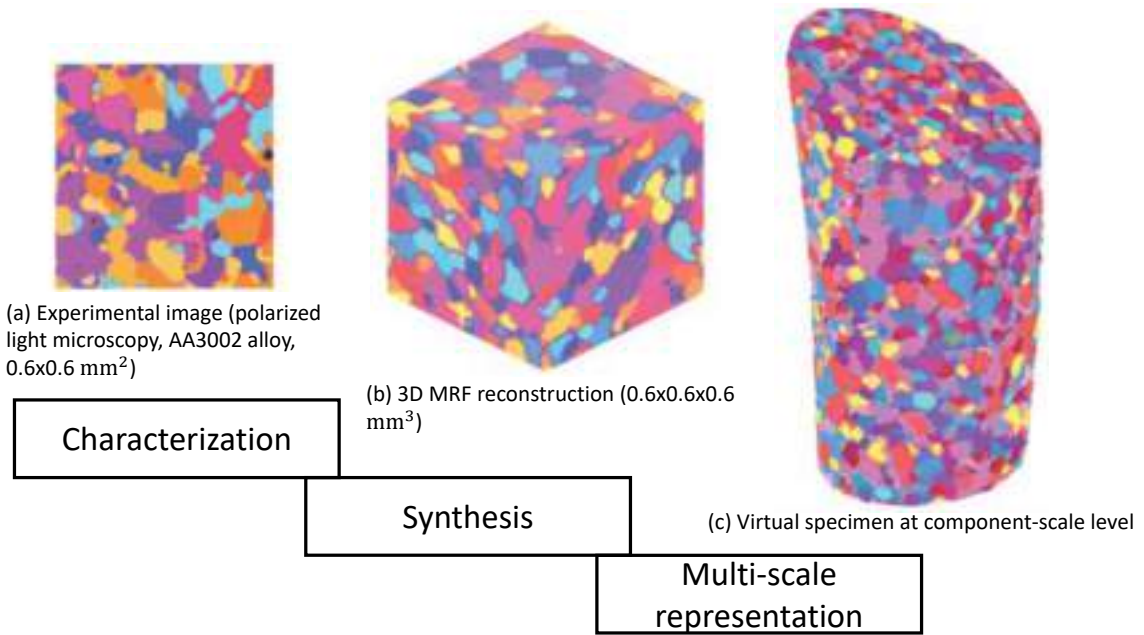
Figure 1.1: *Preliminaries of virtual synthesis of a CAD geometry with microstructural information: (a) experimental acquisition 2D microstructure, (b) MRF for 3D reconstruction of the microstructural unit cell, and (c) embedding the realized 3D microstructure into a virtual CAD geometry.*

1.2.1 Prior Works on Two-Dimensional Microstructural Simulations

Recent works on MRFs [77, 78, 90, 91, 92, 93] are generally based on Claude Shannon's generalized Markov chain [94]. In a one-dimensional (1D) problem, a set of

consecutive pixels/nodes is sequentially arranged to form a template to determine the probability density function (PDF) of the next pixel [95]. An example of the 1D Markov chain is illustrated in Figure 1.2(a). Likewise, a 2D microstructure can be represented, as depicted in Figure 1.2(b), where each particle within the $N \times N$ lattice taking values X_i with $i \in [1, 2, ..., N^2]$. In an Ising-tipe representation, X_i is composed of a binary variable, taking values of $+1$ or -1 (e.g., magnetic moment [84]). However, in crystallography, the values X_i may contain any of G color levels within the range $\{0, 1, ..., G - 1\}$ [96, 87].

Furthermore, contrary to the classical Ising model [84, 96], where each particle is bonded to only its nearest neighbors, as depicted in Figure 1.2(b), in an MRF representation, pixels can interact with multiple particles beyond their immediate neighbors [78, 97, 98]. Figure 1.2(c) demonstrates a 6×6 lattice structure with each pixel/node interacting with several neighbors. Accordingly, using such graph representation, an MRF can be defined as the joint probability density $P(\boldsymbol{X})$ on the set of all possible colorings $\boldsymbol{X}$, subject to a local Markovian property. The local Markov property states that the probability of value X_i, given the states of all neighbors, is conditionally independent of the entire dataset and can be sufficiently conditioned based on its limited number of surrounding particles, i.e., $P(X_i|\text{all particles except } i) \approx P(X_i|\text{neighbors of particle } i)$. The process for reconstruction of 2D microstructure based on an experimental exemplar is described next.

In the 2D MRF reconstruction framework, the synthesized microstructure, denoted as $\boldsymbol{S}$, is grown pixel-by-pixel, starting from a small patch that is randomly drawn from an experimental exemplar, denoted as $\boldsymbol{E}$. The algorithm first finds all windows in $\boldsymbol{E}$ that are similar (based on Euclidean-norm sense) to an unknown pixel's neighborhood from $\boldsymbol{S}$. One of these matching windows is chosen at random, and its center particle is taken to be the newly-synthesized pixel's value in the reconstructed model [78, 90]. A

| | (a) 1D Markov chain | (b) 2D Ising model | (c) 2D undirected graph |
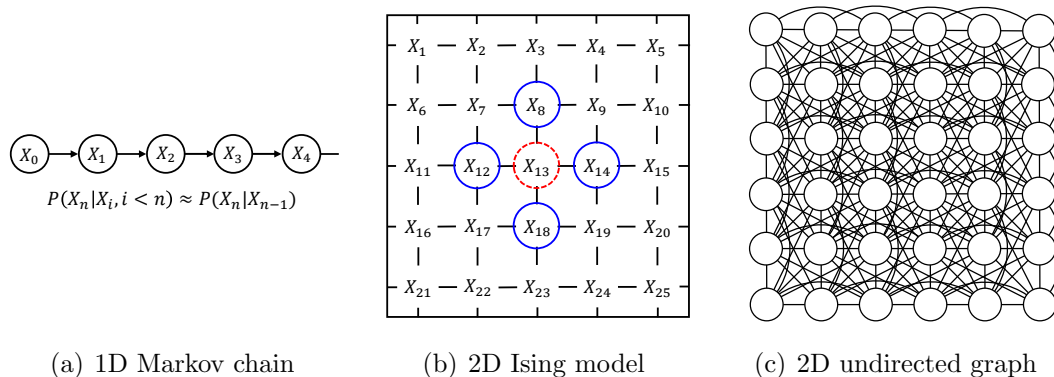
Figure 1.2: *The MRF as an undirected graphical model. Here, circles represent pixels in an image, and bonds are used to connect the neighboring particles: (a) a 1D Markov chain with first-order interactions; (b) a 2D Ising inference representation with the unknown pixel X_{13} conditioned on known nearest neighbors (first-order interactions); and (c) a 2D MRF of size 6×6 with higher-order interactions.*

schematic of the 2D reconstruction process is illustrated in Figure 1.3. Here, given the experimental exemplar, $\boldsymbol{E}$, a synthetic image, $\boldsymbol{S}$, that is statistically representative of $\boldsymbol{E}$ is to be generated. Accordingly, the MRF algorithm starts with a small seed image of size 2×2 that is randomly extracted from $\boldsymbol{E}$ and successively fills in the surrounding unknown pixels based on their known neighbors. For instance, for the unknown center pixel depicted at the center of 3×3 sampling window size on the right, the algorithm refers to $\boldsymbol{E}$ and finds the best-matching window that closely represents the spatial neighborhood of the unknown pixel in $\boldsymbol{S}$. It then takes the center pixel's RGB value from the window and fills the unknown pixel with the same coloring. The filling process continues until convergence, i.e., until all colors remain unchanged.

An example of the 2D reconstruction [78] of an aluminum alloy microstructure, characterized via polarised light microscopy [99], is shown in Figure 1.4. The microstructure is colored in terms of near-cubic (purple) or non-cubic (yellow/red) orientations based on the contrast effects as the specimen rotates relative to the polarised light directions. Using MRF reconstruction, a new microstructure is synthesized from a

sampling window size 3 × 3

Experimental Exemplar (*E*)   Initial Synthesized Image (*S*)   Progress During 1st Iteration
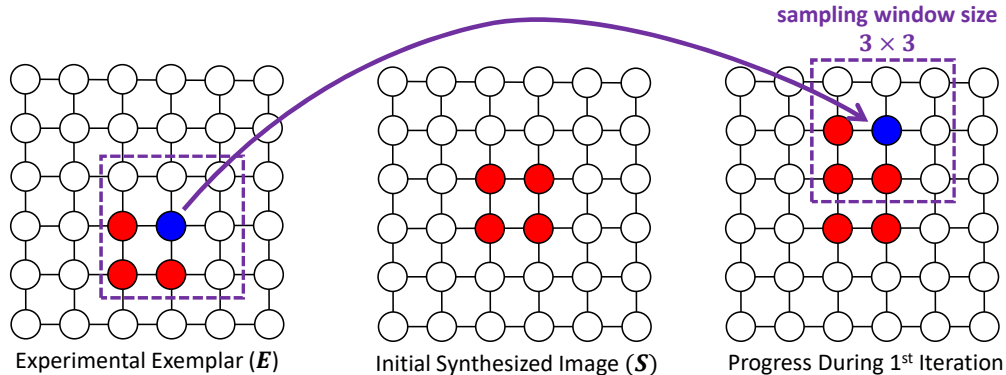
Figure 1.3: *The schematic of 2D MRF sampling approach: the synthesized image (denoted as **S**) is grown from a 2 × 2 seed image (shown in center). As the algorithm progresses, the unknown pixel (shown in blue) is estimated by searching for a window exhibiting a similar spatial neighborhood in the input experimental exemplar (denoted as **E**).*

150×170 pixelated input exemplar shown in Figure 1.4(a) using an interaction window size of 7×7 pixels. The MRF reconstruction is shown in Figure 1.4(b). Only a small part of the larger experimental image, depicted in Figure 1.4(c), is used for the reconstruction.

Moreover, the fraction of cube versus non-cube orientations between the 2D MRF reconstruction and original experimental image in Figure 1.4 is studied using color clouds. The color cloud representation of the orientations is an attempt at showing

(a) Input exemplar   (b) Reconstruction with MRF   (c) Original experimental image
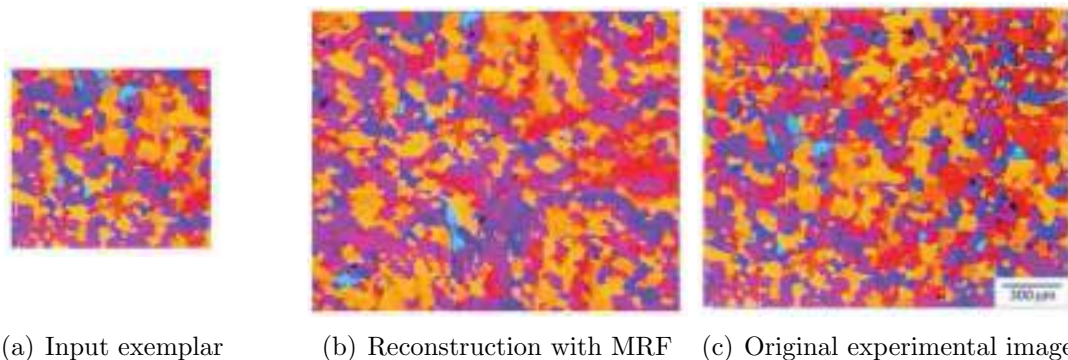
Figure 1.4: *An example of 2D MRF reconstruction technique: (a) input micrograph AA3002 aluminum alloy, (b) MRF reconstruction, and (c) larger microstructure from which the input image is extracted, also shown for comparison.*

9

the pixels in the *color space* rather than the Euclidean space, i.e., the *microstructure*. Hence, color densities are converted into random scattered dots around the spatial position assigned to the color, with the extent of the spatial position being determined by the frequency of which the RGB triplet appears in the image. The results depicted in Figure 1.5 demonstrate a consistent correlation between the color clouds of the reconstructed image and the experimental input image. The texture components (i.e., cube versus non-cube orientations) are well reproduced in the larger synthesized image. Next, in Section 1.2.2, the extension of the 2D sampling strategy is presented for 3D microstructure reconstruction.
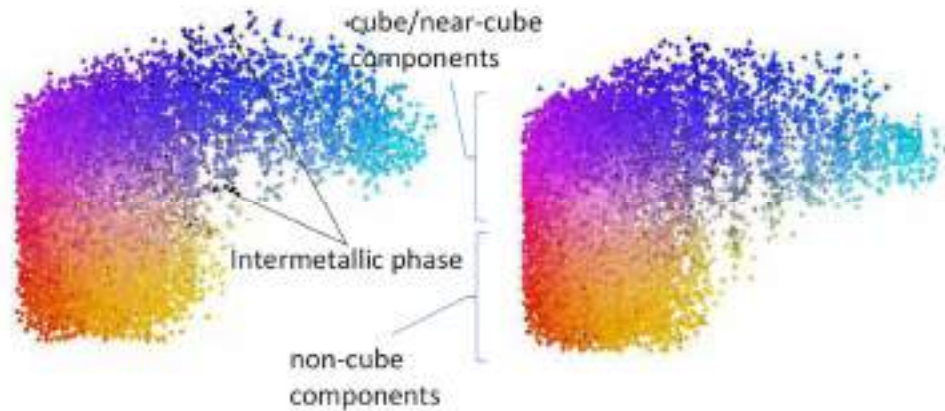
(a) Original experimental image   (b) Reconstruction with MRF

Figure 1.5: *Color blot method is used to compare the distribution of cube/near-cube regions, and intermetallic phases in the experimental and synthesized images.*

1.2.2   Preliminaries of Three-Dimensional Microstructural Synthesis

Similar to the 2D sampling approach, the MRF technique can be extended to generate 3D microstructures if 3D reference images are made available. However, acquiring 3D microstructures from serial sectioning or tomography, as outlined in Section 1.1, is a time-consuming and laborious process. Alternatively, the 3D MRF reconstruction technique, as proposed in Chapter II, can be adapted to generate 3D microstructures from limited numbers of experimentally-acquired 2D exemplars imaged along

orthogonal x, y, and z directions. The 3D MRF reconstruction process is based on an expectation-maximization algorithm [77, 80, 88, 89], carried out in a two-step process. In the first step, similar to the 2D sampling approach, the most likely color of a 3D voxel is estimated by the center pixel of the best-matching windows in all experimentally-obtained 2D exemplars. Note that only a limited (usually, a single) 2D experimental sample(s) are given along each cross-section, which means that the best match may not be an exact match. Thus, for each voxel, a set of three best-matching neighborhoods from all three orthogonal directions, are obtained, possibly with different colors that correspond to the center pixel. Subsequently, in the next step, a unique value of the color is found by weighting colors of best-matching windows through an expression obtained by setting the derivative of the energy function with respect to voxel color to zero [77]. Since the colors of all voxels change after each step, the set of closest input neighborhoods will also change. Hence, these two steps are iterated until convergence, i.e., until all voxels remain unchanged. Here, as an initial condition, a random RGB coloring from the input 2D images is assigned to each voxel. Thereafter, the above two-step optimization process is carried out iteratively in a multi-resolution (or multi-grid) fashion [89]: starting with a coarse voxel mesh while interpolating the results to a finer mesh once the coarser reconstructed image converges to a local minimum. Thereafter, a color histogram matching scheme follows after each iteration to enhance the global textural sampling procedure in the reconstruction framework. More details on the 3D unit cell reconstruction of microstructure using the MRF technique can be found in Chapter II.

In the following, the 3D MRF reconstruction approach is illustrated for an anisotropic lamellar microstructure, as illustrated in Figure 1.6(a), with solid circles in the z section, and interconnected lamellar structures shown in the x and y planes. Throughout every iteration in the MRF reconstruction algorithm, orthogonal cross-sections of all voxels are matched with the best-matching neighborhoods in the input experimen-

tal images. The resulting anisotropic 3D microstructure, depicted in Figure 1.6(b), captures the complex structure that arises from these 2D sectional images. The internal structure of the darker phase, as shown in Figures 1.6(c)-1.6(d), reveals an intricate internal structure that includes merging of interior lamellae while still maintaining statistical similarity to the experimental micrographs. Once a validated 3D microstructural unit cell from 2D experimental images is synthesized, one can embed the information in a larger-scale CAD model. The embedding process, along with a comprehensive literature survey of existing large-scale microstructural syntheses are discussed next.

(a)   (b)   (c)   (d)
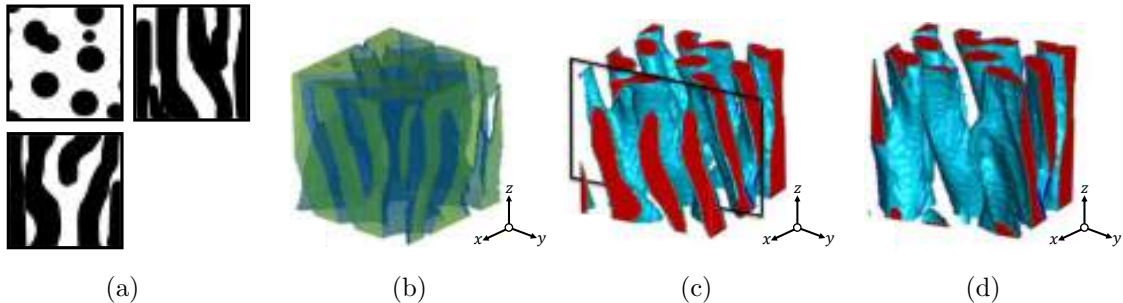
Figure 1.6: *An example of 3D MRF reconstruction technique for an anisotropic lamellar microstructure from three orthogonal slices: (a) orthogonal experimental 2D images closely resemble the cross-sections of the 3D reconstructed model, (b)-(c) MRF reconstruction depicting each phase, and (d) slice showing the internal structure of the lamellae.*

1.3 Generation of Large-Scale Microstructural Models in Metal Additive Manufacturing

Current numerical methods for the prediction of microstructural distributions in metal additive manufacturing are mainly physics-based techniques that require extensive computational efforts [7]. Amongst phase-field [100, 101, 102], kinetic Monte Carlo [103, 104, 105], and cellular automata [106, 107, 108] simulations, the phase-field modeling techniques are often considered the most accurate approaches that for instance can adequately capture the solute concentration, precipitates, and dendrite

shapes [109] in powder-bed fusion (PBF) [110, 111, 112] or direct energy deposition (DED) [113, 114, 115] processes. However, the advantage of using phase-field techniques is obscured by the required computational power, limiting the predictions to atomistic and continuum-length scales. Less costly than phase-field, cellular automata enables scalability for larger domain sizes. Yet, the accuracy can diminish considerably with increasing the cell size [116]. Additionally, the kinetic Monte Carlo simulations (e.g., SPPARKS) [104, 117] allow large-scale predictions but have difficulties simulating the texture distributions and reconstructing complex components, such as non-equilibrium grain structures.

Additionally, modern data-driven microstructure reconstruction methods based on the MRF technique [77, 78, 90, 91, 92, 93] can employ snapshots of conventional 2D prototypes to rapidly generate diverse groups of microstructures for new processing modalities in additive manufacturing, e.g., hatch spacing, layer thickness, scan velocity, and effective laser energy density. To that extent, in Chapter III, an image-based framework based on the MRF reconstruction technique [92] is employed for the real-time description of part-scale microstructure distribution of powder-based additively-manufactured (AM) materials by combining material flow fields that capture microstructural variations in grain growth orientation, anisotropy, and size scaling. Since the software builds global models based on locally-extracted images, it is termed LEGOMAT: Locally-Extracted Globally-Organized Microstructural Model. The first version of LEGOMAT, as presented in Chapter III, is able to embed a single 3D microstructure following the material flow path while allowing the user to specify parameters such as hatch spacing, layer thickness, and scan directions. Here, the algorithm reconstructs digital AM components, consisting of a dozen laser passes and deposition layers, encompassing microstructural information, by mapping every tetrahedral element within the CAD model to a microstructural domain. The algorithm utilizes an iterative patch-based convergence criterion, minimizing the dif-

ference between the tensor fields associated with embedding microstructures to the specified local parameters in the CAD geometry. Such an approach can be used for a rapid reconstruction of 3D maps of microstructures with billions of grains at the component-scale level with user-defined processing modalities. Table 1.1 provides a brief comparison of the LEGOMAT reconstruction approach against existing AM microstructure simulation techniques.

Table 1.1: *Comparison of computational methods for microstructure predictions in metal additive manufacturing against LEGOMAT.*

Method	Computational Cost	Benefit	Challenge
Phase-field	Extremely high	Simulates both solidifications and solid-state phase transformations	Is not suitable for large-scale predictions
Cellular automata	High/intermediate (depending on the spatial domain being constructed)	Simulates solid-state transformations, and enables crystallographic texture predictions	Accuracy of microstructure simulations depending on cell size
Kinetic Monte Carlo	Intermediate	Allows for large-scale domains (dozens of layers and passes)	Unable to predict crystallographic texture, and neglects the effect of temperature accumulation on melt pool geometry
LEGOMAT	Low	Allows for large-scale domains (dozens of layers and passes) and crystallographic texture predictions	Requires microstructural libraries and knowledge of grain growth directions

1.3.1 Preliminaries for Part-Scale Microstructural Synthesis Using LEGO-MAT

The 3D reconstruction methodology described in Section 1.2.2 can be extended to generate any part-scale geometry with underlying microstructural information. In principle, one could use sampling and optimization methodologies to embed microstructures over an engineering CAD model. To demonstrate this, the 3D unit cell microstructure of an aluminum alloy, as obtained directly from serial sectioning and diffraction

technique [118], is embedded into a CAD geometry shown in Figure 1.7. Here in this example, the 3D microstructural unit cell is in the form of voxels colored by grain IDs. The 3D microstructure is then sampled onto the CAD geometry using a patch-based extension of the sampling method described in Section 1.2.1. Additional features such as affine transformations (e.g., scaling and rotation) of the microstructural patches can also be implemented, enabling the user to generate location-specific textural orientation and grain sizes. Further details pertinent to part-scale microstructure generation can be found in Chapter III.

For the above image reconstruction strategies within materials science, where measured features contain physical considerations (e.g., phases, crystal orientations, chemical composition), it is crucial to incorporate the corresponding physics into the reconstruction technique. The MRF technique, as elaborated thus far, employs the full spectrum of RGB color domain for the representation of crystallographic orientations, leading to startlingly robust grain size and textural statistics when compared against experimental exemplars [78, 90, 91, 92, 93]. Such an approach, however, only
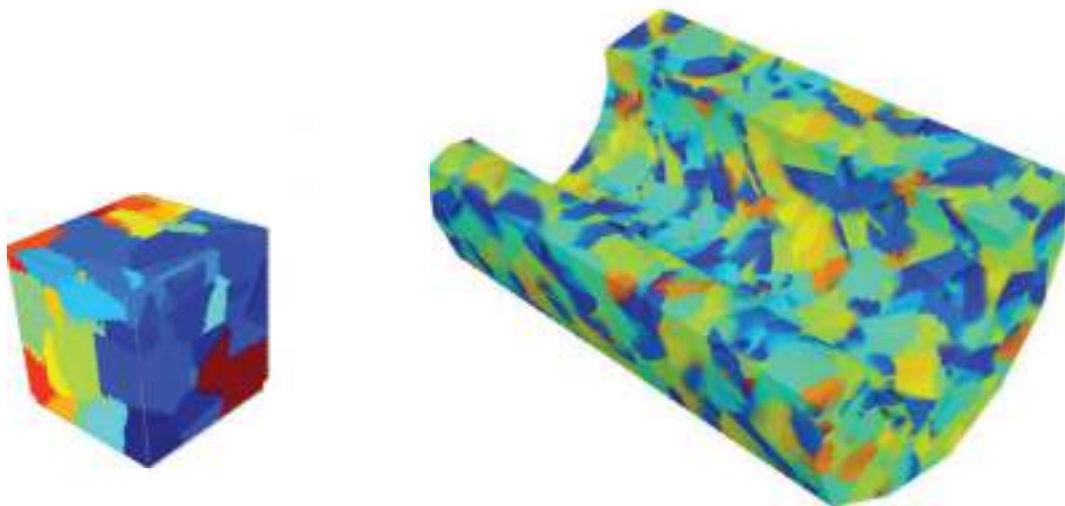
Figure 1.7: *An example of embedding a 3D microstructural representative volume element (left), obtained from serial sectioning, to generate component-scale geometry with microstructural information (right).*

samples local statistics over relatively-small windows and does not enforce any particular physics-based constraints on grain boundary (GB) structures. Nevertheless, in the materials science of GBs, certain facets are preferred, and GB junctions that form during solid-state sintering often follow certain geometric (angular) constraints [119, 120]. Hence, the development of a post-processing step for purposes of segmentation and grain size evolution of reconstructed models is presented next.

1.4 Physics-Based Methods for Simulation of Microstructural Evolution

Since the MRF approach [91, 92, 93] only samples local statistics in the form of per-pixel information and does not enforce any particular physics-based constraints on GB formation [119, 120], it is desirable to implement corresponding physics back into the reconstruction strategy. Accordingly, the need to understand and properly simulate particle shape evolution has led to several mathematical formulations, with the foremost being the *Wulff construction* [121, 122, 123, 124]. Theoretically, the equilibrium shape of a single crystalline structure can be instantiated by the gamma plot (also known as the Wulff plot), i.e., a plot of the orientation-dependent surface-free energy (hereon simply referred to as surface energy). Figure 1.8(a) represents the Wulff construction, where the shape (depicted by the orange line) minimizes the surface energy (represented by the blue line). Surface energies can often be obtained numerically from first principles calculations, such as density functional theory (DFT) [123]. However, these are not transferable to sintering processes as the shapes of interest pertain to higher temperature states (e.g., above 1000 $°C$). Figure 1.8(b) depicts the measured shape of a pore in alumina at 1600 $°C$, the simulated shape of which is illustrated in Figure 1.8(c) as obtained from data in the literature [125]. Generally, the surface energies can be obtained by inverting the crystalline shape

data (commonly referred to as *inverse Wulff construction*) [126, 127]. The inverse
Wulff construction essentially follows the Wulff construction wherein surface energies
are estimated by measuring distances between external surfaces and the center of the
particle because, by Wulff construction, the ratios of these distances are equal to the
ratios of the surface energies of facets at different orientations [128].

| (a) | (b) | (c) |
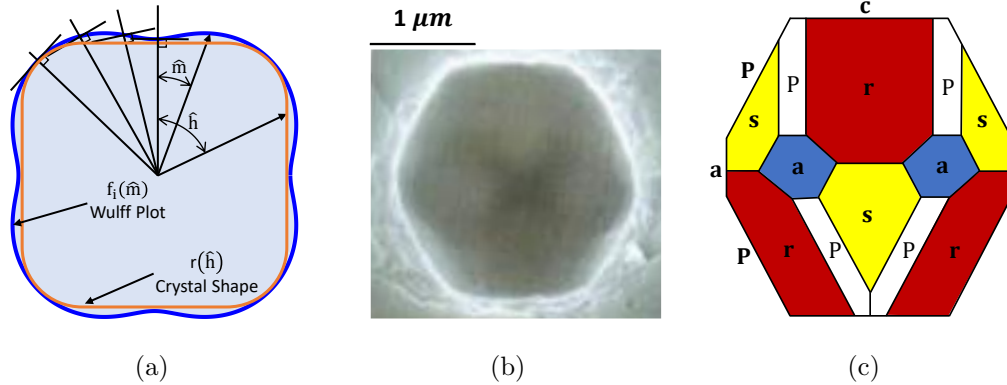
Figure 1.8: *Isolated crystalline structure and Wulff constructions: (a) Wulff shapes
of particles (depicted in orange) minimizing surface energy integral (represented by
blue line), (b) SEM depicting shape of a pore in alumina after 480h at 1600 °C (from
Reference [125]), and (c) the simulated Wulff shape.*

As a result, in Chapter IV, a physics-based algorithm based on graph theoretic tech-
niques is presented for the segmentation and simulations of the microstructural evolu-
tion of polycrystalline aggregates. The functional form of the proposed segmentation
algorithm is based on a Cauchy-Crofton formulation that embodies the underlying
energetic mechanisms of GB formation. Chapter IV accordingly demonstrates a path-
way toward implementation of microstructural evolutions as a post-processing step in
order to enhance the image-based reconstructions presented in Chapters II-III. The
benefits of implementing such physics-based constraints in microstructure reconstruc-
tions are three-fold: (*i*) the polycrystals are segmented from the color space output
of the MRF model, (*ii*) it provides the option to force desired grain shapes (e.g.,
equiaxed vs. columnar grains) during segmentation, and (*iii*) the GB angles/facets
can be adjusted based on global energetics.

1.4.1 Preliminaries for Simulations of Microstructural Evolutions Using Cauchy-Crofton Formula

The principal driving force for simulating particle shapes, coarsening, and grain growth is the reduction of surface energies. A particularly-challenging aspect for computations of surface energies is the estimation of curve lengths and surface areas when utilizing pixel and voxel-based discretizations in the microstructural domains. Accordingly, a mathematical model based on a novel graph representation of pixellated/voxelated images is developed that adopts systematic edge weight functions such that the cost of cutting a crystalline facet is close to the integral of the surface energy over the respective crystalline structure. In this approach, a known result in integral geometry based on Cauchy-Crofton formula is employed to identify globally minimum surface facets in both in 2D and 3D for a given set of constraint parameters.

Identification of the geometry of a particle's boundary (i.e., length in 2D or area in 3D domains) is ambiguous when using pixellated/voxelated images. Consider the case in Figure 1.9(a), where each pixel has a color depending on whether it is located inside or outside the GB. As indicated in Figure 1.9(b), the contour length of the interface is mostly equivocal in the pixelated representation. For instance, if one simply considers the length of the interfacial contours (i.e., lengths of the horizontal/vertical steps that are separating the two colors), they would overestimate the GB interfacial length. This problem is accordingly termed *metrication error* [129, 130]. To overcome the metrication error, researchers in the material science community tend to employ highly-dense unstructured grids that properly align with the GB's interface, as shown in Figure 1.9(c) [131, 132, 133, 134]. However, this approach leads to mesh dependency when computing the contour length. As a result, a novel mathematical model from the field of integral geometry for the prediction of the GB based on the Cauchy-Crofton relation is presented in Chapter IV, where the inherent

dependency on mesh discretization is removed. The main idea in such an approach is that given a contour, the total length of the curve is closely proportional to the number of intersections that it makes at various angles. In terms of pixel/voxel discretizations, Crofton's formula uses interaction weight functions such as those shown in Figure 1.9(d) that remove the effect of metrication while still retaining the benefits of directly using microscopic measurements, as obtained from aforementioned microscopy or reconstruction procedures.

| (a) | (b) | (c) | (d) |
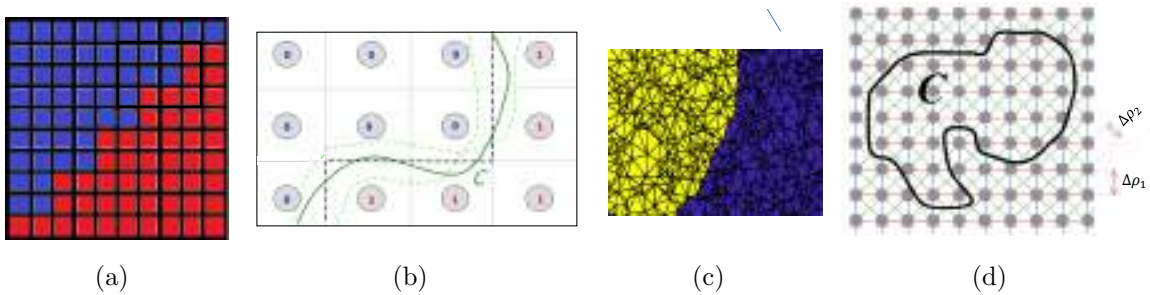
Figure 1.9: *Computing length of a particle's boundary: (a) the length of a particle boundary is ambiguous when using pixellated images, (b) a depiction of possible lengths of the particle boundary, which in return affects the crystalline shape, (c) use of unstructured meshes to capture grain boundaries leads to mesh dependence, and (d) the length of the boundary can be found using Crofton formula based on intersection count.*

Consequently, the problem of particle segmentation is formulated as a graph labeling problem, where each voxel in the microstructural image is treated as a vertex of a simple undirected graph with an energy cost function formulated to a Potts form. Generally, the Potts function consists of two terms; the first term, often referred to as the data term, penalizes deviations from the image data, whereas the second term, referred to as the smoothening term, describes the interface properties between vertices with different labels. Hence, minimizing the energy would allow a preferential selection of facets with minimal energies while retaining the bulk phases measured in the original image. The details of the Cauchy-Crofton formulation are provided in Chapter IV. There, the methodology based on integral Riemannian geometry is

presented for the estimation of the expected surface areas based on the graph label-ing problem on pixellated/voxelated discretizations. This framework is generalized to incorporate arbitrary surface energies (e.g., equiaxed or elongated grain structures) and extended to include the evolution and segmentation of 3D microstructural recon-structions described previously.

1.5 Overview of Property Evaluations for Polycrystalline Microstructure Images

Once the pixel/voxel-based discretization of the underlying polycrystalline structure is instantiated through microscopy or the MRF reconstruction technique, as described in Sections 1.1-1.4, the simulations of mechanical performance/properties (e.g., elastic modulus, yield strength, residual strength, slip response, fatigue life, and stress/strain contours) of the material in industrial applications need to be performed [135]. Recent experiments have observed microscale strain localizations, in the form of fine shear bands, on the surface of polycrystals undergoing large deformation using a combi-nation of scanning electron microscopy (SEM) and digital image correlation (DIC) [136, 137]. These microscale shear bands not only can act as precursors for damage and failure but also have been associated with degradation in material strength, also known as *strain softening* [138, 139]. Similarly, slip localization naturally occurs in deforming polycrystalline aggregates in the form of lamellar bands with fractions of microns in thickness [140]. The spacing between such slip bands decreases with in-creasing plastic deformation [141]. Instabilities such as Lüders bands are preceded by strain-softening and advanced by the formation of new slip bands parallel to the old ones [142, 143, 144, 145]. Micropillar compression experiments [146, 147, 148] have revealed plastic behavior characterized by strain bursts under stress-controlled conditions, where such bursts are associated with local strain gradients in the interior
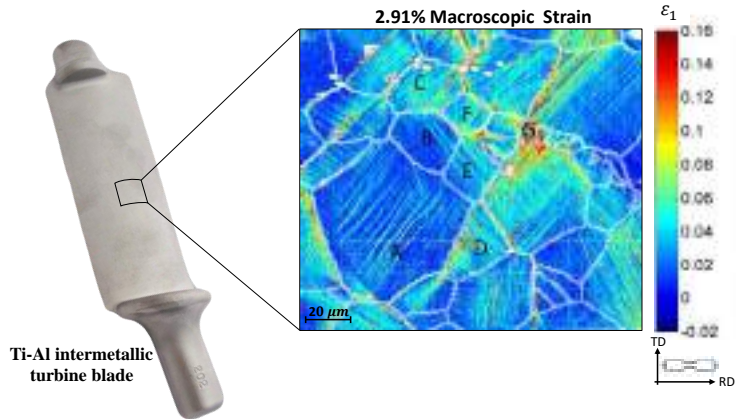
Figure 1.10: *Tensile strain field in a Ti-Al intermetallic turbine blade, as experimentally seen using microscale SEM-DIC, depict intense localization bands within each grain.*

of the material [149]. In-situ SEM-DIC experiments under monotonic loading, as illustrated in Figure 1.10, also reveal sub-grain slip localizations even under positive work-hardening rates [136, 150].

One of the popular numerical techniques for simulating deformation response in polycrystalline aggregates is the crystal plasticity finite element method (CPFEM) [151, 20], which describes the dislocation motions and their interactions using continuum mechanics principles. Finite element (FE) modeling of polycrystalline materials using crystal plasticity (CP) theory [131, 132, 133, 134] has allowed for a greater understanding of mechanical behavior (e.g., stress and strain response), texture evolution, and crystallographic slip response. Such a capability has led to the development of high-strength aluminum alloys [152, 153], soft magnetic materials with low hysteresis [154], and multi-functional alloys with high-field induced strains [155, 156, 157]. Nonetheless, the standard finite element model (FEMs) often run into difficulties when modeling the local mechanical response of materials in the presence of discontinuities (e.g., voids, cracks, and soft precipitates). Additionally, the magnitude of mechanical quantities computed by the standard FEM is also highly dependent on the elemental size [135, 158], necessitating costly iterative mesh re-

finement procedures along with considerable experimental efforts for numerical calibration [159, 160]. Improvements have been proposed for CPFEM to address the issue of mesh dependency. The extended-FEM (X-FEM) and variational multiscale method (VMM) enrich the computational space by introducing a sharp, discontinuous interpolating function to trigger strain localizations [161]. Nevertheless, these techniques are not capable of predicting small-scale localizations naturally as a consequence of the underlying principles. Thus, imperfections are often imposed to trigger the strain localizations [21]. Alternatively, the mesh-free state-based PD technique [162, 163, 164, 165], which replaces the traditional differential equations with an integral form of the non-local continuum mechanics theory, has attracted significant attention for predicting damage nucleation and propagation with an intrinsic characteristic length-scale [166, 167, 168, 169]. Figure 1.11 compares the strain fields obtained by crystal plasticity PD (CPPD) and CPFEM simulations against reference experimental imaging. While both CPPD and CPFEM capture comparable trends in the strain fields, CPPD depicts localized patterns similar to the experiments that are typically shown to be well-resolved, and otherwise smoothed out by CPFEM.
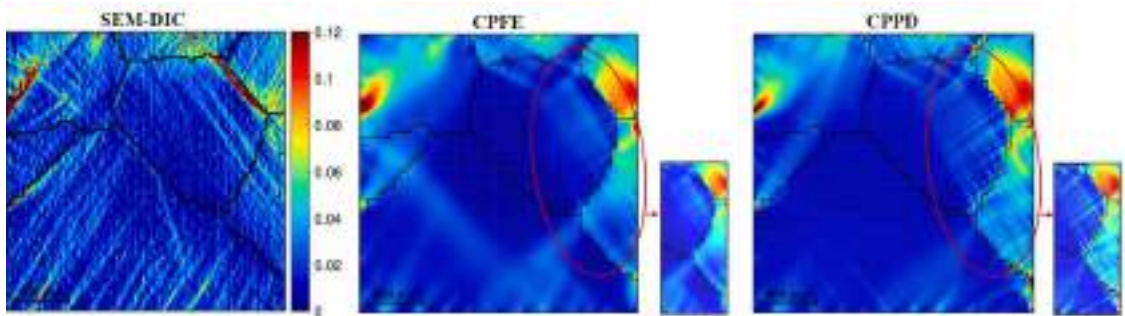
Figure 1.11: *Experimental instrumentations such as SEM with the combination of DIC have shown microscale strain localizations on the surface of polycrystalline aggregates can act as precursors for damage nucleation and degradation in material strength. However, unlike conventional CPFEM, CPPD models are shown to be capable of predicting such finite-scale localizations naturally as a consequence of the underlying physics.*

22

1.5.1 Image-Based Crystal Plasticity Analyses Using Peridynamics

In the initial version of the PD as introduced in Siling [162], a bond-based technique was employed in which forces in-between material particles are assumed to be pair-wise, i.e., equal and direction-reversed. As a consequence of such an assumption, the bond-based PD method is restricted to fixed values of Poisson's ratio [170, 171]. This limits the general applicability of the bond-based PD approach and the possibility for simulations of complex material deformations such as in plasticity [172]. A more comprehensive PD scheme, commonly referred to as the non-ordinary state-based PD (NOSBPD), was subsequently proposed in which force states are defined by the interactions between the material particles [170]. This presents a generalized form of the PD, allowing material particles to carry forces in all directions [173]. In this approach, the non-locality is conveniently applied without the need to alter the underlying constitutive principles and failure criteria [164, 174]. Accordingly, this dissertation employs a non-ordinary state-based version of the PD theory to model microstructural domains consisting of material particles (i.e., pixels in 2D and voxels in 3D) with a uniform discretization as directly obtained via experimental characterization processes or numerical reconstruction techniques.

Although PD has been proven effective in the prediction of discontinuities and damage initiations [164, 165, 175], there are still intrinsic issues with its numerical implementations, among which are (i) zero-energy (also known as hourglass) instability modes, due to the weak integral formulation in non-local approximations of the deformation gradient tensor [166, 176, 177, 178], and (ii) non-trivial treatment of boundary conditions (BCs) [179, 180]. Although recent papers, as discussed in Section 1.5.2, have attempted to resolve the hourglass-like instabilities, they have failed to remove the instability modes altogether. In addition, since PD utilizes an integral-form equation of motion, i.e., different from the partial differential equations (PDEs) in the conven-

tional continuum mechanics, the enforcement of kinematic constraints at boundaries is not able to follow the standard approach [181].

1.5.2 Zero-Energy Instabilities Modes in Crystal Plasticity Peridynamics

A particular problem of interest in this thesis using NOSBPD is the presence of zero-energy instability modes [166, 176, 177, 178]. Such instability modes often worsen with enlarged horizon interactions, inter-particle spacing, and regions with high-strain gradients. Recently, different frameworks have been proposed to mitigate the spurious instability oscillations by introducing fictitious bonds between material particles [179, 182, 183]. Even though these bond-based techniques provide an artificial stiffness for stability by introducing a supplementary term of various forms to the force vector states, they do not provide resolutions to the fundamental instability problem. They are also highly sensitive to particle spacing and require additional parameters that need to be calibrated on a case-by-case basis through repetitive numerical simulations [184]. Moreover, to alleviate the zero-energy mode oscillations, Wu et al. [181] proposed the replacement of the displacement components at the center material particles with a weighted-average displacement of all neighboring particles in their respective horizon interactions. Although this approach eliminates the need for supplementary fictitious bonds, the issue of zero-energy mode oscillations still appears to remain, particularly in the strain/stress fields. In Luo et al. [185], each finite horizon within a nearest-neighbor PD family is assigned a stress point at which derivatives of field variables are computed in order to enhance particle connectivity. Such an approach is further improved in Cui et al. [186] by introducing higher-order PD derivatives, incorporating horizon sizes beyond nearest-neighbor interactions. Subsequent improvements are also proposed based on higher-order operators to solve the non-local PD equations up to an arbitrary degree of accuracy [187, 188, 189, 190, 191, 192]. Although these techniques address the fundamental problem in the correspondence

formulation that leads to zero-energy oscillations, they often require extensive computational efforts, reducing the general applicability of such stabilization procedures in routine mechanical simulations. Accordingly, in Chapter V, a new novel methodology based on the Taylor series expansion of the deformation gradient is proposed for stabilization control across both 2D and 3D material domains.

1.5.3 Improvements to Crystal Plasticity Peridynamics Approach

Chapter V in this dissertation presents, for the first time, a fully explicit implementation of the 3D NOSBPD technique for modeling elastoplastic quasi-static mechanical deformation of 3D polycrystalline for capturing strain localization against experimental comparison [21]. Previous work by Littlewood [182] presents an implementation of elasto-crystal viscoplastic material model within the framework of PD using a simple baseline model of a hard inclusion in a single crystalline structure. The main focus of this work is to study and compare the material response in the vicinity of a cracked and uncracked particle in single crystallines with different orientations.

Moreover, since in microstructural simulations, uniform pixel or voxel-based structured discretizations can be conveniently obtained from microscopy and numerical acquisition techniques [20, 92, 93], Chapter V proposes particle interaction weight functions for uniformly-structured grids based on the NOSBPD implementation of Newmark's dynamic method with artificial damping [193]. In this approach, a tensor formulation of the constraint equations on discrete influence weight functions for both 1D and higher-dimensional microstructural problems is presented based on Taylor series expansion of the deformation gradient [173]. Furthermore, to treat erroneous BCs, additional material layers are introduced to enforce consistent displacement across the boundary particles [77]. As a result, Chapter V presents the first 3D PD implementation of CP by combining key algorithmic features: (*i*) an explicit time-stepping scheme with artificial damping, (*ii*) time-step selection procedure, (*iii*)

higher-order stabilization of zero-energy modes, and (iv) BC implementation. The proposed CPPD model is validated by comparing the deformation texture development in 2D and 3D polycrystals under various compression deformations using three different horizon interactions. Finally, the strain hotspots are assessed in more detail, where CPPD is shown to be successful in capturing localization patterns observed in the experiments (especially those arising at the GBs) or showing signatures of hotspots that are delocalized in the CPFEM simulations.

1.6   Outline of Thesis

This thesis attempts to address the process-microstructure-performance relationships in polycrystalline metals by developing numerical tools that allow for the reconstruction and failure analysis of microstructural aggregates. The image reconstruction and microstructure evolution framework that spans over Chapters II-IV integrates undirected graphical models with adaptive sectional experimental images from electron backscatter diffraction (EBSD) or polarized light microscopy and utilizes analytical tools for quantification/validation of crystallographic features (e.g., grain size statistics, orientation distribution function (ODF), nearest-neighbor grain correlation, etc.) being reconstructed and/or evolved under solid-state sintering. Chapter V presents a NOSBPD technique with CP that provides insight into the microstructure-property relations in metals. Consequently, the thesis is organized as follows:

Chapter II describes the 3D MRF reconstruction process for generating a 3D microstructural representative volume element (RVE) from three orthogonal 2D polycrystalline, imaged on x, y, and z cross sections. The proposed algorithm builds 3D models by matching slices at different voxels to the representative input 2D micrographs, following an optimization procedure that ensures sampled windows meshes seamlessly together in the 3D RVE. This chapter also examines the algorithm's ac-

curate representation of crystallographic orientations and grain morphologies for a variety of micrographs obtained by EBSD and polarized light microscopy. It is demonstrated that the MRF approach simulates both 1-point (e.g., grain size, texture distribution, shape moments) and 2-point (e.g., misorientation angles, grain boundary networks) correlations that closely resemble those from the experimental/analytical models.

Chapter III covers the embedding process of synthesized RVE models over a part-scale CAD geometry. The embedding algorithm employs a constrained graph-based optimization technique that maps every FE within the CAD model to a microstructural domain, while incorporating features such as affine transformations (e.g., scaling and rotation) of the 3D RVE to allow for the generation of anisotropic and spatially-varying crystallographic textures that are applicable in additive manufacturing. The new computational approach enables the generation of 3D global maps of AM microstructures in real-time from a limited set of 2D orthogonal images, using known microstructural patterns seen in experimental characterization techniques. Once generated, these synthetic large-scale AM microstructures can be used in various material performance simulations (e.g., material mechanics, conductivity, etc.) or otherwise provide insights for multi-dimensional analyses involving desirable processing modalities (e.g., scanning pattern, laser velocity, power, etc.) and performance metrics, which is a challenging task to achieve by experimental means alone.

Chapter IV build on the previous two chapters and delivers a novel physics-based numerical framework based on the graph-cuts for simulations of microstructural evolution. In this approach, an energy optimization principle based on the Cauchy-Crofton formulation, which embodies the underlying energetic mechanisms of GB formation, is developed to find the globally-minimum facets (i.e., Wulff shape) in 2D/3D material domains for a given set of Riemannian metrics. The specific computational parame-

terization of the grain boundary characteristics and corresponding growth velocities are obtained via a synchrotron X–ray-based technique. The efficacy of the proposed numerical technique is demonstrated in several case studies and compared against data from in-situ high-energy tomography techniques.

Chapter V provides a workflow for cross-validation of mechanical performance/properties of pixelated/voxelated discretizations as directly obtained from microscopy or MRF numerical techniques. The elastoplastic response of polycrystalline aggregates is computationally simulated by the NOSBPD technique. Despite the advantages of PD formulation of CP for the treatment of deformation in the presence of high-strain gradients, a particular drawback of NOSBPD is the presence of zero-energy instability modes, primarily due to the weak integral formulation in non-local approximations of the deformation gradient tensor. As a result, this chapter focuses on a computational scheme for eliminating the zero-energy mode oscillations using a choice of influence functions that improve the truncation error in a higher-order Taylor series expansion of the deformation gradient. The higher-order stabilization scheme is demonstrated for multi-dimensional examples involving polycrystalline and composite microstructures, along with comparisons against the conventional FEM.

Chapter VI concludes with the contributions and proposes future directions for this dissertation.

CHAPTER II

Three-Dimensional Polycrystalline Microstructure Reconstruction From Orthogonal Images Using Markov Random Field Technique

In this chapter, the numerical method for reconstructing 3D microstructures from 2D sections imaged on orthogonal planes is presented. The algorithm reconstructs 3D models by sampling voxel neighborhoods to representative 2D micrographs based upon a Markovian assumption. The sampling is followed by an optimization procedure, ensuring smoothness across the orthogonal sections of the synthesized voxels. Previous 3D MRF microstructure reconstruction techniques were restricted to traditional grayscale images only. This method now enables the use of the entire RGB spectrum, employing a *histogram matching* step. This chapter additionally examines the algorithm's accurate representation of orientations and morphologies, encompassing a variety of micrographs from EBSD and polarized light microscopy. Using the MRF algorithm, it is shown that both global features such as grain size, texture distribution, and grain neighborhood correlations, as well as localized information such as precipitates and grain boundary networks, closely resemble those shown in the experimental images.

The chapter is organized as follows. First, an overview of the MRF algorithm for unit-

29

cell reconstructions of 3D microstructure from 2D orthogonal images is provided in Section 2.1. There, the effect of sampling windows size on the statistical correlation function of the 3D synthesized model as well as the breakdown of computational cost pertaining to the MRF algorithm is also discussed. This follows by Section 2.2 demonstrating various examples of polycrystalline reconstructions for comparisons of grain sizes statistics, orientation distributions, and nearest neighbor correlations among synthesized and experimental exemplars.

2.1   3D Microstructure Reconstructions From 2D Orthogonal Images

The objective here is to first present the MRF reconstruction methodology in Section 2.1.1. The *histogram matching* extension, which provides the ability to reconstruct color images, is described next in Section 2.1.2. Following this in Section 2.1.3, the computational costs associated with MRF modeling and its correlation with sampling window size is discussed in detail.

2.1.1   MRF Optimization Algorithm

The input to the MRF algorithm consists of either a single experimental image (for isotropic structure) or three orthogonal planar exemplars (for anisotropic microstructure), whereas the output is a statistically-equivalent 3D solid model of the same microstructure. In the following discussion, let $\boldsymbol{S}^x$, $\boldsymbol{S}^y$, and $\boldsymbol{S}^z$ denote the set of orthogonal slices of the microstructure along their respective x, y, and z directions. The symbol $\boldsymbol{V}$ indicates the synthesized 3D microstructure, and $\boldsymbol{V}_v$ represents the color of voxel v in the solid synthesized microstructure. In this algorithm, three layers of color in the RGB channels (as a triplet) are allowed for representation of the phase information. The exploitation of RGB scheme allows for significant flexibility

in the choice of the microstructural colormap, enabling direct visualization of colors throughout the reconstruction.

The sampling algorithm presented here is consistent with the Reference [77], except that the averaging step is performed on each color channel separately. For pedagogy, let us consider how one of the RGB color channels in the 3D microstructure is reconstructed. The hypothesis in the sampling approach is that the color assigned to any voxel follows a Markovian property. That is, the PDF of a voxel given the states of its spatial neighborhood is independent of the entire dataset. Thus, here the neighbors are chosen over relatively small user-assigned windows around the voxel v. The vectors denoting the spatial neighborhood of voxel v in the slices orthogonal to the x, y, and z axes, as depicted in Figure 2.1(a), are denoted as $\boldsymbol{V}_v^x$, $\boldsymbol{V}_v^y$, and $\boldsymbol{V}_v^z$, respectively. Let $\boldsymbol{S}^{x,w}$, $\boldsymbol{S}^{y,w}$, and $\boldsymbol{S}^{z,w}$ denote a window of the same size in the input 2D micrographs. In order to find the coloring of an unknown voxel v, given the neighbor voxels in the x-plane, one needs to compute the CPD of $\boldsymbol{V}_v$ given colorings of x-plane neighbors of v. Explicit construction of such a probability density is often computationally intractable. An alternative approach is to estimate the most likely RGB value of the voxel v by identifying a window $\boldsymbol{S}^{x,w}$ that is most similar to $\boldsymbol{V}_v^x$ in the 2D input micrograph. This window, as shown in Figure 2.1(b), is denoted by $\boldsymbol{S}_v^x$. Similarly, matching windows to the y and the z plane neighborhoods of voxel v are found in the corresponding 2D sectional images, which are respectively denoted as $\boldsymbol{S}_v^y$ and $\boldsymbol{S}_v^z$. Each of these matching windows $\boldsymbol{S}_v^x$, $\boldsymbol{S}_v^y$, and $\boldsymbol{S}_v^z$ may have different RGB coloring for the center pixel. Thus, an optimization methodology is employed to effectively merge these disparate values and to identify a unique coloring for the voxel v. The optimization approach is described next.

Let the value $\boldsymbol{V}_{v,u}^x$ denote the RGB coloring of voxel u in the neighborhood $\boldsymbol{V}_v^x$. Let the values $\boldsymbol{S}_{v,u}^x$ and $\boldsymbol{S}_u^{x,w}$, respectively denote the RGB color of pixel u in the windows

(a) 3D synthesized model   (b) 2D orthogonal exemplars
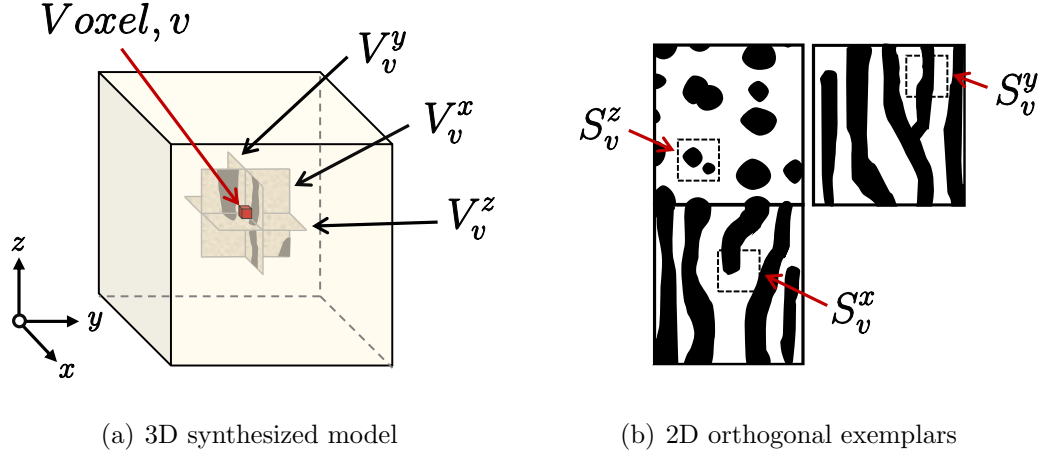
Figure 2.1: *The schematic of 3D microstructure reconstruction from three 2D orthogonal images using MRF sampling algorithm: (a) the neighborhoods of the voxel v in the slices orthogonal to the x, y, and z axes are shown. (b) The windows in the input 2D micrograph shown in dotted lines are denoted by $\boldsymbol{S}_v^i$ for $i = x$, y, and z. These windows closely resemble the neighborhoods of the voxel, v, in the 3D synthesized model.*

$\boldsymbol{S}_v^x$ and $\boldsymbol{S}^{x,w}$. Consequently, the 3D microstructure can be synthesized by posing the problem as a Euclidean distance (L_2) minimization of the energy function (also known as the cost function) formulated below:

$$E(\boldsymbol{V}) = \sum_{i \in \{x,y,z\}} \sum_{v} \sum_{u} \omega_{v,u}^i \|\boldsymbol{V}_{v,u}^i - \boldsymbol{S}_{v,u}^i\|_2^2 \tag{2.1}$$

where $\|.\|_2$ represents the L_2 norm, and $\omega_{v,u}^i$ denotes a per-pixel radially-symmetric weighting factor. In order to preserve the short-range correlations of the microstructure, a Gaussian weighting scheme is used such that the weights for nearby pixels are taken to be higher than pixels farther away. For instance, if the pixel u along the x-plane is placed at a relative location (y_u, z_u) (in lattice units) with respect to the voxel v, then $\omega_{v,u}^x$ is given as:

$$\omega_{v,u}^{x} = \frac{\exp\left(-\dfrac{y_{u}^{2} + z_{u}^{2}}{2\sigma^{2}}\right)}{\sum_{j} \exp\left(-\dfrac{y_{j}^{2} + z_{j}^{2}}{2\sigma^{2}}\right)} \tag{2.2}$$

the summation in the denominator is taken over all the pixels in $\boldsymbol{S}^{x,w}$. Here, the standard deviation σ, is taken to be $0.16 \times w$, where w refers to the window size [90]. Similarly, $\omega_{v,u}^{y}$ and $\omega_{v,u}^{z}$, respectively denoting per-pixel weighting factors in $\boldsymbol{S}^{y,w}$ and $\boldsymbol{S}^{z,w}$, can be computed.

The optimization of the energy function $E(\boldsymbol{V})$ in Equation (2.1), is carried out in two steps: (i) the *searching* step, and (ii) the *expectation* step. In the first step, the energy function is minimized with respect to $\boldsymbol{S}_{v}^{i}$. The assumption here is that the most likely sample from the CPD of the center voxel in the 3D model along a particular direction is the center pixel of the best-matching window in an experimentally-obtained 2D slice on the corresponding plane. Hence, the best-matching neighborhood of voxel v along the x-plane is selected by solving the following minimization problem:

$$\boldsymbol{S}_{v}^{x} = \arg\min_{\boldsymbol{S}^{x,w}} \sum_{u} \omega_{v,u}^{x} \|\boldsymbol{V}_{v,u}^{x} - \boldsymbol{S}_{u}^{x,w}\|_{2}^{2} \tag{2.3}$$

This is an exhaustive search that compares all the windows in the input 2D micrograph to the corresponding x–slice neighborhood of voxel v and identifies a window that leads to a minimum weighted squared distance.

Thus, for each voxel v, a set of three best-matching neighborhoods within the experimental images are identified. Generally, the center pixel values in each of these neighborhoods are composed of different RGB colorings. Yet, a unique value of v

needs to be found by weighting colors pertaining to location v in not only the matching windows of voxel v but also its surroundings. This is done in the second step of the optimization procedure. Here, the optimal color of voxel v is computed by setting the derivative of the energy function with respect to $\boldsymbol{V}_v$ to zero. This leads to the following weighted-average expression for the color of voxel v:

$$\boldsymbol{V}_v = (\sum_{i\in\{x,y,z\}} \sum_u \omega^i_{u,v} \boldsymbol{S}^i_{u,v}) / (\sum_{i\in\{x,y,z\}} \sum_u \omega^i_{u,v}) \tag{2.4}$$

note that the subscripts u and v are switched in the above expression, compared to Equation (2.1). This implies that the optimal color of the voxel v is the weighted-average of the colors at locations corresponding to voxel v in the best-matching windows of voxels u (i.e., $\boldsymbol{S}^i_u$) found within the synthesized 3D solid microstructure. The color channels are averaged independently in the equation above. Since $\boldsymbol{V}_v$ is continuously changing after each step, the set of closest input neighborhoods $\boldsymbol{S}^i_v$ varies accordingly. Hence, the above two steps are repeated until convergence; that is until the set $\boldsymbol{S}^i_v$ remains unchanged.

2.1.2 Histogram Matching Algorithm

The primary issue with the above equations is the assumption that the color space is continuous. Such an assumption allows for the partial derivatives of the energy function, $E(\boldsymbol{V})$, to be obtained. However, the color space is typically discrete and range bound. Consequently, the averaging performed in Equation (2.4), always tends to shrink the color levels. For example the color level 0 always tends to increase, since it is repeatedly averaged with all the color levels that are greater or equal to 0. Similarly, the maximum color level G of each RGB channel (typically equals to 255) has a tendency to decrease, due to it being averaged with other color levels that are always smaller or equal to G. However, the general assumption in MRF reconstruction

34

remains, that the two datasets (i.e., input images and solid synthesized model) have the same range of color levels. To solve this issue, *histogram matching* (also known as histogram specification) is applied after each iteration, allowing for the color levels to be appropriately stretched back to values from 0 to G at each channel. In the image processing community [194, 195], this step is often performed to achieve consistent intensity (e.g., illumination or contrast) across two datasets (i.e., the reference and the target images).

The stretching process is based on the cumulative distribution function (CDF) of colors in the input micrographs. That means, the 2D micrographs are considered as the reference images, whereas the 3D solid model's color histogram is to be matched following each iteration. Here, all three orthogonal images are lumped together in order to generate the reference CDF. In current implementation, the *histogram matching* algorithm is applied separately, for each color channel. Given the reference (2D) and the target (3D) images, the color histograms are obtained by binning the pixels into G discrete intervals. Subsequently, CDFs of the two color histograms H_{2D} and H_{3D} are computed and normalized. For each voxel (with RGB color value $\boldsymbol{V}_v$) in the 3D synthesized model, the color level X in the 2D image is found such that $H_{2D}(X) = H_{3D}(\boldsymbol{V}_v)$. Accordingly, the color level associated with $\boldsymbol{V}_v$ (in the 3D model) is replaced with color level X (from the 2D images). The *histogram matching* scheme is depicted in Figure 2.2.

The application of *histogram matching* using an RGB image is illustrated in Figure 2.3. The first reconstruction (shown on the top of Figure 2.3) is based on the algorithm presented in Reference [77]. Note, that phase information (e.g., grain size, shape, orientation, boundary networks, etc.) is lost within the first few iterations. Though with the current implementation (using *histogram matching*) the volume fraction of each color level is preserved and stays consistent with the input images;
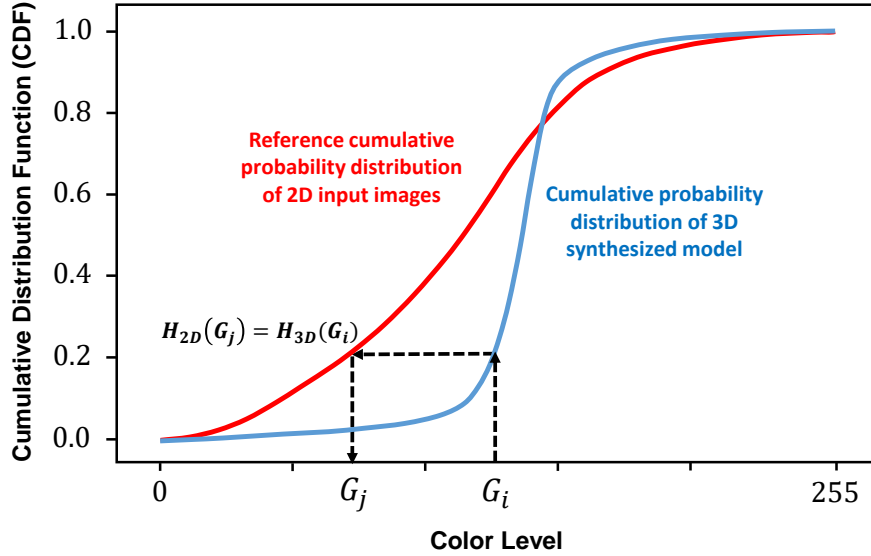
Figure 2.2: *The histogram matching algorithm: given the reference (2D) and the target (3D) images, the color histograms are obtained by binning the colors into 255 discrete intervals. Next, CDFs of the two color histograms, denoted as $H_{2D}(.)$ and $H_{3D}(.)$, are then computed and normalized. The color level G_i in the synthesized 3D image is switched for each RGB channel independently. The new color G_j has the same CDF as input 2D exemplars.*

the result of which is the reconstruction of a representative 3D microstructure. In Figure 2.3, the same 2D micrograph is considered as the reference image for both reconstruction schemes. The snapshots of the 3D solid models at iterations 0, 7, 21, and 35 are shown, respectively.

Although the general approach presented in this chapter is not tied to a specific input resolution, all the input images are resampled to 128×128 pixels prior to MRF reconstruction. As a starting condition for 3D reconstruction, a random RGB color from the input 2D images is assigned to each voxel v. The reconstruction process is then carried out in a multi-resolution (or multi-grid) fashion [77]: starting with a coarse voxel mesh while progressively interpolating the results to a finer mesh once the coarser 3D image has converged to a local optimum. The multi-resolution approach drastically increases the convergence rate to an optimum cost function. As such,
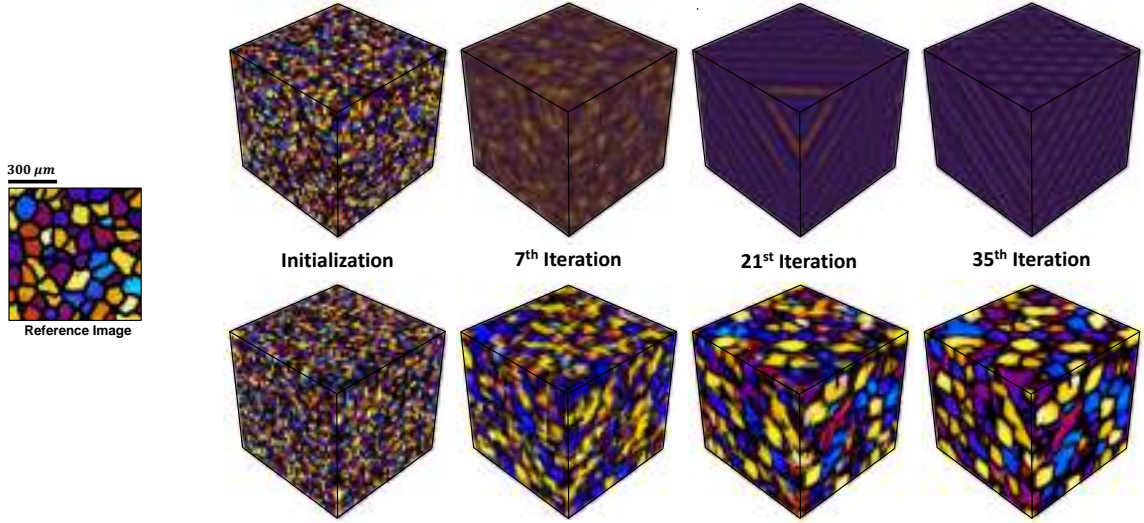
Figure 2.3: *The effect of histogram matching on synthesized 3D microstructure: without histogram matching (as illustrated on the first row), the color space continuously shrinks and phase information is lost after the first few iterations; contrarily, with histogram matching (as shown on the bottom), the color space remains consistent with the input reference image throughout the simulation.*

three resolution levels (32^3, 64^3, and 128^3) are used for presented reconstructions. Respective window sizes of 7, 9, and 11 are chosen in the three resolution levels. The pseudocode in Algorithm 1 summarizes the sampling and reconstruction schemes:

2.1.3 Computational Cost vs. Window Size

Although there are several free parameters throughout the reconstruction strategy, window size is chosen to be the only adjustable variable for simplicity. Window size plays an important role in the MRF reconstruction model. At window sizes much smaller than the correlation lengths, false matches lead to inaccurate reconstructions [78]. Contrarily, at very large window sizes, not enough matching windows can be identified. Additionally, high window sizes require extensive computational power for both sampling and reconstruction. Between these two extremes, there is an ideal window size that needs to be realized through numerical trials. Normally, the window size should be larger than the average microstructural features, especially at

---

Algorithm 1: Pseudocode for 3D MRF reconstruction of size N^3.

Require: Orthogonal 2D images of size N^2 as well as the sampling window size for each level

Ensure: Optimum cost function given in Equation (2.1)

Resize 2D images to L^2, where $L = N/4$

Initialize a random 3D microstructure of size L^3, where $L = N/4$

Initialize level index: $level \leftarrow 1$

while *level < 4* **do**

    while *level unchanged* **do**

        Use Equation (2.3) to identify the best matching windows in orthogonal 2D images (*Searching Step*)

        Use Equation (2.4) to compute the expected voxel channel values (*Expectation Step*)

        for *each channel* **do**

            Compute CDFs of 2D images (H_{2D}) and 3D solid model (H_{3D})

            Find color level X in the 2D images such that $H_{2D}(X) = H_{3D}(\mathbf{V}_v)$

            Replace voxel channel color with color level X (*Histogram Matching Step*)

        end

    end

    Update image size: $L \leftarrow 2L$

    Resize 3D synthesized model to L^3 and 2D images to L^2

    Update level index: $level \leftarrow level + 1$

end

---

low-resolution levels. This allows the MRF algorithm to capture global attributes (e.g., grain boundary network, inter-connectivity, size distribution, etc.) in the polycrystalline microstructure at early iterations while reconstructing finer details (e.g., precipitate, twin, etc.) at later resolution levels. Figure **??** depicts the effect of window size (within the highest resolution level, i.e., 128^3) on the quality of synthesized 3D images. Note that only odd values are allowed for the window size so that the sampled neighborhood is symmetric around the center voxel.

The computational cost to obtain 3D solid models is directly related to the voxel resolution. In other words, higher voxel resolutions (128^3 vs. 64^3) require more computational power to perform *searching* and *expectation steps*. Table 2.1 provides a breakdown of the computational cost as a function of the sampling window size as-

sociated with the highest resolution level. The processing times here correspond to the solid models shown in Figure **??**. Note, simulation times generally vary drastically depending on the iteration number as well as the features being sampled. As shown in Table 2.1, most of the computational burden is related to identifying the best-matching windows in the orthogonal input images (i.e., *searching step*). This is expected as the searching stage consists of an exhaustive approach that compares all the windows in the input micrographs, in order to identify a neighborhood that leads to a minimum weighted squared distance, formulated in Equation (2.3). Furthermore, note that the computational burden associated with performing the *histogram matching* step is typically related to the 3D voxel resolution, and it is independent of the sampling window size. Given this reason, *histogram matching* is excluded from Table 2.1. At the highest grid resolution, the typical time required to perform *histogram matching* is minimal (usually fewer than 5 seconds) when compared to *expectation* and *searching steps*.

Table 2.1: *Breakdown of computational cost associated within the highest resolution (128 × 128 × 128) level of the MRF reconstruction as a function of the sampling window size. For reference, all reconstructions are executed using a single processor and 4 GB of memory.*

	Relative Time (%) Searching Step	Relative Time (%) Expectation Step	Average Time (min)
Window Size 3	65.05	34.95	1.69
Window Size 5	71.94	28.06	5.53
Window Size 7	74.31	25.69	11.09
Window Size 9	78.80	21.20	20.37
Window Size 11	81.31	18.69	32.25

In light of the above discussion regarding the computational burden caused by different window sizes, it is expected that mapping sample images to lower resolutions would significantly improve the overall computational efficiency of the MRF algorithm. Note, the reconstruction scheme presented in this chapter is not tied to a specific input resolution. Thus, any 2D image resolution can be reconstructed, if

needed. The implication is that the user should specify a sufficient pixel resolution that would capture the phenomena of interest.

2.2 Unit-Cell Microstructure Reconstruction Examples

In Section 2.2.1, the MRF algorithm is examined by comparing grain sizes for a previously studied sample in Reference [77] using the Saltykov method. Thereafter in Sections 2.2.2 and 2.2.3, the reconstruction procedure is applied to an orthogonal set of EBSD images and polarized light microscope data of an aluminum alloy to study the nearest neighbor correlation and texture distributions after the MRF reconstruction procedure.

2.2.1 Example 1: Polycrystalline Micrograph With Equiaxed Structure

Here, a polycrystal grayscale micrograph is chosen as an input exemplar. The image is reconstructed in the RGB color space using the algorithm, presented in Section 2.1. In this example, the ability of MRF to accurately model 3D grain size distribution as predicted by the stereological/analytical formula is studied. Such validation has not been done previously for 3D MRF algorithms. Grain size distribution is essential for simulating mechanical properties in polycrystals via Hall-Petch models [196, 197, 198, 199]. The Saltykov approximation method, outlined in Appendix A, provides a closed-form expression for the 3D grain sizes, given a 2D observation. The assumption is that the grains are approximately spherical or equiaxed, which is reasonable given that only one micrograph, as depicted in Figure 2.4(a) is used for all three orthogonal sections. The resultant 3D reconstruction is shown in Figure 2.4(b).

In this example, the 2D grain statistics are captured in the following manner. The incomplete grains on the outer-edge adjacent to the borders of the image are removed. For every inner grain, the maximum possible diameter at all its boundary points is

<div align="center">

50 Pixels

(a) 2D exemplar   (b) 3D reconstructed model

</div>
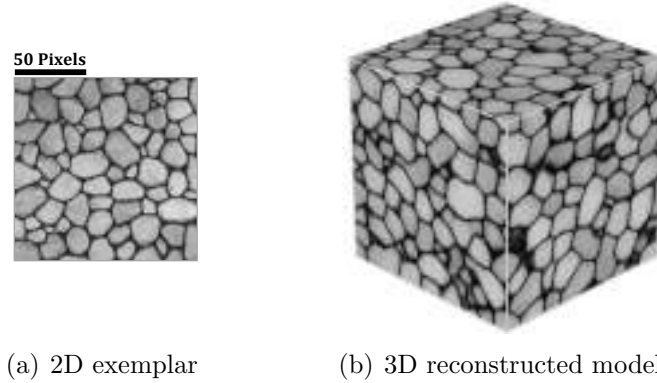
Figure 2.4: *A polycrystalline microstructure reconstruction example with equiaxed grains: (a) the experimental 2D microstructure is used as an exemplar for 3D MRF reconstruction; (b) the 3D MRF synthesized model depicting similar grain morphology as shown in input exemplar.*

computed in pixel units. The PDF of the raw diameter data is then calculated over 24 bins using a log-normal distribution. The result of the Saltykov algorithm on this data is plotted as solid points in Figure 2.5. To obtain the 3D grain size distribution, edge detection is first performed on the solid synthesized structure, followed by segmentation of grains. In the segmentation algorithm, grains are described by the number of connected faces (six-fold connectivity) of a similar color. To obtain the grain size distribution, the same process is followed as that used in the 2D image. That is the external grains are first eliminated, and for each inner grain, the maximum diameter for every boundary voxel is obtained. As illustrated in Figure 2.5, a close agreement between the Saltykov estimation and the sampled grain size distribution from the MRF reconstruction is observed. Minor deviations from Saltykov estimates are seen at the tails of the distribution, where the 3D reconstruction marginally predicts a higher probability of small and large grains.

For the 3D model presented here, one reference image is supplied as an exemplar for all three orthogonal directions. Therefore, the model is assumed to be an equiaxed microstructure. This implies that slices taken from the diagonal directions should

<center>(a)   (b)</center>
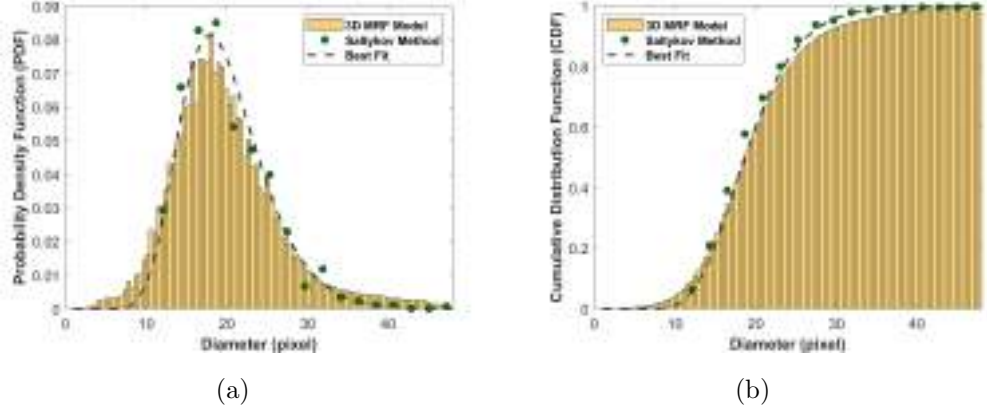
Figure 2.5: *Comparison of grain size statistics of 3D synthesized model against Saltykov analytical approximations: (a) comparison of the PDFs of the 3D synthesized microstructure and the Saltykov prediction, and (b) comparison of the CDFs of the 3D realised grain size distribution with Saltykov prediction.*

exhibit similar statistics as orthogonal planes in the solid 3D model. Hence, for comparison, the grain size distributions of these sections are examined next. The process is carried out for total of 15 orthogonal planes (five in each direction) and 18 oblique sections (three in every face-diagonal direction) across the 3D microstructure shown in Figure 2.4(b). A number of these sectional images are shown in Figure 2.6.

To acquire the sectional grain size statistics, same process as described for 2D input image, is employed. The partial grains adjacent to the borders are eliminated, and for each inner grain, the maximum diameter at every boundary node is computed using pixel units. The probability densities of diameters for both orthogonal and diagonal sections are then computed over 50 bins. As illustrated in Figure 2.7, a close trend between the two data is observed.

2.2.2   Example 2: Reconstruction of EBSD Images

The following EBSD images, shown in Figure 2.8, correspond to an Al-Li alloy after forging to 2.5-inch thickness. Here unlike the previous example in Section 2.2.1, three orthogonal sections are characterized and used for the MRF reconstruction.

<center>42</center>
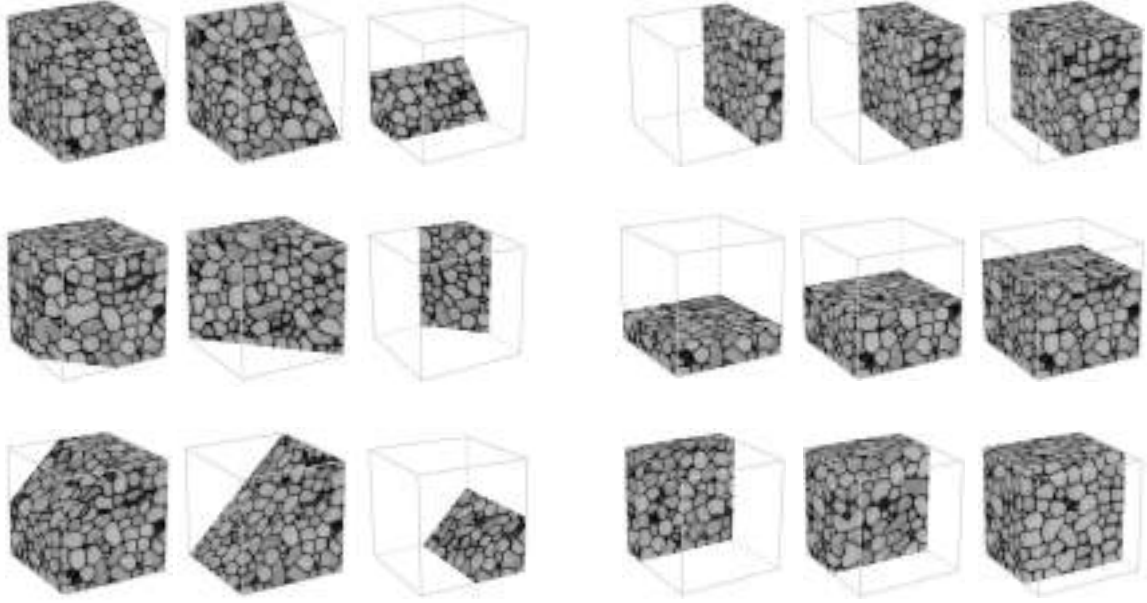
Figure 2.6: *The oblique versus orthogonal cross sections of 3D polycrystalline microstructure: several sectional images of the 3D reconstructed model along diagonal (shown on the left) and orthogonal (shown on the right) directions are illustrated. The grain sizes and shapes along these sections nearly resemble the 2D reference image.*

Experimentally, EBSD data is obtained using a SEM equipped with detectors normal to each plane. To ensure a consistent MRF sampling across all EBSD sections, the orientations need to be remapped such that all the images are observed in the same sample coordinate system.

Here, the raw Euler angle data is mapped to nodes in a discretized ODF. The ODF is a one-point probability function, describing the volume fractions of crystals as a function of orientation. The orientation is represented here using an axis-angle format, as initially proposed by Rodrigues. The format is based on the unique association of orientation with an axis of rotation, $\boldsymbol{n}$, and a counterclockwise rotation angle, θ about $\boldsymbol{n}$ [92, 200, 201]. The Rodrigues' parametrization, $\boldsymbol{r}$, is scaled as $\boldsymbol{r} = \mathbf{n} \cdot \tan(\frac{\theta}{2})$. A proper rotation, $\boldsymbol{R}$, relates the sample orientation to the crystal orientation. Here, the example material's lattice is of cubic symmetry. The 3D orientation space can be reduced to a small subset called the fundamental region that accounts for the
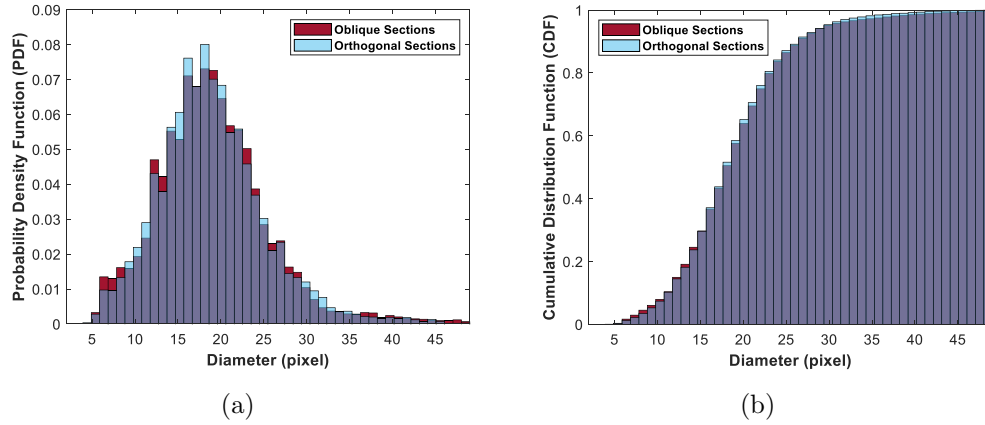
Figure 2.7: *Comparison of grain size statistics along orthogonal and diagonal cross sections in synthesized 3D model: (a) comparison of the PDFs of 3D grain sizes distributions along oblique and orthogonal sections from the 3D synthesized model, and (b) comparison of the CDFs of the 3D grain diameters across oblique and orthogonal cross sections.*

cubic symmetry. The resulting Rodrigues fundamental region is shown in Figure **??**. For numerical analysis, the fundamental region is discretized using a finite-element mesh. The symmetry of the ODF is an additional constraint that must be properly considered. Due to cubic symmetries, several of the nodes in the grid are equivalent. Hence, the ODF is represented using a smaller set of independent nodes, as shown in Figures **??** and **??**.

Each EBSD data point is mapped to the closest independent node in the ODF. If the orientation is close to a non-independent node, the node that is the symmetry equivalent to the dependent node is chosen. The 2D EBSD images are then colored according to the nodal numbers. A simple choice for the colormap is to apply the Rodrigues vector itself as an RGB triplet, after normalization of each Rodrigues vector component to a range of $[0, 255]$. Figure 2.8 shows the orthogonal set of images from the rolled sample; grains are elongated in the rolling direction and shortened in the transverse directions. The grains are colored based on the colormap in Figure 2.8, depicting the color of each independent node in the ODF. Here, three 700×700 EBSD
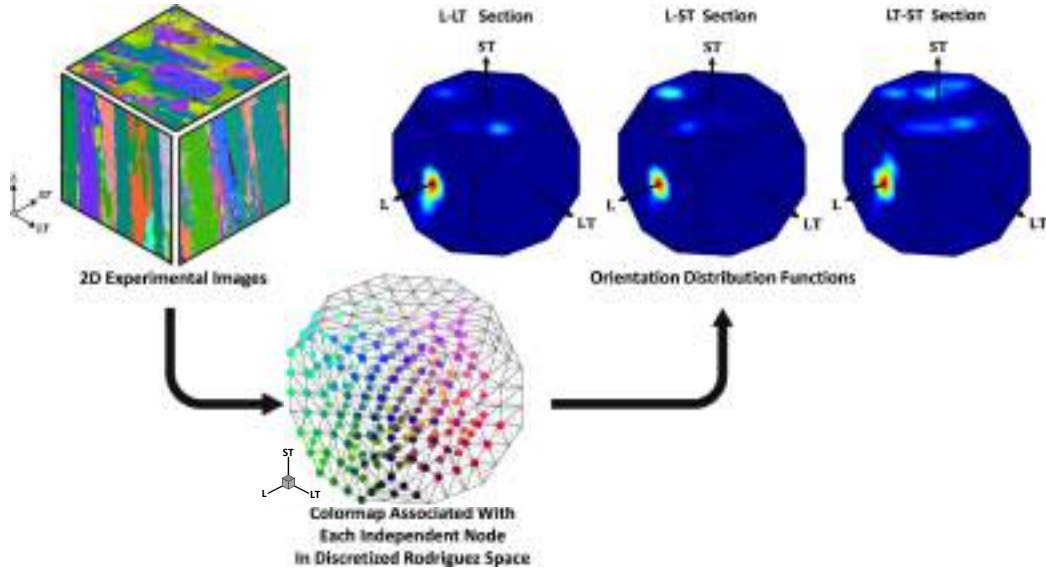
Figure 2.8: *The colormap used for the representation of the independent nodes within the fundamental Rodrigues region: the colormap shows the RGB values of individual nodes in the face-centered cubic (FCC) fundamental region. The pixels' RGB values in the raw 2D orthogonal EBSD images are mapped to the closest node (in Euclidean norm sense) using the colormap. The ODFs of all three input images are similar, after adjusting the relative alignments of the detectors with respect to the sample.*

sections are chosen and resampled to 128×128 images for the reconstruction. The ODFs for all three sections are comparable after correcting for the relative orientation of the camera with respect to the sample, as shown in Figure 2.8. The 3D reconstruction from the MRF algorithm is shown in Figure **??**. A number of different sections of the reconstructed model are also shown in Figure **??**.

In this example, the averaging algorithm tends to smoothen the noise, supplying an overall smoother reconstruction compared to the input 2D images which consist of a significant amount of noise. Since the averaging step in the MRF algorithm introduces deviation of colors from the original 2D colors, an additional step is employed to remap the colors to the independent nodes of the ODF through the colormap shown in Figure 2.8. The top four closest colors in the ODF that closely match the voxel color are first identified. If there is a match within a threshold error, the voxel color remains unaltered. Otherwise, the closest colors (in Euclidean norm sense) to the

colormap are found. Of those colors identified as best matching, one randomly picked to recolor the voxel. It is found that the resulting ODF and pole figures of the MRF reconstructed microstructure match exceptionally well with the measured ODF, as shown in Figures 2.9 and 2.10.

(a) 2D experimental exemplars   (b) 3D synthesized model
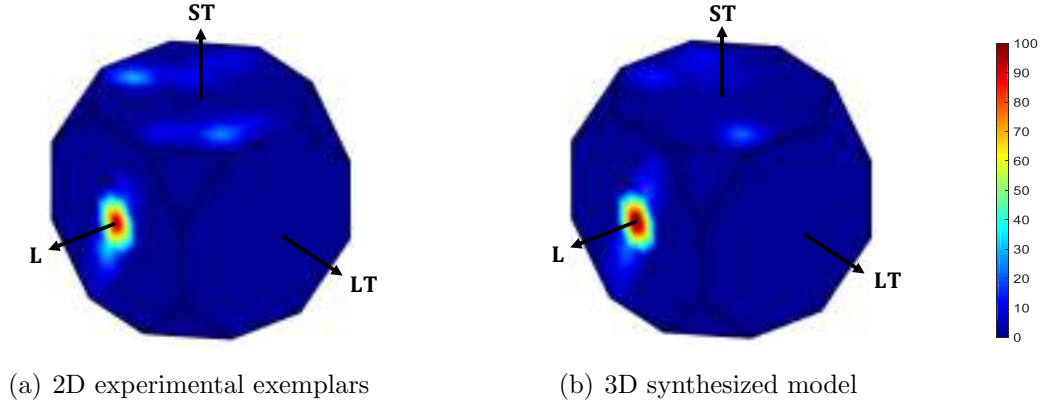
Figure 2.9: *Comparison of the ODFs between (a) the input 2D experimental exemplars and (b) synthesized 3D microstructure.*

In addition, a new analysis is performed, where the reconstruction algorithm is run sequentially, using random slices of the previous 3D model as the input exemplars for the next synthesis. Such an analysis exemplifies the ability of the 3D MRF algorithm to preserve texture statistics, generate distinct equivalent microstructures, and, most importantly, demonstrate how errors can be accumulated after every reconstruction. An example of sequential reconstruction is shown in Figure 2.11. These sequences reveal that our 3D reconstruction strategy succeeds in preserving the original exemplars' orientation distribution. Despite all, due to the averaging step, at some point, deviations in statistics are expected to creep into reconstructions. This is only anticipated after a relatively larger number of reconstructions.

2.2.3 Example 3: Reconstruction of Polarized Light Micrograph

The third example is an optical micrograph of an aluminum alloy obtained from Reference [202]. In this example, the microstructure is first etched with Barker's reagent.

(a) 2D experimental exemplars   (b) 3D synthesized model
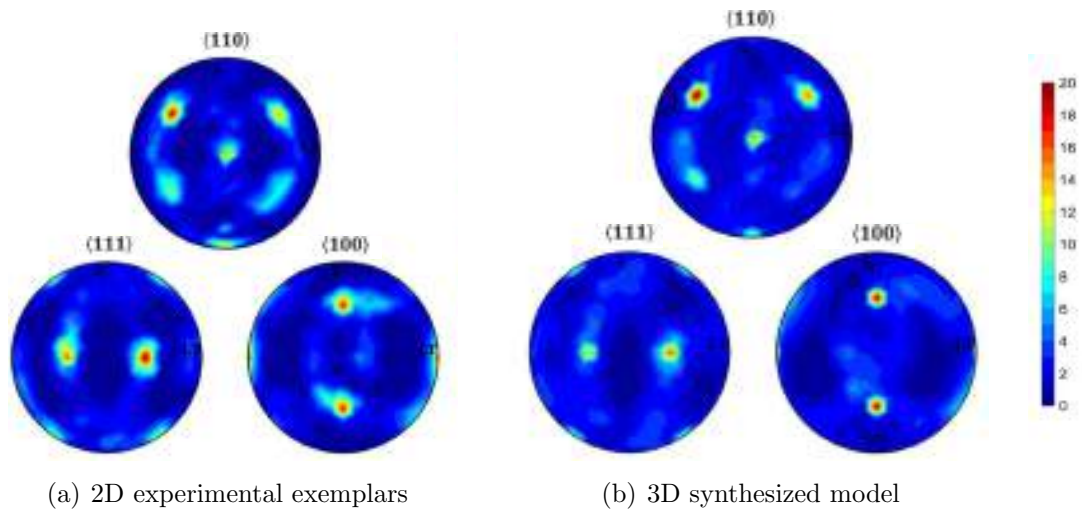
Figure 2.10: *Comparison of the pole figures between (a) the input 2D experimental exemplars and (b) synthesized 3D microstructure.*
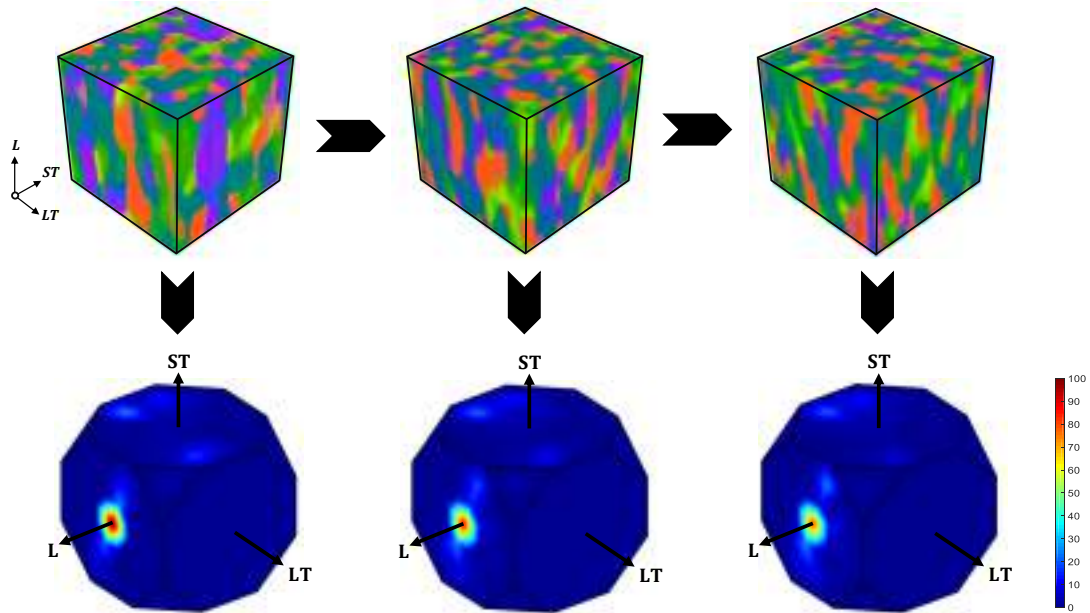
Figure 2.11: *Sequential texture analysis for the MRF reconstruction algorithm: each reconstruction uses three random orthogonal slices of the previous 3D model (shown on its left) as its input exemplars. Here, the orientation distribution of each reconstruction is shown to be consistent with the original exemplars' ODF.*

Next, an electric field is applied to produce a thick oxide layer over the aluminum grains. When exposed to cross-polarized light, interference in these oxide layers produces colors that depend on the grain orientation. For reconstruction purposes, the image is preprocessed such that all grain boundaries are accentuated to demarcate the grains clearly. The 2D microstructure is depicted in Figure **??**. Only one sectional representation is used for the input to the MRF reconstruction algorithm, and the other sections are assumed to be identical (similar to Example 1 in Section 2.2.1). The microstructure is then reconstructed using the MRF algorithm and is shown in Figure **??**. Several orthogonal sections of the 3D synthesized model are also illustrated in Figure **??**.

The goal in this example is to examine the nearest neighbor-grain correlation, which is a critical descriptor relating mechanical properties [203]. For this purpose, the grains are classified in terms of four predominant colors observed in the image: purple (P), blue (B), orange (O), and yellow (Y). The 2D and 3D microstructures with grains marked by this classification are shown in Figure 2.12. For all yellow grains, the number of blue neighbors, as well as all the other neighbors (purple, orange, and yellow), are counted. The same process is repeated for the remaining colors. Similar data is gathered from five slices in each direction (a total of 15 slices) across the 3D synthesized microstructure. The neighbor statistics of the colors are compared in Figure 2.12. In this figure, the x-axis denotes the color of the chosen grain, while the color bars indicate the probability of occurrence of a yellow, orange, purple, or blue neighbor for that specific grain. There are two bars for each neighbor color, one for the 2D microstructure (located on the left-hand side) and another for the 3D reconstructed model (located on the right-hand side), as indicated by the legends in the bar plot. The ranges on the tip of the 3D bars indicate the maximum and minimum values of the neighbor color percentages along the x, y, and z planes. The numbers on the bars indicate the relative percentage difference between the 2D and

3D statistics. The maximum error between the 2D and 3D neighbor statistics is only 3.32%, which is associated with having a purple grain neighboring another purple grain. This example indicates that the MRF algorithm is exceptional in maintaining the nearest grain neighborhoods in the reconstructed image.
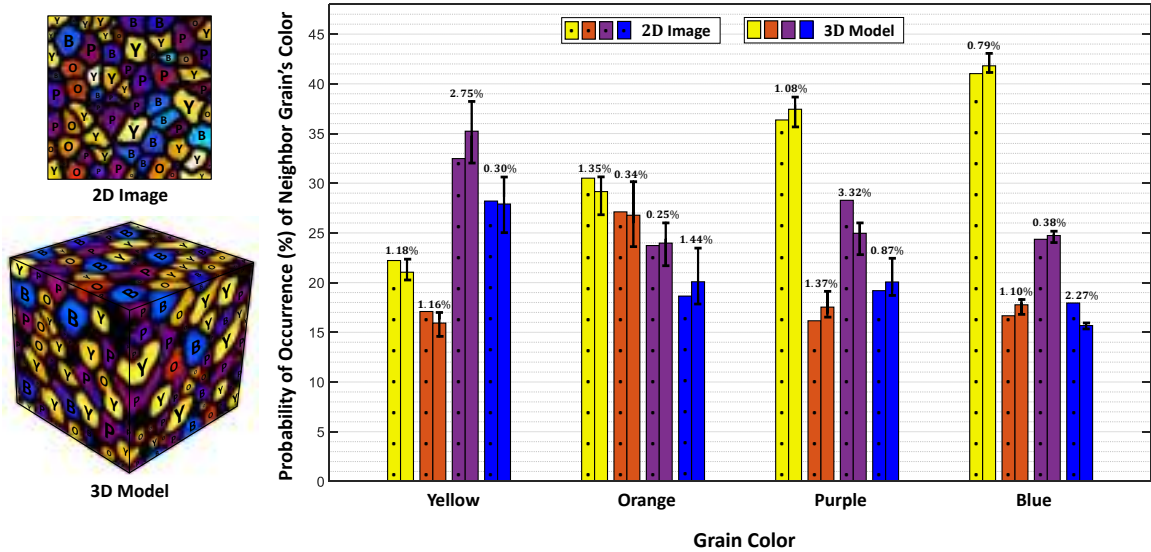
Figure 2.12: *Comparison of the nearest neighbor-grain correlations between synthesized image and experimental exemplar: four predominant colors, purple (P), blue (B), orange (O), yellow (Y), as marked on the 2D and 3D microstructures on the left-hand side are classified. Neighbor statistics of the colors are shown on the right-hand side, where the x-axis denotes the color of the chosen grain, and the bars indicate the probability of occurrence of colored neighbor grains. There are two bars for each neighbor color, one for the 2D image and another for the 3D reconstructed microstructure.*

2.3 Conclusion

A numerical method for reconstructing diverse 3D multi-color microstructures from 2D micrographs imaged on orthogonal planes is presented. The algorithm reconstructs 3D solid models by matching orthogonal sections of the synthesized microstructure to the representative 2D micrographs through an iterative minimization procedure. In this chapter, the new reconstruction algorithm is applied to a wide variety of morphologies, particularly equiaxed and elongated grains. Through the reconstruction of

optical and EBSD datasets, it is shown that the MRF approach is able to precisely capture crucial features of polycrystalline microstructure, such as grain size, orientation distribution, and grain neighborhood correlation. The method can be useful to rapidly create a library of 3D microstructures from 2D micrographs for modeling and simulation purposes.

CHAPTER III

Large-Scale Synthesis of Metal Additively-Manufactured Microstructures Using Lapped Textures

In this chapter, a data-driven framework is developed and examined for creating spatially-varying crystallographic textures over component-scale CAD models. Here, a set of three orthogonal 2D micrographs of an AM stainless steel specimen are first obtained experimentally through EBSD and subsequently converted to a 3D representative unit cell using the Markov Random Field technique, presented in Chapter II. Features such as grain size statistics, crystallographic orientation, and grain boundary misorientation distributions are used to validate the reconstructed 3D microstructure against input experimental EBSD images. The variations of microstructural features during a laser-based additive manufacturing process are subsequently modeled by merging patches from the 3D snapshot of AM microstructural unit cell in a part-scale geometry using a tensor-based optimization process. The optimization algorithm repeatedly pastes microstructural elements from the reconstructed MRF unit cell onto the geometrical CAD domain until it is entirely covered. Here, through a simple graphical user interface (GUI), the user specifies a tensor field over the volumetric CAD model, defining the local control over grain-scale, anisotropy, and crystal growth

orientation. This new approach provides a workflow for reconstructing global maps of AM microstructures in real-time by embedding site-specific images based on known AM microstructural patterns seen in experimental characterization techniques. The numerical results are helpful specifically for the visualization of process-microstructure relationships in metal additive manufacturing techniques.

The following details the structure of this chapter. The LEGOMAT algorithm to embed the MRF synthesized microstructures is presented first in Section 3.1.1. Subsequently, the patch-based optimization process in correlation with material flow paths is described in detail. Thereafter, numerical and experimental results, along with statistical comparisons for verification of grain size, crystal orientation distribution, and grain boundary misorientation angles of the proposed methodology, are presented in Section 3.2. Here, the efficacy (i.e., computational cost and accuracy) of the LEGOMAT reconstruction framework is also compared against known experimental characterization patterns and simulated images from SPPARKS kinetic Monte Carlo [104].

3.1 Large-Scale Microstructure Reconstruction Workflow

In this section, the mathematical formulation and implementation for reconstructing large-scale 3D AM microstructures are discussed. The overall process, as illustrated in Figure 3.1, utilizes two separate algorithms. First, the MRF theory, from Chapter II, is leveraged to reconstruct a representative 3D microstructural unit cell from three orthogonal planar experimental EBSD exemplars. Next, Section 3.1.1 describes the large-scale synthesis process for embedding site-specific unit cells through a tensor-based optimization procedure that efficiently merges patches from the 3D unit cell onto a CAD model.

Although the methodology presented hereon is not tied to any specific image resolu-
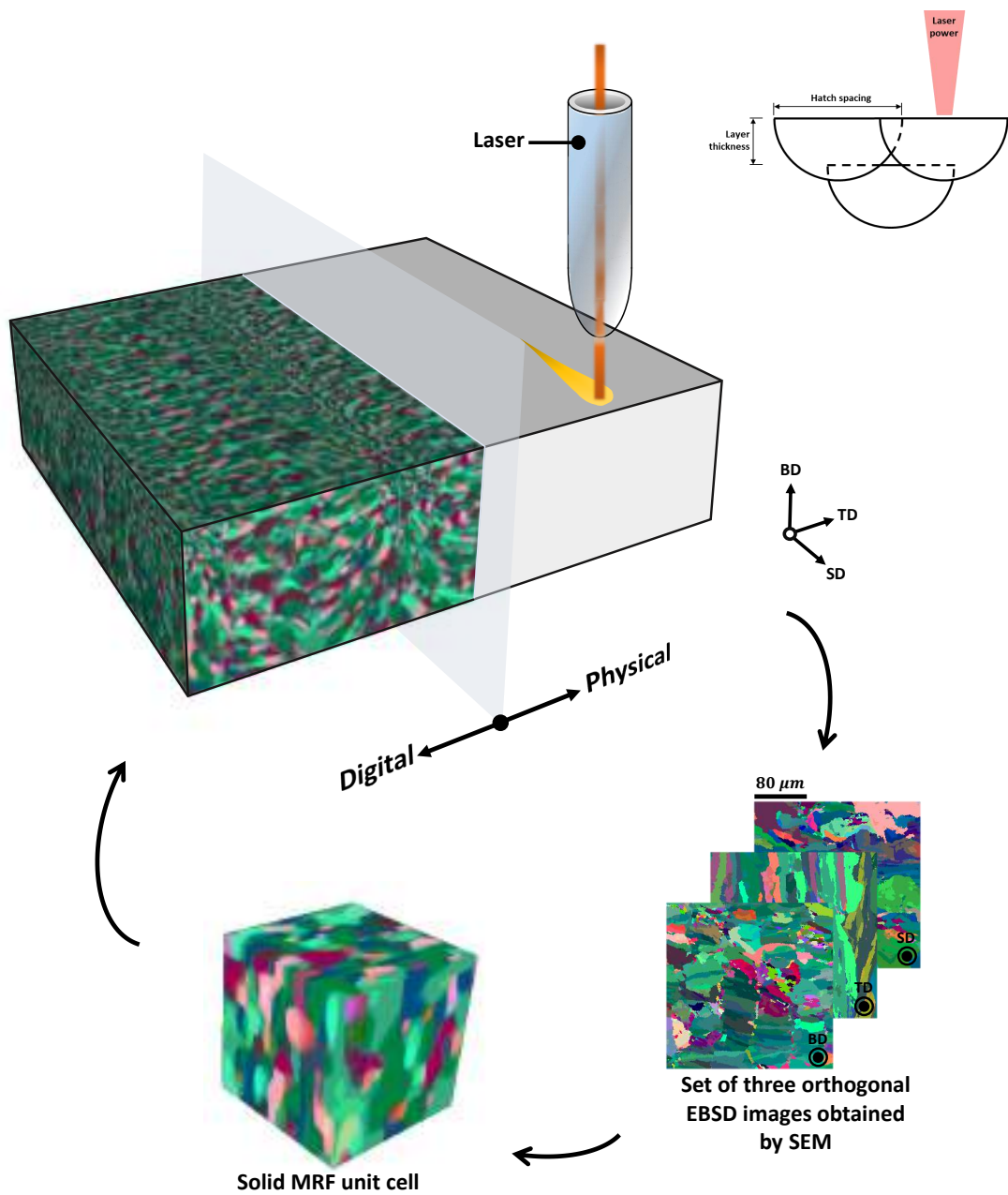
Figure 3.1: *Large-scale synthesis optimization process for embedding site-specific unit cells: full-field component imaging built by using a single site-specific MRF unit cell. Here, a small-scale texture of the AM 316L stainless steel specimen in three orthogonal planes is first extracted through SEM imaging. The 3D microstructure is then reconstructed using the MRF sampling algorithm as introduced in Section 2.1. The laser path, along with other processing parameters such as layer thickness and hatch spacing (imposed by the user), is then used to embed the crystallographic patches from the MRF unit cell onto the CAD model. The BD, SD, and TD axes here represent the building, scanning, and transverse directions, respectively.*

tion, all the input experimental EBSD exemplars are initially resampled to 128×128 pixels prior to the 3D MRF reconstruction. Next, a random RGB triplet from the input planar exemplars is assigned to each voxel in the 3D microstructural unit cell as an initial condition. The MRF optimization process is then carried out in a multi-resolution framework: starting with a coarse voxelated mesh while progressively interpolating the results to a finer resolution. The multi-resolution approach considerably increases the convergence rate associated with the sampling algorithm. The computational cost for the generation of the MRF unit cell is directly related to the pixel resolution and the sampling window size. The detailed computational breakdown however can be found in Section 2.1.3. In the following section, the numerical process associated with the LEGOMAT for embedding the location-specific unit cell in an engineering-scale geometry is discussed.

3.1.1   LEGOMAT Embedding Algorithm

The inputs of the LEGOMAT algorithm consist of a geometrical CAD model and an exemplar solid 3D unit cell of an AM microstructure, as outputted from the MRF reconstruction process. Here, the input CAD geometry is discretized into tetrahedral meshes via Delaunay tetrahedralization algorithm [204]. In return, the LEGOMAT output is of a 3D CAD model filled with microstructural patches from the exemplar 3D unit cell. It is worth noting that the LEGOMAT algorithm, as presented in this chapter, is a stand-alone approach and can be ultimately utilized to reconstruct a wide range of part-scale 3D solid textures using input unit cells obtained from either experimental procedures or other existing numerical techniques (e.g., DREAM.3D, Neper, etc.). The MRF algorithm, however, is notably more suitable for reconstructing small-scale AM unit cells since it can systematically model realistic grain structures (e.g., non-convex and non-equilibrium grain structures) without assuming an idealized morphology based on Voronoi tessellation employed in Neper [47] or su-

perellipsoid geometrical approach in DREAM.3D [71]. Furthermore, the generation of statistically-representative 3D numerical models via DREAM.3D or Neper generally requires information such as spatial distributions and 3D grain shapes, which is not readily attainable from a limited set of orthogonal planar exemplars as used in this approach.

Metal additive manufacturing processes can often be classified based on powder-delivery methods into two general categories: laser engineered net shaping (LENS) and laser powder-bed fusion (LPBF). The LENS process utilizes a carrier gas stream to transport powder through a nozzle directly onto the melt pool at the surface of the build. In LPBF, however, a laser beam often rasters across the metallic powder bed. Although these two manufacturing techniques have markedly different melting and solidification dynamics, they often exhibit similar underlying microstructural patterns. In particular, the solidification process results in the formation of highly-localized non-equilibrium microstructural components within the fusion zone [205, 206, 207]. Additionally, preferred crystallographic growth directions in these manufacturing techniques tend to align the columnar grains in the direction of increasing temperature. For instance, on the SD plane, the columnar grains tend to grow perpendicular to the melt pool's solidification surface, while curving toward the laser beam directions [208, 209]. Hence, the alignment of such complex features in 3D geometrical space while using a single reference 3D snapshot, requires a tensor field (i.e., a set of three orthogonal vector fields) that can thoroughly capture the underlying material growth orientations after the solidification process.

In the current implementation, as illustrated in Figure **??**, a volumetric vector field is specified over the CAD model, simply by manually drawing the material growth directions on the surface and cross-sections of the CAD model. The second direction of the tensor field is then chosen randomly upon embedding each microstructural

element, and the third direction is set to be the cross-product of the two vectors. Alternatively, the volumetric tensor field can be automatically inferred directly by the experimental measurements. However, such measurements are only possible to obtain on external surfaces of the build and not across the interior cross-sections. Though, one can incorporate thermal analyses and simulation softwares to reproduce the volumetric temperature gradient that can ultimately inform the preferred material flow directions [210, 211]. The latter approach is outside the scope of the current methodology. However, it will be incorporated in future studies upon automation of the material growth directions based on a set of input parameters such as hatch spacing, layer thicknesses, and scanning patterns. For interpolation of the user-specified vectors, a Laplacian smoothing scheme [212] is utilized, which has been previously employed in lapped texture synthesis methods [213, 214]. Once the material flow paths are scribed, the local scaling of the grain sizes, as seen in Figure **??**, is specified to incorporate size-varying crystals in the CAD model. Additional details regarding manual specification of material flow fields and grain size scaling are provided in Sections 3.1.1.1 and Section 3.1.1.2, respectively. Next, the LEGOMAT algorithm, as outlined in Section 3.1.1.3, repeatedly pastes the microstructural patches from the MRF unit cell onto the CAD model while aligning the embedding microstructures according to the local tensor orientation and specified scaling parameter. The result of the embedding process is shown in Figure **??** along with a few of its cross-sections across each orthogonal direction.

Contrary to the voxelated filling approach outlined in Section 2.1.1, a patch-based optimization technique is implemented here that uses a tetrahedral discretization to represent the solid geometrical CAD models. This formulation has certain benefits over voxel representation used in Section 2.1.1. The main advantage is it requires a substantially smaller number of elements to approximate the 3D CAD model, resulting in considerably fewer iterations (and equivalently lower computational cost)

to complete its reconstruction task. Next, the manual specifications of the material flow field, grain size scaling, along with the numerical embedding process and its implementation are explained in detail in Sections 3.1.1.1-3.1.1.3.

3.1.1.1 Material Flow Fields

In this work, the preferred crystallographic growth orientations illustrated in Figure ?? are manually drawn as a set of orthogonal vector fields based on known microstructural patterns seen in the experimental characterization techniques. Upon specification of the growth orientations, the LEGOMAT optimization procedure in Section 3.1.1.3 closely follows the local directional vector fields throughout the embedding of the microstructural patches from the MRF unit cell onto the CAD model. In structural systems manufactured by LENS or LPBF techniques with a zig-zag rastering pattern, columnar-shape-like grains are formed away from the laser beam track along the BD surface in-plane to the build. Additionally, on the SD plane, columnar grains tend to elongate perpendicular to the melt pool's solidification boundary while curving in the direction of increasing temperature (i.e., toward laser beam track) [5, 19, 32, 107, 108]. On the TD surface, the elongated grains tend to extend nearly perpendicular to the laser beam track while becoming slightly inclined toward scanning direction at regions closer to the beam track [5, 32, 117, 206, 215, 216]. Accordingly, given an input CAD model and processing modalities, the user can follow the above crystallographic growth patterns by manually drawing the columnar directions across surfaces orthogonal to the laser direction. The second direction of the tensor field is then chosen at random, upon embedding each microstructural element. At the same time, the third direction is set to be the cross-product of the two local vector fields. For volumetric interpolation of these vectors, a Laplacian smoothing scheme [212] is employed to approximate the preferred growth directions across non-trivial faces with unspecified or unknown growth directions. The process for the

manual drawing of the first directional vector pertaining to the crystal growth direction, along with relative experimental images from the work of Rodgers et al. [104] for a LENS build with a zig-zag rastering pattern is shown in Figure 3.2.
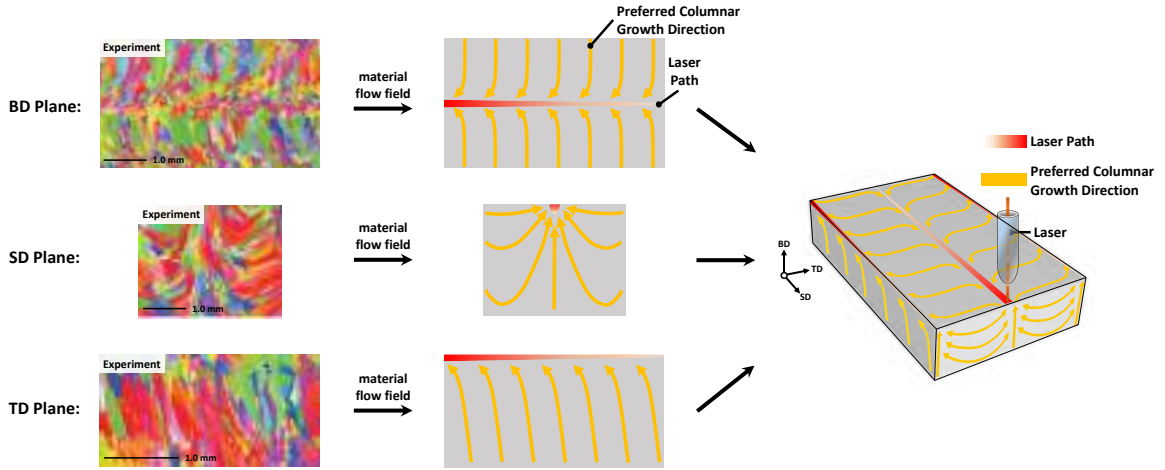
Figure 3.2: *Manual drawing of local vector fields, representing the preferred crystallographic growth orientation, based on known microstructural patterns seen from the experimental characterization techniques. The shown TD image is taken from the centerline of a beam pass. Here, the experimental images are reproduced from the work of Rodgers et al. [104] under the terms of the Creative Commons CC-BY license.*

3.1.1.2 Material Grain Size

As evident from experimental characterization techniques of AM components [5, 104, 117, 206, 216], small grains near the laser path tend to nucleate during the solidification process. These grains, however, quickly transition to much larger elongated grains in between the laser paths. Such transitions often result in three classes of grain morphology depending on spatial location within the build: (*i*) large curved columnar grains on *TD* and *SD* planes, (*ii*) fine equiaxed grains near the laser path on *BD* plane, and (*iii*) large transversely-elongated columnar grains across regions in between the laser paths across *BD* surface. The resulting heterogeneous mixture of elongated and equiaxed grains often has a visible periodicity with the deposition thickness, hatch spacing, and scanning pattern [104]. This transition is further controlled by the thermal gradient and solidification rate at the solid-liquid interface. For

58

instance, the width corresponding to small-scale grains along the laser beam track often tends to grow with increasing laser speed or decreasing power [216]. Figure 3.3 illustrates these grain types in cross-sectional regions orthogonal to the scan direction. Although the curvature of these grains is mainly controlled by the directional vector fields outlined in Section 3.1.1.1, for a more realistic reconstruction, grain-scale parameterization must also be specified before initiating the embedding process in Section 3.1.1.3. Accordingly, in the LEGOMAT approach, the user may enforce smaller grain scales near the laser path in cross-sections perpendicular to the scan direction. Such an approach can efficiently create the equiaxed-to-columnar grain transitions, as elaborated above. The process for the manual specification of the grain size parameterization for an AM build with a zig-zag tracing pattern is shown in Figure 3.3.
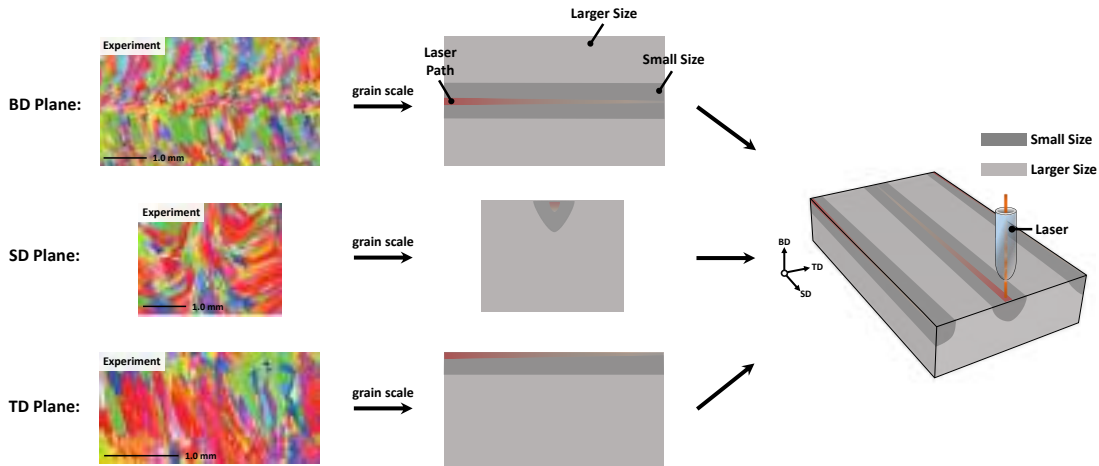
Figure 3.3: *Manual parameterization of grain size scaling by embedding larger grains farther away from the laser path in cross-sections orthogonal to the scan direction. The experimental images shown here are reproduced from the work of Rodgers et al. [104] under the terms of the Creative Commons CC-BY license.*

3.1.1.3 Tensor-Based Optimization Procedure

The LEGOMAT embedding process closely follows the lapped texture reconstruction technique outlined in the work of Praun et al. [214], which was initially developed for 2D texture embedding. Here, in the process of volumetric embedding, a group (or a

patch) of N tetrahedral elements, denoted as T_i for $i = 0, 1, 2, ..., N-1$, is selected in the CAD model such that there are slight variations in the user-defined tensor field across the group. The size of the group of tetrahedral elements is always chosen to be contained within the representative input MRF microstructure. In particular, let the tetrahedron located at the center of the patch, denoted by T_0, constitute as the seeding element. The LEGOMAT algorithm then acquires all neighboring elements of the seed tetrahedron for which the following two conditions are satisfied: (i) the mapped vertices of the tetrahedron T_i are inside the microstructural unit cell, and (ii) the dot product between the tensor fields associated with seed tetrahedron T_0 and the element T_i is greater than zero. In the case of uniform discretization, the total number of assigned elements at each iteration varies considerably based on global processing modalities and relative spatial locations to the laser path. Generally, fewer elements are assigned along the laser path, where grain size scaling is small. In contrast, more significant numbers of tetrahedra are being filled simultaneously at locations closer to the melt pools boundary.

The embedding is based on an optimization process that computes the mapping of the vertices of the 4-node tetrahedral elements T_i within each patch, to locations in the MRF microstructure that closely resemble the user-specified tensor field. In the following discussion, let $\boldsymbol{v}_1, ..., \boldsymbol{v}_4$ represent four vertices of the seed tetrahedron T_0 in the CAD model. Accordingly, the primary aim of the LEGOMAT embedding process is to identify the linear mapping of these nodes to positions $\Psi(\boldsymbol{v}_1), ..., \Psi(\boldsymbol{v}_4)$ in the representative MRF unit cell.

Here, let $\tilde{\boldsymbol{P}}$, $\tilde{\boldsymbol{Q}}$, and $\tilde{\boldsymbol{R}}$ represent the set of three local orthogonal vectors of the tensor field associated with the seed tetrahedron, T_0. Consequently, the barycentric coordinates, denoted as $p_1, ..., p_4$, of tetrahedral element T_0 can be used to represent $\tilde{\boldsymbol{P}}$ as follows:

$$
\begin{cases}
p_1 \boldsymbol{v}_1 + p_2 \boldsymbol{v}_2 + p_3 \boldsymbol{v}_3 + p_4 \boldsymbol{v}_4 = \tilde{\boldsymbol{P}} \\[2mm]
p_1 + p_2 + p_3 + p_4 = 0
\end{cases}
\tag{3.1}
$$

Similarly, $\tilde{\boldsymbol{Q}}$ and $\tilde{\boldsymbol{R}}$ can be represented using $q_1, ..., q_4$ and $r_1, ..., r_4$, respectively. Furthermore, due to the mapping associated with vertices, i.e., $\boldsymbol{v}_j \mapsto \Psi(\boldsymbol{v}_j)$ for $j = \{1, 2, 3, 4\}$, being linear, the mapping of vector $\tilde{\boldsymbol{P}}$ in the CAD model to the corresponding vector $\Psi(\tilde{\boldsymbol{P}})$ in the microstructural space follows the same weighting factors as in Equation (3.1), as formulated below:

$$
\Psi(\tilde{\boldsymbol{P}}) = p_1 \Psi(\boldsymbol{v}_1) + p_2 \Psi(\boldsymbol{v}_2) + p_3 \Psi(\boldsymbol{v}_3) + p_4 \Psi(\boldsymbol{v}_4)
\tag{3.2}
$$

Similarly, $\Psi(\tilde{\boldsymbol{Q}})$ and $\Psi(\tilde{\boldsymbol{R}})$ can be formulated in terms of barycentric coordinates $q_1, ..., q_4$ and $r_1, ..., r_4$, respectively. Ideally, when mapped into the microstructural domain, these vectors should be aligned with the orthogonal $\boldsymbol{x}$, $\boldsymbol{y}$, and $\boldsymbol{z}$ coordinate axes in the microstructure. However, as illustrated in Figure 3.4 slight differences are permitted in order to enforce microstructural continuity in the CAD model. Therefore, difference vectors, denoted as $\boldsymbol{d}_p$, $\boldsymbol{d}_q$, and $\boldsymbol{d}_r$, are defined for the seed tetrahedron, T_0, as follows:

$$
\begin{cases}
\boldsymbol{d}_p = \Psi(\tilde{\boldsymbol{P}}) - (1, 0, 0)^t \\[2mm]
\boldsymbol{d}_q = \Psi(\tilde{\boldsymbol{Q}}) - (0, 1, 0)^t \\[2mm]
\boldsymbol{d}_r = \Psi(\tilde{\boldsymbol{R}}) - (0, 0, 1)^t
\end{cases}
\tag{3.3}
$$

The difference vectors associated with all tetrahedral elements in the patch, i.e., T_i for $i = 0, 1, 2, ..., N - 1$, can be similarly computed. Therefore, let $\boldsymbol{d}_p^i$, $\boldsymbol{d}_q^i$, and $\boldsymbol{d}_r^i$ denote

61
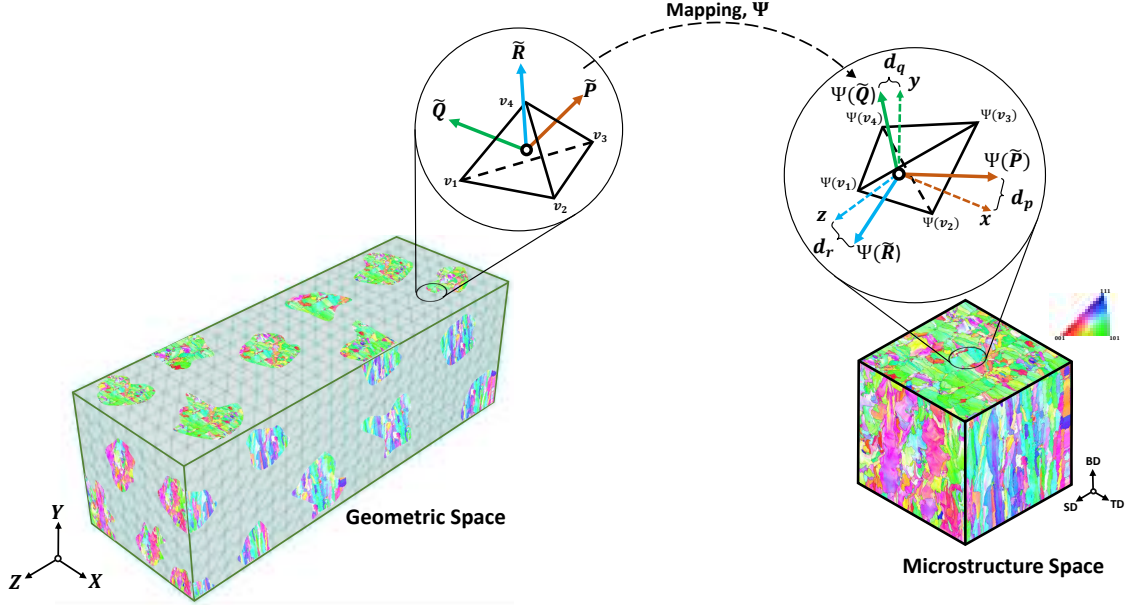
Figure 3.4: *LEGOMAT optimization schematic: the optimization process minimizes the difference vectors $\boldsymbol{d}_p$, $\boldsymbol{d}_q$, and $\boldsymbol{d}_r$ between microstructure coordinate axes $\boldsymbol{x}$,$\boldsymbol{y}$,$\boldsymbol{z}$ and respective transformed tensor axes $\Psi(\tilde{\boldsymbol{P}})$,$\Psi(\tilde{\boldsymbol{Q}})$,$\Psi(\tilde{\boldsymbol{R}})$ for each tetrahedron.*

the difference vectors associated with the tetrahedral element T_i. The LEGOMAT optimization problem is to find the vertex mapping for all 4-node tetrahedra T_i within the patch such that the least-squares functional defined below is minimized:

$$\mathcal{F} = \frac{1}{N} \sum_{i=0}^{N-1} \|\boldsymbol{d}_p^i\|_2^2 + \|\boldsymbol{d}_q^i\|_2^2 + \|\boldsymbol{d}_r^i\|_2^2 \tag{3.4}$$

However, the minima corresponding to Equation (3.4) is unique up to a translation vector. Thus, an additional constraint, as formulated below, is set to fix the center of the seed tetrahedron, T_0, to the center of the microstructural volume:

$$\frac{\Psi(\boldsymbol{v}_1) + \Psi(\boldsymbol{v}_2) + \Psi(\boldsymbol{v}_3) + \Psi(\boldsymbol{v}_4)}{4} = (0.5, 0.5, 0.5)^t \tag{3.5}$$

Consequently, the optimized solution for mapped vertices associated with T_i for

62

$i = 0, 1, 2, ..., N - 1$ from the constrained minimization problem formulated in Equations (3.4)-(3.5), can be efficiently obtained by solving a sparse linear system of equations. Once the patch of tetrahedral elements T_i is fully mapped to the microstructural space, the LEGOMAT optimization procedure randomly continues with another location in the CAD model consisting of an unmapped tetrahedron. The embedding process repeats until all the nodes in the CAD model are mapped to the microstructural unit cell.

The tensor-based optimization procedure elaborated in here is specific to a 4-node tetrahedral discretization. Generally, partitioned elements need to allow for a linear interpolation of coordinates or variables as formulated in Equations (3.1)-(3.2). Accordingly, a 10-node tetrahedron will have non-linear interpolants and so need further modifications in the LEGOMAT optimization algorithm to implement the mapping process of the tensor fields in the CAD model onto the MRF microstructure. The LEGOMAT algorithm and its GUI for the manual drawing of material growth direction and grain size scaling are implemented using *C++* and *OpenGL*. Furthermore, large-scale simulation times generally vary drastically depending on the complexity of material flow fields (e.g., number of paths, layers, etc.) and the mesh density in the CAD model. Amongst all the steps described in Section 3.1.1, the manual drawing of the volumetric vector field is the most time-consuming process, especially for multi-layer, multi-track scenarios. Nonetheless, LEGOMAT reconstruction framework is fairly inexpensive in terms of computation and memory for representing large-scale solid models.

3.2 Component-Scale Microstructure Reconstruction Example of 316L Stainless Steel

In this section, the process parameters for manufacturing and image acquisition of EBSD sections of the AM 316L stainless steel specimen are explained. Thereafter, the results for reconstructing digital twins using a set of locally orthogonal planar images are highlighted. The efficacy of the MRF algorithm is assessed by comparing the crystallographic orientations, grain boundary misorientations, and grain size statistics of the synthetic and experimental images. Next, the LEGOMAT algorithm is used to simulate various part-scale AM microstructures consisting of multi-layer and multi-track processes. The part-scale results are then compared against known experimental imaging and simulated microstructures using SPPARKS kinetic Monte Carlo simulator [104].

The 316L stainless steel specimen was fabricated via a selective laser melting (SLM) 280 HL machine, equipped with two 400 W continuous wave (CW) Ytterbium fiber laser beams with approximately 80 μm diameter at the focal point. The SLM 280 HL machine is composed of a building platform with a maximum capacity of 280 $\times$ 280 $\times$ 350 mm^3. Prior to the operation, argon gas was flooded into the chamber to lower the oxygen level below 0.1%. The pre-alloyed 316L stainless steel powder, with particle sizes between $30 - 50$ μm, was used as the printing substance. A fully-dense cuboid of $10 \times 6 \times 10$ mm^3 sample was fabricated for microscopic analysis using the manufacturer-recommended guidelines with core processing parameters of 200 W laser power, 800 mm/s scanning speed, 30 μm layer thickness, and 120 μm hatch spacing. The AM volume was printed using a bi-directional scanning technique in which the laser beam moved across each layer in a zig-zag pattern. The cuboidal sample was then sequentially polished through diamond suspensions of 9 μm, 6 μm, and 3 μm. This is followed by alumina suspensions of 1 μm and 0.05 μm, intending

to achieve fine smooth faces. The EBSD analyses of three orthogonal $700 \times 700 \ \mu m^2$ faces of the cuboidal specimen were subsequently performed using a high-resolution SEM TESCAN MIRA3, equipped with an EDAX Hikari XP EBSD detector. The orthogonal sections were mounted sequentially using a slow-set epoxy. Each EBSD scan was taken at $30 \ kV$ voltage and $1.0 \ \mu m$ step size. The EBSD camera parameters were set to 1×1 binning, high-gain, and low-exposure to achieve an average confidence index (CI) of 0.6.

Once the experimental EBSD images were generated, the raw Euler angles were mapped to nodes in a discretized ODF. The ODF provides a probability density of the crystallographic textures by describing the Euler angles associated with each node in the Rodrigues space. The lattice structure of the material of interest in this chapter (i.e., 316L stainless steel) is of cubic symmetry. Such a lattice structure reduces the orientational space to a small subset, called the fundamental region, as illustrated in Figure **??**, that accounts for the cubic lattice structures in the scanned material. For numerical analysis, the fundamental region can be discretized using a tetrahedral finite-element mesh, as shown in Figure 3.5(a). Due to symmetry, several of these nodes in the grid are equivalent, which reduces the discretized ODF even further to a smaller set of independent nodes. As a result, measured EBSD images can be colored based on these independent nodal numbers. A simple choice for the colormap, as depicted in Figure 3.5(b), is to apply the Rodrigues vector itself for each independent node as an RGB triplet.

Subsequently, for MRF reconstruction, a subset of experimental EBSD sections of size $256 \times 256 \ \mu m^2$ along each orthogonal axis is selected and resampled to 128×128 pixels. Note, the reconstruction scheme presented here is not tied to a specific input resolution. Thus, any 2D image resolution can be reconstructed, if needed. The implication is that the user should ensure to specify a sufficient pixel resolution to
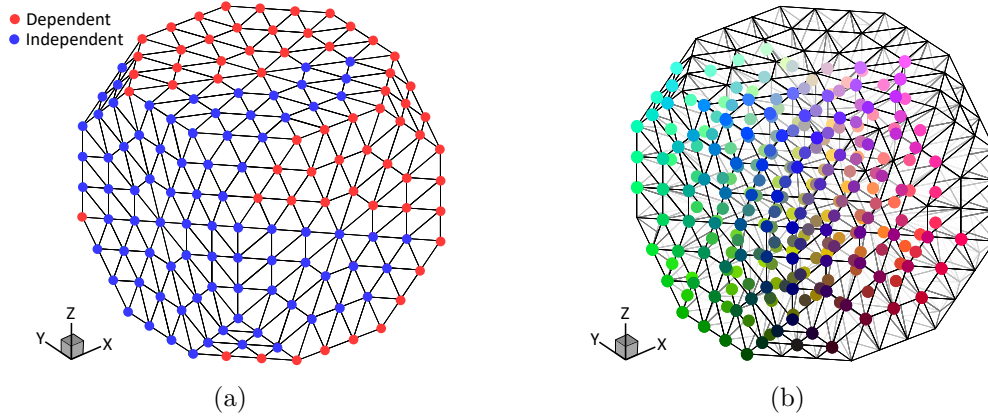
Figure 3.5: *Illustration of the colormap associated with discretized ODF: (a) the discretized Rodrigues fundamental region for cubic symmetry with independent nodes along the external surface, colored blue, (b) applied colormap showing the RGB values of independent nodes in the fundamental region. Here, the internal elements have been faded for better visualization of the RGB colormap.*

capture the phenomena of interest. Following this, the texture colorings corresponding to *TD* and *SD* directions were adjusted such that they represent a similar color histogram as of *BD* image. The additive manufacturing processes tend to create large variations in the crystallographic texture across a specimen. As such, performing *histogram matching* can establish a consistent texture in the volumetric MRF unit cell, as images are taken at different locations within the specimen. Figure 3.6(a) elucidates the orthogonal set of images for 316L stainless steel specimen as inputted to the MRF reconstruction algorithm. The 3D EBSD image from the MRF algorithm is shown in Figure 3.6(b). A number of different sections of the reconstructed model across *TD* direction are also shown in Figure 3.6(c). The averaging step performed in Equation (2.4) tends to smoothen the noises within the MRF synthetic model, hence providing an overall smoother reconstruction compared to input 2D exemplars.

Following the reconstruction of the MRF unit cell, each color level of the synthesized model is mapped to an independent node in the fundamental Rodrigues region using the colormap shown in Figure 3.5(b). For every voxel in the unit cell, the four

(a) 2D experimental exemplars

(b) 3D reconstruction

(c) Cross-sections of 3D reconstructed model along *TD*
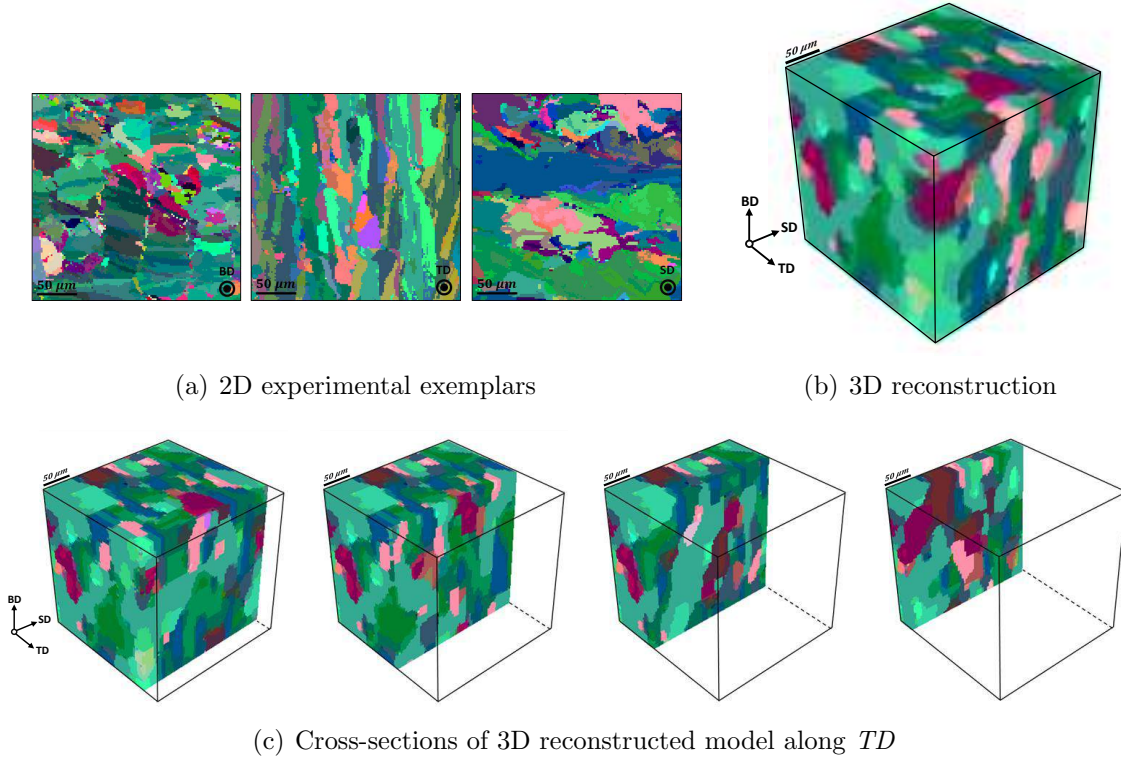
Figure 3.6: *Illustration of the experimental 2D exemplars and synthesized 3D images of AM* 316*L stainless steel: (a) set of orthogonal experimental EBSD images of AM* 316*L stainless steel microstructure as inputted in MRF sampling algorithm, (b) representative 3D MRF reconstructed model, and (c) numerous sectional images of the reconstructed model along TD axis.*

closest colors (in Euclidean norm sense) in the discretized ODF space are identified. The voxel coloring remains unaltered, provided the sampled RGB triplet is within the user-specified threshold. Otherwise, the RGB coloring of the voxel is replaced randomly with one of the four closest independent nodes in the ODF fundamental region. As depicted in Figures 3.7(a)-3.7(b), it is found that the resulting pole figures of the MRF reconstructed microstructure closely resemble the measured texture distribution. Such an assessment exhibits the ability of the MRF unit cell reconstruction algorithm to accurately simulate the textural description of AM microstructures.

Once the RGB triplets are mapped through the discretized ODF colormap, the grain boundary misorientation angles can be conveniently calculated. In the scheme of
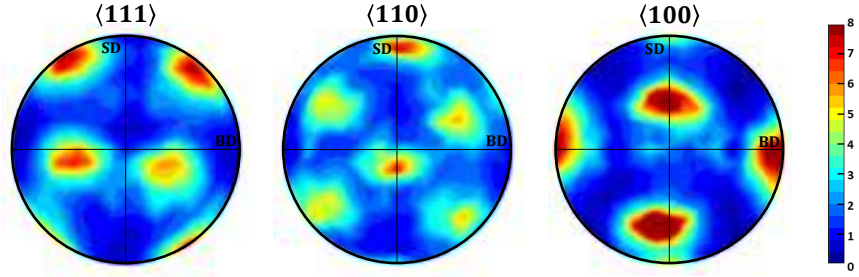
(a) 2D experimental exemplars
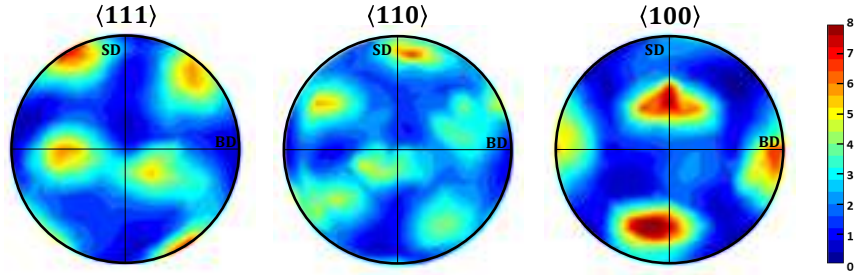
(b) 3D synthesized mode

Figure 3.7: *Texture comparison using* $\langle 111 \rangle$, $\langle 110 \rangle$, *and* $\langle 100 \rangle$ *pole figures for (a) the orthogonal experimental images, against (b) the synthesized 3D MRF microstructure.*

grain boundary geometry, the misorientation is defined in terms of the required angle ϕ to bring the two neighboring grains into coincidence about an axis common to both lattices. Such parameterization is concisely known as the angle-axis misorientation pair. To perform mathematical manipulations, the misorientation is conveniently expressed as a 3×3 orthonormal matrix, denoted as $\boldsymbol{M}$. Consequently, for two interfacing grains denoted as grains A and B, the columns of the matrix $\boldsymbol{M}$ are the direction cosines that define the rotation of the crystal coordinate systems of grain B to grain A, as grain A being the reference grain. The misorientation angle is obtained from the matrix $\boldsymbol{M}$ as follows:

$$2 \cos \phi + 1 = \text{tr}(\boldsymbol{M}) \tag{3.6}$$

where $\text{tr}(.)$ is defined to be the trace or the sum of elements on the main diagonal for

an input matrix.

Furthermore, due to the symmetric nature of the crystallography involved, the axes of grain B can be chosen in more than one way in respect to the reference grain A. For cubic symmetry, this multiplicity is precisely 24; that is, there are 24 unique (but equivalent) ways in which the misorientation matrix M can be expressed. This results in 24 angle-axis pairs. Although these angle-axis pairs are all equivalent, it is conventional to report the lowest angle solution when describing a misorientation angle. Accordingly, low-angle grain boundaries (LAGBs), defined as $\phi < 15°$, are often immediately obvious.

For the assessment of grain boundary misorientation angles of the MRF reconstruction, the reconstructed 3D image is properly segmented first. The GB misorientation angles are then computed slice-by-slice using eight-fold connectivity, where the crystal orientation (i.e., Rodrigues vectors) of every voxel is being compared against its adjacent neighbors (along the horizontal, vertical, and diagonal directions) positioned on each cross-section. If the frequency of the most repeating orientation index in the 3×3 window is within a specified threshold, the two most frequent Rodrigues vectors inside the sampling window are identified. Following this, the misorientation angle between the two most frequently-occurring orientation indices is computed. The same process is followed for the orthogonal experimental images. Figures 3.8(a)-3.8(b) illustrates the spatial distribution of grain boundary misorientation angles for experimental and 3D synthesized EBSD images, respectively. As expected, the low-angle boundaries ranging between 0°-15°, as illustrated in Figure 3.8, are highly pronounced in both sets of images. The corresponding spatial distribution of misorientation angles of the sections in Figure 3.6(c) are also depicted in Figure 3.8(c). Thereafter, the high-angle grain boundary (HAGB) misorientation values (referred to as misorientation angles greater or equal to 15°) are sorted to allow for a quantitative comparison between

(a) 2D experimental exemplars

(b) 3D reconstruction

(c) Cross-sections of 3D reconstructed model along *TD*
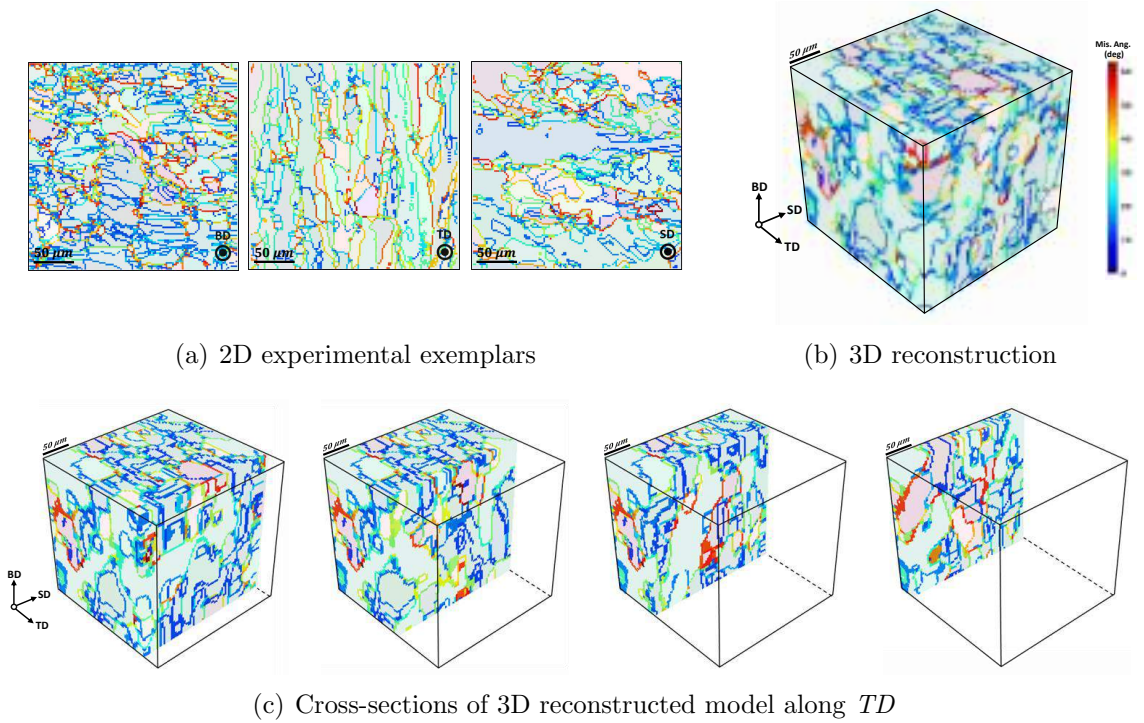
Figure 3.8: *Illustration of the spatial distribution of grain boundary misorientation angles for: (a) set of orthogonal experimental images of* 316*L stainless steel AM microstructure, (b) representative 3D MRF reconstructed model, and (c) numerous sectional images of the MRF reconstructed model along TD axis.*

the experimental and synthesized images. The probability densities of the HAGBs for the set of three orthogonal images and cross-sections of the reconstructed MRF model, as seen in Figure 3.9 are then calculated over 21 bins. Here, because of the cubic symmetry of the measured specimen's lattice structure, the maximum unique misorientation angle possible is limited to 62.8°. Overall, a close agreement between the scanned and reconstructed MRF images is observed, with the 3D reconstruction marginally predicting a lower probability for misorientation angles ranging between $40° - 52°$.

Next, the ability of the MRF algorithm to accurately model grain size statistics of the 316L stainless steel microstructure along *TD* axis as compared to the respective input experimental exemplar is examined. Grain size distribution is essential for simulating
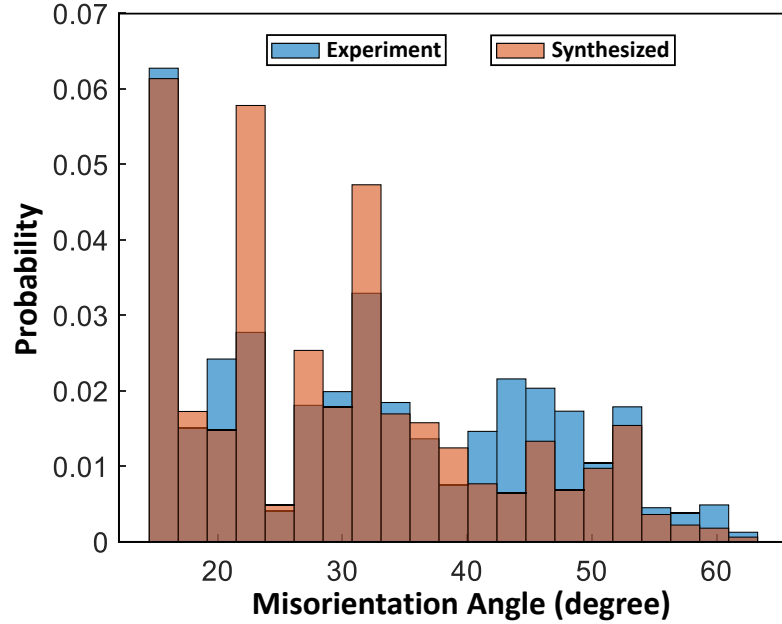
Figure 3.9: *Comparison of PDF of HAGB misorientations of the 3D synthesized MRF microstructure against experimental images. Here, the probability densities of the misorientation angles are computed over* 21 *bins. The maximum unique misorientation angle possible due to cubic symmetry is* 62.8°.

mechanical properties in AM structures using Hall-Petch models [196, 197]. In this assessment, grain sizes of the 2D EBSD image are obtained using the following procedure. The incomplete grains along the outer edges adjacent to the borders of the experimental EBSD image are removed. For every inner crystal, the grain areas, along with the ratio of the major over minor diameters of the best-fitting ellipse with an equivalent normalized second central moments, are computed and stored. Afterward, abnormally small and large grains are removed from the measured grain area dataset. The histograms of the grain area and the corresponding aspect ratio for each grain, as depicted in Figures 3.10(a)-3.10(b) respectively, are then plotted over 21 bins using a log-normal fit. Similarly, to capture the grain size distribution of the 3D synthesized unit cell, slices along the *TD* axis are extracted, and the same process as used in the 2D exemplar is applied. That is, the external grains for every slice are first eliminated, and for each inner grain, the grain area and its respective aspect ratio are

obtained. Here, aspect ratios near one represent near-circular (i.e., equiaxed) grain morphology. In contrast, values close to ∞ represent needle-like cross-sections. When comparing grain size statistics, both the simulated and experimental log-normal distributions peak near 160 μm^2, indicating a considerable fraction of small-size grains in the dataset. Additionally, on the *TD* plane, nearly 51.9% and 47.6% of the grains in experimental and simulated images, respectively, have aspect ratios ranging from 5 to 20. This implies that a large fraction of the realized 316L stainless steel microstructure on *TD* surface consists of highly-elongated morphologies, which is also evident in Figure 3.6. Overall, as illustrated in Figure 3.10, close agreements between the input experimental image and MRF reconstruction are observed [217], with minor deviations seen for the low-frequency components, where the 3D MRF reconstruction marginally predicts a lower probability.

(a)   (b)
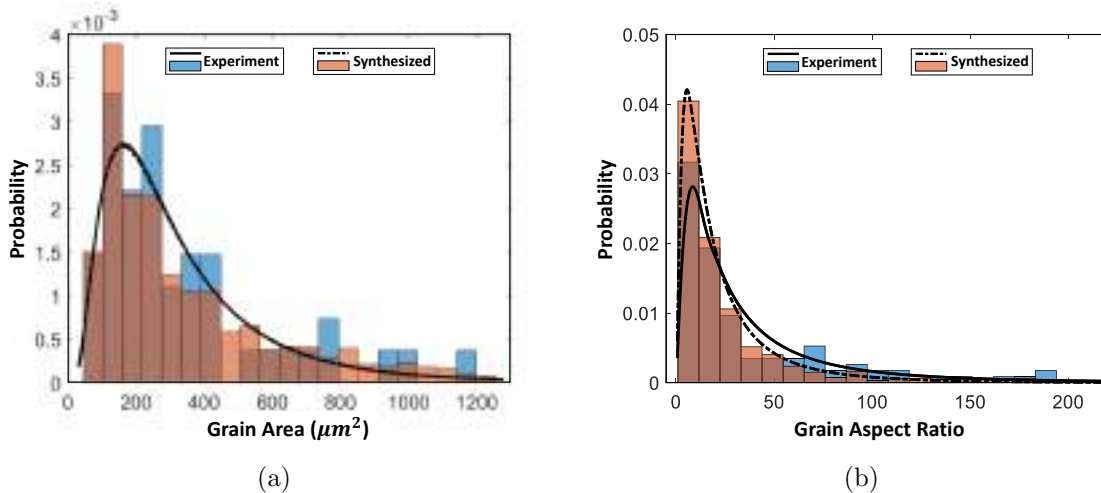
Figure 3.10: *Comparison of PDFs for (a) grain size statistics, and (b) aspect ratio of the 3D synthesized microstructure against experimental dataset along TD axis. The probability densities of the measured statistics are computed over* 21 *bins and fitted using a log-normal distribution.*

Thereafter, the LEGOMAT reconstruction technique follows by constructing global models shown in Figure **??**, based on the single locally-extracted MRF microstructure shown in Figure 3.6(b). The LEGOMAT approach presented in this chapter is

not tied to the MRF numerical reconstruction algorithm only and can be coupled with a wide variety of unit cell microstructural exemplars obtained from other computational frameworks (e.g., Voronoi tessellation [20], DREAM.3D [71], Neper [47], supervised learning [45], etc.) or even experimental 3D characterization techniques [32, 35, 36]. The MRF reconstruction algorithm, however, is particularly advantageous for building realistic small-scale AM unit cells from a single set of orthogonal 2D planar exemplars. The LEGOMAT numerical approach is to embed the reconstructed 3D microstructures in the CAD geometry based on experimentally observed insights on AM microstructure formation, as it is inherently controlled by solidification rate and thermal gradient which are also functions of laser parameters (e.g., speed, power) and the laser path (e.g., hatch spacing, layer thickness). The effects of cooling rate and temperature gradient history on microstructural patterns during the solidification process have been well studied in literature [108, 208, 209, 215]. Key components seen in the solidification process include: (i) smaller grain growth near the laser track because of high-temperature profile at the solid-liquid interface, (ii) elongated grains away from the laser spot in-plane to the surface of the build, and (iii) on SD face, the elongated grains tend to grow perpendicular to the melt pool's solidification surface, bending toward the laser track [218, 219]. The resulting heterogeneous mixture of elongated and equiaxed grains often has a visible periodicity with the deposition thickness, hatch spacing, and scanning pattern.

The preferred crystallographic growth direction is often specified primarily by the heat flow direction. The grain size scaling of a build, on the other hand, often decreases with increasing laser speed or decreasing laser power [216]. As a result of such geometrical principles, a natural way to describe grain formation during the solidification process is to align microstructural unit cells in the 3D geometrical space using a material flow field as shown in Figure **??**(left). Generally, these user-drawn vector fields work best when they are divergence-free, as artifacts can appear around material

flow fields with singularities (e.g., sink or source points). The issue of microstructural artifacts with singular vector fields can often be alleviated to some extent by locally enhancing the mesh density (subdividing the tetrahedral elements) at such regions, or equivalently by reducing the grain size scaling, prior to LEGOMAT optimization procedure. In addition to the material flow fields, the grain size scaling is represented using the same approach as described in Section 3.1.1.2, with smaller grains along the laser path gradually transitioning to columnar grains near the melt pool's boundary. Such geometric reconstruction methodology can systematically simulate the preferred grain growth directionality and size scaling for large-scale engineering components manufactured by laser additive manufacturing processes consisting of several passes and deposition layers. Figure **??**(right) presents the final reconstructed outputs, displaying the grain sizes and shapes that result from the LEGOMAT optimization procedure for various simulations, ranging from single-layer to multi-layer multi-track scenarios. This method can readily extend to simulate dozens of deposition layers and hundreds of laser passes. The CAD models for the block geometries illustrated in Figures **??**-**??** contain 22992, 31424, and 51312 linear tetrahedral elements, respectively. Once generated, these synthetic large-scale AM microstructures can be used in various material performance simulations (e.g., material mechanics, conductivity, etc.) [20, 21, 220, 221] or otherwise provide insights for multi-dimensional analysis involving desirable processing modalities and performance metrics [117], which is an extremely difficult task to achieve by experimental means alone.

To further demonstrate the flexibility of the presented LEGOMAT strategy, an assessment of the LEGOMAT simulated microstructure against SPPARKS kinetic Monte Carlo simulation [104] with respective experimental EBSD images is provided. The build in this example is deposited using LENS technique with a defocused high-power laser beam, rastering back and forth at a scan rate of 10.58 mm/s, with intended layer thickness and hatch spacing of 1.25 mm and 2 mm, respectively. Such a processing

pattern results in similar formation principle as outlined in Sections 3.1.1.1-3.1.1.2. In short, curved columnar grains are formed on *TD* and *SD* planes, and on the *BD* plane, large grains elongate across the central regions while transitioning to finer grains along each laser track [222]. These grain types are illustrated in Figure 3.11 alongside three orthogonal cross-sections of the build. The illustrated *TD* images in Figure 3.11 are taken from the centerline of the beam pass. Qualitatively on *BD* plane, both simulated microstructures correctly alternate between fine grains at the center to larger transversely-elongated structures. Additionally, in the *SD* plane, vertically-oriented grains found at the center of each pass transition to exceptionally curved grains in between. The grains along the *TD* plane illustrate vertically-elongated grains slightly incline toward the scan direction at the top. The strength of the LEGOMAT approach, as presented in this example, is its ability to efficiently create 3D microstructures with spatially-varying highly-curved non-convex structures over large regions at significantly lower computational cost than existing large-scale texture synthesis algorithms applicable for additive manufacturing. Additionally, as depicted in Figure 3.11, physics-based models such as the kinetic Monte Carlo simulator often have difficulty modeling the textural descriptions (e.g., grain size and curvature) of AM specimens. As a result, the LEGOMAT algorithm offers an alternative solution for the rapid visualization of microstructural variations with diverse processing parameters. This is exceedingly important as AM microstructures vary both globally with machine inputs and locally with build geometry, hence making experimental characterization of AM build seemingly impossible.

Additionally, since experimental information along all three orthogonal directions is available, quantitative comparisons of the experimental and simulated results are possible. Figure 3.12 displays histograms of grain size statistics for both SPPARKS (on top) and LEGOMAT (on bottom) against the experimental microstructures across the three orthogonal planes illustrated in Figure 3.11. To obtain the grain size statistics,
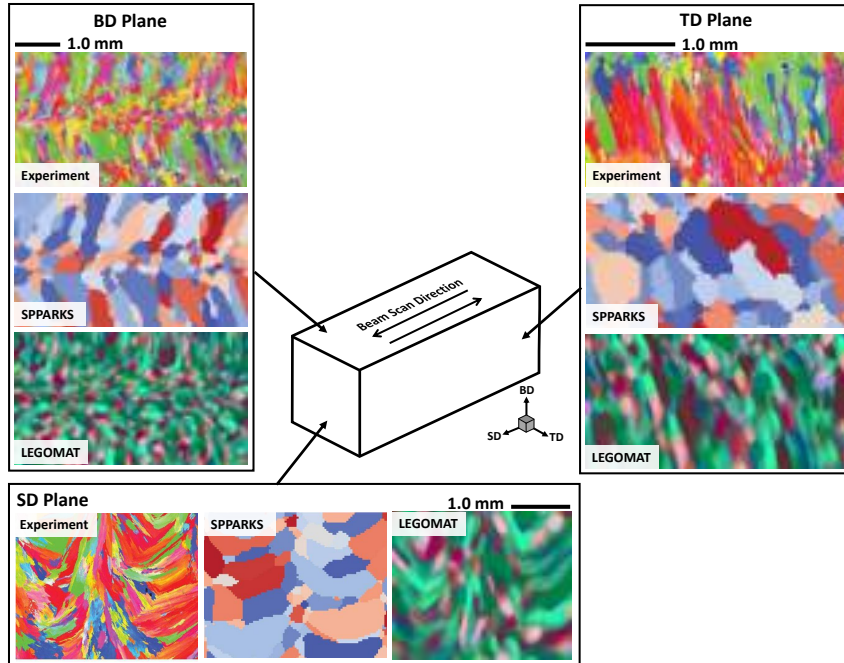
Figure 3.11: *Comparison between experimental and simulated AM microstructures using SPPARKS kinetic Monte Carlo simulator and LEGOMAT geometrical approach along orthogonal planes. The experimental and SPPARKS simulated images shown here are reproduced from the work of Rodgers et al. [104] under the terms of the Creative Commons CC-BY license.*

similar procedure as in Figure 3.10 is applied. That is, all images are first segmented and boundary grains along the border are removed. The grain area of all inner grains, excluding abnormally small and large grains, is obtained and subsequently plotted using a log-normal fit. Across each orthogonal plane, the LEGOMAT's log-normal distribution is found to be closely following the experimental distribution. This is while SPPARKS simulated results are shown to deviate significantly for smaller-scale grain sizes.

The simulated results presented for LEGOMAT reconstruction framework show significant promise for generating large-scale AM microstructures. However, the manual drawing of the volumetric vector field can be relatively time-consuming, especially for multi-layer, multi-track examples. For instance, it takes the user about 18 minutes to create a direction field for the CAD model shown in Figure **??**(c), whereas the

76

| (a) *SD* plane | (b) *BD* plane | (c) *TD* plane |
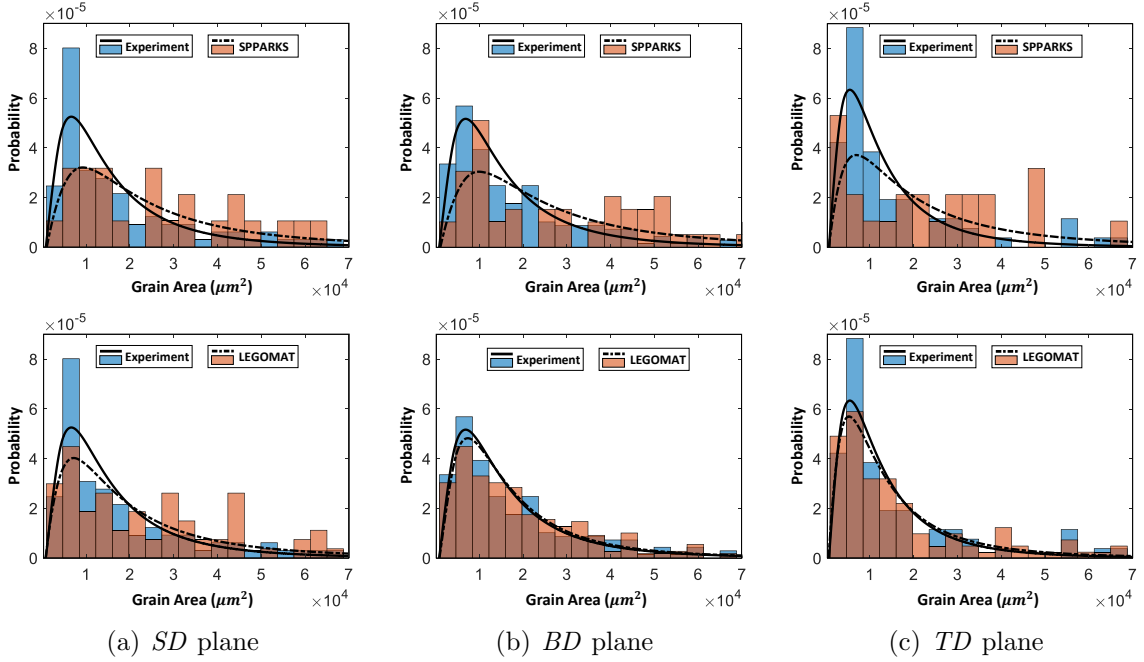
Figure 3.12: *Comparison of grain size statistics for simulated SPPARKS kinetic Monte Carlo [104] (on top) and LEGOMAT (on bottom) techniques against experimental images across orthogonal (a) SD, (b) BD, and (c) TD planes.*

scaling parametrization of the patches takes about 8 minutes, and only 7 minutes to finalize the numerical computation pertaining to LEGOMAT embedding process using a PC with 3.0 GHz CPU and 64.0 GB RAM. Consequently, future work will focus on automating the manual drawing of the preferred direction field as well as the parameterization of grain scaling based on a set of user-defined processing parameters (e.g., hatch spacing, layer thicknesses, and scanning pattern, etc.). Nonetheless, the LEGOMAT methodology presented in this chapter is still significantly computationally inexpensive compared to existing physics-based models [101, 102, 104, 106, 108] for representing large-scale AM solid textures.

Furthermore, the current LEGOMAT reconstruction framework is limited to embedding a single 3D microstructural snapshot in the CAD model. However, the LEGOMAT approach can benefit from multiple input 3D exemplars imaged across various spatial locations. One approach for direct implementation of spatial variations of

the AM microstructure is to exploit the mean locations of the input microstructural measurements in order to partition the CAD geometry in the form of a Voronoi diagram. Mathematically, the measured locations directly correspond to the centroid of the convex hull within each partition, which is also correlated with differences in microstructural features (e.g., grain size, shape, etc.). Accordingly, the Voronoi diagram can provide a geometrical partitioning of the CAD specimen where the best-matching measured 3D unit cell can be identified (based on its relative spatial coordinates to the laser path) and then be sampled for the patching/embedding process. Additionally, a numerical method can be developed to progressively enhance the resultant embedding process conditioned on available input datasets. Here, geometric partitioning of the CAD specimen can be updated as new measured 3D microstructures become available. In this approach, regions in the CAD model for which new reclassifications are available will be partitioned and then progressively re-sampled/re-patched. Work on this is still in progress and will be reported in future articles.

3.3 Conclusions

In this chapter, an image-based framework is introduced for 3D microstructure synthesis of metal AM materials over very large length-scale CAD models. The complete workflow from orthogonal 2D experimental EBSD images to a full-field microstructural CAD visualization is an important and novel contribution in this work. Here, a set of three EBSD exemplars imaged on orthogonal planes of a 316L stainless steel specimen manufactured by SLM process is first obtained via SEM acquisition technique. The microstructures are subsequently converted to a 3D representative unit cell using the MRF sampling technique. The MRF algorithm reconstructs 3D images through matching orthogonal neighborhoods of each voxel to the sectional experimental micrographs while ensuring that the sampled voxels taken from the 2D input exemplars have meshed together seamlessly in the 3D synthesized image.

Thereafter, statistical analyses of microstructural features, such as grain size, orientation distribution, and grain boundary misorientation angles for the reconstructed 3D microstructures, are carried out against the original 2D EBSD images. The results demonstrate that MRF can effectively predict both textural and morphological descriptions of AM microstructures at a small-length scale.

The variations of 3D microstructures during a laser additive manufacturing process at larger length-scales are then captured using the LEGOMAT tensor-based optimization process. The LEGOMAT optimization procedure embeds 3D microstructures in a part-scale CAD geometry accordant with the user-specified material flow fields that efficiently incorporates microstructural variations (e.g., grain size, shape, curvature, anisotropy, and growth direction) in structural systems consisting of several laser paths and deposition layers. Such formulation is shown to be highly effective for modeling the location-specific microstructural geometries seen in experimental characterization techniques. For instance, across BD surface, fine-size equiaxed grains often nucleate near the laser track and then quickly transition to larger transversely-elongated grains in between the laser paths. Similarly, on the TD plane near the laser beam track, elongated grains tend to incline toward the scanning direction. On the SD plane, the columnar grains tend to grow perpendicular to the melt pool's solidification surface, curving toward the laser beam direction. As a result, the LEGOMAT approach can provide in real-time, an efficient methodology to describe textural components in 3D geometrical CAD space via a user-defined tensor field, capturing the preferred growth directions during the solidification process. Due to large-scale microstructure reconstruction model being primarily based on geometrical principles, the LEGOMAT methodology is extremely robust and requires minimal computational power and memory, compared to existing phase-field simulations. Near-term future work will focus on (i) implementing an encoder that accepts a number of input microstructural unit cells while down selects the best 3D exemplar during each

embedding iteration based on relative spatial location of the microstructural patch within the CAD model to its nearest laser path, and (*ii*) automating the manual specifications of the preferred growth orientation and grain size parameterization.

CHAPTER IV

Physics-Based Evolution of Microstructural Features Using Graph-Cut

This chapter introduces a novel numerical framework based on graph-theoretic techniques to investigate the evolution of microstructures in isolated particles. The primary factor governing the formation of crystalline structures, precipitate coarsening, and grain growth is the reduction of orientation-dependent surface-free energies. Consequently, the equilibrium shape of the crystalline structure, commonly known as the Wulff shape, can be accurately determined by minimizing its surface energies. However, modeling Wulff constructions numerically presents challenges, particularly in estimating the curve lengths and surface areas of crystalline facets in respective pixelated 2D and voxelated 3D micrographs, presented in Chapters II and III, where adding GB edges/facets can introduce high metrication errors. To address such limitations, this chapter applies the concept of graph-cuts from integral geometry [129] to compute the expected lengths of GBs using a pairwise formulation. The framework is further generalized to incorporate anisotropic grain growth in 2D microstructures using an optimization principle that captures the underlying energetic mechanisms pertinent to grain formation. These ideas can be directly extended to 3D microstructures, and the necessary modifications to the framework are provided, along with applications for segmenting and denoising voxelated meshes developed

in Chapter II. Additionally, to demonstrate the effectiveness of the graph-cut approach, proof-of-concept cases are presented and compared with data obtained from in-situ tomographic and analytical techniques, validating the efficacy of the proposed physics-based numerical framework for accurate prediction and quantification of microstructure evolution.

The following details the structure of this chapter. First, the Cauchy-Crofton formulation is reviewed in Section 4.1.1 for 2D problems. Thereafter in Sections 4.1.2 and 4.1.3, the numerical implementation of the graph-cut technique, along with the use of Riemannian metrics, are outlined for anisotropic surface energies. Sections 4.1.4 and 4.1.5 introduce the pairwise optimization technique for the simulation of isolated particles and polycrystalline structures. Here, the process to correct GB angles by minimizing the interfacial energy within the constraints posed through γ-plots is described. This follows by Section 4.1.6 outlining the implementation of the Cauchy-Crofton formulation in the 3D material domains. Subsequently, Section 4.2 illustrates and discusses numerical examples for several multi-dimensional problems. Notably, in Section 4.2.1, numerical results are obtained for computations of grain circumference at various pixel densities against analytical solutions for a given isolated particle. Implementation of surface energies as Riemannian metric is then examined in Section 4.2.2. Thereafter in Sections 4.2.3 and 4.2.4, the Cauchy-Crofton results are examined for modeling grain evolutions across single 2D particles and polycrystalline aggregates, respectively. Section 4.2.5 then follows to demonstrate a 3D example for segmentation of polycrystalline microstructures as directly obtained from the MRF reconstruction approach. The proposed Cauchy-Crofton technique is shown to be efficient in all numerical examples for the segmentation and simulation of crystalline structures across multi-dimensional problems.

4.1 Methodology

This section discusses the mathematical formulation and implementation for the segmentation and evolution of crystalline particles. First outlined in Section 4.1.1, the Cauchy-Crofton relations, from a previously-published work by Boykov et al. [129], is summarized. Next, the numerical implementation of the Cauchy-Crofton approach to pixelated microstructural images is presented in Section 4.1.2. These applications are then extended to generalized microstructural models using Riemannian surface energies as established in Section 4.1.3. Subsequently, the pairwise optimization techniques for simulating particle evolution and grain growth in 2D microstructural images are introduced in Sections 4.1.4 and 4.1.5, respectively. Finally, Section 4.1.6 provides the extension of the Cauchy-Crofton techniques to 3D voxelated problems for denoising and segmentation purposes of the synthesized MRF images.

4.1.1 Cauchy-Crofton Formulation

The computations of the boundary of a particle (i.e., length in 2D and areas in 3D), when using pixelated images obtained through empirical devices [223, 224, 225] or routine computational techniques [47, 60, 66, 71], can be often intractable. For instance, consider the circular particle illustrated in Figure 4.1, where each pixel is colored/labeled depending on whether it is positioned inside or outside the GB. In such a representation, one can estimate the perimeter of the interface by summing up the edges separating the red and blue regions, as indicated by the solid gray line on the right-hand side. However, this procedure tends to falsify the GB interface [129, 130] due to *metrication* error. To overcome these issues, concepts from integral geometry, specifically Cauchy-Crofton relations [129] have been shown to be effective and more accurate than other numerical methods, e.g., thresholding [226], region growing [227, 228, 229], and Moore-neighbor contour tracing algorithm [230, 231]. A formal discussion of these relations is out of the scope of this chapter. However, inter-

ested readers are encouraged to refer to Reference [232] for a complete and rigorous introduction to the topic. This chapter will adopt a much more applied outlook.
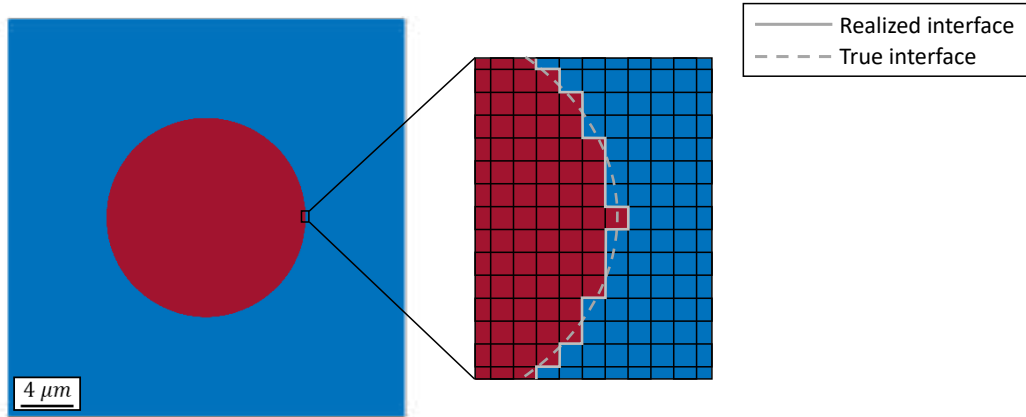
Figure 4.1: *Identification of particle's boundary in pixellated images is generally intractable. A depiction of possible lengths of the particle boundary, which in turn affects the crystalline shape, can be found using the Cauchy-Crofton technique based on intersection count.*

The main idea in Cauchy-Crofton pursued in this chapter is that given a contour, as illustrated in Figure 4.2(a), the total perimeter is proportional to the number of intersections it makes with the 'family' of lines at various angles. This theorem makes the basis of the many methods developed later in the chapter. However, before going into this theorem's applications, it is necessary to define a measure on the set of lines. Hence, in the following discussion, consider a straight line in the $\mathbb{R}^2$, denoted as L, determined by its normal parameters ρ and ϕ, as indicated in Figure 4.2(b). In this parameterization, each line can be sufficiently described by a point in $\mathcal{L} = \{(\rho, \phi) : \rho \geq 0, \phi \in [0, 2\pi]\}$. This parameterization is illustrated in Figure 4.2(c). Accordingly, the Lebesque measure [233] for a subset of straight lines $\xi \subset \mathcal{L}$, can be defined by the integral $\int_\xi d\rho d\phi$.

Furthermore, let C represent a rectifiable curve in $\mathbb{R}^2$ with Euclidean length $|C|_\epsilon$. The Cauchy-Crofton formula [233] establishes a connection between Euclidean length, $|C|_\epsilon$, and a set of straight lines, $L(\rho, \phi)$, intersecting it, as follows:
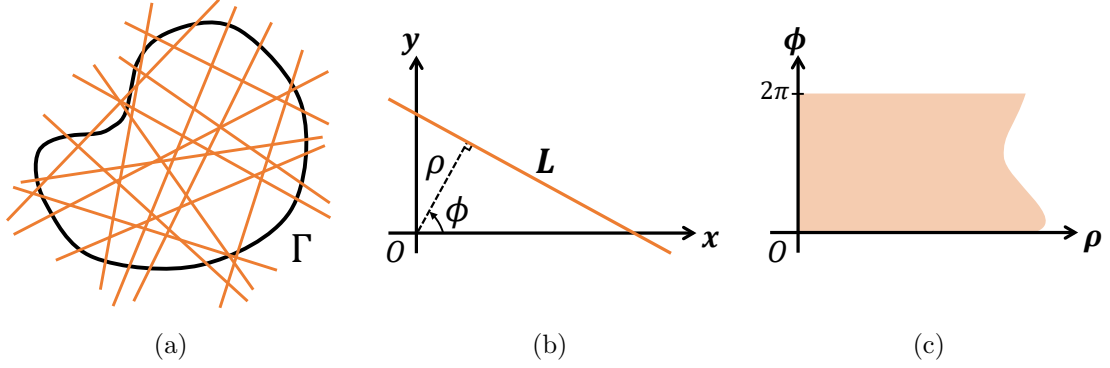
Figure 4.2: *Illustration for Cauchy-Crofton relations and parameterization of a line in $\mathbb{R}^2$: (a)* length(Γ) *is proportional to the numbers of intersections it makes with lines at different angles, (b) parameterization of a line, L, in terms of ρ and ϕ, and (c) set of all lines in $\mathbb{R}^2$, represented as $\mathcal{L}$, using the (ρ, ϕ)-coordinates.*

$$|C|_\epsilon = \frac{1}{2} \int_{\mathcal{L}} n_c(L) d\mathcal{L} = \frac{1}{2} \int_0^{2\pi} \int_0^\infty n_c(\rho, \phi) d\rho d\phi \qquad (4.1)$$

where function $n_c(L)$ specifies the number of times any given line, $L(\rho, \phi)$, intersects with the curve, C, and ρ and ϕ respectively represent the non-negative radius and polar angle restricted to the interval $[0, 2\pi]$ pertinent to line L.

4.1.2 Numerical Approximation to Cauchy-Crofton Relation

In 2D pixelated structures, each node, denoted by its spatial coordinates, i.e., $\nu_n \equiv (p_n, q_n)$, is embedded in a regular grid-like fashion with cells of size δ. Consequently, a connection between two nodes, e.g., $\{\nu_n, \nu_m\}$, can be represented in the form of a vector, denoted as $\overrightarrow{e_{nm}} = (p_m - p_n, q_m - q_n)$. Here, let $\mathcal{N}_R$ represent a stencil used to connect R numbers of neighboring nodes in the image. The elements of the stencil consist of ordered pairs of vectors of the form $\overrightarrow{e_k}$ with their respective weights, $w_k \in \mathbb{R}^+$. Hence, given the pixel ν_n and an stencil family $\{\overrightarrow{e_k}, w_k\} \in \mathcal{N}_R$, a connection can be drawn to $\nu_m = (p_n, q_n) + \overrightarrow{e_k}$ with an interaction energy set as w_k, assuming

85

constant weights within each family of edge-lines. Some examples of possible stencils, where subscripts represent the numbers of neighborhood interactions, are illustrated in Figure 4.3 for 2D domain. The example in Figure 4.4(a) depicts a regular grid with all nodes having an identical $\mathcal{N}_8$ stencil as in Figure 4.3(b).

(a) $\mathcal{N}_4$, 4-neighbor stencil   (b) $\mathcal{N}_8$, 8-neighbor stencil   (c) $\mathcal{N}_{16}$, 16-neighbor stencil
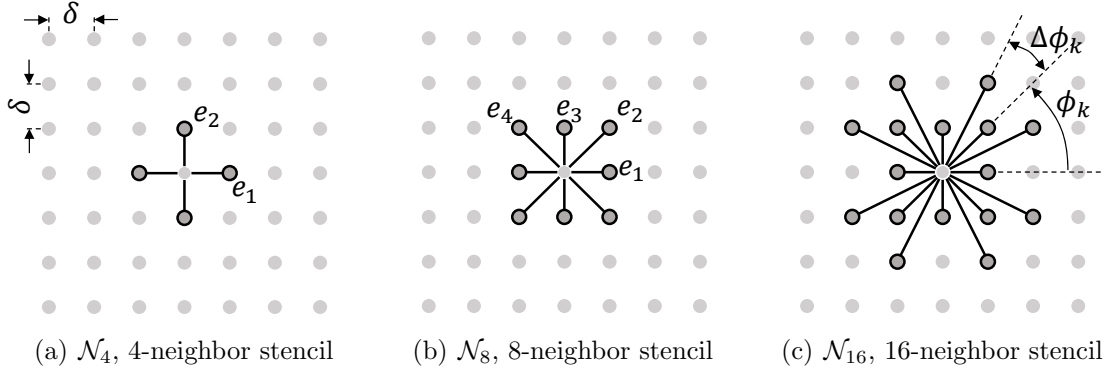
Figure 4.3: *Examples of possible* 2D *neighborhood interactions in a structured pixelated discretization with uniform spacing δ respectively using (a)* 4-*neighbor,(b)* 8-*neighbor, and (c)* 16-*neighbor stencils.*

(a) 2D grid with 8-neighbor interaction   (b) One family of lines
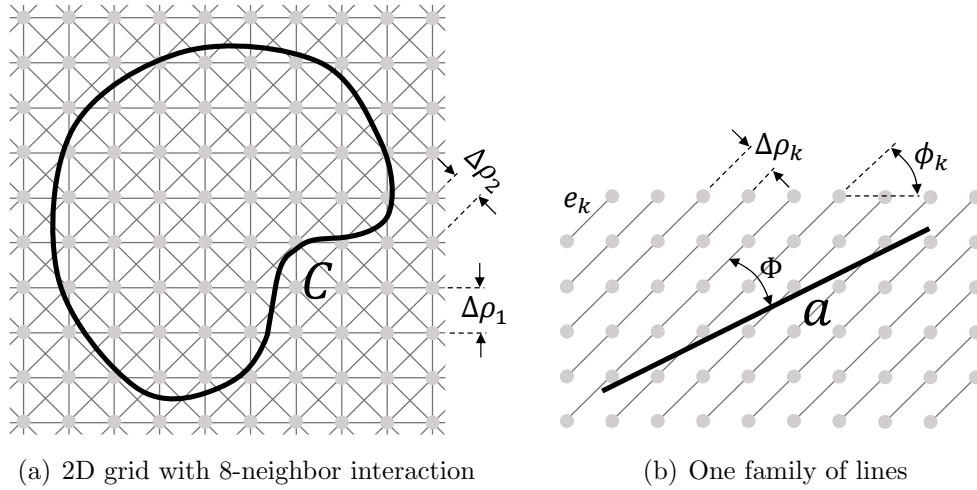
Figure 4.4: *Illustration of (a) a regular* 2D *pixelated grid with uniform spacing δ using an $\mathcal{N}_8$ stencil, and (b) a single family of lines on the corresponding* 2D *grid.*

Accordingly, by choosing an appropriate partitioning of the set $[0, 2\pi] \times \mathbb{R}$, Equation (4.1) can be approximated numerically by its partial sum, as follows:

$$|C|_\epsilon \approx \frac{1}{2} \sum_{k=1}^{|\mathcal{N}_R|} \left(\sum_i n_c(i,k) \Delta\rho_k \right) \Delta\phi_k = \sum_{k=1}^{|\mathcal{N}_R|} n_c(k) \cdot \frac{\delta^2 \cdot \Delta\phi_k}{2 \cdot ||\overrightarrow{e_k}||_2} \qquad (4.2)$$

where the approximation error on the left-hand side is due to the difference between an integral and its partial sum, and as partitioning becomes finer, by incorporating stencils with higher-neighborhood interactions, the error of approximation converges to zero. Here, index i enumerates lines in the kth family of lines, $n_c(i,k)$ counts intersections of line i in the kth family with curve C, and $n_c(k) = \sum_i n_c(i,k)$ returns the total number of intersections for the curve C with the kth family. Additionally, as depicted in Figure 4.4, $\Delta\rho_k$ denotes the distance between two adjacent lines in the kth family, and $\Delta\phi_k$ quantifies the angle difference of link e_k with its nearest link, i.e., $\Delta\phi_1 = \phi_2 - \phi_1$, $\Delta\phi_2 = \phi_3 - \phi_2$, ...

Assuming constant edge weights within each element of the stencil, Equation (4.2) can be simplified as follows:

$$|C|_\epsilon \approx \sum_{k=1}^{|\mathcal{N}_R|} n_c(k) \cdot w_k \qquad (4.3)$$

where,

$$w_k = \frac{\delta^2 \cdot \Delta\phi_k}{2 \cdot ||\overrightarrow{e_k}||_2} \qquad (4.4)$$

87

4.1.3 Implementation of Anisotropic Surface Energies

The Cauchy-Crofton approximation in Equation (4.1) can also incorporate surface energies, denoted as $\gamma(\overrightarrow{n})$ for facets with face normal $\overrightarrow{n}$, in the form of w_k. This can be achieved by choosing a metric space, $\mathcal{M}$, such that the following relation holds for all phase boundaries:

$$|C|_{\mathcal{M}} = \int \gamma(\overrightarrow{n}(s))ds \tag{4.5}$$

where $|C|_{\mathcal{M}}$ denotes the length of the boundary in the given metric, $\mathcal{M}$.

For microstructure applications, a special case is considered where the curve's length is measured using a constant Riemannian metric, denoted by $\boldsymbol{D}$, as follows:

$$|C|_{\mathcal{M}} = \int \sqrt{\overrightarrow{t}^T \cdot \boldsymbol{D} \cdot \overrightarrow{t}}\, ds \tag{4.6}$$

where $\boldsymbol{D}$ is a positive definite matrix, specifying the local Riemannian metric at any given pixel in the image, and $\overrightarrow{t}$ is a unit tangent vector to the contour, C. If the surface energy can be represented as the integrand in Equation (4.6) (or in general, as the summation of integrands for different $\boldsymbol{D}$'s), then the Cauchy-Crofton formula leads to values of weights, w_k, for the kth link of the pixel, p, as follows:

$$w_k = \frac{\delta^2 \cdot ||\overrightarrow{e_k}||_2^2 \cdot \Delta\phi_k \cdot \det \boldsymbol{D}}{2 \cdot (\overrightarrow{e_k}^T \cdot \boldsymbol{D} \cdot \overrightarrow{e_k})^{3/2}} \tag{4.7}$$

Using these weights, the surface energy integral in Equation (4.5) can be computed by summing up the weights of all intercepts on the particle surface. It is worth noting that arbitrary surface energy functions cannot be modeled in this manner. It was shown by [130] that the most general case that can be considered in this framework is when $|C|_{\mathcal{M}}$ is measured with respect to a subclass of Finsler metric. Interested readers are referred to their work for further discussion on this topic.

4.1.4 Simulations of Particle Evolution

The problem of grain segmentation can be formulated as a graph labeling problem. Each pixel in the image is treated as a vertex of a simple undirected graph, $\mathcal{G}(\mathcal{V}, \mathcal{C})$, where $\mathcal{V}$ and $\mathcal{C}$ denote the sets of all vertices and connections in the graph, respectively. Here, each vertex, $\nu_n \in \mathcal{V}$, is assigned a label, $L_n \in \{l_1, .., l_M\}$, representing a grain ID. The value of M denotes the total number of grains in the micrograph. A cost function is assigned based on the graph's completed labeling, with $\boldsymbol{L} = (L_1, \ldots, L_N)$ treated as a sequence and N denoting the total number of vertices. The cost, $F(\boldsymbol{L})$, for given labeling $\boldsymbol{L}$ of the graph is formulated to a Potts form as follows:

$$F(\boldsymbol{L}) = \sum_{\nu_n \in \mathcal{V}} H(|L_n - I_n|) + \sum_{(n,m) \in E} J_{nm}(1 - \delta_{L_n - L_m}) \tag{4.8}$$

where H denotes the Heaviside function and $\boldsymbol{I} = (I_1, \ldots, I_N)$ are the measured grain IDs in the tomographic image, indexed in the same order as the vertices of the graphs. Furthermore, the parameter J_{nm} incorporate surface energies, denoted as $\gamma(\overrightarrow{n})$ for facets with face normal $\overrightarrow{n}$, in the form of $J_{nm} = w_k$, and the symbol $\delta_{L_n - L_m}$ represents the Kronecker delta. The first term in Equation (4.8) is referred to as the data term, penalizing deviations from the image data. Whereas the second term is referred to as the smoothening term and describes the interface properties between vertices with different labelings, written typically in terms of surface area. Using the Cauchy-

Crofton formulation, the interaction energies, denoted as J_{nm}, can be encoded such that the second term in Equation (4.8) evaluates the expected surface energies of the interface between the clusters of different labels. Hence, minimization of the energy would allow a preferential selection of facets with minimal energy while retaining the bulk phases measured in the original image.

4.1.5 Grain Growth Modeling

The local energy at the GB is often higher than the grains' corresponding bulk energies. This energy provides a thermodynamic driving force for the motion of the GB. Generally, the motion of GB decreases its surface area (or length in 2D), appearing as growth in a few grains and consequent decay/annihilation of other grains. Computational approaches such as the Monte Carlo Potts model [234, 235], level sets [236], and phase-field methods [124, 237] have been used to simulate the behavior of multiple grains. A typical problem involves the initialization of a mesh and modeling the motion of grains using energy or probability-based criteria. Methods like the Potts model and cellular automata use probabilistic rules for evolution and do not capture the detailed local physics that leads to abnormal grain growth. Level set and phase field methods are well suited for modeling surface energies but are limited to obtaining local minima. The approach presented here is an extension of the Cauchy-Crofton segmentation method explained in Section 4.1.4 and is an altogether new approach compared to those aforementioned techniques in the literature. Advantages of the formulation include the realization of a global minimum for energy [238, 239, 240] and use with voxelated images [241].

As the level set method, the approach presented here handles topological changes of the evolving interface. The particular advantage of the proposed computational approach lies in its ability to target global minima of shapes using image-based meshes. Previous work [242, 243] has applied this methodology successfully to the problems

such as meshing and crack formation in polycrystals, and preliminary work towards grain growth is illustrated in Reference [244]. Experimentally-measured grain growth velocities from experiments will be used to simulate grain growth, including the effect of initial size distribution and texture. The presented work shows that the methodology captures the necessary physics of microstructure evolution in terms of annihilation and merger of grains. The method also has the flexibility to use different surface energy functions using the novel notion of summation of Riemannian metrics. The method is briefly explained next.

Grain growth in 2D is evaluated by minimizing the functional as follows [245]:

$$F(C) = \int_A b \, dA + \int_C \gamma(\vec{n}(s)) ds \qquad (4.9)$$

where $\gamma(\vec{n})$ is the surface energy defined for interface C with unit normal $\vec{n}$ and b is the bulk energy density. Consider a smooth curve, C_0, that is defining the GB interface, where each point is displaced as $dC = v\Delta t$, with v denoting the normal velocity of the GB and Δt denoting the time step. The point-wise position of the new curve is given as $C(s) = C_0(s) + dC(s)$ where s is the arc-length parameterization of C_0. A distance measure between C_0 and C, as illustrated in Figure 4.5, can be estimated using following relation (proof in [246]):

$$\text{dist}^2(C, C_0) = 2 \int_{\Delta C} D_o(p) dp$$

where p denotes points in the region ΔC between the two contours (region shaded green in Figure 4.5), and the function $D_o(p)$ is a distance from point p to the nearest

point on curve C_0.
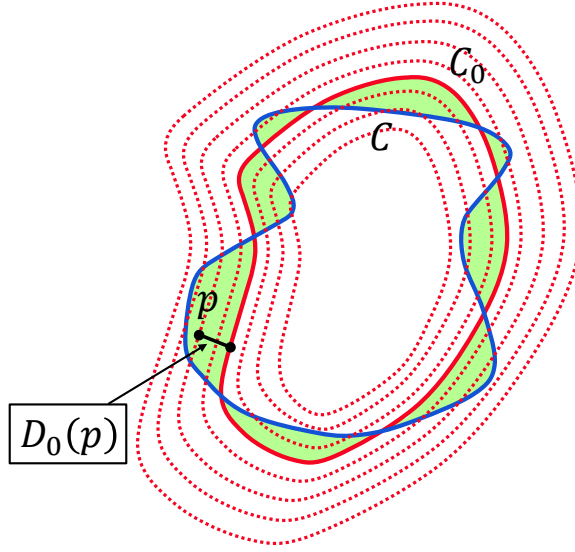
Figure 4.5: *Gradient flow evolution transforms the shape of contours giving the largest energy decrease.*

With these definitions in place, a graph-based minimizer for simulating grain growth dynamics can be developed as follows:

$$C_{t+\Delta t} = argmin_C \left(\mu F(C) + \frac{\text{dist}^2(C, C_t)}{2\Delta t} \right) \qquad (4.10)$$

where C_t denotes the interface at time t, $C_{t+\Delta t}$ is the evolved interface at time $t + \Delta t$, and μ denotes the mobility of the GB [247]. Efficient graph-based algorithms to minimize such functionals are available [241]. It can be proven [244] that the normal velocity, v, of a grain C between grain i and j when using this approach, is given by the well-known curvature-driven velocity [245]:

$$v = \mu \left(\gamma \kappa + (b_i - b_j) \right) \qquad (4.11)$$

where κ is the curvature of the GB. A critical aspect of the minimization process

described in Equation (4.10) is the accurate estimation of grain surface areas to compute the interfacial energy in $F(C)$. For this, the Cauchy-Crofton-based encoding of interfacial energies that was described previously is implemented. Although the discussion thus far has focused on 2D cases only, similar expressions are available in three dimensions, as subsequently explained.

4.1.6 Extension to Three-Dimensional Material Domains

The Cauchy-Crofton formula can also be extended to estimate the surface areas of hypersurfaces in higher dimensions [248]. In this case, the Cauchy-Crofton formulation as written in Equation (4.2) is modified as follows. Let M be a 3D surface with an area A. The measure of the set of straight lines (counted with multiplicities) which meets M is equal to $\pi^2 A/2$. The numerical version of this relation can be formalized by following the same strategy to construct stencils, $\mathcal{N}_R$ in 3D. The weights of the connections are estimated as:

$$w_k = \frac{\delta^3 \cdot ||\overrightarrow{e_k}||_2^3 \cdot \Delta\Phi_k \cdot \det \boldsymbol{D}}{\pi \cdot (\overrightarrow{e_k}^T \cdot \boldsymbol{D} \cdot \overrightarrow{e_k})^2}$$

where contrary to 2D case, $\Delta\Phi_k$ correspond to a given partitionin gof unit sphere among angular orientations Φ_1, Φ_2, ..., and it is evaluated using the strategy proposed in [129, 249, 250]. Each vector $\overrightarrow{e}_k$ is projected onto a unit sphere. The intersecting points are then used as a germ/grain for the Voronoi tessellation of the sphere. The surface area of each spherical domain is then used as the weight for the corresponding direction.

4.2 Results and Discussion

Here, the Cauchy-Crofton algorithm is examined for the simulation and segmentation of 2D and 3D microstructural images. Specifically, Section4.2.1 presents numerical findings for the computation of GB interface at different pixel densities for an individual particle. The utilization of surface energies as a Riemannian metric is then explored in Section4.2.2. Sections4.2.3 and 4.2.4 investigate the Cauchy-Crofton results concerning the modeling of grain evolutions in single particles and polycrystalline aggregates, respectively. Lastly, Section4.2.5 further showcases a 3D example, demonstrating the segmentation of polycrystalline microstructures obtained through the MRF reconstruction approach. The proposed Cauchy-Crofton technique proves to be efficient in all numerical examples, enabling the simulation of crystalline structures across multi-dimensional problems.

4.2.1 Example 1: Computation of Particles Circumference

For the first case study, the computation of the particle's circumference in terms of the lengthwise pixel density is demonstrated as a proof-of-concept. Here, a circular grain with a radius $r = 8 \ \mu m$, as illustrated in Figure 4.6, is examined. It is intuitive that as the pixel resolution, which is commonly measured in terms of the number of pixels per micrometer-length (PPM), increases, the realized granular shape resembles a circle more closely. Accordingly, in this example, the lengthwise pixel density is successively doubled, reaching pixel densities up to 64 PPM. Thereafter, computational techniques, such as Cauchy-Crofton relations, as formulated in Equation (4.2), and modified Moore-neighbor contour tracing algorithm [230], are compared for an accurate representation of the circular grain. The first three images composed of the lowest pixel densities are shown in Figures 4.6(a)-4.6(c).

Next, the *metrication* error, which relates the relative difference between the actual

(a) Resolution: 1 PPM   (b) Resolution: 2 PPM   (c) Resolution: 4 PPM
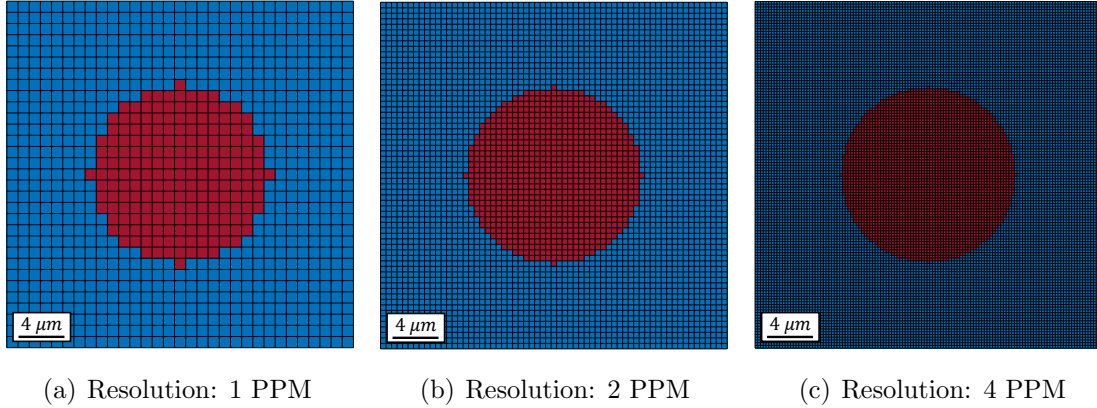
Figure 4.6: *Illustration of a circular particle of the radius $r = 8$ μm with three vary-ing lengthwise pixel densities. In this example, the lengthwise resolution is doubled consecutively as measured by the number of pixels per micrometer-length (PPM). In-tuitively, the realized red feature closely resembles a circular shape as the resolution improves.*

circular perimeter and the length obtained from the modified Moore-neighbor con-tour tracing algorithm, is compared with the Cauchy-Crofton formula at different pixel densities. As depicted in Figure 4.7, when incorporating fine resolutions, small neighborhood interactions with $\mathcal{N}_4$ stencil, which consists of only the horizontal and vertical neighbors, still results in relatively accurate estimates, compared to modified Moore-neighbor contour tracing algorithm. However, when working with a coarse lattice structure, such as Figure 4.6(a), the neighborhood interactions need to in-crease in order to include more intersecting lines at different angles. For instance, at a low resolution of 1 PPM, Cauchy-Crofton with $\mathcal{N}_{28}$ stencil can precisely estimate the actual feature perimeter, with the error being around 0.5%. Additionally, as the lengthwise pixel resolution doubles, Cauchy-Crofton's estimates improve substantially across different horizon interactions, whereas the metrication error increases, eventu-ally plateauing at around 5.5%.
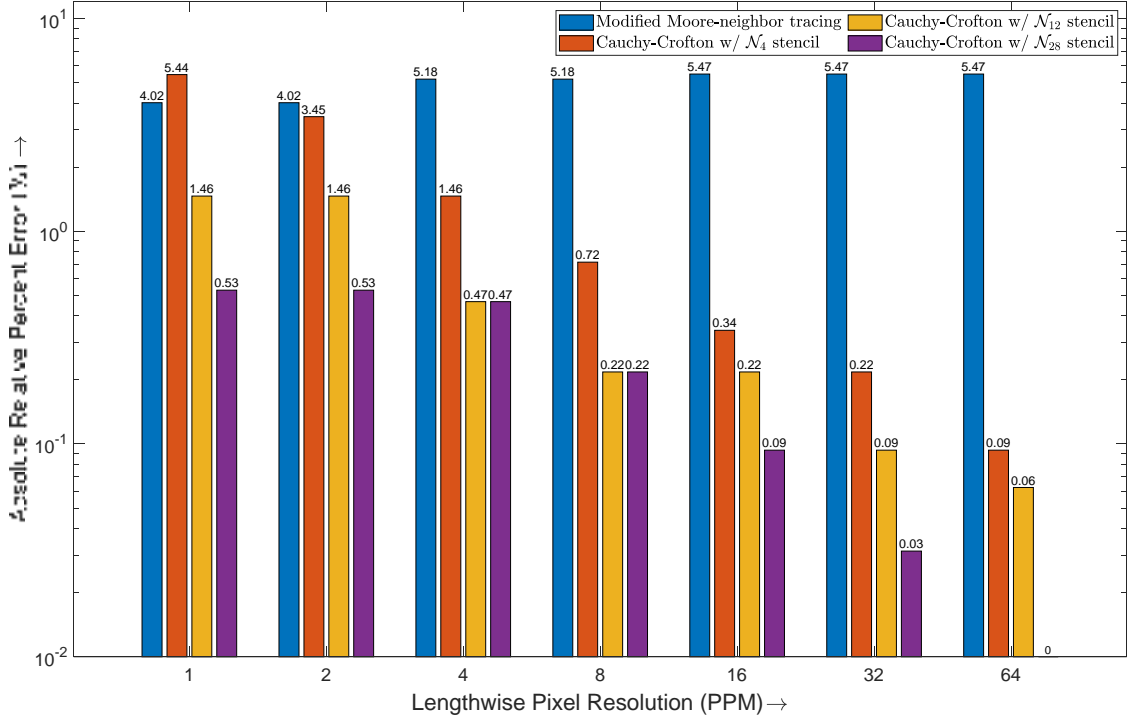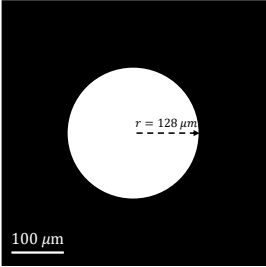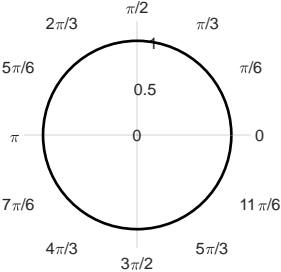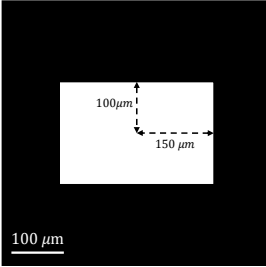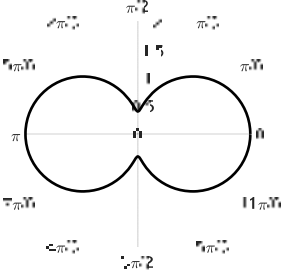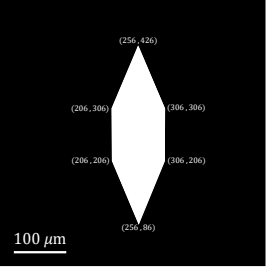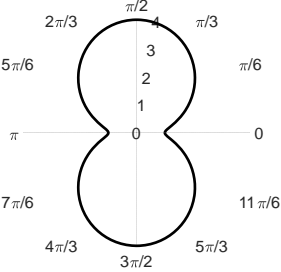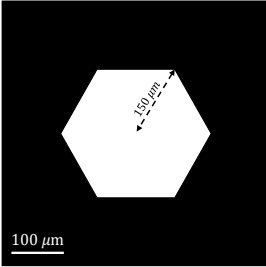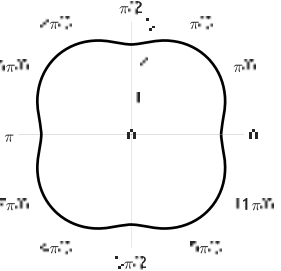
Figure 4.7: *Comparison of Cauchy-Crofton formulation against modified Moore-neighbor tracing algorithm for calculations of the perimeter of the particle in terms of image resolution. Here, Cauchy-Crofton approximations with three stencils of the form $\mathcal{N}_4$, $\mathcal{N}_{12}$, and $\mathcal{N}_{28}$ are used to compute the grains circumference at various image resolutions. The Cauchy-Crofton estimates have higher accuracy with increased pixel interactions, whereas the Moore-neighbor contour tracing accuracy diminishes and plateaus at around 5.5%.*

4.2.2 Example 2: Implementation of Surface Energies as Riemannian Metrics

The Cauchy-Crofton formula is used to compute surface integrals for different particle shapes. Generally, the surface integrals estimated by Cauchy-Crofton tend to have higher accuracy with increased pixel interactions, with the error ultimately converging to zero. Here, the estimated values are computed by representing the surface energy integral in terms of a Riemannian contour length as described in Equation (4.6). Examples of the use of the Cauchy-Crofton formula for different surface energy (i.e., γ-plots) and particle shapes are shown in Table 4.1 and compared with the analytical integrals. It is shown that the Cauchy-Crofton results are consistent with the

analytical solutions.

Table 4.1: *Various examples for the Cauchy-Crofton formula with different surface energies for a given particle shape contour.*

Contour	γ-plot	Analytical $\int \gamma ds$	Cauchy-Crofton $\int \gamma ds$
		804.3	804
		1040.0	1040
		1132.9	1122
		2391.2	2384

In the past, a variety of approaches have been used for the segmentation and com-

putation of the particle size distribution from tomographic images. These include methods such as Delaunay tessellation, medial axis, and watershed-based methods [251, 252]. Delaunay and medial axis methods are better suited for spherical particles, while watershed methods require arbitrarily set parameters to generate results [253]. In sintering theories, these segmented particles can be used to compute various descriptors, including pore coordination number distribution [254, 255], particle/pore size distribution [256, 257, 258], distribution of particle shape metrics such as shape moment invariants [259, 260]. Many of these metrics are known for the case of spherical particles but are not well known for polyhedral particles as well as for bimodal/trimodal particle distributions. Accordingly, the use of surface energies to perform segmentation based on Wulff construction, as presented in this chapter, is novel.

4.2.3 Example 3: Wulff Shape Construction

Previous examples successfully illustrate the computation of surface integrals using Riemannian metrics. This example further incorporates shape evolution problems to capture the contour with minimum surface energies, also known as the Wulff shape. The equilibrium shape of isolated crystals is given by the Wulff construction based on orientation-dependant γ-plots for a fixed volume. Hence, as the first case study, the evolution of a circular-shaped grain is considered, as depicted in Figure 4.8, with Riemannian matrix $D_{11} = 4$, $D_{12} = D_{21} = 0$, and $D_{22} = 25$. It is observed that the grain gradually reduces its width while growing in height to achieve minimum surface energy. It is worth noting that if the total surface energy is minimized without constraining the volume, the algorithm eventually shrinks the particle to zero, as that is the lowest surface energy one can obtain. Hence, a constraint is placed on the volume such that the algorithm dilates the shape vertically after several iterations since, based on the γ-plot, the energy is lowest along the vertical facets. Figure 4.8(right)

represents the Wulff construction, where the crystalline shape (depicted in orange) minimizes the surface energy (represented as a blue line).
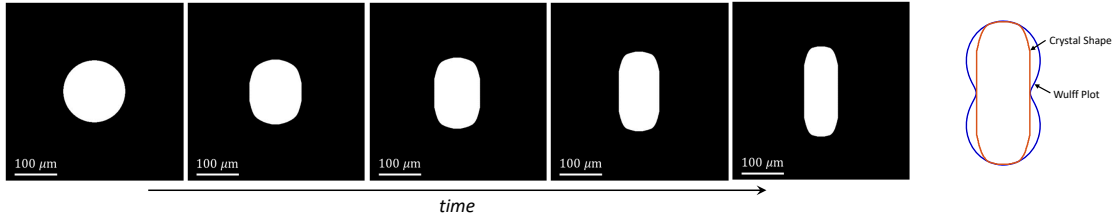
Figure 4.8: *Simulation of grain evolution for a circular-shaped grain with Riemannian surface energy denoted by $D_{11} = 4$, $D_{12} = D_{21} = 0$, and $D_{22} = 25$.*

Next, the Cauchy-Crofton is shown to be useful for denoising microstructural images. The results are presented in Figure 4.9, where the procedure shows to smoothen the data by relabeling the noisy pixels. Moreover, using a larger stencil and finer densities, especially along the GB, can provide better results in terms of the curvature of grains.
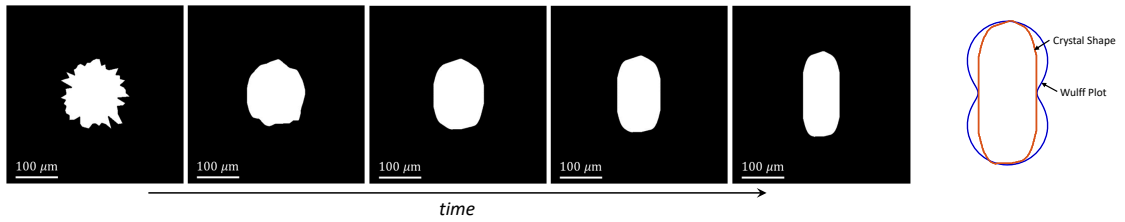
Figure 4.9: *Simulation of grain evolution for a noisy circular-shaped grain with Riemannian surface energy denoted by $D_{11} = 4$, $D_{12} = D_{21} = 0$, and $D_{22} = 25$.*

4.2.4 Example 4: Evolution of 2D Polycrystalline Microstructure

This section examines the Cauchy-Crofton formulation for topological changes of the evolving interfaces in a 2D polycrystalline microstructure. Accordingly, the simulation of 2D polycrystalline microstructure is considered in Figure 4.10. As expected, smaller grains in the initial configuration depicted on the left-hand side are annihilated as time progresses. This illustrates that the Cauchy-Crofton methodology captures the necessary physics of microstructure evolution in terms of annihilation and merger of

polycrystals. In microstructural aggregates, the energy at the GB is typically higher than the bulk energies of the grains themselves. This energy serves as a thermodynamic driving force for the simulation of grain growth. Hence, the motion of the GB leads to a decrease in its surface area, resulting in the growth of a few grains while the remaining grains decay or annihilate. Computational techniques, such as the Monte Carlo Potts model [234, 235], level sets [236], and phase-field methods [124, 237], have been employed to simulate the behavior of polycrystals. The particular advantage of the proposed computational approach lies in its ability to target global minima of shape using image-based meshes. In future work, experimentally-measured grain growth velocities from experiments will be supplemented to simulate grain growth, including the effect of initial size distribution and texture.

time
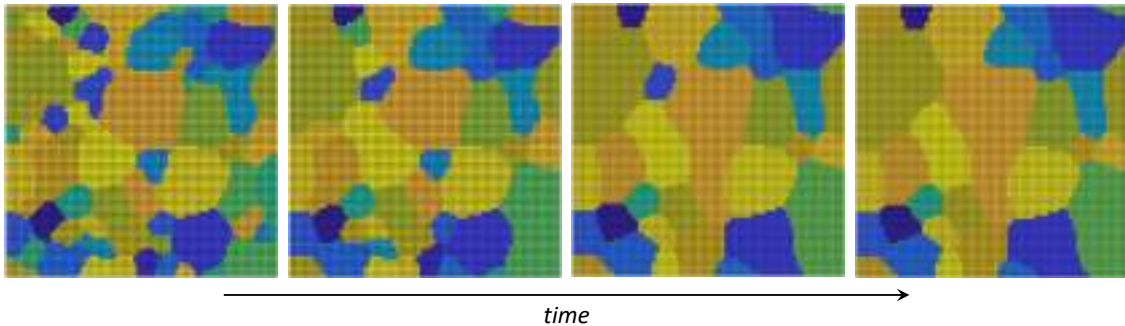
Figure 4.10: *Simulation of grain growth in 2D polycrystalline structure using Cauchy-Crofton formula.*

4.2.5 Example 5: Segmentation of MRF 3D Reconstructions

The Cauchy-Crofton method is also shown to be robust against noise and partial volume effects. As a result, in the next case study, the Cauchy-Crofton algorithm is supplied as the post-processing step for the output of MRF reconstruction, discussed in Chapter II. Here, a 3D diffraction contrast tomography (DCT) microstructure of Al-Cu alloy [42], shown in Figure 4.11, is taken as a proof-of-concept for the proposed coupling reconstruction-segmentation technique. The raw Euler angles are mapped to a discretized ODF, accounting for the cubic symmetry of the scanned material.

Subsequently, each voxel in DCT data is mapped to the closest independent node within the ODF. The DCT microstructure is then colored according to the nodal numbers. Thereafter, all slices within each orthogonal direction (i.e., x, y, and z) of the original DCT data are extracted and categorized based on their underlying 2D grain size statistics and texture distributions. The best three orthogonal slices of the original 3D DCT dataset are selected as the input exemplars for the MRF reconstruction process, discussed in Chapter II. These planar exemplars are illustrated in Figure 4.11. As illustrated in Figure 4.12(a)-4.12(b), these exemplars display similar cumulative pole figures to the original 3D dataset. The reconstruction process is followed by the segmentation procedure, outlined in Chapter IV. Herein, the measured microstructure contains mostly spherical grains (i.e., equiaxed crystals), and so in the following, the Riemannian matrix, D, is set to the identity matrix, i.e., $D = I$. The resulting segmented image of the Cauchy-Crofton process is shown in Figure 4.11.

Subsequently, the Euler angles associated with each voxel in the synthesized solid model can be mapped to a discretized pole figure, i.e., a graphical representation of the stereographic projection of crystal orientations onto a particular plane. Two pole figures (e.g., $\langle 100 \rangle$ and $\langle 111 \rangle$) are sufficient to fully define the crystallographic orientations of each grain. As depicted in Figure 4.12(a)-4.12(c), it is found that the pole figures of the experimental DCT model match exceptionally well to the respective pole figures of the segmented 3D model shown in Figure 4.11.
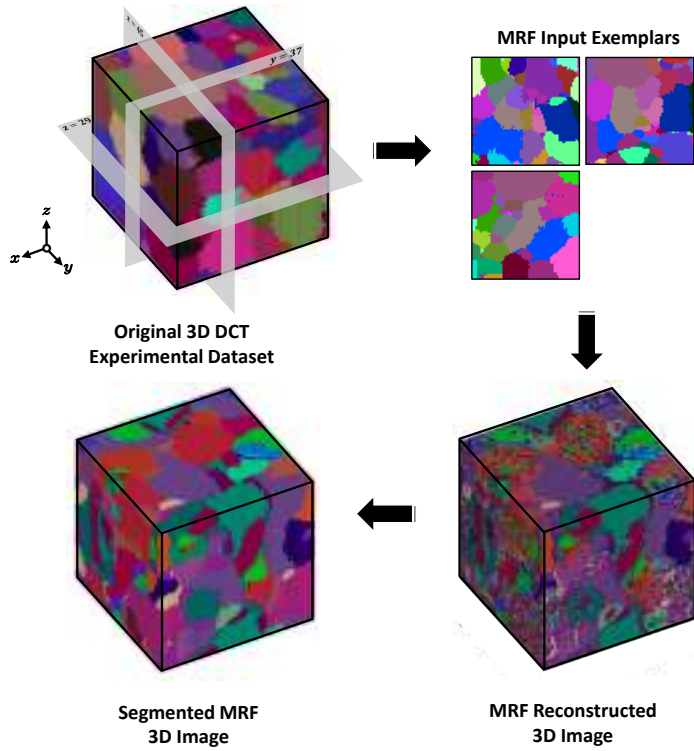
Figure 4.11: *Coupling Cauchy-Crofton segmentation algorithm to augment the MRF reconstructions: three orthogonal planar images of the original DCT dataset are extracted for MRF reconstruction. The Cauchy-Crofton segmentation technique is followed for the segmentation of the reconstructed 3D image.*

(a)   (b)   (c)
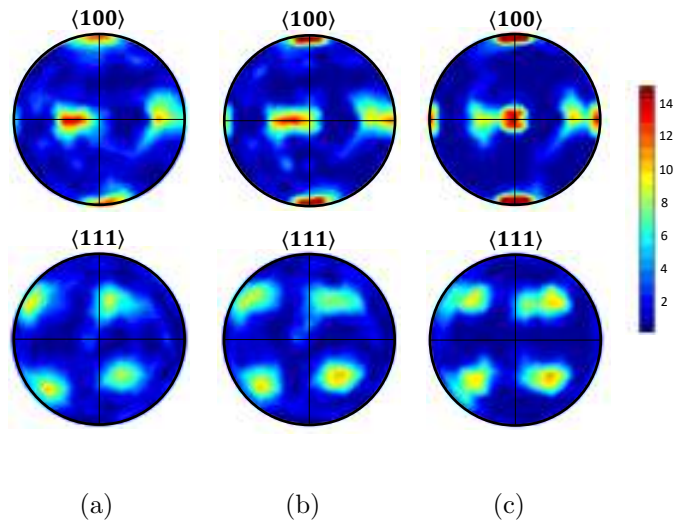
Figure 4.12: *Comparison of $\langle 100 \rangle$ and $\langle 111 \rangle$ pole figures for (a) the original 3D DCT sample against (b) the MRF planar input exemplars and (c) the segmented 3D synthesized image.*

Additionally, the 3D grain statistics of the synthesized models are examined against the experimental image. Here, the external grains along the outer surfaces of the 3D image are eliminated. Edge detection based on six-fold connectivity is then performed on the internal grains. The raw volumetric data (in voxel units) is then calculated over 32 bins using a lognormal fit. As illustrated in Figure 4.13, a close agreement between the original 3D DCT and synthesized images is observed.
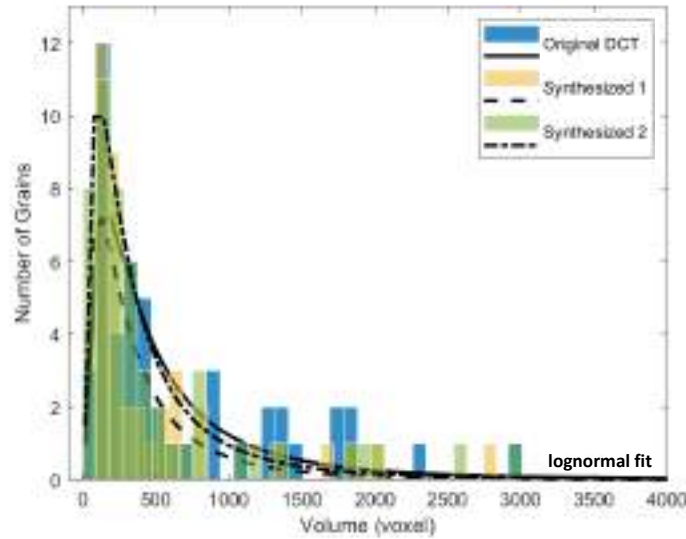
Figure 4.13: *Comparison of the grain size distribution of the 3D microstructures for the original DCT dataset and two segmented MRF images.*

Figure 4.14 demonstrates the effect of using the Cauchy-Crofton weights for the segmentation process. Figure 4.14(a) shows the result without the use of Cauchy-Crofton weights, which results in metrication artifacts with abnormally flat grains. However, use of Cauchy-Crofton formula ($\mathcal{N}_{26}$ in Figure 4.14(b) and $\mathcal{N}_{122}$ in Figure 4.14(c)) systematically improves grain shapes. Accordingly, using a larger stencil provides better results in terms of the curvature of grains.

| (a) | (b) | (c) |
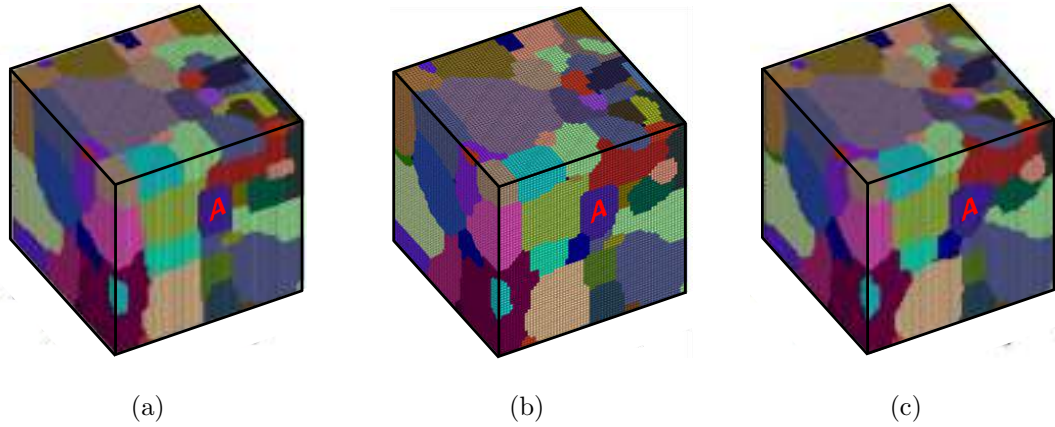
Figure 4.14: *Segmentation of 3D microstructure as a graph labeling problem: (a) reconstruction without the use of Cauchy-Crofton weights results in metrication artifacts with unusual flat grains. 3D microstructure after segmentation procedure using (b) $\mathcal{N}_{26}$ and (c) $\mathcal{N}_{122}$.*

4.3 Conclusions

In this chapter, a physics-based model is developed to simulate multiphase flow for studying microstructure evolution using a pairwise energy form. This formulation is more computationally intensive than the modified Moore-neighbor tracing algorithm, but at the same time, metrication errors are severely suppressed. Additionally, a basic 2D Riemannian metric based on the implementation of the Cauchy-Crofton formulation was verified for modeling 2D microstructural evolution using several test cases with pixelated meshes. It is shown that the methodology captures the necessary physics of microstructure evolution in terms of annihilation and merger of grains. Moreover, the equilibrated solution matches the analytical conditions at the triple-point junctions. The evolution laws for anisotropic length metrics are identified and are used to simulate non-equiaxed microstructures. The ideas can be extended towards the segmentation of 3D microstructures where unlabelled grains in experimental images can be identified by minimizing data cost and by using a regularization term for the surface energy. This procedure can also be used to remove the noisy voxels of images while preserving the overall data microstructure. Future work may include

the inclusion of strain energy, in addition to bulk and interfacial energy, in the formulation to model other material science problems such as growth and coarsening of precipitates within a grain [261]. This work has identified a few areas where further research is required to improve microstructure evolution models. In its present state, the surface energies that can be represented in the pairwise formulation are restricted by corresponding length metrics that can be modeled using Crofton relations. This restriction is a significant hurdle in developing a complete simulation suite for microstructure evolution, where GB energy is much more complicated. This work has also shown that metrication errors can be suppressed using concepts from integral geometry.

CHAPTER V

Image-Based Crystal Plasticity Analysis of Microstructures

As described previously in Chapters II-IV, uniform pixel or voxel-based structured discretizations can be conveniently obtained from microscopy and numerical acquisition techniques [20, 92, 93]. Subsequently, once the underlying structure of a material is realized, modeling mechanical performance for aerospace applications remains an area of interest in the material science community. As a result, here in this chapter, the NOSBPD technique is employed to simulate fine-scale localizations in polycrystalline microstructures undergoing elastoplastic deformation. Microscale data from electron microscopy and DIC have indicated that slip localizations arise early in deformation and act as precursors to mechanical failure and fracture mechanisms [136, 137]. However, classical numerical approaches such as CPFEM are generally unable to predict the emergence and distribution of such localizations. Alternatively, the PD formulation has attracted significant attention for its unique treatment of deformation in the presence of high-strain gradient fields, providing a unique capability for solving problems involving discontinuities. The correspondence-based PD models, however, often suffer from zero-energy mode instabilities, primarily due to the approximations of the non-local deformation gradient tensor. This chapter focuses on a computational scheme for eliminating the zero-energy mode oscillations for both 1D

and higher-dimensional problems using a choice of influence functions that improve the truncation error in a Taylor series expansion of the deformation gradient. The novelty here is a tensor-based derivation of the linear constraint equations, which can be used to systematically identify the particle interaction weight functions for various user-specified horizon radii. The proposed stabilization scheme is shown to be highly effective in suppressing the spurious zero-energy mode oscillations in all numerical examples while enabling efficient simulations of strain localizations across material interfaces.

The chapter is organized as follows. A review of the non-ordinary state-based PD is first outlined in Section 5.1. In Section 5.2, a brief explanation on the origin of zero-energy modes follows. The higher-order approximation theory of deformation gradient is then proposed in Section 5.3. Numerical examples are shown and discussed in Section 5.6 for various multi-dimensional problems. Notably, in Section 5.6.1, the higher-order approximation results for a number of long-range interactions are compared against the analytical solutions and PD methods without any stabilization control [262] for a simple case of 1D cantilever bar. Effects of zero-energy mode oscillations on 2D polycrystalline microstructures involving texture evolution are then introduced in Section 5.6.2. Thereafter, the CPPD numerical results are examined against conventional CPFE techniques in modeling fine length-scale shear bands across polycrystalline aggregates. This follows by Sections 5.6.3-5.6.5 that respectively demonstrate 3D examples of composite and polycrystalline microstructures subjected to Dirichlet boundary conditions. Here, the proposed PD technique is shown to be superior to CPFE models in simulating the sharp small-scale strain localizations across the microstructural interface.

5.1 Non-Ordinary State-Based Peridynamics

In this section, the NOSBPD theory is briefly reviewed. Thereafter, the discretization process along with an overview of the numerical algorithm, is outlined. Next, the zero-energy mode oscillation and its relationship with the material point interactions are discussed. In Section 5.3, a novel solution for suppressing the zero-energy instability noise for 1D, 2D, and 3D problems using higher-order approximations of deformation gradients is introduced. Next, in Section 5.4, a boundary treatment based on constant deformation gradient is introduced that encompasses large horizon interactions.

The non-ordinary state-based PD theory forms the foundation of the present work. This model was first proposed by Silling et al. [170] and consists of a non-local integral reformulation of the classical continuum mechanical theory. Unlike bond-based PD models [162, 263], which are restricted to a specific Poisson's ratio, the state-based PD theory can be generalized to include various classical constitutive material models, enabling the integration with crystal elastoplasticity [21]. Here, consider a material particle in the reference configuration at position $\mathbf{x}$, which can only interact with its neighboring points in a self-centered horizon $\mathcal{H}_{\mathbf{x}}$, within a finite radius δ. Given the displacement field $\mathbf{u}$ of the material particle at $\mathbf{x}$, the deformed location of the corresponding material particle in the current configuration is represented as $\mathbf{y} = \mathbf{x} + \mathbf{u}$. Here, as depicted in Figure 5.1, the reference configuration of the body is denoted as $\mathcal{B}_0$ at time $t = t_0$ and the deformed configuration as $\mathcal{B}_1$ at time t_1.

Let $\mathbf{x}'$ denote the position of a particular material particle belonging to $\mathcal{H}_{\mathbf{x}}$, and $\boldsymbol{\xi} = \mathbf{x}' - \mathbf{x}$ denote a bond between the respective material particle at $\mathbf{x}'$ and the center particle at $\mathbf{x}$. The deformation vector state, indicated as $\underline{\mathbf{Y}}[\mathbf{x}, t]\langle \mathbf{x}' - \mathbf{x}\rangle$, maps the bond $\boldsymbol{\xi}$ in the reference configuration to its deformed counterpart, i.e., $\underline{\mathbf{Y}}[\mathbf{x}, t]\langle \mathbf{x}' - \mathbf{x}\rangle = \mathbf{y}' - \mathbf{y}$. The corresponding deformation gradient tensor $\mathbf{F}(\mathbf{x}, t)$, can be defined in terms of $\underline{\mathbf{Y}}[\mathbf{x}, t]\langle \mathbf{x}' - \mathbf{x}\rangle$, as follows:

$$\mathbf{F}(\mathbf{x}, t) = \left(\int_{\mathcal{H}_{\mathbf{x}}} \omega (\underline{\mathbf{Y}}[\mathbf{x}, t] \langle \mathbf{x}' - \mathbf{x} \rangle \otimes \boldsymbol{\xi}) dV_{\mathbf{x}'} \right) \mathbf{K}^{-1}(\mathbf{x}) \tag{5.1}$$

where ω is a weight function, quantifying the impact of neighboring particles on the center particle at $\mathbf{x}$. Here, the weight function ω, can be selected as a radially-symmetric parameter based on the initial bond length, i.e., $\omega = \omega(|\boldsymbol{\xi}|)$. Also, $\mathbf{K}(\mathbf{x})$ is a symmetric, positive-definite shape tensor, defined as:

$$\mathbf{K}(\mathbf{x}) = \int_{\mathcal{H}_{\mathbf{x}}} \omega (\boldsymbol{\xi} \otimes \boldsymbol{\xi}) dV_{\mathbf{x}'} \tag{5.2}$$

Therefore, the governing equations of state-based PD at time t can be formulated as follows:

$$\rho \ddot{\mathbf{u}}(\mathbf{x}, t) = \mathbf{L}(\mathbf{x}, t) + \mathbf{b}(\mathbf{x}, t)$$
$$\mathbf{L}(\mathbf{x}, t) = \int_{\mathcal{H}_{\mathbf{x}}} (\underline{\mathbf{T}}[\mathbf{x}, t] \langle \mathbf{x}' - \mathbf{x} \rangle - \underline{\mathbf{T}}[\mathbf{x}', t] \langle \mathbf{x} - \mathbf{x}' \rangle) dV_{\mathbf{x}'} \tag{5.3}$$

where $\underline{\mathbf{T}}[\mathbf{x}, t] \langle \mathbf{x}' - \mathbf{x} \rangle$ is a force vector state, operating on the bond $\boldsymbol{\xi}$ for the particle at position $\mathbf{x}$ and time t. Here, $\mathbf{L}(\mathbf{x}, t)$ is the summation of the forces per unit reference volume due to the interactions of the particle at location $\mathbf{x}$ with its neighboring particles inside the self-centered horizon $\mathcal{H}_{\mathbf{x}}$. Furthermore, vector $\mathbf{b}(\mathbf{x}, t)$ denotes the body force density corresponding to the material particle at $\mathbf{x}$ and time t, while ρ refers to the material density.

In correspondence with the classical continuum theories, the force state $\underline{\mathbf{T}}[\mathbf{x}, t] \langle \mathbf{x}' - \mathbf{x} \rangle$ is related to the first Piola-Kirchoff (PK-I) stress tensor, denoted as $\mathbf{P}(\mathbf{x}, t)$, via the
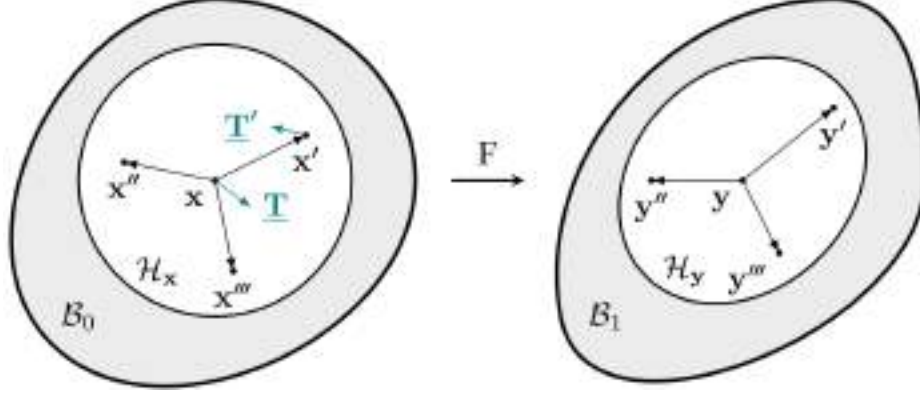
Figure 5.1: *Kinematics of NOSBPD. $\mathcal{B}_0$ denotes the reference configuration of the body, while $\mathcal{B}_1$ is the deformed configuration. The particle at $\mathbf{x}$ is bonded to its neighboring particles, located at $\mathbf{x}'$, $\mathbf{x}''$, and $\mathbf{x}'''$, within a finite region $\mathcal{H}_{\mathbf{x}}$. The body deforms so the particle at $\mathbf{x}$ displaces to $\mathbf{y}$. The mapping can be described by the corresponding deformation gradient $\mathbf{F}(\mathbf{x}, t)$. $\underline{\mathbf{T}} = \underline{\mathbf{T}}[\mathbf{x}, t]\langle \mathbf{x}' - \mathbf{x}\rangle$ and $\underline{\mathbf{T}}' = \underline{\mathbf{T}}[\mathbf{x}', t]\langle \mathbf{x} - \mathbf{x}'\rangle$ are force vector states in the reference configuration for particles locating at $\mathbf{x}$ and $\mathbf{x}'$, respectively. In the non-ordinary state-based PD theory, these two force vectors are not necessarily parallel and can be obtained from the classical stress tensor.*

following equation:

$$\underline{\mathbf{T}}[\mathbf{x}, t]\langle \mathbf{x}' - \mathbf{x}\rangle = \omega \mathbf{P}(\mathbf{x}, t)\mathbf{K}^{-1}(\mathbf{x})\boldsymbol{\xi} \tag{5.4}$$

Hence, $\mathbf{P}(\mathbf{x}, t)$ can be computed from a classical constitutive model using the deformation gradient $\mathbf{F}(\mathbf{x}, t)$. Compared with the governing equations of classical continuum mechanics, no spatial derivative appears in Equation (5.3). This places fewer restrictions on the regularity properties of deformation descriptors. Furthermore, it is worth noting that despite the current PD model being non-ordinary, the balance of angular momentum is ensured due to the relation in Equation (5.4) [21, 170].

In this chapter, an explicit dynamic relaxation method with the quasi-static assumption and a careful time-step selection, as outlined in Appendix B, is adopted. Nonlinear problems involving static solutions can alternatively be solved iteratively as a dynamic problem using artificial damping.

110

5.1.1 Numerical Discretization Scheme and Algorithm

Assume there are N neighboring particles surrounding the central material particle located at $\mathbf{x}$, then Equation (5.3) can be discretized for a specific time frame $t = t_n$ as in the following, while neglecting the body force $\mathbf{b}(\mathbf{x})$:

$$\mathbf{L}(\mathbf{x}) = \sum_{i=1}^{N} \left(\underline{\mathbf{T}}[\mathbf{x}]\langle \mathbf{x}_i' - \mathbf{x}\rangle - \underline{\mathbf{T}}[\mathbf{x}_i']\langle \mathbf{x} - \mathbf{x}_i'\rangle \right) V_{\mathbf{x}_i'} = \mathbf{0} \qquad (5.5)$$

where $\mathbf{x}_i'$ is the location of the ith neighboring particle in $\mathbf{x}$'s horizon, and $V_{\mathbf{x}_i'}$ is its corresponding volume. Next, the deformation gradient $\mathbf{F}(\mathbf{x})$, for the material particle at $\mathbf{x}$ at the specific time frame $t = t_n$, can be discretized as:

$$\mathbf{F}(\mathbf{x}) = \left(\sum_{i=1}^{N} \omega_i (\mathbf{y}_i' - \mathbf{y}) \otimes (\mathbf{x}_i' - \mathbf{x}) V_{\mathbf{x}_i'} \right) \mathbf{K}^{-1}(\mathbf{x}) \qquad (5.6)$$

where $\mathbf{y}'$ and $\mathbf{y}$ represent the images (i.e., the deformed positions) of material particles at $\mathbf{x}'$ and $\mathbf{x}$, respectively, and ω_i denotes the weight function of the ith particle within the horizon of the center particle at $\mathbf{x}$. Similarly, the shape tensor, $\mathbf{K}(\mathbf{x})$, can be computed as:

$$\mathbf{K}(\mathbf{x}) = \sum_{i=1}^{N} \omega_i (\mathbf{x}_i' - \mathbf{x}) \otimes (\mathbf{x}_i' - \mathbf{x}) V_{\mathbf{x}_i'} \qquad (5.7)$$

Given the constitutive model, represented by an operator $\mathcal{F}$, the force states $\underline{\mathbf{T}}[\mathbf{x}]\langle \mathbf{x}_i' - \mathbf{x}\rangle$ for the particle at $\mathbf{x}$ and $\underline{\mathbf{T}}[\mathbf{x}_i']\langle \mathbf{x} - \mathbf{x}_i'\rangle$ for the particle at $\mathbf{x}'$, as found in Equation (5.5), can be obtained from:

$$\underline{\mathbf{T}}[\mathbf{x}]\langle\mathbf{x}_i' - \mathbf{x}\rangle = \omega_i \mathcal{F}\big(\mathbf{F}(\mathbf{x})\big)\mathbf{K}^{-1}(\mathbf{x})(\mathbf{x}_i' - \mathbf{x})$$

$$\underline{\mathbf{T}}[\mathbf{x}_i']\langle\mathbf{x} - \mathbf{x}_i'\rangle = \omega_i \mathcal{F}\big(\mathbf{F}(\mathbf{x}_i')\big)\mathbf{K}^{-1}(\mathbf{x}_i')(\mathbf{x} - \mathbf{x}_i') \tag{5.8}$$

Yet, in order to acquire $\mathbf{F}(\mathbf{x}_i')$ and $\mathbf{K}(\mathbf{x}_i')$ for the particle at $\mathbf{x}_i'$, information about the ith particle's horizon must be determined. Figure 5.2 is an illustration of interactions of one particle with its nearest neighbors in a 2D material domain.
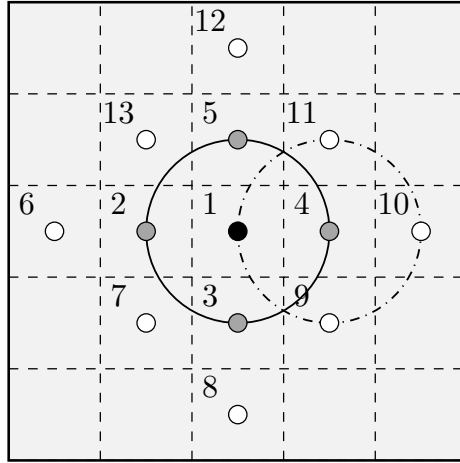
Figure 5.2: *Particle interactions with closest neighbors in a2DPD model. Particles $i = 2, 3, 4, 5$ are the nearest neighbors of the particle 1 (denoted as the center particle at $\mathbf{x}$); while particles $i = 1, 9, 10, 11$ are the nearest neighbors of the particle 4 (denoted as the particle at $\mathbf{x}_i'$). In this case, all 13 particles shown above should be included in order to obtain $\mathbf{L}(\mathbf{x})$ at particle $\mathbf{x}$ in Equation (5.5).*

With all force vector states obtained, the adaptive dynamic relaxation scheme (ADRS), as elaborated in Appendix B, is applied to solve the equation $\mathbf{L}(\mathbf{x}) = \mathbf{0}$. For a 2D problem, the global equation of motion can be organized as a vector system with a size of $2 \times N_{\text{total}}$, where N_{total} is the total number of particles in the simulation. Since $\mathbf{L}(\mathbf{x})$ is completely dependent on the current field, the system can be explicitly started with an initial guess of displacement, velocity, and acceleration fields. During dynamic iterations in one loading step, two absolute errors, denoted as ε_1 and ε_2, are

calculated at each iteration with the definitions as:

$$\varepsilon_1 = \frac{\|\mathbf{L}(\mathbf{x})\|_2}{N_{\text{total}}} \text{ and } \varepsilon_2 = \frac{\|\delta\mathbf{u}\|_2}{N_{\text{total}}} \tag{5.9}$$

where $\|.\|_2$ denotes a Euclidean norm. The first error ε_1, describes the degree to which $\mathbf{L}(\mathbf{x})$ approaches zero, while the second error ε_2, denotes the magnitude of displacement increments between two adjacent iteration steps. In order to normalize the error from initial guesses, two corresponding relative errors e_1 and e_2 are then monitored, as computed below:

$$e_1 = \frac{\varepsilon_1}{\varepsilon_1^0} \text{ and } e_2 = \frac{\varepsilon_2}{\varepsilon_2^0} \tag{5.10}$$

where ε_1^0 and ε_2^0 are the initial absolute errors in each loading step. Iterations stop only when both criteria are satisfied, i.e., $e_{1,2} < e_l$ with $e_l = 10^{-6}$. All quantities are then updated into the next loading step. To improve the computational performance, parallel libraries such as OpenMP and OpenMPI, are adopted in the code. Given that kinematic properties, such as the displacement $\mathbf{u}$ and deformation gradient $\mathbf{F}$, are known beforehand due to the use of an explicit method, the constitutive model can be applied to different particles in parallel. In other words, the computation involved in acquiring $\mathbf{P}(\mathbf{x}) = \mathcal{F}(\mathbf{F}(\mathbf{x}))$ and $\mathbf{P}(\mathbf{x}') = \mathcal{F}(\mathbf{F}(\mathbf{x}'))$ corresponding to the material particles at $\mathbf{x}$ and $\mathbf{x}'$, respectively, are completely independent. The computation domain is therefore partitioned into several groups in order to parallelize the calculation of the stress tensors. Finally, all information is gathered in the assembly of the vector system $\mathbf{L}(\mathbf{x})$. The flowchart in Figure 5.3 summarizes the important numerical steps within the non-local state-based PD scheme described above.

In the presented PD framework, a crystal elastoplasticity model with deformation
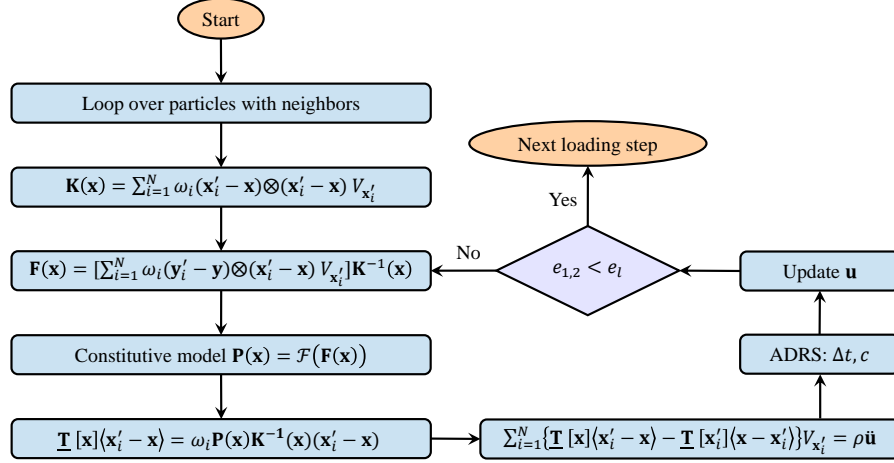
Figure 5.3: *Flowchart for the explicit NOSBPD scheme using ADRS.*

twinning, as elaborated in Section 5.5, is incorporated, where a generalized Hooke's law characterizes the elastic behavior of the microstructure and is accompanied by a rate-independent CP formulation to model the plastic constitutive behavior [158]. The rate-independent CP constitutive model implementation is elaborated in detail in [172, 264].

5.2 Zero-Energy Modes

The PD technique used in this chapter incorporates a correspondence material model in determining the bond forces from the PK-I stress tensor. The inherent stability issue of zero-energy modes is essentially the result of non-unique mapping between deformation states and force states via the PD deformation gradient tensor [173, 181, 185, 191]. To better understand the origin of zero-energy numerical oscillations, a simple example is discussed next. Consider a 2D uniform lattice as illustrated in Figure 5.4, where $\mathbf{x}$ and $\mathbf{x}'$ indicate the positions of the central material particle and one of its neighbors, respectively, at the original configuration. Let $\mathbf{F}_{\mathrm{old}}(\mathbf{x}, t)$ denote the initial deformation gradient, while $\mathbf{F}_{\mathrm{new}}(\mathbf{x} + \mathbf{u}_{\mathrm{d}}, t)$ represents the deformation gradient after a small displacement disturbance $\mathbf{u}_{\mathrm{d}}$, applied to the center particle at

x. The new deformation gradient $\mathbf{F}_{new}(\mathbf{x} + \mathbf{u}_d, t)$ can be then calculated based on Equation (5.1) as:

$$
\begin{aligned}
\mathbf{F}_{new}(\mathbf{x} + \mathbf{u}_d, t) &= \left(\int_{\mathcal{H}_\mathbf{x}} \omega(\underline{\mathbf{Y}}_{new}[\mathbf{x} + \mathbf{u}_d, t]\langle \mathbf{x}' - \mathbf{x} - \mathbf{u}_d \rangle \otimes \boldsymbol{\xi}) dV_{\mathbf{x}'} \right) \mathbf{K}^{-1}(\mathbf{x}) \\
&= \left(\int_{\mathcal{H}_\mathbf{x}} \omega \left[(\underline{\mathbf{Y}}_{old}[\mathbf{x}, t]\langle \mathbf{x}' - \mathbf{x} \rangle - \mathbf{u}_d) \otimes \boldsymbol{\xi} \right] dV_{\mathbf{x}'} \right) \mathbf{K}^{-1}(\mathbf{x}) \\
&= \mathbf{F}_{old}(\mathbf{x}, t) - \mathbf{u}_d \otimes \left(\int_{\mathcal{H}_\mathbf{x}} \omega \boldsymbol{\xi} dV_{\mathbf{x}'} \right) \mathbf{K}^{-1}(\mathbf{x}) \qquad (5.11)
\end{aligned}
$$

With the assumption of a regular lattice discretization and a spherically-symmetric influence function ω, the integration term on the right-hand side becomes zero. This is the case of admissible displacement fields producing the same deformation gradient and potential energy, which is appropriately called the zero-energy mode. This is a common stability issue when using correspondence material methods with mesh-free discretizations [265, 266].
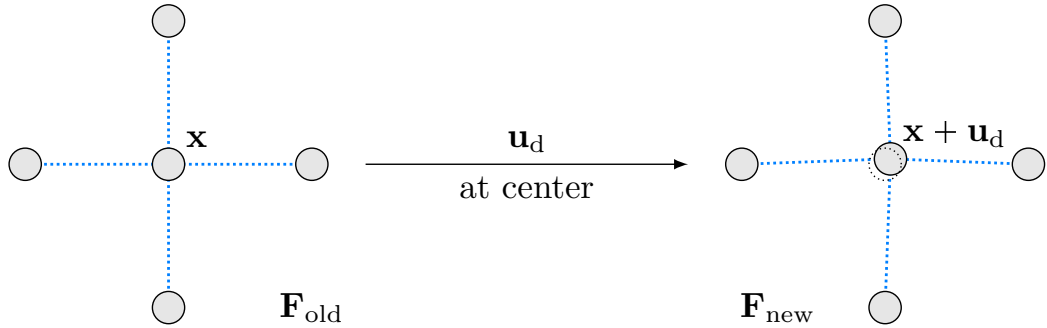
Figure 5.4: *An illustration of zero-energy modes in a 2D regular lattice. A small disturbance applied to the center particle has no impact on the calculation of the deformation gradient.*

One of the previous ideas to address the zero-energy mode instability issue includes the introduction of the artificial force state, $\underline{\mathbf{T}}_a[\mathbf{x}]\langle \mathbf{x}' - \mathbf{x} \rangle$, for the particle at location $\mathbf{x}$ and bond $\mathbf{x}' - \mathbf{x}$, as follows:

$$\underline{\mathbf{T}}[\mathbf{x}, t]\langle \mathbf{x}' - \mathbf{x}\rangle = \omega \mathbf{P}(\mathbf{x}, t)\mathbf{K}^{-1}(\mathbf{x})\boldsymbol{\xi} + \underline{\mathbf{T}}_{\mathrm{a}}[\mathbf{x}, t]\langle \mathbf{x}' - \mathbf{x}\rangle \qquad (5.12)$$

The artificial force term can be calculated using interconnected springs or average displacement states [179, 185]. The linear springs introduced between particles can be represented as:

$$\underline{\mathbf{T}}_{\mathrm{a}}[\mathbf{x}, t]\langle \mathbf{x}' - \mathbf{x}\rangle = C_1\omega[\mathbf{u}(\mathbf{x}') - \mathbf{u}(\mathbf{x})] \qquad (5.13)$$

where C_1 is a spring constant. Alternatively, the following method computes an added force based on the average of displacement states over a given horizon size, as follows:

$$\underline{\mathbf{T}}_{\mathrm{a}}[\mathbf{x}, t]\langle \mathbf{x}' - \mathbf{x}\rangle = C_2 \int_{\mathcal{H}_{\mathbf{x}}} \omega[\mathbf{u}(\mathbf{x}') - \mathbf{u}(\mathbf{x})]dV_{\mathbf{x}'} \qquad (5.14)$$

Although these supplementary forces have a suppression effect on the zero-energy modes, their efficacy highly depends on the mesh size and the problem itself. Additionally, to determine the optimum values of the artificial coefficients (i.e., C_1 and C_2) preliminary calculations need to be performed beforehand [173, 179]. Yet, none of these methods completely suppresses zero-energy modes. Alternatively, in Section 5.3, a thorough discussion on the accuracy and stability of a novel explicit numerical scheme, termed higher-order approximation theory, towards the elimination of the zero-energy mode oscillations is described.

5.3 Higher-Order Approximation Theory

The higher-order approximation method was initially proposed in Yaghoobi et al. [173] for 2D lattice structures and later enhanced in Javaheri et al. [221]. The basic idea

is to adjust the influence weight functions based on a Taylor series expansion to better approximate the deformation gradient. This approach is shown to be highly effective in suppressing spurious zero-energy mode oscillations. In addition, higher-order approximations are easily implementable within the state-based PD framework, where larger horizon sizes can be used.

In the continuum mechanics, the relation between the deformed bond $\delta\mathbf{y} = \mathbf{y}' - \mathbf{y}$, and the reference bond $\delta\mathbf{x} = \mathbf{x}' - \mathbf{x}$, as illustrated in Figure 5.1, can be expressed via the Taylor series expansion, as follows:

$$\mathbf{y}' - \mathbf{y} = \frac{\partial\mathbf{y}}{\partial\mathbf{x}}(\mathbf{x}' - \mathbf{x}) + O[(\mathbf{x}' - \mathbf{x})^2] \tag{5.15}$$

where the notation O denotes the order of the leading error term. Here, $\frac{\partial\mathbf{y}}{\partial\mathbf{x}}$ is equivalent to the deformation gradient tensor. In order to incorporate the state-based PD deformation gradient, a tensor product on the reference bond $\mathbf{x}' - \mathbf{x}$ is first performed on both sides of Equation (5.15), and the result is then integrated over the initial horizon $\mathcal{H}_\mathbf{x}$, as follows:

$$\int_{\mathcal{H}_\mathbf{x}} \omega[(\mathbf{y}' - \mathbf{y}) \otimes (\mathbf{x}' - \mathbf{x})]dV_{\mathbf{x}'} = \int_{\mathcal{H}_\mathbf{x}} \frac{\partial\mathbf{y}}{\partial\mathbf{x}}\omega[(\mathbf{x}' - \mathbf{x}) \otimes (\mathbf{x}' - \mathbf{x})]dV_{\mathbf{x}'} + O[(\mathbf{x}' - \mathbf{x})^3] \tag{5.16}$$

Therefore, the deformation gradient tensor at time t can be approximated by:

$$\mathbf{F}(\mathbf{x}, t) = \frac{\partial\mathbf{y}}{\partial\mathbf{x}} = \left(\int_{\mathcal{H}_\mathbf{x}} \omega[(\mathbf{y}' - \mathbf{y}) \otimes (\mathbf{x}' - \mathbf{x})]dV_{\mathbf{x}'}\right)\mathbf{K}^{-1}(\mathbf{x}) + O(\mathbf{x}' - \mathbf{x}) \tag{5.17}$$

Once the error term, i.e., $O(\mathbf{x}' - \mathbf{x})$, is eliminated, Equation (5.17) becomes the same

117

as Equation (5.1), where $\mathbf{K}(\mathbf{x})$ is defined as the shape tensor in the state-based PD model. Note that the leading error term in Equation (5.17) is of the first order of the distance between material particles located at $\mathbf{x}'$ and $\mathbf{x}$. In order to achieve a more accurate deformation gradient, appropriate influence function values ω, for the required horizon can be chosen to artificially increase the leading error order. This is explained for multi-dimensional domains in Section 5.3.1. The specific contribution area of this chapter is developing a set of higher-order tensor equations to efficiently identify the constraint formulations for the influence weight functions when using the higher-order approximation method.

5.3.1   Multi-Dimensional Discrete Formulation

Hereon, the multi-dimensional Taylor series expansion is applied for deriving weight function values ω across 1D, 2D, and 3D material domains with a constant particle spacing h for $\delta \leq 3h$, where δ denotes the interacting horizon radius. This chapter incorporates a uniform particle discretization, i.e., equally-spaced particles along a line in 1D, quadrilateral discretizations in 2D, or cubic patterns in 3D having a constant particle spacing h with a fixed particle volume ΔV. Accordingly, the influence function values ω are always assumed to be spherically-symmetric, i.e., $\omega = \omega(|\boldsymbol{\xi}|)$. For the sake of simplicity, the Einstein tensor notation is adopted in the following discussion. The shape tensor $\mathbf{K}(\mathbf{x})$ in Equation (5.2), and the deformation gradient tensor $\mathbf{F}(\mathbf{x}, t)$ in Equation (5.1) can alternatively be expressed in Einstein notation, as follows:

$$K_{ij} = \int_{\mathcal{H}_\mathbf{x}} \omega \delta x_i \delta x_j dV_{\mathbf{x'}} \tag{5.18}$$

$$F_{pq} = \left(\int_{\mathcal{H}_\mathbf{x}} \omega \delta y_p \delta x_j dV_{\mathbf{x'}} \right) K_{jq}^{-1} \tag{5.19}$$

Due to the symmetric nature of the particle discretizations, the shape tensor in Equation (5.18) can be reformulated as:

$$K_{ij} = \sum_{a=1}^{N} \omega_a (\delta x_i \delta x_j)_a \Delta V = \Omega(\omega_1, \omega_2, \omega_3, ...)h^2 \Delta V \delta_{ij} \tag{5.20}$$

where N is the total number of neighboring material particles within the horizon $\mathcal{H}_\mathbf{x}$, δ_{ij} is the Kronecker delta function, and Ω is a function of all independent ω_1, ω_2, ..., ω_N in the horizon. For instance, consider a 2D quadrilateral particle discretization as depicted in Figure 5.5, with a horizon size $\delta = 2h$. While there are a total of 12 neighboring material particles within the given horizon radius $\delta = 2h$, due to the radially-symmetric nature of the discretization pattern, only three independent weight function values are labeled, i.e., $\omega_1 = \omega(h)$, $\omega_2 = \omega(\sqrt{2}h)$, and $\omega_3 = \omega(2h)$.

Consequently, by substituting Equation (5.20) into Equation (5.19), the deformation gradient can be reformulated as:

$$F_{pq} = \frac{\delta_{jq}}{h^2 \Omega \Delta V} \int_{\mathcal{H}_\mathbf{x}} \omega \delta y_p \delta x_j dV_{\mathbf{x'}} = \frac{1}{h^2 \Omega} \sum_{a=1}^{N} \omega_a (\delta y_p \delta x_q)_a \tag{5.21}$$

Accordingly, a multi-dimensional Taylor series expansion of the deformed bond $\delta\mathbf{y}$ on the reference bond $\delta\mathbf{x}$ is required. The first three leading terms are shown here

119
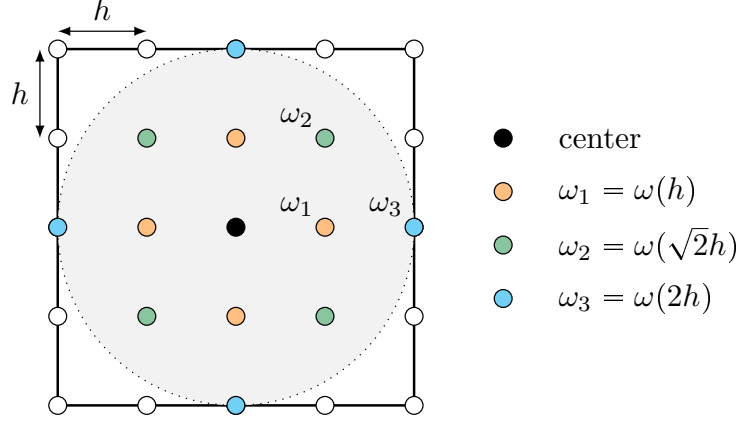
Figure 5.5: *Independent weight function values for a 2D quadrilateral particle pattern. Here, ω is a radially-symmetric weight function on neighboring material particles. The horizon radius is $\delta = 2h$, with h denoting the distance between the nearest particles.*

without showing the derivations:

$$\delta y_p = F_{pi}\delta x_i + \frac{1}{2!}G_{pij}\delta x_i \delta x_j + \frac{1}{3!}H_{pijk}\delta x_i \delta x_j \delta x_k + O(h^4) \qquad (5.22)$$

where $F_{pi} = \frac{\partial \delta y_p}{\partial \delta x_i}$ is the deformation gradient; $G_{pij} = \frac{\partial^2 \delta y_p}{\partial \delta x_i \delta x_j}$ and $H_{pijk} = \frac{\partial^3 \delta y_p}{\partial \delta x_i \delta x_j \delta x_k}$ are the second-order and third-order derivatives, respectively.

Finally, by substituting Equation (5.22) into Equation (5.21), the deformation gradient then turns into:

$$F_{pq} = F_{pq} + \frac{1}{2!h^2\Omega}G_{pij}\sum_{a=1}^{N}\omega_a(\delta x_i \delta x_j \delta x_q)_a + \frac{1}{3!h^2\Omega}H_{pijk}\sum_{a=1}^{N}\omega_a(\delta x_i \delta x_j \delta x_k \delta x_q)_a + O(h^3)$$

$$(5.23)$$

Accordingly, it is possible to achieve higher-order approximations by selecting explicit weight functions in Equation (5.23). It is worth noting that in a spherically-symmetric

and intact discretization, for every bond $(\delta\mathbf{x})_m$, there is another bond $(\delta\mathbf{x})_n$ symmetric about the origin such that $(\delta\mathbf{x})_m = -(\delta\mathbf{x})_n$. Hence, when there are odd δx-products, the summation terms in Equation (5.23) become:

$$\sum_{a=1}^{N} \omega_a(\delta x_i \delta x_j \ldots \delta x_m)_a = 0 \tag{5.24}$$

As odd δx-product summations vanish, symmetric particle patterns with intact horizons always lead to an accuracy order equal or greater than $O(h^2)$. One additional equation, as formulated below, needs to be satisfied to obtain a higher truncation error in the order of $O(h^4)$:

$$A_{ijkl} = \sum_{a=1}^{N} \omega_a(\delta x_i \delta x_j \delta x_k \delta x_l)_a = 0 \tag{5.25}$$

Furthermore, the satisfaction of the following two equations leads to higher accuracy, in the order of $O(h^6)$:

$$\begin{cases} A_{ijkl} = \sum_{a=1}^{N} \omega_a(\delta x_i \delta x_j \delta x_k \delta x_l)_a = 0 \\ B_{ijklrs} = \sum_{a=1}^{N} \omega_a(\delta x_i \delta x_j \delta x_k \delta x_l \delta x_r \delta x_s)_a = 0 \end{cases} \tag{5.26}$$

Criteria outlined in Equations (5.25) and (5.26) hold true regardless of the material dimensions, i.e., 1D line, 2D quadrilateral, or 3D cubic patterns. The final selection of weight function values should satisfy the constraint inequality $\Omega(\omega_1, \omega_2, \omega_3, ...) \neq 0$ to ensure the shape tensor $\mathbf{K}(\mathbf{x})$ obtained in Equation (5.20) is invertible. It is worth noting that larger horizon sizes with more independent weight function values often lead to increased orders of truncation error.

The weight function values for a 1D particle-discretized bar with a constant spacing h, and horizon sizes up to $\delta = 4h$ are tabulated in Table 5.1. For the sake of simplicity and unity, the weight function value corresponding to the particle closest to the center particle is set to be 1, i.e., $\omega_1 = 1$. Additionally, the order of leading truncation error increases when the horizon size δ grows, providing a more accurate deformation gradient. For a 1D bar with a horizon $\delta = 2h$ as depicted in Figure 5.6, there are 5 material particles at x_{i+j} for $j = 0, \pm 1, \pm 2$ with only two independent weight functions ω_1 and ω_2, pertaining to particles at $x_{i\pm 1}$ and $x_{i\pm 2}$, respectively. Hence, setting $\omega_1 = 1$ and $\omega_2 = -1/16$ produces a fourth-order leading error of the form $O(h^4)$ in the Taylor series expansion of the deformation gradient in Equation (5.23) when $\delta = 2h$.
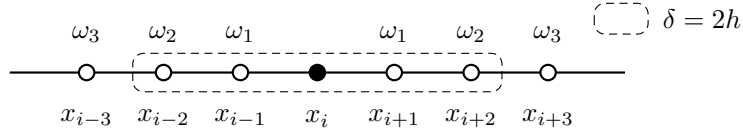
Figure 5.6: *Example of a 1D particle-discretized bar with a constant spacing h. Here, ω is a symmetric weight function. Dashed box with $\delta = 2h$ illustrates the horizon of the center particle x_i, including only the nearest four particles.*

Table 5.1: *Higher-order approximation weight functions for 1D particle discretization with a constant spacing h.*

Horizon Size	Weight Function Values				Leading Error
	ω_1	ω_2	ω_3	ω_4	
$\delta = h$	1	0	0	0	$O(h^2)$
$\delta = 2h$	1	-1/16	0	0	$O(h^4)$
$\delta = 3h$	1	-1/10	1/135	0	$O(h^6)$
$\delta = 4h$	1	-1/8	1/63	-1/896	$O(h^8)$

Next is a brief discussion on the number of non-trivial components in the fourth-order tensor A_{ijkl} for a 2D quadrilateral discretization pattern. First of all, it is worth noting the subscript indices can be swapped, as follows:

$$A_{ijkl} = A_{jikl} = A_{ijlk} \tag{5.27}$$

Consequently, in the case of 2D quadrilateral particle pattern, where subscript indices can only take on values 1 and 2, only six components of tensor A_{ijkl} are independent. These independent elements are A_{1111}, A_{2111}, A_{2211}, A_{2221}, and A_{2222}.

Secondly, due to the axis symmetry of the horizon and particle discretization, the coordinate index 1 and 2 can be swapped, yielding to the following two constraints:

$$A_{1111} = A_{2222} \text{ and } A_{2111} = A_{1112} \tag{5.28}$$

Thirdly, assume that there is a bond with rectangular coordinates (x, y) and a weight function ω_1. Owing to the symmetry of coordinate axes, three other bonds with respective coordinates $(-x, y)$, $(-x, -y)$, and $(x, -y)$ are expected to be in the same horizon as well. Hence, based on the definition in Equation (5.25), the A_{2221} entry becomes:

$$A_{2221} = \omega_1 y^2 (xy - xy + xy - xy) = 0 \tag{5.29}$$

Eventually, only two components of the fourth-order tensor A_{ijkl} are non-zero. These components are A_{1111} and A_{2211}.

Consistent with 1D discretizations, the weight function value corresponding to the particle closest to the center particle is set to be 1, i.e., $\omega_1 = 1$. In order to achieve $O(h^4)$, two more independent weight function values (i.e., ω_2 and ω_3) need to be calculated. Consequently, the horizon with radius $\delta = 2h$ in Figure 5.7 is the smallest

horizon size that can achieve a truncation error in the order of $O(h^4)$ in the 2D quadrilateral pattern. In terms of horizons with excess independent weight functions, but not enough to achieve higher-order truncation errors, the weight function values are generally not unique. These horizon selections could possibly bring noise or numerical oscillations to the ultimate solutions. As a result, the numerical simulations in Section 5.6 primarily focus on horizon sizes with unique weight function values, as tabulated in Tables 5.2-5.3. Typically, the magnitude of weight function values decrease from the closest particles to distant particles, and the value on the farthest particle should be non-zero.

For 2D quadrilateral patterns, horizon sizes up to $\delta = 3h$ are studied. Figure 5.7 illustrates all possible spatial distributions of neighboring particles for different horizon sizes. Here, only a quarter of the interacting circular space is depicted due to the symmetric nature of material particle discretization. The unique weight function values for these horizon sizes are obtained using the following process. The constraint equations for the weight function values to achieve the desired leading error, such as Equations (5.25) and (5.26), are identified. These constraints typically lead to a multiple non-unique set of weight functions for a given horizon size δ. As such, additional equations from the next set of higher-order constraint equations that do not contain the ω_1 term are added to the existing set of constraint equations. The solution to such a constraint set leads to a unique set of weight function values for the specific material interaction. Table 5.2 shows these unique weight function values to achieve the corresponding higher-order accuracy for the 2D quadrilateral discretization. The constraint solutions that have either resulted in a zero influence function value at the material particle farthest from the center particle or led to a non-invertible shape tensor are excluded from Table 5.2.

Similarly, for 3D cubic patterns, the horizon sizes up to $\delta \leq 3h$ are investigated,
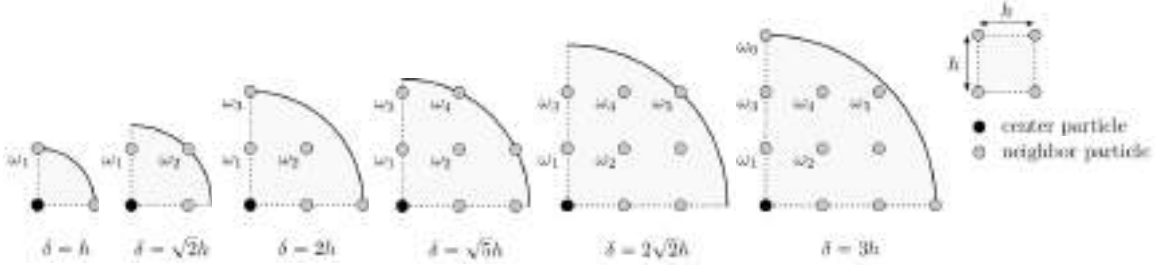
Figure 5.7: *All possible 2D horizon shapes with a quadrilateral particle discretization up to $\delta = 3h$. Since the weight function ω is radially-symmetric, only a quarter of interacting circular regions are depicted for each horizon size δ.*

Table 5.2: *Higher-order approximation weight functions for a 2D quadrilateral discretization pattern with a constant spacing h. Here, horizon sizes in Figure 5.7 that either encompass a zero influence function value at the farthest material particle within the given horizon radius or lead to a non-invertible shape tensor are excluded.*

Horizon Size	Weight Function Values						Leading Error
	ω_1	ω_2	ω_3	ω_4	ω_5	ω_6	
$\delta = h$	1	0	0	0	0	0	$O(h^2)$
$\delta = 2h$	1	0	-1/16	0	0	0	$O(h^4)$
$\delta = 3h$	1	0	-1/10	0	0	1/135	$O(h^6)$

where h represents the spacing between nearest particles. Figure 5.8 illustrates all possible distributions of neighboring material particles for different horizon sizes δ. Here, similar to the 2D quadrilateral distribution, only a small portion of the interacting sphere is illustrated due to the symmetric nature of ω. Subsequently, a similar procedure as for 2D quadrilateral discretization is employed to derive the most optimal unique weight function values. Weight function values that either result in a zero value for the material particle farthest within the horizon shape or lead to a non-invertible shape tensor are disregarded in numerical simulations. Table 5.3 shows the unique weight function values to achieve corresponding higher accuracy for 3D cubic patterns.
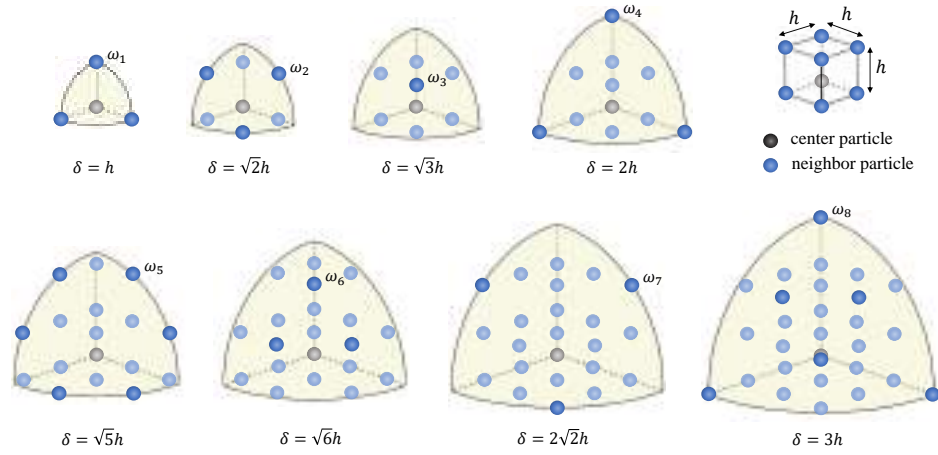
Figure 5.8: *All possible 3D horizon shapes with a cubic particle discretization up to $\delta = 3h$. Since the weight function ω is spherically-symmetric, only one-eighth of the interacting spherical regions are depicted for each horizon size δ.*

Table 5.3: *Higher-order approximation weight functions for a 3D cubic discretization pattern with a constant spacing h. Here, horizon sizes in Figure 5.8 that either encompass a zero influence function value at the farthest material particle within the given horizon radius or lead to a non-invertible shape tensor are excluded.*

Horizon Size	Weight Function Values								Leading Error
	ω_1	ω_2	ω_3	ω_4	ω_5	ω_6	ω_7	ω_8	
$\delta = h$	1	0	0	0	0	0	0	0	$O(h^2)$
$\delta = 2h$	1	0	0	-1/16	0	0	0	0	$O(h^4)$
$\delta = 3h$	1	-80/267	16/89	-25/178	14/267	-8/267	-2/267	1/267	$O(h^6)$

5.4 Boundary Treatment

Conventional constraint conditions, such as Dirichlet and Neumann boundary conditions, are supposed to be imposed in different forms, as the PD governing equations are applied in the non-local formulation. In the case of simulations with no boundary treatment, defect horizons can still approximate the deformation gradient across the boundary layer. However, as the horizon size δ increases, irregular defects ultimately lead to disordered and unstable solutions around the particles located at the margins. Since higher-order approximations are derived using the internal particles with a fully symmetric horizon, defect horizons along the external boundary are expected to give rise to numerical errors when approximating the deformation gradient. One possible solution, as suggested by Macek and Silling [267], is to apply an inward fictitious material layer along the boundary layer. As illustrated in Figure 5.9(a), the thickness or depth of the fictitious boundary layer should be equal to the horizon size δ, to ascertain that prescribed constraints are sufficiently enforced on the real material region. The same discretization spacing should be applied in both the fictitious boundary layer and the real material domain. Shadow particles are therefore introduced in the fictitious layer, as shown in Figure 5.9(b).

(a) Inward fictitious layer   (b) Shadow particles
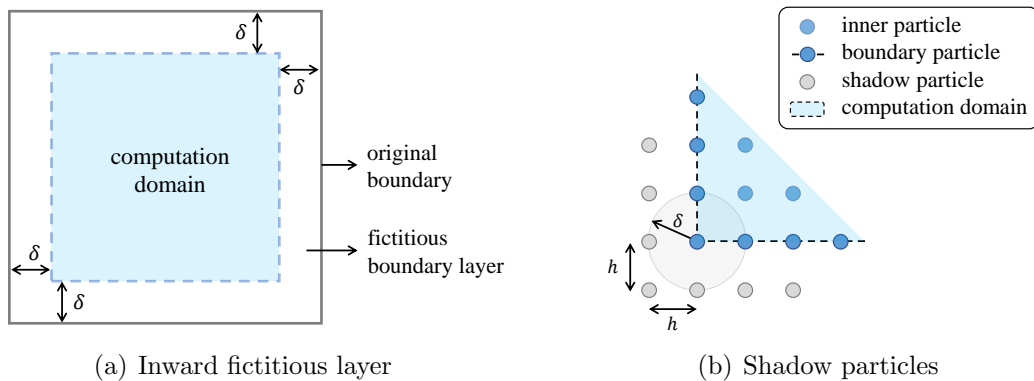
Figure 5.9: *Boundary treatment on a 2D polycrystalline domain. (a) The fictitious boundary layer is inward, possessing a thickness equal to the prescribed horizon radius δ. (b) A horizon of $\delta = h$ is illustrated in this plot, where h is the particle spacing.*

Considering no information is provided outside the original boundary, Madenci et al. [164] suggested that the prescribed displacement vector should be the same as that of the closest material particle at the boundary. This operation results in zero strain and stress across the fictitious boundary layer. An alternative option is to apply a constant deformation gradient across the fictitious boundary layer. In this chapter, displacements on shadow particles are prescribed based on a constant deformation gradient. Consequently, stress at shadow particles can be calculated by the correspondence constitutive model. This special boundary treatment has been particularly effective when larger-horizon interactions are applied, encompassing simulations beyond the nearest-neighbor PD family [185]. With such a boundary treatment procedure, all information (e.g., displacement and stress) on shadow particles are presumably known, in contrast with boundary particles where only the displacement field is given [164].

5.5   Crystal Elastoplasticity Theory

Generalized Hooke's law characterizes the elastic behavior of the polycrystal, accompanied by a rate-independent CP formulation to model the plastic constitutive behavior [158]. The deformation gradient, $\mathbf{F}$, forms the primary kinematic descriptor of deformation and assumes a multiplicative decomposition into its constituent elastic, $\mathbf{F}^{\mathrm{e}}$, and plastic, $\mathbf{F}^{\mathrm{p}}$, parts which can be properly expressed as $\mathbf{F} = \mathbf{F}^{\mathrm{e}}\mathbf{F}^{\mathrm{p}}$. Here, dislocation slip on specific slip systems is assumed to be the primary mechanism by which plastic deformation is accommodated. This occurs on a finite number of slip systems which can be completely identified by crystallographic plane normals and directions. A simple schematic of different configurations with the slip systems under deformation is shown in Figure 5.10.

The kinematics of plasticity is encoded in the plastic part of the velocity gradient which is expressed as a linear combination of slip rates on individual slip systems as

128
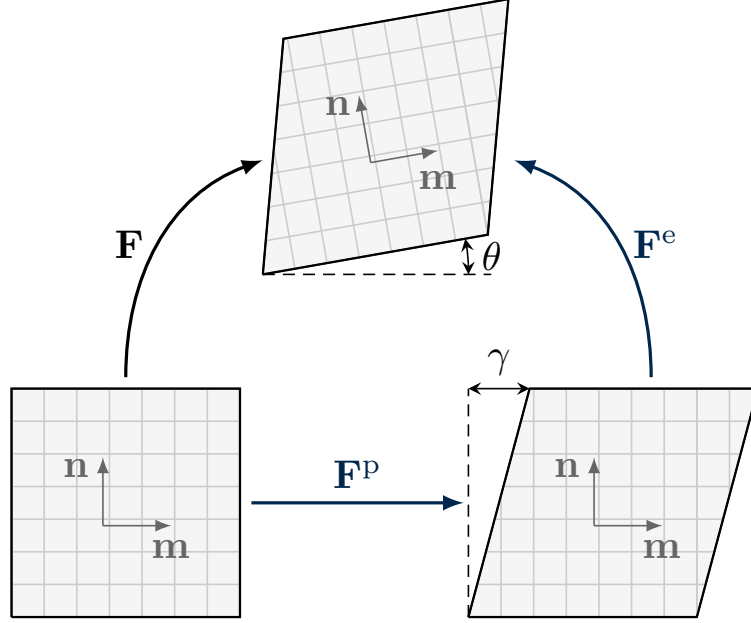
Figure 5.10: *Schematic of slip systems under deformation gradient* $\mathbf{F} = \mathbf{F}^{\mathrm{e}}\mathbf{F}^{\mathrm{p}}$. $\mathbf{m}$ *and* $\mathbf{n}$ *are the slip direction and normal vector, respectively.* γ *is the shear strain due to plastic deformation gradient* $\mathbf{F}^{\mathrm{p}}$ *while* θ *is the angle of rotation under elastic deformation gradient* $\mathbf{F}^{\mathrm{e}}$.

follows:

$$\mathbf{L}^{\mathrm{p}} = \dot{\mathbf{F}}^{\mathrm{p}}\mathbf{F}^{\mathrm{p}-1} = \sum_{\alpha} \dot{\gamma}^{\alpha}\mathbf{S}_0^{\alpha}\mathrm{sign}(\tau^{\alpha}) \tag{5.30}$$

where $\dot{\gamma}^{\alpha}$ is the plastic slip rate, τ^{α} refers to the resolved shear stress, and $\mathbf{S}_0^{\alpha} = \mathbf{m}_0^{\alpha} \otimes \mathbf{n}_0^{\alpha}$ denotes the Schmid tensor, all corresponding to the αth slip system. Here, $\mathrm{sign}(\cdot)$ denotes the signum function, which returns 1 when its argument is positive and 0 otherwise. The elastic constitutive law relates the second Piola-Kirchoff stress (henceforth referred to as the intermediate stress) in the intermediate configuration to the Green-Lagrange elastic strain, which is its elastic power conjugate deformation measure. The intermediate stress is related to the Cauchy stress, $\boldsymbol{\sigma}$, by the relation: $\bar{\mathbf{T}} = \det \mathbf{F}^{\mathrm{e}}\mathbf{F}^{\mathrm{e}-1}\boldsymbol{\sigma}\mathbf{F}^{\mathrm{e}-\mathrm{T}}$. This stress measure is used to compute the resolved shear stress on the αth slip system defined by $\tau^{\alpha} = \bar{\mathbf{T}} \cdot \mathbf{S}_0^{\alpha}$. The elastic constitutive law

takes the form $\bar{\mathbf{T}} = \mathcal{L}^e \cdot \bar{\mathbf{E}}^e$, where $\mathcal{L}^e$ is the fourth-order anisotropic elastic stiffness tensor, and $\bar{\mathbf{E}}^e$ is the Green-Lagrange elastic strain defined as $\bar{\mathbf{E}}^e = \frac{1}{2}(\mathbf{F}^{eT}\mathbf{F}^e - \mathbf{I})$. To accommodate the phenomenon of strain hardening an evolution equation for the slip system resistance is prescribed as follows [158]:

$$\dot{s}^\alpha(t) = \sum_\beta h^{\alpha\beta}(t)\dot{\gamma}^\beta(t) \; ; \; s^\alpha(0) = \tau_0^\alpha \tag{5.31}$$

$$h^{\alpha\beta}(t) = \begin{cases} h_0^\beta \left(1 - \frac{s^\beta(t)}{s_s^\beta}\right)^a & \text{if } \mathbf{n}^\alpha = \mathbf{n}^\beta \\ qh_0^\beta \left(1 - \frac{s^\beta(t)}{s_s^\beta}\right)^a & \text{if } \mathbf{n}^\alpha \neq \mathbf{n}^\beta \end{cases}$$

where $h^{\alpha\beta}$ is the hardening coefficient matrix, $\dot{\gamma}^\beta(t) > 0$ is the plastic shearing rate on the βth slip system, τ_0^α is the initial slip system resistance on the αth slip system, q captures latent hardening, s_s^β is the saturation stress on slip system β, and h_0^β dictates the maximum value of the hardening coefficient associated with a slip system β. The rate-independent CP constitutive model implementation is elaborated in Appendix C, while detailed derivations are presented in References [172].

5.6   Results and Discussion

Here, the non-local state-based PD algorithm is examined for a 1D elastic bar with a varying Young's modulus of elasticity. The resultant displacements of the PD scheme with the higher-order stabilization (HOS) approach are compared against analytical solutions as well as numerical algorithms with no stability implementation. Thereafter, 2D and 3D numerical schemes are tested for different microstructures. Comparisons are performed against analytical, experimental, and FEM solutions as needed. The examples aim to demonstrate that increasing the order of interactions

in material particles can improve the accuracy of the numerical solution and reduce the hourglass instability modes of the non-local state-based PD framework.

5.6.1 Example 1: 1D Cantilever Bar

The classic 1D cantilever elastic bar example [173, 179, 185], as depicted in Figure 5.11(a), is conducted for validation of the higher-order implementation. Here, the bar has a total length L_{tot}, and a constant cross-sectional area A. Displacement constraints are applied on each side of the bar, i.e., $u(x = 0) = 0$ and $u(x = L_{tot}) = u_{end}$. In this 1D example, u_{end} is set to be $0.005L_{tot}$. A variable Young's modulus, as plotted in Figure 5.11(b), is also adopted as follows:

$$
E(x) = \begin{cases} E_0 & 0 \leq x \leq L_{\text{tot}}/2 \\ E_0\left(1 + \frac{\beta}{2\alpha}\frac{1}{\sqrt{x/L_{\text{tot}}-1/2}}\right)^{-1} & L_{\text{tot}}/2 < x \leq L_{\text{tot}} \end{cases} \tag{5.32}
$$

Consequently, the corresponding analytical displacement $u(x)$ can be computed to be as follows:

$$
u(x) = \begin{cases} \alpha x & 0 \leq x \leq L_{\text{tot}}/2 \\ \alpha x + \beta L_{\text{tot}}\sqrt{x/L_{\text{tot}} - 1/2} & L_{\text{tot}}/2 < x \leq L_{\text{tot}} \end{cases} \tag{5.33}
$$

where parameters are set as $\alpha = 0.001$, $\beta = 0.004\sqrt{2}$, $L_{\text{tot}} = 1$, and $E_0 = 1$.

Subsequently, a uniform mesh with 500 equally-distant material particles is employed to study the effect of using higher-order approximations framework on the resultant axial displacements $u(x)$, under outward displacement constraint $u_{end} = 0.005L_{\text{tot}}$. A comparison between the higher-order approximation solutions and those with no stabilization control method [262] is shown in Figure 5.12. Since a higher-order ap-
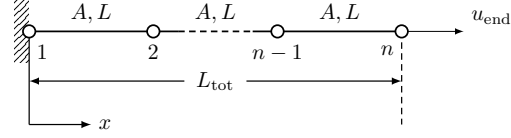
(a) 1D elastic bar
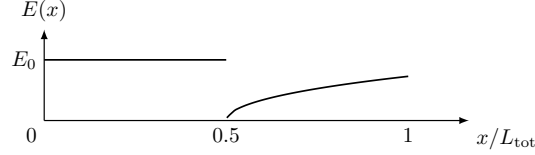
(b) Variable Young's modulus

Figure 5.11: *1D cantilever bar. (a) A 1D elastic bar under tension with displacement constraints is used to study the effect of using higher-order approximations of the deformation gradient. (b) The example exhibits a varying Young's modulus along the x-axis.*

proximation approach only takes effect in large-horizon families, i.e., $\delta > h$, two horizon selections $\delta = 2h$ and $\delta = 3h$, are illustrated in Figure 5.12. As the horizon size increases, the hourglass oscillations grow dramatically if no control method is applied. In contrast, the higher-order approximation method suppresses the numerical oscillations in both cases (i.e., $\delta = 2h$ and $\delta = 3h$) and dampens the zero-energy modes effectively.

5.6.2   Example 2: 2D Polycrystalline Microstructure

Here, a $1 \times 1 \ mm^2$ polycrystalline microstructure with 21 grains, synthetically generated by Voronoi tessellation [20], is considered. In this example, 12 different orientation angles from the interval $[-\pi/2, \pi/2)$ are distributed randomly among grains. The discretized computational domain, as depicted in Figure 5.13, is based on a uniform 50×50 particle discretization for PD technique, and 50×50 square-faced elements for FEM. With the number of particles being the same as the number of elements, the material particles in the PD model are located at the center of elements in the FE model. Consequently, each material particle occupies a constant area in the reference

132

(a) $\delta = 2h$

(b) $\delta = 3h$
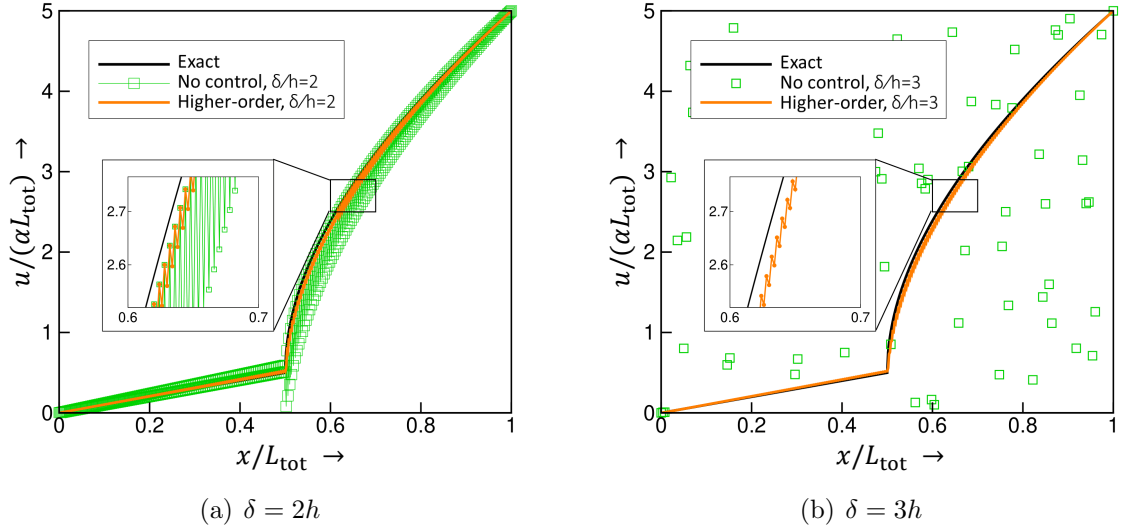
Figure 5.12: *Effect of zero-energy modes on the displacement field of 1D bar obtained from the higher-order approximation approach with two different horizon sizes (a) $\delta = 2h$ and (b) $\delta = 3h$. Results are based on a uniform mesh with 500 material particles.*

configuration that is equal to the corresponding enclosed FE area. Linear basis functions and traditional implicit solvers are employed in the FEM. Although different solvers are applied in PD and FE models, the same constraint on errors is set, i.e., $e_l = 10^{-6}$.

Furthermore, a compression velocity gradient, as shown below, with plane strain assumptions is applied on microstructure boundaries to simulate the process of y-axis compression:

$$\mathbf{L} = \eta \begin{bmatrix} 1 & 0 \\ 0 & -1 \end{bmatrix} \tag{5.34}$$

where $\eta = 0.0020$ denotes a constant strain rate. Each simulation is performed over 30 steps with the corresponding velocity gradient leading to a final strain around 0.06. The isotropic elastic stiffness matrix is taken as $C_{11} = 2$, $C_{12} = 1$, and $C_{33} = 2$ (in

GPa).

The inward boundary treatment, as elaborated in Section 5.4, is then applied to constrain the velocity gradient of the fictitious boundary particles to that shown in Equation (5.34) for the PD model. As the horizon radius δ grows, the boundary layer thickness (equal to the horizon radius) increases, and the number of material particles within the computational domain decreases. Figure 5.13 provides an example illustrating the effect of enforcing the inward boundary treatment. In Figure 5.13(a), low-magnitude stress values are captured around the external edges without the fictitious boundary layer. This is mainly because of the erroneous deformation gradient approximated by the defect horizons. In contrast, the stress field obtained from the boundary enforcement, as depicted in Figure 5.13(b), shows no spurious values along the four outermost edges.

(a) No boundary treatment

(b) Boundary enforcement
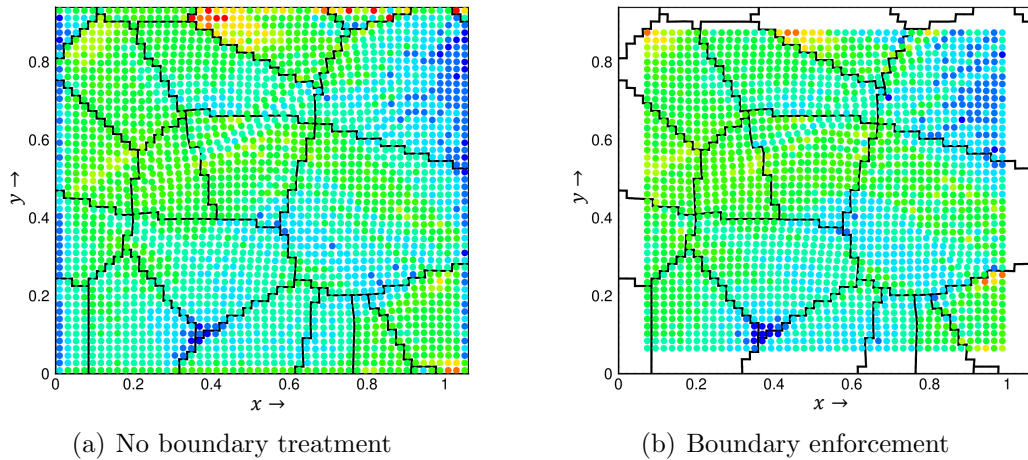
Figure 5.13: *The effect of boundary treatment on PD stress distributions with a horizon size $\delta = 3h$.*

Next, Figure 5.14 provides a comparison of the PD and FE techniques for modeling crystal orientation changes of the same polycrystal under a y-axis compression test, using three different horizon selections in Table 5.2. In the following, the quantification of the crystal orientation changes is briefly explained. In 2D polycrystals,

each grain can be characterized by a rotation tensor, denoted as $\mathbf{R}$, relating the local crystal lattice frame to the reference sample frame. Given an orientation θ (i.e., the angle between crystal and sample axes), the associated rotation matrix supports parametrization as $\mathbf{R} = \cos(\theta)\mathbf{I} - \sin(\theta)\mathbf{E}$, where $\mathbf{E}$ is a 2D alternator (i.e., $E_{11} = E_{22} = 0, E_{12} = -E_{21} = 1$), and $\mathbf{I}$ is a 2D identity tensor. Consequently, the rotation tensor can be evaluated through a polar decomposition of the elastic deformation gradient as $\mathbf{F} = \mathbf{R}\mathbf{U}$. The spin tensor $\mathbf{\Phi}$ can then be expressed as $\mathbf{\Phi} = \dot{\mathbf{R}}\mathbf{R}^{\mathrm{T}} = -\dot{\theta}\mathbf{E}$, where $\dot{\theta} = \frac{\partial\theta}{\partial t}$ is the crystal reorientation velocity. Alternatively, in the component form, the crystal reorientation velocity can be expressed as $\dot{\theta} = (\Phi_{21} - \Phi_{12})/2$. Accordingly, using the reorientation velocity, the crystal texturing is tracked by $\Delta\theta = \dot{\theta}\Delta t$ at each time step.

Reorientation of grains predicted by PD and FE models are compared in Figure 5.14 at the final strain value of 0.06. The overall reorientation contours and locations of the shear bands are mostly similar between the two models at the same degree of mesh refinement. The localized shear bands seen from FE simulations are comparatively more diffuse due to the lack of an internal length-scale. Along the direction of arrows, the width of a shear band obtained by PD simulations is smaller, and its boundary is more conspicuous, which are qualitatively closer to those seen in experiments [21, 136, 137, 268]. It is clear from Figure 5.14 that zero-energy modes are effectively suppressed in all long-range horizon selections. This is in agreement with the 1D elastic bar tension test seen previously in Section 5.6.1, where the HOS implementations are compared against the solutions with no stabilization control.

Additionally, as evident from PD simulations in Figure 5.14, larger horizon interactions make the reorientation results more stable. Nevertheless, it is shown in Yaghoobi et al. [173] that by including more neighboring particles, the higher-order approximation framework may lead to less stable results if the increased horizon size is not

135

(a) FE (b) PD, $\delta = h$ (c) PD, $\delta = 2h$ (d) PD, $\delta = 3h$
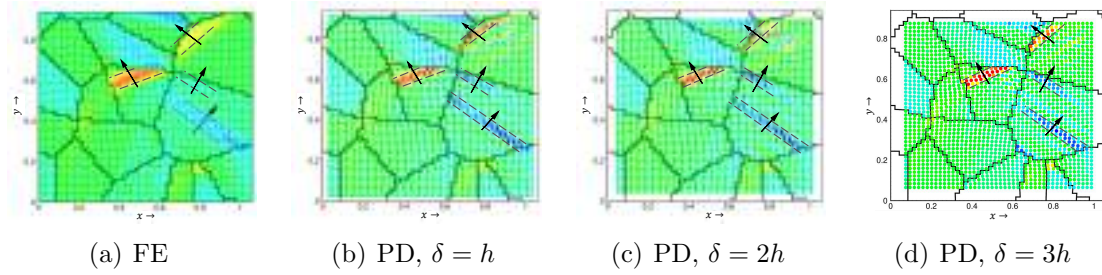
Figure 5.14: *Orientation changes for* 2500 *particles under a y-axis compression test for FE and PD results with three different horizon sizes at final strain of* 0.06. *Along the direction of arrows, sharper and more number of shear bands can be seen in PD results. Here, δ is the horizon radius, and h is the distance between the nearest material particles. The margin around the boundary in PD models is due to the inward boundary treatment.*

able to obtain a greater accuracy (e.g., $\delta = h$ vs. $\delta = \sqrt{2}h$). This is different from the 1D bar test in Section 5.6.1, in which larger horizon sizes consistently reduced the spurious zero-energy mode oscillations.

5.6.3   Example 3: 3D Matrix with Soft Precipitate

For the first 3D example, a cubic matrix of dimensions $3 \times 3 \times 3 \ mm^3$ along with a central spherical precipitate with a diameter $0.875 \ mm$ having a lower modulus, as illustrated in Figure 5.15, is modeled using both FE and PD techniques. The transversely-isotropic elastic matrix is assigned with the following stiffness constants: $C_{11}^{mat} = 59.3$, $C_{12}^{mat} = 25.7$, $C_{13}^{mat} = 21.4$, $C_{33}^{mat} = 61.5$, and $C_{44}^{mat} = 16.4$ (in GPa). Contrarily, the stiffness constants assigned to the spherical precipitate are reduced by a factor of 10, i.e., $C_{ij}^{ppt} = 0.1 \times C_{ij}^{mat}$, where C_{ij}^{ppt} denotes the (i,j) entry of the elastic stiffness tensor pertaining to the precipitate particles. Here, both materials are assumed to be elastic under a small deformation. Thus, the strain tensor is computed as $\epsilon = \frac{1}{2}(\mathbf{F} + \mathbf{F}^T) - \mathbf{I}$, where $\mathbf{I}$ is the identity tensor. Also, Cauchy stress tensor $\sigma = \mathbf{C} : \epsilon$ is used in lieu of $\mathbf{P}$ in Equation (5.4), assuming a small deformation, where $\mathbf{C}$ represents the elastic stiffness tensor.

136
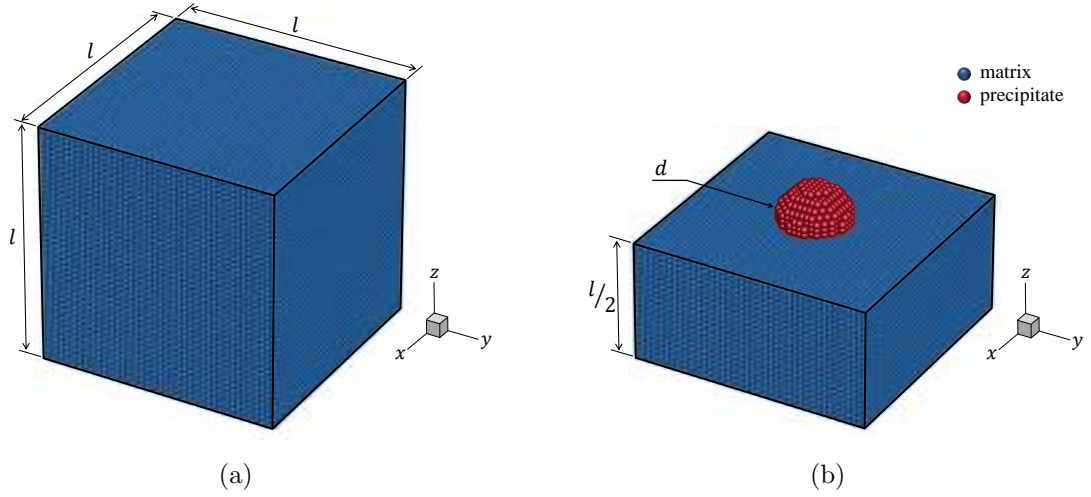
Figure 5.15: *Illustration of the 3D matrix with soft precipitate in the middle. (a) A 3D matrix microstructure (colored in blue) with dimension $l = 3$ mm consisting of a soft precipitate (colored in red) with diameter $d = 0.8750$ mm locating at the center. The material domain is discretized into $48 \times 48 \times 48$ particles with a constant inter-particle spacing $h = 62.5$ μm. (b) This illustration provides the interior information along the slice $z = 1.5$ mm. The spherical precipitate is fully retained for a better visualization.*

The cubic material domain represented in Figure 5.15(a) is discretized into a $48 \times 48 \times 48$ structured particle grid. A similar discretization refinement is adopted for the FE simulation, where each linear hexahedral volumetric element encompasses the material particle in the PD model. In addition, Dirichlet boundary conditions dictated by the following diagonal velocity gradient, are applied to the microstructure boundaries to simulate an x-axis tension up to 0.02 strain:

$$\mathbf{L} = \begin{bmatrix} 1.0 & 0 & 0 \\ 0 & -0.5 & 0 \\ 0 & 0 & -0.5 \end{bmatrix} \tag{5.35}$$

Subsequently, numerical PD simulations are carried out using the higher-order influence weight functions tabulated in Table 5.3 for $\delta = h$, $2h$, $3h$, and weighting

value coefficients without any stabilization framework for $\delta = 2h$, $3h$ [262]. An inward boundary treatment, as outlined in Section 5.4, is then enforced to constrain the velocity gradients of the shadow particles in PD models. Figure **??** depicts the variations in y-displacement contours at the midsection $z = 1.5\ mm$ for stabilized PD framework using horizon sizes of $\delta = h$, $2h$, and $3h$ at the final strain value 0.02. FEM simulation prediction is also included for comparison. Although the overall displacement fields are mostly similar between PD and FE models, the localizations around the precipitate as obtained from FEM simulation are comparatively more diffuse due to the lack of an internal length-scale.

Next, Figure **??** depicts the variations in the x-displacement contours for PD technique with and without the stabilization control of zero-energy modes, across the midsection $z = 1.5\ mm$ using horizon sizes $\delta = 2h$ and $3h$ at the final strain value 0.02. For the case of a PD scheme without any control of zero-energy modes (termed 'no control'), an influence function of the form $\omega = \frac{1}{\|\boldsymbol{\xi}\|_2}$ is employed [262], where $\boldsymbol{\xi}$ denotes the bond vector associated with neighboring material particles. While 'no control' simulations tend to produce significant increases in erroneous zero-energy modes with successive horizon sizes, the resultant displacements with higher-order approximation scheme (termed 'higher-order') illustrates stabilized solutions for both horizon sizes $\delta = 2h$ and $3h$. Figure 5.16 depicts the profiles of x-displacements through centerline along the x-direction for the contours shown in Figure **??**. The plots here are also compared against the FEM solution as seen in Figure **??**. Figure 5.16(a) exhibits the emergence of the instability modes for the 'no control' case of $\delta = 2h$ right across the interface of soft precipitate and stiff matrix, as the hourglass oscillations grow dramatically within the spherical precipitate. In the case of $\delta = 3h$ shown in Figure 5.16(b), the hourglass oscillations significantly worsen for 'no control' procedure, affecting the displacements even along the stiff matrix. In both horizon sizes, the resulting contours pertaining to the higher-order approximation

scheme effectively dampen the hourglass oscillations and remain close to the FEM solution.
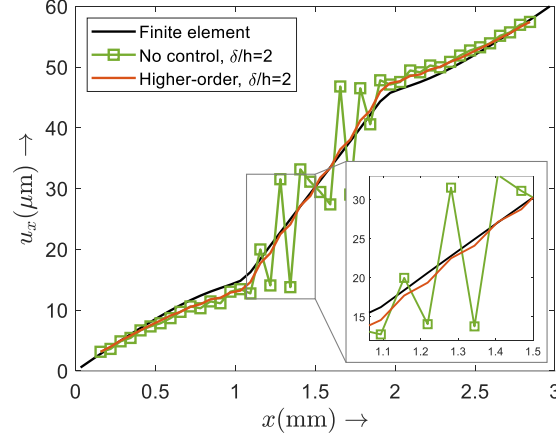
(a) $\delta = 2h$
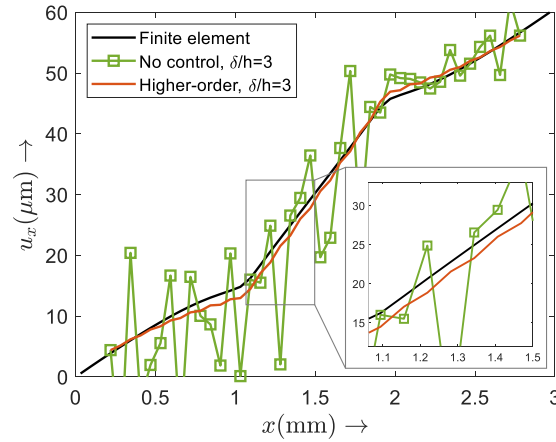
(b) $\delta = 3h$

Figure 5.16: *Contours of x-displacements through centerline along the x-direction for two horizon interactions (a) $\delta = 2h$ and (b) $\delta = 3h$, respectively at final strain.*

Thereafter, four additional stiffness constants are assigned to the spherical precipitate using the following ratios: $r_c = 10^{-2}$, 10^{-3}, 10^{-4}, and 10^{-5}, where $C_{ij}^{ppt} = r_c \times C_{ij}^{mat}$. As the stiffness ratio decreases, the precipitate properties tend toward the properties of a void with a zero modulus. As observed in the previous examples, the interface between a stiff and soft material has particularly sharp gradients in the strain and stress fields. Hence, a non-local theory becomes advantageous due to its ability in

139

capturing discontinuities without enforcing any traction boundary conditions around the precipitate interface. Figure 5.17 illustrates x- and z- component displacements along the midsection $z = 1.5\ mm$ as obtained from the stabilized non-local PD simulation using the horizon size $\delta = 3h$ for all the stiffness ratios considered. As the stiffness of the precipitate decreases towards that of a void, one would expect a decreased force transmission across the precipitate interface, and consequently, a decreased displacement at the void's center. As demonstrated in Figure 5.17, the stabilized higher-order PD model correctly captures the zero displacements at the center as the elastic modulus pertaining to the spherical precipitate decreases.

Figure 5.18 denotes the plots for component-wise displacements at the center of the precipitate as a function of the stiffness ratio r_c, for different horizon sizes δ. Here, the FEM predicts close to a constant non-zero displacement at the center. However, one would expect convergence toward a zero-displacement since no force transmission occurs across the precipitate interface in the case of a zero-modulus material, e.g., vacuum. Despite that, PD, a non-local method, depicts a faster convergence toward a zero center-displacement with growing horizon sizes δ, as the stiffness ratio r_c decreases. For a given horizon size δ, the absolute value of all the displacement components decreases with reducing stiffness ratio r_c. The convergence rate of the non-local PD solutions to the zero-displacement at the center of the precipitate depends on the horizon size, δ. This is expected as the non-local horizons utilize the information from both sides (i.e., low and high stiffness particles) to capture the sharp strain gradient. Additionally, with a given stiffness ratio r_c, the absolute values of the displacement components drop with increasing horizon size δ. As the horizon size δ increases, the sharp gradient around the void's interface is captured more efficiently since there are more particles to decide upon the interface behavior.

(a) $r_c = 10^{-2}$ (b) $r_c = 10^{-3}$ (c) $r_c = 10^{-4}$

(d) $r_c = 10^{-5}$ (e) $r_c = 10^{-2}$ (f) $r_c = 10^{-3}$

(g) $r_c = 10^{-4}$ (h) $r_c = 10^{-5}$
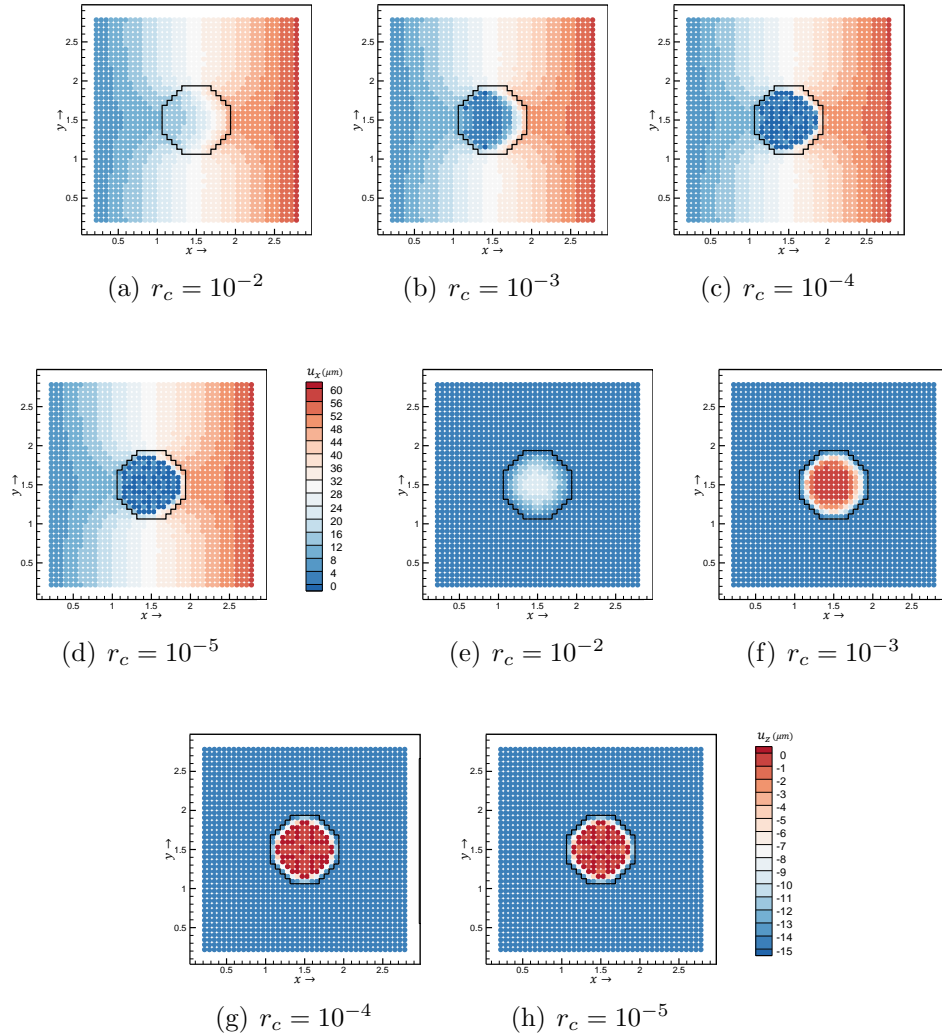
Figure 5.17: *Comparison of (a)-(d) x-displacements and (e)-(h) z-displacements (both in µm) along midsection z = 1.5 mm for varying stiffness ratios as obtained from the high-order stabilized PD model with δ = 3h.*

5.6.4   Example 4: 3D Polycrystalline Microstructure with Spherical Void

The previous 3D example demonstrates the efficacy of the HOS scheme in the case of an elastic matrix. Here, the example includes an elastoplastic 3D model of the polycrystalline aggregates using a soft precipitate with a stiffness ratio $r_c = 0.1$. Specifically, a 3D polycrystalline microstructure consisting of 78 grains with dimensions $l = 3$ mm, and a soft precipitate with diameter $d = 0.8750$ mm at the center is considered. The 3D material domain is discretized into $48 \times 48 \times 48$ particles with

141
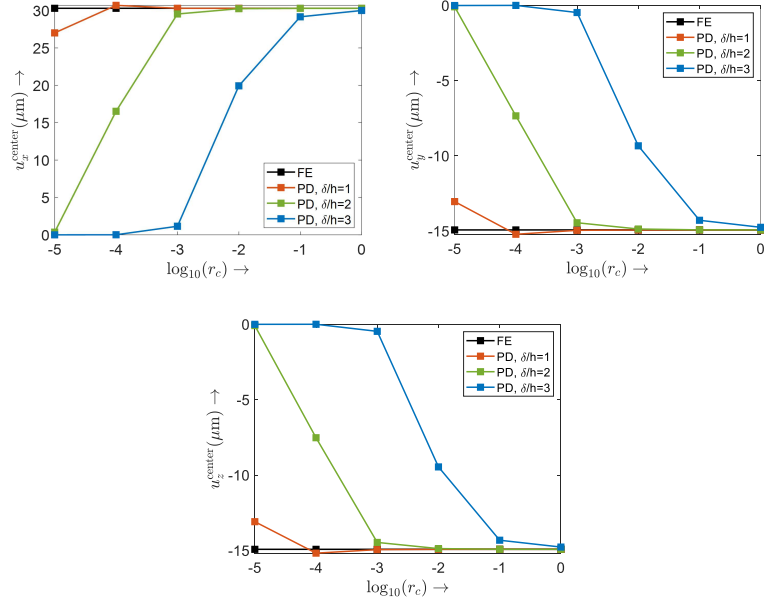
Figure 5.18: *Variations in the displacement components at the center of the spherical precipitate in terms of the stiffness ratio r_c, for different horizon sizes δ.*

a constant inter-particle spacing $h = 62.5\ \mu m$ as shown in Figure 5.19(a). Moreover, Figure 5.19(b) illustrates the interior cross-section of the 3D polycrystalline microstructure along slice $z = 1.5\ mm$ without depicting the precipitate region. The polycrystal is simulated with properties of WE43 alloy-T5 temper, as provided in Lakshmanan et al. [21] with 18 slip systems, including 3 basal$\langle a \rangle$, 3 prismatic$\langle a \rangle$, 6 pyramidal$\langle a \rangle$, and 6 pyramidal$\langle c + a \rangle$ slip systems. For interested readers, a detailed review of Magnesium alloy crystal plasticity models can be found in Ref. [269, 270, 271].The boundary conditions are the same as those considered in Section 5.6.3.

Figure **??** depicts the x- and y- strains, with and without control of zero-energy modes, along the midsection $z = 1.5\ mm$ using a horizon size $\delta = 3h$. For the case of the PD scheme without any control of zero-energy modes (termed 'no control'), an influence function $\omega = \frac{1}{\|\boldsymbol{\xi}\|_2}$ is employed [262] similar to the previous example in Section 5.6.3. The 'no control' case shows patchy/pixellated locations not just along the precipitate
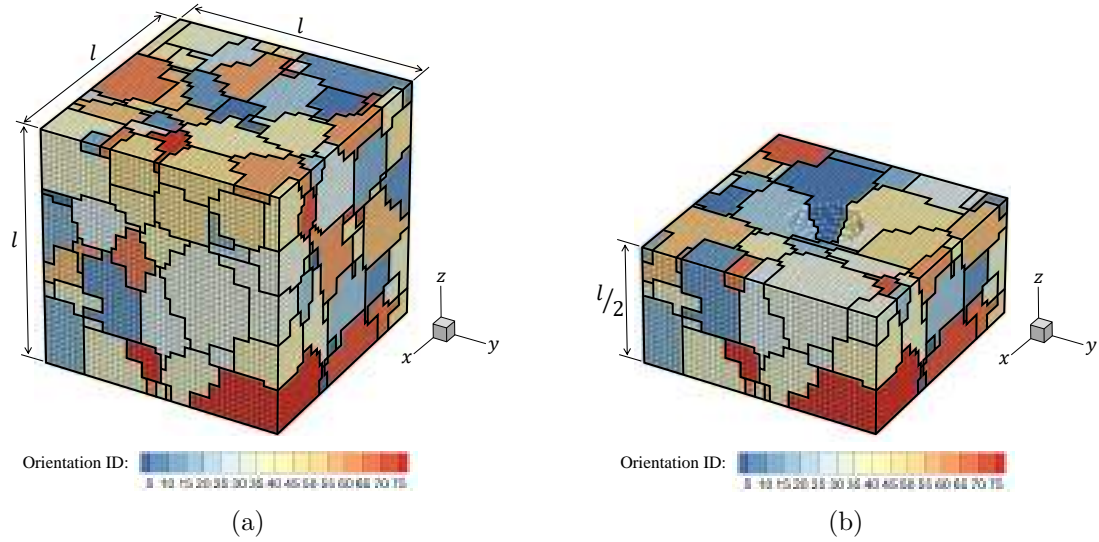
Figure 5.19: *3D polycrystalline microstructure with a spherical void. (a) A 3D polycrystalline microstructure consisting of 78 grains with dimensions $l = 3$ mm and a soft precipitate with diameter $d = 0.8750$ mm at the center. (b) Interior of the 3D microstructure along slice $z = 1.5$ mm. The spherical precipitate at the center is removed for a better visualization. Grains with similar orientation ID share the same Rodrigues orientation vector. The black lines denote grain boundaries.*

interface (similar to the elastic matrix example) but also within the grains, where one can expect strain localizations across grain boundaries due to property variations as a function of crystal orientations (i.e., across hard and soft grains depending on their crystal orientations relative to the loading direction). Nevertheless, the results associated with the HOS scheme show an effective control of the erroneous zero-energy mode oscillations.

Next, the PD results are compared against the FEM solution in Figure **??**, which depicts the profile of equivalent strain at midsection $z = 1.5$ mm for horizon sizes $\delta = h$, $2h$, and $3h$. Unlike the 3D composite microstructure in Section 5.6.3, where there exist significant strain localizations only around the interface of the precipitate; here, there are expected to be strain concentrations across the granular interfaces as well. In the FEM solution, the interfacial strain localizations are computed to be significantly more pronounced than the granular strain localizations within each

crystal. Contrastingly, the PD solution identifies both strain localizations, along the precipitate boundary as well as granular interfaces. Additionally, the PD results are stable across the three horizon sizes $\delta = h$, $2h$, and $3h$. Implementation of the HOS control in these examples required no additional computational cost per time step, as the influence function values are explicitly adjusted for each user-defined horizon interaction δ. However, as shown in Silling et al. [263], the maximum stable time step for PD is, in general, also a function of the horizon radius for long-range interactions (i.e., $\delta > h$) and needs to be scaled based on the von Neumann stability analysis as the horizon radius δ rises [185].

5.6.5 Example 5: CPPD Simulations vs SEM-DIC Experimental Data

Here, the CPPD framework predictions are compared with state-of-the-art in-situ SEM-DIC data of WE43 magnesium alloy [272]. SEM-DIC is a useful in-situ, non-destructive technique for characterizing microscopic surface strains. A speckle pattern placed on the microstructure during thermomechanical loading is tracked by the DIC setup, which is then post-processed to obtain the surface displacement fields, from which the surface strains can be computed. Details of the SEM-DIC experiments that were performed for the WE43 alloys are described in greater detail in Reference [273]. The primary material used for the experiments is a hot-rolled annealed WE43 plate with a thickness of 31 mm, subjected to T5 temper condition. EBSD scans of the surface prior to loading were used to extract grain orientation information. Intergranular and intragranular strain localization patterns are widely observed throughout the microstructure under tensile loading, while no twinning is recorded. The comparison of CPPD with experimental results for the above experiment is examined.

The mechanical test is modeled using CPPD as a boundary value problem (BVP) using the EBSD map of the microstructure within the DIC window. The displacement of the boundary of the microstructure is obtained from experiments and these are used

144

to set up displacement BCs on the lateral boundaries. Measurements are made on the surface of the sample, which is a traction-free surface, and hence, the top and bottom surfaces in the simulation are traction-free. For the sake of comparison with an FE implementation, the same problem is simulated using the PRISMS-CPFE framework [172].

Figure **??** provides an example of the CPPD computational domain. The thickness of the plate is set equal to the distance between the nearest particles, while the horizon size is set equal to the smallest inter-particle distance. The four sides of the plate are displacement-constrained based on DIC experimental data. In each loading step, 0.2% of the final displacement is imposed so that 500 displacement increments are arrive at the total displacement. In addition, the bottom surface is constrained only in the z-direction. Simulations are performed with 200 particles, in both x and y directions. Additionally, for each level of refinement, 2 and 3 slices of particles are constructed so that 8 different cases are simulated in total. The initial damping ratio is set to $c_0 = 0.5$.

The corresponding FEM problem involves a $200 \times 200 \times 1$ grid with displacement BCs on the lateral boundaries (obtained from the experiment) and the remaining two surfaces being traction-free. The final displacement on the boundary is achieved in 1000 simulation steps using the same constitutive model and parameters as done for the CPPD simulations.

Figure **??** depicts the comparison of the x and y components of displacement between experimental data, CPPD simulations (using 200 particles and 3 slices), and CPFE simulation. Tables 5.4 and 5.5 tabulate the grain averaged displacement components. A very good match is obtained for the grain-averaged displacement field predictions between CPPD, CPFE, and experiments, as evidenced by the percentage difference with the experiment. This affirms, on the first level, the ability of the

145

CPPD framework to solve elasto-plastic BVPs directly comparable with experimental measurements.

Table 5.4: *Comparison of grain-averaged displacement component u.*

Grain ID	u(Exp)	u(200)	Error(%)	u(CPFE)	Error(%)
13	131.214	129.4983	1.3076	131.3805	0.2169
14	93.3969	92.0990	1.3897	93.6352	0.2551
16	161.7453	156.2533	3.3955	155.6439	3.7722
19	124.3817	121.1535	2.5954	123.6302	0.6042
23	138.9585	139.0753	0.0840	138.5096	0.3230
27	96.4904	95.8660	0.6471	96.1437	0.3593
28	116.7845	113.0817	3.2246	113.7660	2.5847

Table 5.5: *Comparison of grain-averaged displacement component v.*

Grain ID	u(Exp)	u(200)	Error(%)	u(CPFE)	Error(%)
13	47.1972	47.0030	0.4144	46.5021	1.4727
14	46.7184	44.7065	4.3063	44.0925	5.6207
16	71.2743	66.7874	6.2952	67.0213	5.9671
19	36.3375	39.0665	7.5103	40.0881	10.3215
23	33.5344	33.6929	0.4727	34.7998	3.7734
27	38.1632	35.7701	6.2708	34.8351	8.7207
28	27.5032	27.3063	0.7160	27.6984	0.7098

Next, the predictions in strain components are compared quantitatively. Since the displacement components in 2D are recorded in the experiment, the data is post-processed to extract the in-plane strain components ϵ_{xx}, ϵ_{yy} and ϵ_{xy}. Figure **??** shows the comparison in the three strain components between experiments and CPPD simulations with both discretizations. Qualitatively the strain fields look similar between experiments, CPPD, and CPFE. To verify that the strain fields are also similar in an averaged sense, the mean strain fields in each grain are tabulated in

Tables 5.6 and 5.8. Grains with their respective orientation IDs are depicted in Figure **??**.

Table 5.6: *Comparison of grain-averaged strain component ϵ_{xx}.*

Grain ID	ϵ_{xx}(Exp)	ϵ_{xx}(200)	Error(%)	ϵ_{xx}(CPFE)	Error(%)
13	0.04098	0.03461	15.5482	0.03396	17.1246
14	0.03446	0.03018	12.4256	0.03027	12.1663
16	0.04336	0.06783	56.4480	0.06588	51.9527
19	0.02124	0.02045	3.7538	0.01911	10.0501
23	0.02842	0.03226	13.5155	0.03361	18.3105
27	0.01915	0.01607	16.0673	0.01647	13.9886
28	0.01784	0.01633	8.4606	0.01670	6.374

Table 5.7: *Comparison of grain-averaged strain component ϵ_{yy}.*

Grain ID	ϵ_{yy}(Exp)	ϵ_{yy}(200)	Error(%)	ϵ_{yy}(CPFE)	Error(%)
13	-0.02160	-0.0236	9.4808	-0.02412	11.6862
14	-0.01450	-0.01750	20.6573	-0.01722	18.7973
16	-0.02024	0.02695	33.1052	-0.02462	21.6700
19	-0.01200	-0.00952	20.6618	-0.00717	40.2660
23	-0.01860	-0.01986	6.7538	-0.02037	9.5068
27	-0.00714	-0.01123	57.2670	-0.01153	61.4748
28	-0.00716	-0.00625	12.6451	-0.00675	5.6594

Table 5.8: *Comparison of grain-averaged strain component ϵ_{xy}.*

Grain ID	ϵ_{xy}(Exp)	ϵ_{xy}(200)	Error(%)	ϵ_{xy}(CPFE)	Error(%)
13	0.008463	-0.007252	185.6957	0.001733	79.5209
14	-0.000586	-0.004273	628.5678	-0.004056	592.239
16	0.000837	0.0005	40.305	-0.0004487	153.551
19	0.002951	0.001927	34.6781	0.001093	62.9728
23	0.007106	0.004915	30.8361	0.003429	51.7704
27	0.001594	-0.002358	247.8851	-0.003940	347.0241
28	0.000337	0.001583	369.444	0.001886	459.8341

The tabulated results showcase, to some extent, the ability and efficacy of the CPPD framework to predict the grain-averaged strain components. Grain 42 is an outlier because it forms but a tiny fraction of the microstructure under consideration.

While both CPPD and CPFE depict signatures of strain localization, the patterns are relatively finer (as also seen in the experiment) in CPPD for the same element size/interparticle spacing, or equivalently the kinematic fields are relatively smoothed out in CPFE. Hence, these strain localization signatures resulting from CPPD simulations are investigated in the following. The comparison depicts the overall success of CPPD in predicting the normal strain components and, specifically, the localization patterns arising at the boundaries of the domain. Strain hotspots in the interior of the material or at the grain boundaries are seen as signatures in simulations. Still, these are delocalized across multiple points instead of appearing in a more prominent or singular manner.

5.7   Conclusion

In this chapter, a higher-order approximation to the non-local deformation gradient is developed to suppress zero-energy instability modes in PD models beyond nearest-neighbor interactions. In microstructural simulations, pixel or voxel-based structured discretizations are often preferred as they can be readily obtained directly from microscopy, tomographic imaging, or numerical acquisition techniques. As a result, a mesh-less non-ordinary state-based implementation of the PD via Newmark's dynamic method with artificial damping is employed for solving deformation and stress fields on structured grids. However, such correspondence-based PD models often suffer from zero-energy mode oscillations, which, as studied in this chapter, can be effectively mitigated by choosing material weight functions via a Taylor series expansion of the deformation gradient. The novelty here is a tensor-based derivation of the linear

constraint equations, which can be used to systematically identify the particle inter-action weight functions for various user-specified horizon radii. It is demonstrated that unique weighting value coefficients can be obtained by combining the governing equations for the desired leading truncation error, along with an additional set of constraint equations from the next higher-order approximations that do not contain first-order interaction weight functions.

The efficacy of the HOS method is first demonstrated for a simple 1D elastic cantilever bar, where results are compared with exact and PD solutions with no stabilization control. The zero-energy modes are demonstrated to be effectively dampened us-ing the proposed higher-order particle interaction weight functions. Next, in the case of 2D polycrystalline microstructures, observed shear bands are shown to be stable across different horizon sizes while being relatively sharper and more local-ized within intergranular regions relative to the FEM solution. The proposed HOS scheme is also demonstrated for examples involving 3D composite and polycrystalline microstructures, along with comparisons against the FE technique. In addition to the stabilization scheme effectively suppressing the zero-energy mode oscillations, it is shown that the PD approach, unlike FEM, converges towards a zero-displacement in the precipitate with a decrease in the stiffness. Overall, the presented stabiliza-tion scheme can lead to high-quality and consistent non-ordinary state-based results for PD simulations beyond nearest-neighbor interactions. Furthermore, the proposed higher-order approximation framework can be directly applied to PD problems involv-ing discontinuities such as damage/fracture propagation, once an appropriate damage continuum model is adopted. All the codes and examples constituting the current CPPD implementation will be available in an open-source platform to the community upon publication of the work.

CHAPTER VI

Conclusions and Future Work

The chapter is organized as follows. First, a comprehensive summary of this thesis is provided in Section 6.1. This follows by Section 6.2, supplementing the future work for each chapter.

6.1   Summary

It is commonly observed from experimental characterization techniques that slices taken in a specific direction from a solid 3D microstructure 'look alike'. This measure of similarity can be systematically quantified through an underlying stationary probability distribution that generates all possible microstructural samples. However, quantifying this high-dimensional joint probability distribution explicitly for all pixels is computationally intractable. To address this issue, new sampling and optimization methods are presented to simulate the stationary distribution pertaining to microstructural formations. For many polycrystalline structures, the probability of a pixel color can be sufficiently conditioned based on the state of its surrounding neighbors. Hence, in this work, polycrystalline are represented as undirected probabilistic graphical models, alternatively known as MRFs, with each pixel interacting with its neighbors over a relatively-small sampling window size. Hence, a robust numerical method for reconstructing diverse microstructures from three 2D micrographs

imaged on orthogonal planes is presented in which the algorithm reconstructs 3D images through matching slices at different voxels to representative input 2D exemplars. This process is posed as an iterative two-step optimization procedure where the first step involves searching for patches in the 2D micrographs that closely resemble the spatial neighborhood of the 3D voxel, followed by a second step involving optimization of an energy function that ensures various patches from the 2D micrographs mesh together seamlessly in the 3D model. It is shown that the MRF approach can precisely capture both 1-point (e.g., grain size, orientation distribution) and 2-point (e.g., misorientation angles, shape moments) correlations consistent with experimental patterns. Subsequently, to capture the variations of the 3D microstructures at larger length scales, a tensor-based optimization process is employed to iteratively embed microstructural patches onto the part-scale CAD geometry based on user-specified material flow fields and grain size scaling that are often inferred from experimental characterization techniques. The efficacy of this new approach is demonstrated for generations of full-field microstructure maps of AM structure with millions of grains in real-time and has been shown to be more efficient than existing phase-field and kinetic Monte Carlo simulations in literature.

For the aforementioned image reconstruction strategies in materials applications, where measured features contain physical considerations, it is crucial to incorporate the corresponding physics back into the reconstruction technique. Nevertheless, the MRF techniques only sample local statistics over relatively-small windows and do not enforce any particular physics-based constraints on GB formation. Hence, a novel physics-based numerical framework that utilizes graph-theoretic techniques is examined, as a post-reconstruction step, for the spatio-temporal evolution of synthesized polycrystalline microstructures. One crucial factor in numerically modeling GB structure is the computation of lengths in 2D and surface areas in 3D from pixelated/voxelated images. To address this shortcoming, the concept of graph-cuts from

151

integral geometry is employed in order to compute the expected lengths of GB facets based on a pairwise labeling problem. The framework is then extended to employ anisotropic grain growth using an energy optimization principle. The Cauchy-Crofton method was applied against noise and partial volume effects for MRF reconstructions.

Lastly, the theory of NOSBPD is used to investigate the structure-performance relationships in polycrystalline aggregates. This work led to a 3D PD implementation of CP and highlights its significant aspects, including explicit time-stepping with artificial damping, a time-step selection procedure, higher-order stabilization of zero-energy modes, and boundary condition implementation. Although this approach offers a unique capability to solve problems involving singularities (e.g., fracture and crack propagation), it often encounters numerical instabilities known as zero-energy mode oscillations. These instabilities primarily arise from the weak integral formulation used in non-local approximations of the deformation gradient tensor. Hence, a numerical scheme based on high-order Taylor series expansion of the deformation gradient is employed to eliminate the spurious zero-energy mode oscillations. The particular contribution of this thesis lies in a tensor-based derivation of linear constraint equations, which systematically identifies particle interaction weight functions for different user-specified horizon radii. The effectiveness of the higher-order stabilization scheme is demonstrated in this paper through multi-dimensional problems involving polycrystalline microstructures. The results are compared against conventional FEMs, showcasing the proposed stabilization scheme's ability to significantly suppress the undesired zero-energy mode oscillations in all numerical examples. The CPPD predictions are further compared to a recent experimental study of uniaxial tension in a magnesium WE43 alloy, indicating overall agreement in predicted localization patterns.

6.2 Future Work Direction

The proposed methodologies can be supplemented and extended in multiple ways, as described in the following:

6.2.1 3D Unit-Cell Microstructure Reconstruction

In Chapter II, MRF was used to reconstruct a wide variety of microstructures, using just the surface images. The model was successful in cases where the 2D images carry all the statistics of the 3D microstructure. The presumption behind MRF reconstruction methodology is that input surface images are representative (i.e., having similar grain morphology and textural information) to every slice in their respective directions. This requires the user to carefully select volumetric regions in which one single image can adequately describe the entire dataset along that particular axis. This approach is efficient in capturing a wide variety of microstructural features. However, there are samples for which the above requirement is insufficient. Figure 6.1 demonstrates a synthesized 3D microstructure with a non-uniform morphology. Here, grains are densely populated at $z = 128$ and scarcely generated on $z = 0$ slice. Due to the nature of the given microstructure, no single image can thoroughly capture the varying morphology along the z direction. As a result, to reconstruct an equivalent 3D model using MRF, one needs to take into account the statistics of additional orthogonal or oblique sections in their exemplars [80].
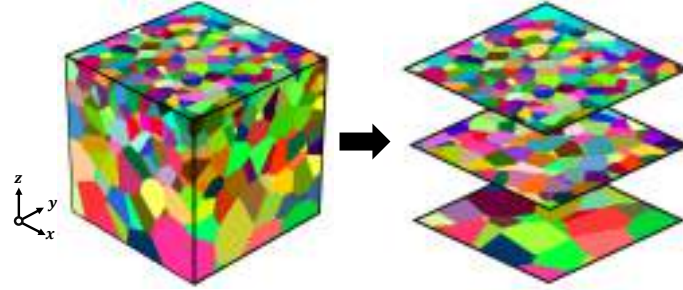
Figure 6.1: *Limitation of MRF algorithm to reconstruct graded microstructures in z direction: this example is specifically selected to illustrate the limitation of the MRF reconstruction algorithm as presented in Chapter II in this paper. The varying morphology of the given microstructure along the z direction can not be captured by only one single image orthogonal to that axis. Consequently, the MRF algorithm can not be used to properly reconstruct such a 3D model. Here, the slices on the right-hand side correspond to $z = 0$, 64, and 128, respectively.*

6.2.2   Large-Scale Microstructure Synthesis

In Chapter III, the LEGOMAT approach was presented to synthesize the microstructural variations in a large component by using tensor fields to generate the size and orientation of the microstructural patches at different locations in the specimen. One limitation of the texture optimization approach is that the embedded microstructural patches are not necessarily continuous beyond the group of tetrahedral elements where the local parameters (i.e., scaling and directionality) are similar. Consequently, this can result in crystalline structures along the boundary of patches being partially cut-off in some instances, especially when modeling slowly-varying microstructures, e.g., microstructures with large precipitates. For illustration, the unit-cell polycrystal shown in Figure 2.4, is embedded over a curved cylindrical CAD model, as shown in Figure 6.2(a), using the LEGOMAT algorithm with a uniform grain size scaling throughout. Here, in Figure 6.2(b), the seamlines become noticeable when embedding low-frequency components. This, however, can be alleviated to an extent by increasing the mesh density or equivalently subdividing local tetrahedral meshes in the regions along the patch boundary. Nonetheless, in the case of AM microstruc-

tures, these seams are less pronounced due to the highly-stochastic nature of the AM microstructure. Yet, it is important to optimize the alignment between adjacent patches within the CAD model to avoid seamlines that occur along the intersecting surfaces of tetrahedral groups from neighboring patches.

(a)   (b)
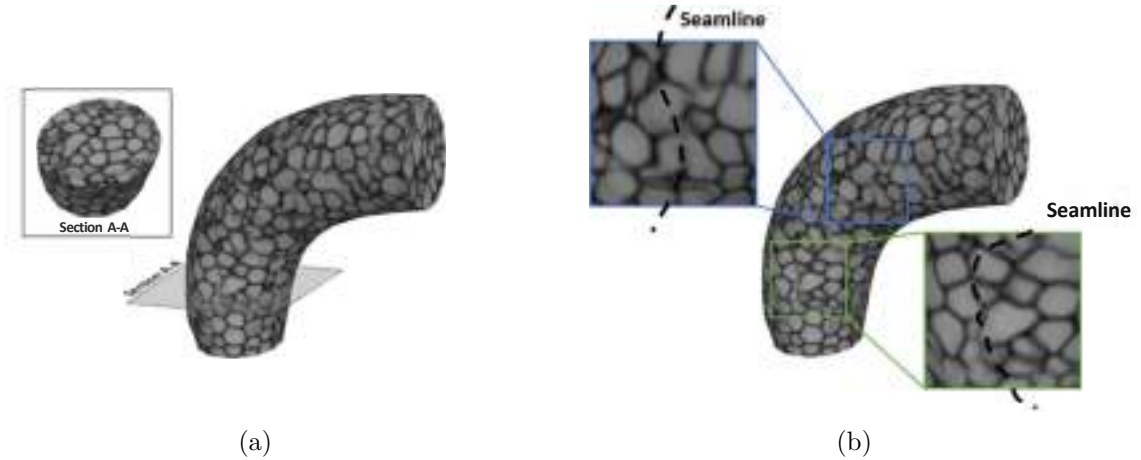
Figure 6.2: *Limitation of LEGOMAT algorithm resulting in noticeable seamlines when embedding low-frequency components: (a) LEGOMAT embedding for polycrystal pattern in a curved cylinder filed with cobblestone-like texture, (b) cut-off crystalline structures across patch boundary.*

Additionally, during the generation of the volumetric tensor fields, there may be singularity conditions where different tensors lead to sharp changes across the microstructure, e.g., near the laser paths where the tensor fields meet. This can often be resolved via mesh refinement or smoothing user-specified vectors using the Laplacian technique [212]. Furthermore, to increase the physical representability of the microstructures in additive manufacturing, one should incorporate thermal analysis to reproduce the volumetric temperature gradient that can ultimately inform the preferred material flow directions, and thus, the imposed tensor fields in the LEGOMAT embedding process [210, 211]. Accordingly, in the future, the generations of process-dependent flow fields can be automated by specifying grain growth directions based on a set of input parameters, such as hatch spacing, layer thicknesses, and scanning patterns using thermal simulations.

Finally, the use of multiple RVE datasets from a library to represent multi-material microstructures should be of interest. An interesting application of this can be in the large-scale reconstruction of specimens from adaptive microscopy, as illustrated in Figure 6.3, where microstructures are imaged at different locations, and the LEGO-MAT is supplied to predict the microstructures at the interface. Further microscopy can refine these regions, but the LEGOMAT embedding algorithm can reduce the number of experimental measurements needed.
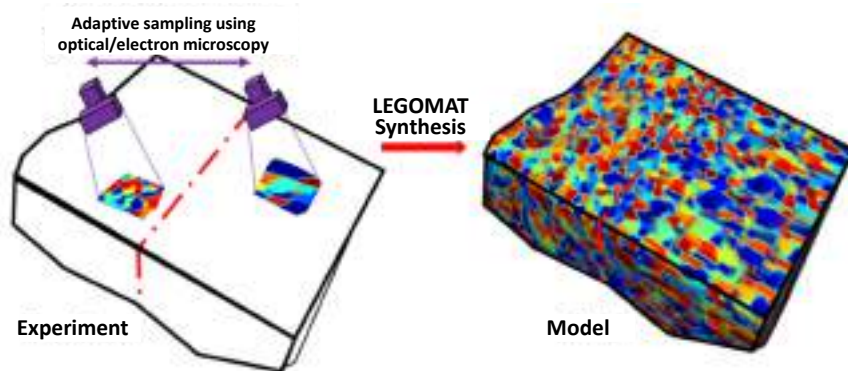
Figure 6.3: *Generations of full-field microstructural maps from limited microscopic scans of adaptively-selected regions.*

6.2.3 Physics-Based Evolution of Reconstructed Microstructures

In Chapter IV, a basic 2D Riemannian metric based on the implementation of the Cauchy-Crofton formulation was verified for modeling 2D microstructural evolution using several test cases with pixelated meshes. Furthermore, a brief extension to the 3D domains for denoising and segmentation of microstructures obtained from MRF reconstruction algorithm was shown. Since the MRF algorithm is a global optimizer, the local features are not sharply obtained. Hence, the reconstruction strategies can benefit from the use of the Cauchy-Crofton formula as a post-processing step to recover GBs. Hence, future work should attend to the following aspects:

- The 2D microstructure evolution case should be extended to anisotropic GB

energies. For this purpose, one needs to develop a regression technique to determine the Riemannian metric combination that best approximates any given surface energy.

$$\gamma = \sum_i \sqrt{\tau^T \cdot \boldsymbol{D_i} \cdot \tau} \tag{6.1}$$

- Validation of the 3D Cauchy-Crofton algorithm using test cases similar to the ones shown here for 2D. The surface area of a 3D object using the Riemannian metric and Cauchy-Crofton formula can be derived as follows:

$$\int \gamma ds = \int \sqrt{(\det \boldsymbol{D}) \cdot \boldsymbol{n}^T \cdot \boldsymbol{D}_i^{-1} \cdot \boldsymbol{n}} ds \tag{6.2}$$

- Extension of the microstructure evolution algorithm to 3D should be considered. The main issue with this is the computational expense of performing graph-cut evolution on 3D grids. This can be solved using adaptive grids that are refined only at the GBs where evolution occurs. Parallelization of the codes should also be considered.

6.2.4 Peridynamic Modeling of Microstructure Plasticity

In Chapter V, mechanical modeling of microstructures was performed using PD, taking advantage of voxel grids as directly generated by the MRF algorithm. The results are similar to FEM for small horizon sizes but can capture localization features when the horizon size increases. The significant advantage with the NOSBPD approach is that conventional continuum constitutive models can be used in formalism. We demonstrated implementation of conventional crystal plasticity models in this formalism including modeling of mechanisms such as twinning [274, 275, 276]. In the future work, the code can be extended to address problems such as capturing size effects in plasticity [277, 278] and fracture modeling [243]. a continuum damage model

can be added in the new CPPD model to captures fracture and failure at the microstructural scale. Past efforts have relied on various crack initiation criteria and crack path search algorithms for performing crack prediction in polycrystalline materials [279] while NOSB peridynamics presented in this work is expected to evolve the cracks naturally by including a simple damage evolution law such as Gurson model at macro-scale or energy based models at microstructural scales based on cohesive energies of facets and GBs.

APPENDICES

APPENDIX A

Saltykov Method for Quantification of 3D Grain Size Distribution

The Saltykov approximation method provides a closed-form expression for the 3D grain size distributions from 2D observations [280]. The primary assumption when using Saltykov is that the realized grains are approximately equiaxed/circular. As a result, when given a 2D equiaxed structure, as shown in Figure A.1(a), the Saltykov formula can be employed to unfold the 2D apparent grain-size distribution into the actual 3D PDF, denoted as $F(R)$. The derivation used here is based on Figure A.1(b), where $z = \sqrt{R^2 - r^2}$ corresponds to a random cut location across a sphere of radius R with r being its apparent 2D grain size. Since the probability of z follows a uniform distribution (i.e., $P(z) = \frac{1}{R}$), the probability of r can be computed in a closed-form by the change of variables, as follows:

$$P_r(r) = P(z)\left|\frac{dz}{dr}\right| = \frac{r}{R\sqrt{R^2 - r^2}} \tag{A.1}$$

Integrating Equation (A.1) leads to:

$$P(r_1 < r < r_2) = \int_{r_1}^{r_2} P_r(r)dr = \frac{1}{R}\left(\sqrt{R^2 - r_1^2} - \sqrt{R^2 - r_2^2}\right) \qquad \text{(A.2)}$$

where R corresponds to the 3D grain size; r_1 and r_2 are respectively the lower and upper limits of the interval for 2D grain size, and $P(r_1 < r < r_2)$ is the probability to cut the section within the defined interval.
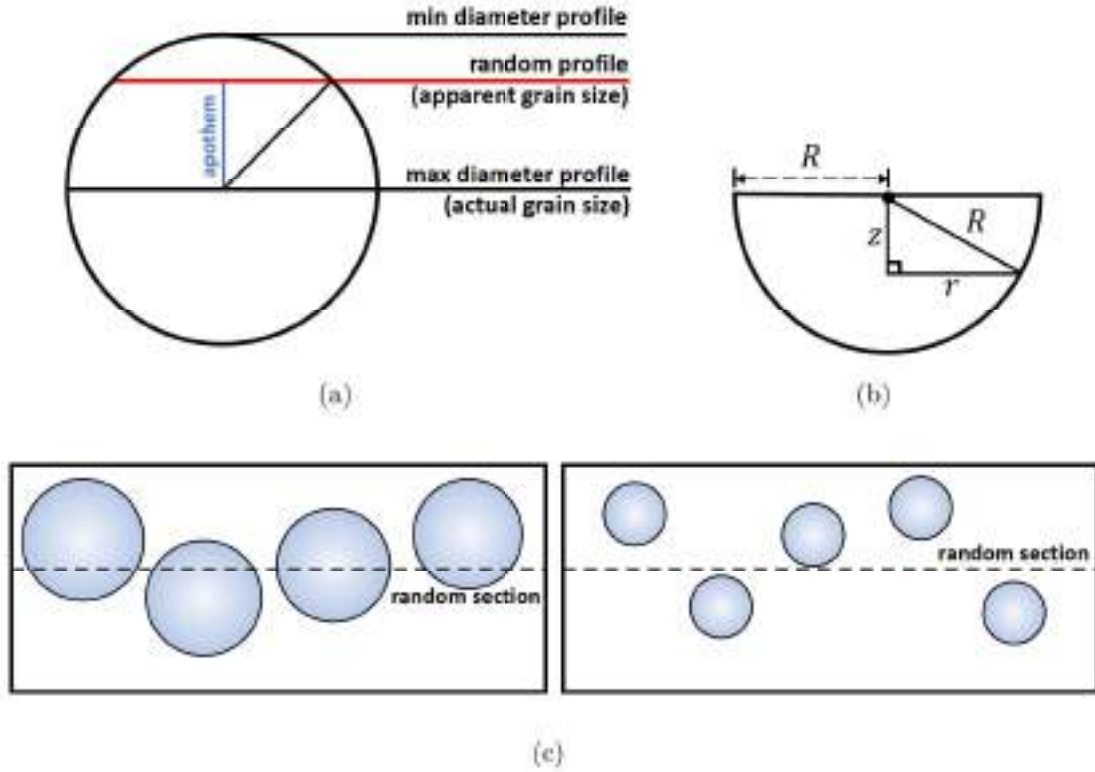
Figure A.1: *The schematic pertinent to the Saltykov closed-form approximation: (a) grains are assumed as spheres with a random section seen in the 2D image; (b) probability of a given 3D grain size R given its 2D section with radius r can be obtained by a change of variables; and (c) in the case where multiple 3D structures exist, the Saltykov estimate takes into account the probability that a plane can cut a sphere of radius R. Hence, the spheres of larger radii are more likely to intersect the section plane.*

Furthermore, the probability that a plane cuts a sphere of radius R is $2R$ (per unit length). The likelihood of cutting such spheres depends not only on their numbers but also on their sizes, since larger spheres are more likely to intersect a random section

plane, as shown in Figure A.1(c). Also, the likelihood of a sphere with a radius R in the unit volume is calculated to be $F(R)\Delta$. Here, Δ denotes the width of the bins used to quantify the grain size statistics and can be calculated as follows:

$$\Delta = \frac{R_{max} - R_{min}}{k} \tag{A.3}$$

where k equals the total number of bins in the grain size distribution plot.

Hence, the probability of a 2D section with radius r can be numerically approximated by taking the product of Equation (A.2) with $2RF(R)\Delta$ and by summing it over all the bins, as follows:

$$P(r_1 < r < r_2) = 2\Delta \sum_i \left(\sqrt{R_i^2 - r_1^2} - \sqrt{R_i^2 - r_2^2} \right) F(R_i) \tag{A.4}$$

As a result, Equation (A.4) can be inverted to obtain a closed-from approximation for quantification of 3D grain size distribution, $F(R)$, when 2D sectional observations are available.

APPENDIX B

Adaptive Dynamic Relaxation Scheme

In the absence of body forces, the equation of motion, as shown in Equation (5.3) can be rewritten in a vector form, as follows:

$$\ddot{\mathbf{u}}(\mathbf{x}, t) + c\dot{\mathbf{u}}(\mathbf{x}, t) = \mathbf{f}(\mathbf{u}, \mathbf{x}, t) \tag{B.1}$$

where c is a damping coefficient, and the force vector $\mathbf{f}$ is defined as $\mathbf{f}(\mathbf{u}, \mathbf{x}, t) = \mathbf{\Lambda}^{-1}\mathbf{L}(\mathbf{x}, t)$, in which $\mathbf{\Lambda}$ is a diagonal fictitious density matrix. Based on the adaptive dynamic relaxation method, the most desired density matrix and damping coefficient can be determined using Greschgorin's theorem and Rayleigh's quotient, respectively [281].

Let $\mathbf{u}^n$, $\dot{\mathbf{u}}^n$, $\ddot{\mathbf{u}}^n$, and $\mathbf{f}^n$ denote the displacement, velocity, acceleration, and force vector fields for a given material particle at $t = t_n$, respectively. In the central difference scheme, the velocity and acceleration vectors can be approximated as follows:

$$\dot{\mathbf{u}}^n \approx \frac{\mathbf{u}^{n+1} - \mathbf{u}^{n-1}}{2\Delta t} \tag{B.2}$$

$$\ddot{\mathbf{u}}^n \approx \frac{\mathbf{u}^{n+1} - 2\mathbf{u}^n + \mathbf{u}^{n-1}}{\Delta t^2} \tag{B.3}$$

where Δt refers to the incremental time step. Substituting Equations (B.2) and (B.3) into Equation (B.1), while rearranging the terms yields to an updated scheme for the displacement field:

$$\mathbf{u}^{n+1} = \frac{2\Delta t^2 \mathbf{f}^n + 4\mathbf{u}^n + (c\Delta t - 2)\mathbf{u}^{n-1}}{2 + c\Delta t} \tag{B.4}$$

Accordingly, Equation (B.5) is employed to estimate $\mathbf{u}^{-1}$ for initialization of the displacement update:

$$\mathbf{u}^{-1} = \mathbf{u}^0 - \Delta t \dot{\mathbf{u}}^0 + \frac{\Delta t^2}{2} \ddot{\mathbf{u}}^0 \tag{B.5}$$

where $\mathbf{u}^0$, $\dot{\mathbf{u}}^0$, and $\ddot{\mathbf{u}}^0$ are the initial displacement, velocity, and acceleration vectors, respectively. The velocity and acceleration vectors may subsequently be updated using Equations (B.2) and (B.3). With the assumption of a unit diagonal matrix $\boldsymbol{\Lambda}$, the time step Δt can be selected based on Greschgorin's theorem [281], as expressed in the following:

$$\Delta t \leq \sqrt{\frac{4\Lambda_{ii}}{\sum_j |K_{ij}|}} = \sqrt{\frac{4}{\sum_j |K_{ij}|}} = \sqrt{\frac{4}{||\mathbf{K}||_\infty}} \tag{B.6}$$

where Λ_{ii} represents the diagonal coefficients of the density matrix, $\mathbf{K}$ denotes the

stiffness matrix of the system, and $|| \cdot ||_\infty$ denotes the vector-induced matrix ∞ norm. Since the stiffness matrix K_{ij} is not explicitly computed, another approximation scheme can be applied for the computation of time step size. An appropriate value of Δt for the 1D PD model is based on the wave speed, denoted as c_s, using the Courant-Friedrichs-Lewy (CFL) condition [265]:

$$\Delta t \leq \frac{2\Delta x}{c_s} \tag{B.7}$$

where Δx represents the minimal grid size, or the minimal bond length in PD modeling. In higher-dimensional problems however, the CFL condition becomes stringent. For an n-dimensional problem with a uniform grid, the critical Δt may be estimated as:

$$\Delta t \leq \frac{2\Delta x}{n} \sqrt{\frac{\rho}{E_{max}}} \tag{B.8}$$

where E_{max} is the largest eigenvalue of the elastic stiffness matrix. It is worth noting that the CFL condition in Equation (B.8) can be conservative since the derivation is based solely on the nearest neighbors [263].

Next, the damping ratio, c, is selected based on the lowest frequency of the system using Rayleigh's quotient [281]:

$$c^n = 2\sqrt{\frac{(\mathbf{u}^n)^{\mathrm{T}}\mathbf{k}^n\mathbf{u}^n}{(\mathbf{u}^n)^{\mathrm{T}}\mathbf{u}^n}} \tag{B.9}$$

where $\mathbf{k}^n$ is a diagonal local stiffness matrix given by:

$$k_{ii}^n = -\frac{1}{\Lambda_{ii}} \frac{f_i^n - f_i^{n-1}}{u_i^n - u_i^{n-1}} = -\frac{f_i^n - f_i^{n-1}}{u_i^n - u_i^{n-1}} \qquad \text{(B.10)}$$

Here, f_i^n is the ith component of the force vector $\mathbf{f}$, at time $t = t_n$. Since the local stiffness matrix calculation involves division by the difference of displacements in consecutive time steps, it is plausible to encounter a division by zero. Accordingly, the local stiffness k_{ii}^n is set to zero, when the difference between displacement fields vanishes. Finally, a guess damping ratio, c_0, can be chosen to start the computation.

APPENDIX C

Crystal Plasticity Constitutive Update Scheme

All quantities below are described relative to the undeformed (also known as reference) configuration, and quantities at the current time step are denoted by subscript $(n + 1)$. Given the deformation gradient $\mathbf{F}_{n+1}$, the update procedure below numerically computes the PK-I stress (numerically converged) $\mathbf{P} = \mathcal{F}(\mathbf{F}_{n+1})$, where the operator $\mathcal{F}$ denotes the constitutive model. Implicit time integration scheme of Equation (5.30) results in the following approximation with the additional assumption that $\Delta\gamma \ll 1$[1]:

$$\mathbf{F}^{\mathrm{p}} = \exp\Big(\Delta t \sum_{\alpha} \dot{\gamma}^{\alpha} \mathbf{S}_0^{\alpha} \mathrm{sign}(\tau^{\alpha})\Big)\mathbf{F}^{\mathrm{p}}{}_n \approx \Big(\mathbf{I} + \sum_{\alpha} \Delta\gamma^{\alpha} \mathbf{S}_0^{\alpha} \mathrm{sign}(\tau^{\alpha})\Big)\mathbf{F}^{\mathrm{p}}{}_n \qquad \text{(C.1)}$$

where $\Delta\gamma^{\alpha} = \dot{\gamma}^{\alpha}\Delta t$. Substituting Equation (C.1) into the multiplicative decomposition relation $\mathbf{F} = \mathbf{F}^{\mathrm{e}}\mathbf{F}^{\mathrm{p}}$ and rearranging terms yields:

$$\mathbf{F}^{\mathrm{e}} = \mathbf{F}^{\mathrm{e}}{}_{\mathrm{trial}}\Big(\mathbf{I} - \sum_{\alpha} \Delta\gamma^{\alpha} \mathbf{S}_0^{\alpha} \mathrm{sign}(\tau^{\alpha})\Big) \qquad \text{(C.2)}$$

---

[1]This assumption will be invoked through the rest of the calculations so as to obtain linear approximations whenever necessary.

where $\mathbf{F}^e{}_{\text{trial}} = \mathbf{F}_{n+1}\mathbf{F}^p{}_n^{-1}$ is the trial elastic deformation gradient. The initial condition $\mathbf{F}^p(0) = \mathbf{I}$ signifies that the reference configuration is plastically undeformed. The Green-Lagrange elastic strain measure computed using Equation (C.2) then takes the form:

$$\bar{\mathbf{E}}^e = \frac{1}{2}\left(\mathbf{F}^{e\mathrm{T}}\mathbf{F}^e - \mathbf{I}\right) = \bar{\mathbf{E}}^e_{\text{trial}} - \frac{1}{2}\sum_\alpha \Delta\gamma^\alpha \mathbf{B}^\alpha \text{sign}(\tau^\alpha) \tag{C.3}$$

where $\bar{\mathbf{E}}^e_{\text{trial}}$ and $\mathbf{B}^\alpha$ are defined as:

$$\bar{\mathbf{E}}^e_{\text{trial}} = \frac{1}{2}\left((\mathbf{F}^e{}_{\text{trial}})^{\mathrm{T}}\mathbf{F}^e{}_{\text{trial}} - \mathbf{I}\right), \tag{C.4}$$

$$\mathbf{B}^\alpha = (\mathbf{S}_0^\alpha)^{\mathrm{T}}(\mathbf{F}^e{}_{\text{trial}})^{\mathrm{T}}\mathbf{F}^e{}_{\text{trial}} + (\mathbf{F}^e{}_{\text{trial}})^{\mathrm{T}}\mathbf{F}^e{}_{\text{trial}}\mathbf{S}_0^\alpha \tag{C.5}$$

Using Equation (C.3) the intermediate stress $\bar{\mathbf{T}} = \mathcal{L}^e \cdot \bar{\mathbf{E}}^e$ takes the form:

$$\bar{\mathbf{T}} = \bar{\mathbf{T}}_{\text{trial}} - \frac{1}{2}\sum_\alpha \Delta\gamma^\alpha \mathcal{L}^e \cdot \mathbf{B}^\alpha \text{sign}(\tau^\alpha_{\text{trial}}) \tag{C.6}$$

where $\bar{\mathbf{T}}_{\text{trial}} = \mathcal{L}^e \cdot \bar{\mathbf{E}}^e_{\text{trial}}$.

A trial resolved shear stress $\tau^\alpha_{\text{trial}} = \bar{\mathbf{T}}_{\text{trial}} : \mathbf{S}_0^\alpha$ is then computed so that potentially active set of slip systems (denoted as $\mathcal{PA}$) may be identified based on the criterion that $|\tau^\alpha_{\text{trial}}| - s^\alpha > 0$. The active systems (for which $\dot{\gamma}^\alpha > 0$) are assumed to follow the Kuhn-Tucker consistency condition: $|\tau^\alpha| = s^\alpha$. Substituting Equation (C.6) into the consistency yields:

$$|\tau^\alpha| = s^\alpha \implies |\tau^\alpha_{\text{trial}}| - \frac{1}{2}\text{sign}(\tau^\alpha_{\text{trial}})\left(\sum_\beta \Delta\gamma^\beta \mathcal{L}^e \cdot \mathbf{B}^\beta \text{sign}(\tau^\beta_{\text{trial}})\right) : \mathbf{S}^\alpha_0 = s^\alpha_n + \sum_\beta h^{\alpha\beta}(s^\beta)\Delta\gamma^\beta$$

$$\implies \left(h^{\alpha\beta} + \frac{1}{2}\text{sign}(\tau^\alpha_{\text{trial}})\text{sign}(\tau^\beta_{\text{trial}})\left(\mathcal{L}^e \cdot \mathbf{B}^\beta\right) : \mathbf{S}^\alpha_0\right)\Delta\gamma^\beta = |\tau^\alpha_{\text{trial}}| - s^\alpha$$

where $\alpha, \beta \in \mathcal{PA}$ and it is assumed that $\text{sign}(\tau^\alpha) = \text{sign}(\tau^\alpha_{\text{trial}})$. When the consistency conditions are written out for all the potentially active slip systems, the following linear system can be obtained:

$$\sum_{\beta \in \mathcal{PA}} A^{\alpha\beta}\Delta\gamma^\beta = b^\alpha \tag{C.7}$$

where

$$A^{\alpha\beta} = h^{\alpha\beta} + \frac{1}{2}\text{sign}(\tau^\alpha_{\text{trial}})\text{sign}(\tau^\beta_{\text{trial}})\left(\mathcal{L}^e \cdot \mathbf{B}^\beta\right) : \mathbf{S}^\alpha_0,$$

$$b^\alpha = |\tau^\alpha_{\text{trial}}| - s^\alpha \tag{C.8}$$

Once the linear system is solved, a consistency check is performed to determine whether the potentially active systems are active, i.e., if $\Delta\gamma^\beta \geq 0$; $\forall \beta \in \mathcal{PA}$. Any system which fails consistency is removed from the set of potentially active systems. The entire procedure is repeated until $\Delta\gamma^\beta > 0$; $\forall \beta \in \mathcal{PA}$ at which point the potentially active slip systems are indeed active.

BIBLIOGRAPHY

BIBLIOGRAPHY

[1] National-Research-Council. *Integrated computational materials engineering: a transformational discipline for improved competitiveness and national security.* National Academies Press, 2008.

[2] Wei Xu, Edward W. Lui, Aaron Pateras, Ma Qian, and Milan Brandt. In situ tailoring microstructure in additively manufactured Ti-6Al-4V for superior mechanical performance. *Acta Materialia*, 125:390–400, 2017.

[3] Patrick Köhnen, Maike Letang, Maximilian Voshage, Johannes H. Schleifenbaum, and Christian Haase. Understanding the process-microstructure correlations for tailoring the mechanical properties of L-PBF produced austenitic advanced high strength steel. *Additive Manufacturing*, 30:100914, 2019.

[4] Carolin Körner, Harald Helmer, Andreas Bauereiß, and Robert F Singer. Tailoring the grain structure of IN718 during selective electron beam melting. In *MATEC Web of Conferences*, volume 14, page 08001. EDP Sciences, 2014.

[5] Tomasz Kurzynowski, Konrad Gruber, Wojciech Stopyra, Bogumiła Kuźnicka, and Edward Chlebus. Correlation between process parameters, microstructure and properties of 316L stainless steel processed by selective laser melting. *Materials Science and Engineering: A*, 718:64–73, 2018.

[6] Narendran Raghavan, Ryan Dehoff, Sreekanth Pannala, Srdjan Simunovic, Michael Kirka, John Turner, Neil Carlson, and Sudarsanam S. Babu. Numerical modeling of heat-transfer and the influence of process parameters on tailoring the grain morphology of IN718 in electron beam additive manufacturing. *Acta Materialia*, 112:303–314, 2016.

[7] Theofilos Gatsos, Karim A. Elsayed, Yuwei Zhai, and Diana A. Lados. Review on computational modeling of process–microstructure–property relationships in metal additive manufacturing. *JOM*, 72(1):403–419, 2020.

[8] Wentao Yan, Stephen Lin, Orion L. Kafka, Yanping Lian, Cheng Yu, Zeliang Liu, Jinhui Yan, Sarah Wolff, Hao Wu, Ebot Ndip-Agbor, et al. Data-driven multi-scale multi-physics models to derive process–structure–property relationships for additive manufacturing. *Computational Mechanics*, 61(5):521–541, 2018.

[9] Patrick I. O'Toole, Milan J. Patel, Chao Tang, Dayalan Gunasegaram, Anthony B. Murphy, and Ivan S. Cole. Multiscale simulation of rapid solidification of an aluminium-silicon alloy under additive manufacturing conditions. *Additive Manufacturing*, page 102353, 2021.

[10] Gurmeet Singh, Anthony M. Waas, and Veera Sundararaghavan. Understanding defect structures in nanoscale metal additive manufacturing via molecular dynamics. *Computational Materials Science*, 200:110807, 2021.

[11] Bob Baoping He. Introduction to two-dimensional X-ray diffraction. *Powder Diffraction*, 18(2):71–85, 2003.

[12] Pavel Krakhmalev, Gunnel Fredriksson, Krister Svensson, Igor Yadroitsev, Ina Yadroitsava, Mattias Thuvander, and Ru Peng. Microstructure, solidification texture, and thermal stability of 316L stainless steel manufactured by laser powder-bed fusion. *Metals*, 8(8):643, 2018.

[13] Qiang Zhang, Jing Chen, Pengfei Guo, Hua Tan, Xin Lin, and Weidong Huang. Texture and microstructure characterization in laser additive manufactured Ti-6Al-2Zr-2Sn-3Mo-1.5Cr-2Nb titanium alloy. *Materials & Design*, 88:550–557, 2015.

[14] Hong Qin, Vahid Fallah, Qingshan Dong, Mathieu Brochu, Mark R. Daymond, and Mark Gallerneault. Solidification pattern, microstructure and texture development in laser powder-bed fusion (LPBF) of Al10SiMg alloy. *Materials Characterization*, 145:29–38, 2018.

[15] Michael A. Groeber, B. K. Haley, Michael D. Uchic, Dennis M. Dimiduk, and Somnath Ghosh. 3D reconstruction and characterization of polycrystalline microstructures using a FIB-SEM system. *Materials Characterization*, 57(4-5):259–273, 2006.

[16] Robert T. DeHoff. Quantitative serial sectioning analysis: Preview. *Journal of Microscopy*, 131(3):259–263, 1983.

[17] George Spanos. Foreword: Scripta materialia viewpoint set on 3D characterization and analysis of materials. *Scripta Materialia*, 1(55):3, 2006.

[18] Dorte Juul Jensen. *Three-Dimensional Orientation Imaging*, pages 91–104. Springer US, Boston, MA, 2000.

[19] Dunyong Deng, Ru Lin Peng, Håkan Brodin, and Johan Moverare. Microstructure and mechanical properties of Inconel 718 produced by selective laser melting: Sample orientation dependence and effects of post heat treatments. *Materials Science and Engineering: A*, 713:294–306, 2018.

[20] Sriram Ganesan, Iman Javaheri, and Veera Sundararaghavan. Constrained Voronoi models for interpreting surface microstructural measurements. *Mechanics of Materials*, page 103892, 2021.

[21] Aaditya Lakshmanan, Jiangyi Luo, Iman Javaheri, and Veera Sundararaghavan. Three-dimensional crystal plasticity simulations using peridynamics theory and experimental comparison. *International Journal of Plasticity*, 142:102991, 2021.

[22] Joseph E. Bishop, John M. Emery, Corbett C. Battaile, David J. Littlewood, and Andrew J. Baines. Direct numerical simulations in solid mechanics for quantifying the macroscale effects of microstructure and material model-form error. *JOM*, 68(5):1427–1445, 2016.

[23] Gene E. Ice and Bennett C. Larson. Three-dimensional X-ray structural microscopy using polychromatic microbeams. *MRS Bulletin*, 29(3):170–176, 2004.

[24] Michael Groeber, Somnath Ghosh, Michael D. Uchic, and Dennis M. Dimiduk. A framework for automated analysis and simulation of 3D polycrystalline microstructures.: Part 1: Statistical characterization. *Acta Materialia*, 56(6):1257–1273, 2008.

[25] Michael Groeber, Somnath Ghosh, Michael D. Uchic, and Dennis M. Dimiduk. A framework for automated analysis and simulation of 3D polycrystalline microstructures.: Part 2: Synthetic structure generation. *Acta Materialia*, 56(6):1274–1287, 2008.

[26] Ilke Arslan, Emmanuelle A. Marquis, Mark Homer, Michelle A. Hekmaty, and Norman C. Bartelt. Towards better 3-D reconstructions by combining electron tomography and atom-probe tomography. *Ultramicroscopy*, 108(12):1579–1585, 2008.

[27] Singanallur V. Venkatakrishnan, Lawrence F. Drummy, Michael Jackson, Marc De Graef, Jeff Simmons, and Charles A. Bouman. Model-based iterative reconstruction for bright-field electron tomography. *IEEE Transactions on Computational Imaging*, 1(1):1–15, 2014.

[28] John W. Gibbs, K. Aditya Mohan, E. Begum Gulsoy, Ashwin J. Shahani, Xianghui Xiao, Charles A. Bouman, Marc. De Graef, and Peter W. Voorhees. The three-dimensional morphology of growing dendrites. *Scientific Reports*, 5(1):1–9, 2015.

[29] David M. Saylor, Joseph Fridy, Bassem S. El-Dasher, Kee-Young Jung, and Anthony D. Rollett. Statistically representative three-dimensional microstructures based on orthogonal observation sections. *Metallurgical and Materials Transactions A*, 35(7):1969–1979, 2004.

[30] David J. Rowenhorst, A. Gupta, Chia R. Feng, and George Spanos. 3D crystallographic and morphological analysis of coarse martensite: Combining EBSD and serial sectioning. *Scripta Materialia*, 55(1):11–16, 2006.

[31] Jonathan E. Spowart. Automated serial sectioning for 3-D analysis of microstructures. *Scripta Materialia*, 55(1):5–10, 2006.

[32] David J. Rowenhorst, Lily Nguyen, Aeriel D. Murphy-Leonard, and Richard W. Fonda. Characterization of microstructure in additively manufactured 316L using automated serial sectioning. *Current Opinion in Solid State & Materials Science*, 24(3):100819, 2020.

[33] Henning F. Poulsen, Dorte Juul Jensen, and Gavin B. M. Vaughan. Three-dimensional X-ray diffraction microscopy using high-energy X-rays. *MRS Bulletin*, 29(3):166–169, 2004.

[34] Jean-Yves Buffiere, Emilie Ferrie, Henry Proudhon, and Wolfgang Ludwig. Three-dimensional visualisation of fatigue cracks in metals using high resolution synchrotron X-ray micro-tomography. *Materials Science and Technology*, 22(9):1019–1024, 2006.

[35] Eric Maire and Philip John Withers. Quantitative X-ray tomography. *International Materials Reviews*, 59(1):1–43, 2014.

[36] Samuel A. McDonald, P. Reischig, Christian Holzner, Erik M. Lauridsen, Philip J. Withers, Arno P. Merkle, and Michael Feser. Non-destructive mapping of grain orientations in 3D by laboratory X-ray microscopy. *Scientific Reports*, 5:14665, 2015.

[37] Ulrich Lienert, Shiu F. Li, Christopher M. Hefferan, Jonathan Lind, Robert M. Suter, Joel V. Bernier, Nathan R. Barton, Matthew C. Brandes, Michael J. Mills, Matthew P. Miller, B. Jakobsen, and Wolfgang Pantleon. High-energy diffraction microscopy at the advanced photon source. *JOM*, 63(7):70–77, Jul 2011.

[38] Donald W. Brown, Levente Balogh, Darrin Byler, Chris M. Hefferan, James F. Hunter, Peter Kenesei, Shiu Fai Li, John Lind, Stephen R. Niezgoda, and Robert M. Suter. Demonstration of near field high energy X-ray diffraction microscopy on high-z ceramic nuclear fuel material. In *Mechanical Stress Evaluation by Neutrons and Synchrotron Radiation VII*, volume 777 of *Materials Science Forum*, pages 112–117. Trans Tech Publications, 4 2014.

[39] John F. Bingert, Robert M. Suter, Jonathan Lind, Shiu Fai Li, Reeju Pokharel, and Carl P. Trujillo. High-energy diffraction microscopy characterization of spall damage. In *Dynamic Behavior of Materials, Volume 1*, pages 397–403. Springer, 2014.

[40] Philip Eisenlohr, Pratheek Shanthraj, Brendan R. Vande Kieft, Thomas R. Bieler, Wenjun Liu, and Ruqing Xu. Subsurface grain morphology reconstruction by differential aperture X-ray microscopy. *JOM*, 69(6):1100–1105, 2017.

[41] Reeju Pokharel. Overview of high-energy X-ray diffraction microscopy (HEDM) for mesoscale material characterization in three-dimensions. In *Materials Discovery and Design*, pages 167–201. Springer, 2018.

[42] Jiwoong Kang, Ning Lu, Issac Loo, Nancy Senabulya, and Ashwin J. Shahani. Polyproc: A modular processing pipeline for X-ray diffraction tomography. *Integrating Materials and Manufacturing Innovation*, 8(3):388–399, 2019.

[43] Jette Oddershede, Jun Sun, Nicolas Gueninchault, Florian Bachmann, Hrishikesh Bale, Christian Holzner, and Erik Lauridsen. Non-destructive characterization of polycrystalline materials in 3D by laboratory diffraction contrast tomography. *Integrating Materials and Manufacturing Innovation*, 8(2):217–225, 2019.

[44] Joel V. Bernier, Robert M. Suter, Anthony D. Rollett, and Jonathan D. Almer. High-energy X-ray diffraction microscopy in materials science. *Annual Review of Materials Science*, 50:395–436, 2020.

[45] Ramin Bostanabad, Wei Chen, and Daniel W. Apley. Characterization and reconstruction of 3D stochastic microstructures via supervised learning. *Journal of Microscopy*, 264(3):282–297, 2016.

[46] Ramin Bostanabad, Anh Tuan Bui, Wei Xie, Daniel W. Apley, and Wei Chen. Stochastic microstructure characterization and reconstruction via supervised learning. *Acta Materialia*, 103:89–102, 2016.

[47] Romain Quey and Loïc Renversade. Optimal polyhedral description of 3D polycrystals: Method and application to statistical and synchrotron X-ray diffraction data. *Computer Methods in Applied Mechanics and Engineering*, 330:308–333, 2018.

[48] Shaohua Chen, Antony Kirubanandham, Nikhilesh Chawla, and Yang Jiao. Stochastic multi-scale reconstruction of 3D microstructure consisting of polycrystalline grains and second-phase particles from 2D micrographs. *Metallurgical and Materials Transactions A*, 47(3):1440–1450, 2016.

[49] Akbar Bagri, George Weber, Jean-Charles Stinville, William Lenthe, Tresa Pollock, Christopher Woodward, and Somnath Ghosh. Microstructure and property-based statistically equivalent representative volume elements for polycrystalline ni-based superalloys containing annealing twins. *Metallurgical and Materials Transactions A*, 49(11):5727–5744, 2018.

[50] Tristan N. Ashton, Donna Post Guillen, and William H. Harris. An algorithm to generate synthetic 3D microstructures from 2D exemplars. *JOM*, 72(1):65–74, 2020.

[51] Swantje Bargmann, Benjamin Klusemann, Jürgen Markmann, Jan Eike Schnabel, Konrad Schneider, Celal Soyarslan, and Jana Wilmers. Generation of 3D representative volume elements for heterogeneous materials: A review. *Progress in Materials Science*, 96:322–384, 2018.

[52] Romain Quey, Paul R. Dawson, and Fabrice Barbe. Large-scale 3D random polycrystals for the finite element method: Generation, meshing and remeshing. *Computer Methods in Applied Mechanics and Engineering*, 200(17-20):1729–1745, 2011.

[53] Abhijit P. Brahme, Mohammed H. Alvi, David M. Saylor, Joseph M. Fridy, and Anthony D. Rollett. 3D reconstruction of microstructure in a commercial purity aluminum. *Scripta Materialia*, 55(1):75–80, 2006.

[54] Atsuyuki Okabe. Spatial tessellations. *International Encyclopedia of Geography: People, the Earth, Environment and Technology: People, the Earth, Environment and Technology*, pages 1–11, 2016.

[55] David G. Evans and Steven M. Jones. Detecting Voronoi (area-of-influence) polygons. *Mathematical geology*, 19:523–537, 1987.

[56] Keshi S. Zhang, Mao S. Wu, and Ruqiang Feng. Simulation of microplasticity-induced deformation in uniaxially strained ceramics by 3-D Voronoi polycrystal modeling. *International journal of plasticity*, 21(4):801–834, 2005.

[57] Ricardo A. Lebensohn, Olivier Castelnau, Rénald Brenner, and Pierre Gilormini. Study of the antiplane deformation of linear 2-D polycrystals with different microstructures. *International journal of solids and structures*, 42(20):5441–5459, 2005.

[58] Osamu Watanabe, Hussein M. Zbib, and Eiji Takenouchi. Crystal plasticity: micro-shear banding in polycrystals using Voronoi tessellation. *International Journal of Plasticity*, 14(8):771–788, 1998.

[59] David J. Heeger and James R. Bergen. Pyramid-based texture analysis/synthesis. In *Proceedings of the 22nd Annual Conference on Computer Graphics and Interactive Techniques*, pages 229–238. Citeseer, 1995.

[60] Jeremy S. De Bonet. Multiresolution sampling procedure for analysis and synthesis of texture images. In *Proceedings of the 24th Annual Conference on Computer Graphics and Interactive Techniques*, pages 361–368, 1997.

[61] Eero P. Simoncelli and Javier Portilla. Texture characterization via joint statistics of wavelet coefficient magnitudes. In *Proc 5th IEEE International Conference on Image Processing*, volume 1, 1998.

[62] Veera Sundararaghavan and Nicholas Zabaras. Classification and reconstruction of three-dimensional microstructures using support vector machines. *Computational Materials Science*, 32(2):223–239, 2005.

[63] Salvatore Torquato. *Random heterogeneous materials: Microstructure and macroscopic properties*, volume 16. Springer Science & Business Media, 2013.

[64] Christofer L. Y. Yeong and Salvatore Torquato. Reconstructing random media. *Physical Review E*, 57(1):495, 1998.

[65] Yang Jiao, Eric Padilla, and Nikhilesh Chawla. Modeling and predicting microstructure evolution in lead/tin alloy via correlation functions and stochastic material reconstruction. *Acta Materialia*, 61(9):3370–3377, 2013.

[66] David T. Fullwood, Stephen R. Niezgoda, and Surya R. Kalidindi. Microstructure reconstructions from 2-point statistics using phase-recovery algorithms. *Acta Materialia*, 56(5):942–948, 2008.

[67] Hongyi Xu, Dmitriy A. Dikin, Craig Burkhart, and Wei Chen. Descriptor-based methodology for statistical characterization and 3D reconstruction of microstructural materials. *Computational Materials Science*, 85:206–216, 2014.

[68] Celal Soyarslan, Swantje Bargmann, Marc Pradas, and Jörg Weissmüller. 3D stochastic bicontinuous microstructures: Generation, topology and elasticity. *Acta Materialia*, 149:326–340, 2018.

[69] Anthony D. Rollett, David Saylor, Joseph M. Fridy, B. S. El-Dasher, Abhijit Brahme, Sukbin Lee, C. Cornwell, and R. Noack. Modeling polycrystalline microstructures in 3D. In *AIP Conference Proceedings*, volume 712, pages 71–77. AIP, 2004.

[70] Anthony D. Rollett, Sukbin Lee, R. Campman, and G. S. Rohrer. Three-dimensional characterization of microstructure by electron back-scatter diffraction. *Annual Review of Materials Research*, 37:627–658, 2007.

[71] Michael A. Groeber and Michael A. Jackson. DREAM.3D: A digital representation environment for the analysis of microstructure in 3D. *Integrating Materials and Manufacturing Innovation*, 3(1):56–72, 2014.

[72] Xiaohui Tu, Ahmad Shahba, Jinlei Shen, and Somnath Ghosh. Microstructure and property based statistically equivalent RVEs for polycrystalline-polyphase aluminum alloys. *International Journal of Plasticity*, 115:268–292, 2019.

[73] Simone Falco, Jiawei Jiang, Francesco De Cola, and Nik Petrinic. Generation of 3D polycrystalline microstructures with a conditioned Laguerre-Voronoi tessellation technique. *Computational Materials Science*, 136:20–28, 2017.

[74] Tarasankar DebRoy, Huiliang Wei, J. S. Zuback, Tuhin Mukherjee, John W. Elmer, John O. Milewski, Allison M. Beese, Alexander E. Wilson-Heid, Amitava De, and Wei Zhang. Additive manufacturing of metallic components–process, structure and properties. *Progress in Materials Science*, 92:112–224, 2018.

[75] Ramin Bostanabad, Yichi Zhang, Xiaolin Li, Tucker Kearney, L. Catherine Brinson, Daniel W. Apley, Wing Kam Liu, and Wei Chen. Computational microstructure characterization and reconstruction: Review of the state-of-the-art techniques. *Progress in Materials Science*, 95:1–41, 2018.

[76] David T. Fullwood, Stephen R. Niezgoda, Brent L. Adams, and Surya R. Kalidindi. Microstructure sensitive design for performance optimization. *Progress in Materials Science*, 55(6):477–562, 2010.

[77] Veera Sundararaghavan. Reconstruction of three-dimensional anisotropic microstructures from two-dimensional micrographs imaged on orthogonal planes. *Integrating Materials and Manufacturing Innovation*, 3(1):19, 2014.

[78] Abhishek Kumar, Lily Nguyen, Marc De Graef, and Veera Sundararaghavan. A Markov random field approach for microstructure synthesis. *Modelling and Simulation in Materials Science and Engineering*, 24(3):035015, 2016.

[79] Xingchen Liu and Vadim Shapiro. Random heterogeneous materials via texture synthesis. *Computational Materials Science*, 99:177–189, 2015.

[80] David M. Turner and Surya R. Kalidindi. Statistical construction of 3-D microstructures from 2-D exemplars collected on oblique sections. *Acta Materialia*, 102:136–148, 2016.

[81] Kris Popat and Rosalind W. Picard. Novel cluster-based probability model for texture synthesis, classification, and compression. In *Visual Communications and Image Processing'93*, volume 2094, pages 756–768. SPIE, 1993.

[82] Rupert Paget and I. Dennis Longstaff. Texture synthesis via a noncausal nonparametric multiscale markov random field. *IEEE transactions on image processing*, 7(6):925–931, 1998.

[83] Song Chun Zhu, Yingnian Wu, and David Mumford. Filters, random fields and maximum entropy (Frame): towards a unified theory for texture modeling. *International Journal Computer Vision*, 27(2):107–126, 1998.

[84] Ernst Ising. *Beitrag zur theorie des ferro-und paramagnetismus.* PhD thesis, Grefe & Tiedemann, 1924.

[85] Mircea Grigoriu. Nearest neighbor probabilistic model for aluminum polycrystals. *Journal of engineering mechanics*, 136(7):821–829, 2010.

[86] Salvatore Torquato and Henry W. Haslach Jr. Random heterogeneous materials: Microstructure and macroscopic properties. *Appl. Mech. Rev.*, 55(4):B62–B63, 2002.

[87] Alexei A. Efros and Thomas K. Leung. Texture synthesis by non-parametric sampling. In *Proceedings of the 7th IEEE International Conference on Computer Vision*, volume 2, pages 1033–1038. IEEE, 1999.

[88] Vivek Kwatra, Irfan Essa, Aaron Bobick, and Nipun Kwatra. Texture optimization for example-based synthesis. In *ACM Transactions on Graphics*, volume 24, pages 795–802. ACM, 2005.

[89] Johannes Kopf, Chi-Wing Fu, Daniel Cohen-Or, Oliver Deussen, Dani Lischinski, and Tien-Tsin Wong. Solid texture synthesis from 2D exemplars. In *ACM Transactions on Graphics*, volume 26, page 2. ACM, 2007.

[90] Pinar Acar and Veera Sundararaghavan. A Markov random field approach for modeling spatio-temporal evolution of microstructures. *Modelling and Simulation in Materials Science and Engineering*, 24(7):075005, 2016.

[91] Arulmurugan Senthilnathan, Pınar Acar, and Marc De Graef. Markov random field based microstructure reconstruction using the principal image moments. *Materials Characterization*, page 111281, 2021.

[92] Iman Javaheri and Veera Sundararaghavan. Polycrystalline microstructure reconstruction using Markov random fields and histogram matching. *Computer-Aided Design*, 120:102806, 2020.

[93] Iman Javaheri, Mohsen Taheri Andani, and Veera Sundararaghavan. Large-scale synthesis of metal additively-manufactured microstructures using Markov random fields. *Computational Materials Science*, 206:111228, 2022.

[94] Claude Elwood Shannon. A mathematical theory of communication. *The Bell system technical journal*, 27(3):379–423, 1948.

[95] Julian Keilson. Markov chain models–rarity and exponentiality. Technical report, California University Berkeley Operations Research Center, 1974.

[96] Julian Besag. Spatial interaction and the statistical analysis of lattice systems. *Journal of the Royal Statistical Society: Series B (Methodological)*, 36(2):192–225, 1974.

[97] Jeff Simmons, Craig Przybyla, Stephen Bricker, Dae Woo Kim, and Mary Comer. Physics of MRF regularization for segmentation of materials microstructure images. In *2014 IEEE International Conference on Image Processing (ICIP)*, pages 4882–4886. IEEE, 2014.

[98] Stan Z. Li. *Markov random field modeling in computer vision*. Springer Science & Business Media, 2012.

[99] N.J. Wittridge and Robert D. Knutsen. A microtexture based analysis of the surface roughening behaviour of an aluminium alloy during tensile deformation. *Materials Science and Engineering: A*, 269(1-2):205–216, 1999.

[100] Carl E. Krill and Longqing Chen. Computer simulation of 3-D grain growth using a phase-field model. *Acta Materialia*, 50(12):3059–3075, 2002.

[101] Trevor Keller, Greta Lindwall, Supriyo Ghosh, Li Ma, Brandon M. Lane, Fan Zhang, Ursula R. Kattner, Eric A. Lass, Jarred C. Heigel, Yaakov Idell, et al. Application of finite element, phase-field, and CALPHAD-based methods to additive manufacturing of Ni-based superalloys. *Acta Materialia*, 139:244–253, 2017.

[102] Supriyo Ghosh, Li Ma, Nana Ofori-Opoku, and Jonathan E. Guyer. On the primary spacing and microsegregation of cellular dendrites in laser deposited Ni-Nb alloys. *Modelling and Simulation in Materials Science and Engineering*, 25(6):065002, 2017.

[103] Elizabeth A. Holm, Mark A. Miodownik, and Anthony D. Rollett. On abnormal subgrain growth and the origin of recrystallization nuclei. *Acta Materialia*, 51(9):2701–2716, 2003.

[104] Theron M. Rodgers, Jonathan D. Madison, and Veena Tikare. Simulation of metal additive manufacturing microstructures using kinetic Monte Carlo. *Computational Materials Science*, 135:78–89, 2017.

[105] Theron M. Rodgers, Daniel Moser, Fadi Abdeljawad, Olivia D. Underwood Jackson, Jay D. Carroll, Bradley H. Jared, Dan S. Bolintineanu, John A. Mitchell, and Jonathan D. Madison. Simulation of powder-bed metal additive manufacturing microstructures with coupled finite difference-Monte Carlo method. *Additive Manufacturing*, 41:101953, 2021.

[106] A. Zinoviev, O. Zinovieva, V. Ploshikhin, V. Romanova, and R. Balokhonov. Evolution of grain structure during laser additive manufacturing. simulation by a cellular automata method. *Materials & Design*, 106:321–329, 2016.

[107] Javed Akram, Pradeep Chalavadi, Deepankar Pal, and Brent Stucker. Understanding grain evolution in additive manufacturing through modeling. *Additive Manufacturing*, 21:255–268, 2018.

[108] Amir Reza Ansari Dezfoli, Weng-Sing Hwang, Wei-Chin Huang, and Tsung-Wen Tsai. Determination and controlling of grain structure of metals after laser incidence: Theoretical approach. *Scientific Reports*, 7:41527, 2017.

[109] Eisuke Miyoshi, Tomohiro Takaki, Munekazu Ohno, Yasushi Shibuta, Shinji Sakane, and Takayuki Aoki. Large-scale phase-field simulation of three-dimensional isotropic grain growth in polycrystalline thin films. *Modelling and Simulation in Materials Science and Engineering*, 27(5):054003, 2019.

[110] Shoujin Sun, Milan Brandt, and Mjlam Easton. Powder-bed fusion processes: An overview. *Laser Additive Manufacturing*, pages 55–77, 2017.

[111] Ranadip Acharya, John A. Sharon, and Alexander Staroselsky. Prediction of microstructure in laser powder-bed fusion process. *Acta Materialia*, 124:360–371, 2017.

[112] Austin T. Sutton, Caitlin S. Kriewall, Ming C. Leu, and Joseph W. Newkirk. Powder characterisation techniques and effects of powder characteristics on part properties in powder-bed fusion processes. *Virtual and Physical Prototyping*, 12(1):3–29, 2017.

[113] Mousa Javidani, J. Arreguin-Zavala, J. Danovitch, Y. Tian, and Mathieu Brochu. Additive manufacturing of AlSi10Mg alloy using direct energy deposition: Microstructure and hardness characterization. *Journal of Thermal Spray Technology*, 26(4):587–597, 2017.

[114] Abdollah Saboori, Donato Gallo, Sara Biamino, Paolo Fino, and Mariangela Lombardi. An overview of additive manufacturing of titanium components by directed energy deposition: Microstructure and mechanical properties. *Applied Sciences*, 7(9):883, 2017.

[115] Do-Sik Shim, Gyeong-Yun Baek, Jin-Seon Seo, Gwang-Yong Shin, Kee-Poong Kim, and Ki-Yong Lee. Effect of layer thickness setting on deposition characteristics in direct energy deposition (DED) process. *Optics & Laser Technology*, 86:69–78, 2016.

[116] Johannes A. Koepf, Martin R. Gotterbarm, Matthias Markl, and Carolin Körner. 3D multi-layer grain structure simulation of powder-bed fusion additive manufacturing. *Acta Materialia*, 152:119–126, 2018.

[117] Evdokia Popova, Theron M. Rodgers, Xinyi Gong, Ahmet Cecen, Jonathan D. Madison, and Surya R. Kalidindi. Process-structure linkages using a data science approach: Application to simulated additive manufacturing data. *Integrating Materials and Manufacturing Innovation*, 6(1):54–68, 2017.

[118] Siddiq M. Qidwai, Alexis C. Lewis, and Andrew B. Geltmacher. Using image-based computational modeling to study microstructure–yield correlations in metals. *Acta Materialia*, 57(14):4233–4247, 2009.

[119] S. Ranganathan. On the geometry of coincidence-site lattices. *Acta Crystallographica*, 21(2):197–199, 1966.

[120] C. C. Yang, Anthony D. Rollett, and William W. Mullins. Measuring relative grain boundary energies and mobilities in an aluminum foil from triple junction geometry. *Scripta Materialia*, 44(12):2735–2740, 2001.

[121] Josiah Willard Gibbs. On the equilibrium of heterogeneous substances. *American Journal of Science*, 3(96):441–458, 1878.

[122] GXXV Wulff. Xxv. zur frage der geschwindigkeit des wachsthums und der auflösung der krystallflächen. *Zeitschrift für Kristallographie-Crystalline Materials*, 34(1-6):449–530, 1901.

[123] Georgios D. Barmparis, Zbigniew Lodziana, Nuria Lopez, and Ioannis N. Remediakis. Nanoparticle shapes by using Wulff constructions and first-principles calculations. *Beilstein Journal of Nanotechnology*, 6(1):361–368, 2015.

[124] Johannes Hötzer, Marco Seiz, Michael Kellner, Wolfgang Rheinheimer, and Britta Nestler. Phase-field simulation of solid state sintering. *Acta Materialia*, 164:184–195, 2019.

[125] Mikito Kitayama and Andreas M Glaeser. The Wulff shape of alumina: III, undoped alumina. *Journal of the American Ceramic Society*, 85(3):611–622, 2002.

[126] John W. Cahn and WC Carter. Crystal shapes and phase equilibria: a common mathematical basis. *Metallurgical and Materials Transactions A*, 27(6):1431–1440, 1996.

[127] Fuming Lai, Yigang Chen, and Haibo Guo. Inverse Wulff construction for surface energies of coexisting and missing surfaces of crystal particles. *Journal of Crystal Growth*, 508:1–7, 2019.

[128] LD Marks and L Peng. Nanoparticle shape, thermodynamics and kinetics. *Journal of Physics: Condensed Matter*, 28(5):053001, 2016.

[129] Yuri Boykov and Vladimir Kolmogorov. Computing geodesics and minimal surfaces via graph cuts. *IEEE International Conference in Computer Vision*, 3:26–33, 2003.

[130] Vladimir Kolmogorov and Yuri Boykov. What metrics can be approximated by geo-cuts, or global optimization of length/area and flux. In *Tenth IEEE International Conference on Computer Vision*, volume 1, pages 564–571. IEEE, 2005.

[131] Stephen V. Harren and Robert J. Asaro. Nonuniform deformations in polycrystals and aspects of the validity of the Taylor model. *Journal of the Mechanics and Physics of Solids*, 37(2):191–232, 1989.

[132] A. J. Beaudoin, H. Mecking, and Fred Kocks. Development of localized orientation gradients in FCC polycrystals. *Philosophical Magazine A*, 73(6):1503–1517, 1996.

[133] Richard C. Becker and S. Panchanadeeswaran. Effects of grain interactions on deformation and local texture in polycrystals. *Acta Metallurgica et Materialia*, 43(7):2701–2719, 1995.

[134] Curt A. Bronkhorst, Surya R. Kalidindi, and Lallit Anand. Polycrystalline plasticity and the evolution of crystallographic texture in FCC metals. *Philosophical Transactions of the Royal Society of London. Series A: Physical and Engineering Sciences*, 341(1662):443–477, 1992.

[135] Shang Sun and Veera Sundararaghavan. A peridynamic implementation of crystal plasticity. *International Journal of Solids and Structures*, 51(19-20):3350–3360, 2014.

[136] Adam D. Kammers and Samantha Daly. Digital image correlation under scanning electron microscopy: Methodology and validation. *Experimental Mechanics*, 53(9):1743–1761, 2013.

[137] Adrien Guery, François Hild, Félix J. Latourte, and Stéphane Roux. Slip activities in polycrystals determined by coupling DIC measurements with crystal plasticity calculations. *International Journal of Plasticity*, 81:249–266, 2016.

[138] Erhard Hornbogen and Karl-Heinz Zum Gahr. Distribution of plastic strain in alloys containing small particles. *Metallography*, 8(3):181–202, 1975.

[139] Zdenek P. Bazant, Ted B. Belytschko, and Ta-Peng Chang. Continuum theory for strain-softening. *Journal of Engineering Mechanics*, 110(12):1666–1692, 1984.

[140] Stephen V. Harren, H. E. Deve, and Robert J. Asaro. Shear band formation in plane strain compression. *Acta Metallurgica*, 36(9):2435–2480, 1988.

[141] M. Zhang, Florent Bridier, Patrick Villechaise, José Méndez, and David L. McDowell. Simulation of slip band evolution in duplex Ti–6Al–4V. *Acta materialia*, 58(3):1087–1096, 2010.

[142] Julian F. Hallai and Stelios Kyriakides. Underlying material response for Lüders-like instabilities. *International Journal of Plasticity*, 47:1–12, 2013.

[143] Diana Yuzbekova, Anna A. Mogucheva, Daria A. Zhemchuzhnikova, Tatiana A. Lebedkina, Mikhaïl A. Lebyodkin, and Rustam Kaibyshev. Effect of microstructure on continuous propagation of the Portevin–Le Chatelier deformation bands. *International Journal of Plasticity*, 96:210–226, 2017.

[144] John A. Shaw and Stelios Kyriakides. Initiation and propagation of localized deformation in elasto-plastic strips under uniaxial tension. *International journal of plasticity*, 13(10):837–871, 1997.

[145] Taylor R. Jacobs, David K. Matlock, and Kip O. Findley. Characterization of localized plastic deformation behaviors associated with dynamic strain aging in pipeline steels using digital image correlation. *International Journal of Plasticity*, 123:70–85, 2019.

[146] Dennis M. Dimiduk, Chris Woodward, Richard LeSar, and Michael D. Uchic. Scale-free intermittent flow in crystal plasticity. *Science*, 312(5777):1188–1190, 2006.

[147] Julia R. Greer, Warren C. Oliver, and William D. Nix. Size dependence of mechanical properties of gold at the micron scale in the absence of strain gradients. *Acta Materialia*, 53(6):1821–1830, 2005.

[148] Jinyu Zhang, Gang Liu, and Junsun R. Sun. Strain rate effects on the mechanical response in multi-and single-crystalline Cu micropillars: Grain boundary effects. *International Journal of Plasticity*, 50:1–17, 2013.

[149] Robert Maaß, Steven Van Petegem, Helena Van Swygenhoven, Peter M. Derlet, Cynthia A. Volkert, and Daniel Grolimund. Time-resolved laue diffraction of deforming micropillars. *Physical Review Letters*, 99(14):145505, 2007.

[150] McLean P. Echlin, Jean C. Stinville, Victoria M. Miller, William C. Lenthe, and Tresa M. Pollock. Incipient slip and long range plastic strain localization in microtextured Ti-6Al-4V titanium. *Acta Materialia*, 114:164–175, 2016.

[151] Franz Roters, Philip Eisenlohr, Luc Hantcherli, Denny D. Tjahjanto, Thomas R. Bieler, and Dierk Raabe. Overview of constitutive laws, kinematics, homogenization and multiscale methods in crystal plasticity finite-element modeling: Theory, experiments, applications. *Acta Materialia*, 58(4):1152–1211, 2010.

[152] Hirofumi Inoue and Takayuki Takasugi. Texture control for improving deep drawability in rolled and annealed aluminum alloy sheets. *Materials Transactions*, 48(8):2014–2022, 2007.

[153] Olaf Engler and Jürgen Hirsch. Texture control by thermomechanical processing of AA6xxx Al-Mg-Si sheet alloys for automotive applications—a review. *Materials Science and Engineering: A*, 336(1-2):249–262, 2002.

[154] Veera Sundararaghavan and Nicholas Zabaras. A multi-length scale sensitivity analysis for the control of texture-dependent properties in deformation processing. *International Journal of Plasticity*, 24(9):1581–1605, 2008.

[155] Eric M. Summers, Rob Meloy, and Suok-Min Na. Magnetostriction and texture relationships in annealed galfenol alloys. *Journal of Applied Physics*, 105(7):07A922, 2009.

[156] Ruoqian Liu, Abhishek Kumar, Zhengzhang Chen, Ankit Agrawal, Veera Sundararaghavan, and Alok Choudhary. A predictive machine learning approach for microstructure optimization and materials design. *Scientific Reports*, 5:11551, 2015.

[157] Pinar Acar and Veera Sundararaghavan. Linear solution scheme for microstructure design with process constraints. *AIAA Journal*, 54(12):4022–4031, 2016.

[158] Lallit Anand and Mrityunjay Kothari. A computational procedure for rate-independent crystal plasticity. *Journal of the Mechanics and Physics of Solids*, 44(4):525–558, 1996.

[159] Marion Calcagnotto, Dirk Ponge, Eralp Demir, and Dierk Raabe. Orientation gradients and geometrically necessary dislocations in ultrafine grained dual-phase steels studied by 2D and 3D EBSD. *Materials Science and Engineering: A*, 527(10-11):2738–2746, 2010.

[160] Timothy J Ruggles and David T. Fullwood. Estimations of bulk geometrically necessary dislocation density using high resolution EBSD. *Ultramicroscopy*, 133:8–15, 2013.

[161] Francisco Armero and Krishna R. Garikipati. An analysis of strong discontinuities in multiplicative finite strain plasticity and their relation with the numerical simulation of strain localization in solids. *International Journal of Solids and Structures*, 33(20-22):2863–2885, 1996.

[162] Stewart A. Silling. Reformulation of elasticity theory for discontinuities and long-range forces. *Journal of the Mechanics and Physics of Solids*, 48(1):175–209, 2000.

[163] Thomas L. Warren, Stewart A. Silling, Abe Askari, Olaf Weckner, Micahel A. Epton, and Jifeng Xu. A non-ordinary state-based peridynamic method to model solid material deformation and fracture. *International Journal of Solids and Structures*, 46(5):1186–1195, 2009.

[164] Erdogan Madenci and Erkan Oterkus. *Peridynamic Theory and Its Applications*. Springer, 2014.

[165] Walter H. Gerstle. *Introduction to practical peridynamics: computational solid mechanics without stress and strain*, volume 1. World Scientific Publishing Co Inc, 2015.

[166] Michael R. Tupek and R. Radovitzky. An extended constitutive correspondence formulation of peridynamics based on nonlinear bond-strain measures. *Journal of the Mechanics and Physics of Solids*, 65:82–92, 2014.

[167] Sahir N. Butt and Günther Meschke. Peridynamic analysis of dynamic fracture: influence of peridynamic horizon, dimensionality and specimen size. *Computational Mechanics*, 67(6):1719–1745, 2021.

[168] Abigail Agwai, Ibrahim Guven, and Erdogan Madenci. Predicting crack propagation with peridynamics: A comparative study. *International Journal of Fracture*, 171(1):65–78, 2011.

[169] Xin Gu, Qing Zhang, and Erdogan Madenci. Non-ordinary state-based peridynamic simulation of elastoplastic deformation and dynamic cracking of polycrystal. *Engineering Fracture Mechanics*, 218:106568, 2019.

[170] Stewart A. Silling, Michael A. Epton, Olaf Weckner, Jifeng Xu, and E. Askari. Peridynamic states and constitutive modeling. *Journal of Elasticity*, 88(2):151–184, 2007.

[171] Stewart A. Silling and Richard B. Lehoucq. Peridynamic theory of solid mechanics. *Advances in Applied Mechanics*, 44:73–168, 2010.

[172] Mohammadreza Yaghoobi, Sriram Ganesan, Srihari Sundar, Aaditya Lakshmanan, Shiva Rudraraju, John E. Allison, and Veera Sundararaghavan. PRISMS-plasticity: An open-source crystal plasticity finite element software. *Computational Materials Science*, 169:109078, 2019.

[173] Amin Yaghoobi and Mi G. Chorzepa. Higher–order approximation to suppress the zero-energy mode in non-ordinary state-based peridynamics. *Computers and Structures*, 188:63–79, 2017.

[174] Michael R. Tupek, Julian J. Rimoli, and R. Radovitzky. An approach for incorporating classical continuum damage models in state-based peridynamics. *Computer Methods in Applied Mechanics and Engineering*, 263:20–26, 2013.

[175] Youn D. Ha and Florin Bobaru. Studies of dynamic crack propagation and crack branching with peridynamics. *International Journal of Fracture*, 162(1-2):229–244, 2010.

[176] Stewart A. Silling. Stability of peridynamic correspondence material models and their particle discretizations. *Computer Methods in Applied Mechanics and Engineering*, 322:42–57, 2017.

[177] Pan Li, Zhiming Hao, and Wenqiang Zhen. A stabilized non-ordinary state-based peridynamic model. *Computer Methods in Applied Mechanics and Engineering*, 339:262–280, 2018.

[178] Xin Gu, Qing Zhang, Erdogan Madenci, and Xiaozhou Xia. Possible causes of numerical oscillations in non-ordinary state-based peridynamics and a bond-associated higher-order stabilized model. *Computer Methods in Applied Mechanics and Engineering*, 357:112592, 2019.

[179] M. Scot Breitenfeld, Philippe H. Geubelle, Olaf Weckner, and Stewart A. Silling. Non-ordinary state-based peridynamic analysis of stationary crack problems. *Computer Methods in Applied Mechanics and Engineering*, 272:233–250, 2014.

[180] Huilong Ren, Xiaoying Zhuang, Yongchang Cai, and Timon Rabczuk. Dual-horizon peridynamics. *International Journal for Numerical Methods in Engineering*, 108(12):1451–1476, 2016.

[181] Chengtang Wu and Bo Ren. A stabilized non-ordinary state-based peridynamics for the nonlocal ductile material failure analysis in metal machining process. *Computer Methods in Applied Mechanics and Engineering*, 291:197–215, 2015.

[182] David J. Littlewood. A nonlocal approach to modeling crack nucleation in AA 7075-t651. In *ASME 2011 International Mechanical Engineering Congress and Exposition*, pages 567–576. American Society of Mechanical Engineers, 2011.

[183] David J. Littlewood. Simulation of dynamic fracture using peridynamics, finite element modeling, and contact. In *ASME International Mechanical Engineering Congress and Exposition*, volume 44465, pages 209–217, 2010.

[184] Ji Wan, Zhuang Chen, Xihua Chu, and Hui Liu. Improved method for zero-energy mode suppression in peridynamic correspondence model. *Acta Mechanica Sinica*, 35(5):1021–1032, 2019.

[185] Jiyangyi Luo and Veera Sundararaghavan. Stress-point method for stabilizing zero-energy modes in non-ordinary state-based peridynamics. *International Journal of Solids and Structures*, 2018.

[186] Hao Cui, Chunguang Li, and Hong Zheng. A higher-order stress point method for non-ordinary state-based peridynamics. *Engineering Analysis with Boundary Elements*, 117:104–118, 2020.

[187] Erdogan Madenci, Atila Barut, and Michael Futch. Peridynamic differential operator and its applications. *Computer Methods in Applied Mechanics and Engineering*, 304:408–451, 2016.

[188] Erdogan Madenci, Mehmet Dorduncu, Atila Barut, and Nam Phan. Weak form of peridynamics for nonlocal essential and natural boundary conditions. *Computer Methods in Applied Mechanics and Engineering*, 337:598–631, 2018.

[189] Timon Rabczuk, Huilong Ren, and Xiaoying Zhuang. A nonlocal operator method for partial differential equations with application to electromagnetic waveguide problem. *Computers, Materials & Continua 59 (2019), Nr. 1*, 2019.

[190] Erdogan Madenci, Mehmet Dorduncu, Nam Phan, and Xin Gu. Weak form of bond-associated non-ordinary state-based peridynamics free of zero energy modes with uniform or non-uniform discretization. *Engineering Fracture Mechanics*, 218:106613, 2019.

[191] Hailong Chen. Bond-associated deformation gradients for peridynamic correspondence model. *Mechanics Research Communications*, 90:34–41, 2018.

[192] Hailong Chen and Benjamin W. Spencer. Peridynamic bond-associated correspondence model: Stability and convergence properties. *International Journal for Numerical Methods in Engineering*, 117(6):713–727, 2019.

[193] Jiangyi Luo, Ali Ramazani, and Veera Sundararaghavan. Simulation of microscale shear bands using peridynamics with an adaptive dynamic relaxation method. *International Journal of Solids and Structures*, 130:36–48, 2018.

[194] Dinu Coltuc, Philippe Bolon, and Jean-Marc Chassery. Exact histogram specification. *IEEE Transactions on Image Processing*, 15(5):1143–1152, 2006.

[195] Dori Shapira, Shai Avidan, and Yacov Hel-Or. Multiple histogram matching. In *2013 IEEE International Conference on Image Processing*, pages 2269–2273. IEEE, 2013.

[196] Shang Sun and Veera Sundararaghavan. A probabilistic crystal plasticity model for modeling grain shape effects based on slip geometry. *Acta Materialia*, 60(13-14):5233–5244, 2012.

[197] Mohsen Taheri Andani, Aaditya Lakshmanan, Veera Sundararaghavan, John Allison, and Amit Misra. Quantitative study of the effect of grain boundary parameters on the slip system level hall-petch slope for basal slip system in Mg-4Al. *Acta Materialia*, 200:148–161, 2020.

[198] Mohsen Taheri Andani, Aaditya Lakshmanan, Veera Sundararaghavan, John Allison, and Amit Misra. Estimation of micro-hall-petch coefficients for prismatic slip system in Mg-4Al as a function of grain boundary parameters. *Acta Materialia*, 226:117613, 2022.

[199] Mohsen Taheri Andani, Aaditya Lakshmanan, Mohammadreza Karamooz-Ravari, Veera Sundararaghavan, John Allison, and Amit Misra. A quantitative study of stress fields ahead of a slip band blocked by a grain boundary in unalloyed magnesium. *Scientific reports*, 10(1):1–8, 2020.

[200] Veera Sundararaghavan and Nicholas Zabaras. Linear analysis of texture property relationships using process-based representations of Rodrigues space. *Acta Materialia*, 55(5):1573–1587, 2007.

[201] Pinar Acar and Veera Sundararaghavan. Utilization of a linear solver for multiscale design and optimization of microstructures. *AIAA Journal*, pages 1751–1759, 2016.

[202] Tom Quested. Micrograph 712 and full record. Department of Materials Science and Metallurgy at University of Cambridge. CC BY-NC-SA 2.0 UK. URL: www.doitpoms.ac.uk/miclib/micrograph_record.php?id=712, 2003. (accessed: 07.19.2019).

[203] Veera Sundararaghavan, Abhishek Kumar, and Shang Sun. Crystal plasticity simulations using nearest neighbor orientation correlation function. *Acta Materialia*, 93:12–23, 2015.

[204] Hang Si. On refinement of constrained Delaunay tetrahedralizations. In *Proceedings of the 15th International Meshing Roundtable*, pages 509–528. Springer, 2006.

[205] Huiliang Wei, John W. Elmer, and Tarasankar A. DebRoy. Origin of grain orientation during solidification of an aluminum alloy. *Acta Materialia*, 115:123–131, 2016.

[206] Yanis Balit, Eric Charkaluk, and Andrei Constantinescu. Digital image correlation for microstructural analysis of deformation pattern in additively manufactured 316L thin walls. *Additive Manufacturing*, 31:100862, 2020.

[207] Emil Cederberg, Vahid A. Hosseini, Chamara Kumara, and Leif Karlsson. Physical simulation of additively manufactured super duplex stainless steels–microstructure and properties. *Additive Manufacturing*, 34:101269, 2020.

[208] Huiliang Wei, John W. Elmer, and Tarasankar A. DebRoy. Crystal growth during keyhole mode laser welding. *Acta Materialia*, 133:10–20, 2017.

[209] Huiliang Wei, John W. Elmer, and Tarasankar A. DebRoy. Three-dimensional modeling of grain structure evolution during welding of an aluminum alloy. *Acta Materialia*, 126:413–425, 2017.

[210] Vahid Fallah, Masoud Alimardani, Stephen F. Corbin, and Amir Khajepour. Temporal development of melt-pool morphology and clad geometry in laser powder deposition. *Computational Materials Science*, 50(7):2124–2134, 2011.

[211] Xibing Gong and Kevin Chou. Phase-field modeling of microstructure evolution in electron beam additive manufacturing. *JOM*, 67(5):1176–1182, 2015.

[212] David A. Field. Laplacian smoothing and Delaunay triangulations. *Communications in Applied Numerical Methods*, 4(6):709–712, 1988.

[213] Kenshi Takayama, Makoto Okabe, Takashi Ijiri, and Takeo Igarashi. Lapped solid textures: Filling a model with anisotropic textures. In *ACM SIGGRAPH 2008 Papers*. Association for Computing Machinery, New York, NY, USA, 2008.

[214] Emil Praun, Adam Finkelstein, and Hugues Hoppe. Lapped textures. In *Proceedings of the 27th Annual Conference on Computer Graphics and Interactive Techniques*, page 465–470, USA, 2000.

[215] Arnoldo Badillo and Christoph Beckermann. Phase-field simulation of the columnar-to-equiaxed transition in alloy solidification. *Acta Materialia*, 54(8):2015–2026, 2006.

[216] Črtomir Donik, Jakob Kraner, Irena Paulin, and Matjaž Godec. Influence of the energy density for selective laser melting on the microstructure and mechanical properties of stainless steel. *Metals*, 10(7):919, 2020.

[217] Arulmurugan Senthilnathan, Iman Javaheri, Hengduo Zhao, Veera Sundararaghavan, Marc DeGraef, and Pınar Acar. Uncertainty quantification of metallic microstructures using principal image moments. *Computational Materials Science*, 215:111775, 2022.

[218] Sebastien Dryepondt, Peeyush Nandwana, Patxi Fernandez-Zelaia, and Fred List III. Microstructure and high temperature tensile properties of 316L fabricated by laser powder-bed fusion. *Additive Manufacturing*, 37:101723, 2021.

[219] Filippo L. Vecchiato, Henry C. de Winton, Paul A. Hooper, and Mark R. Wenman. Melt pool microstructure and morphology from single exposures in laser powder-bed fusion of 316L stainless steel. *Additive Manufacturing*, 36:101401, 2020.

[220] Marianne M. Francois, Amy Sun, Wayne E. King, Neil Jon Henson, Damien Tourret, Ccut Allan Bronkhorst, Neil N. Carlson, Christopher Kyle Newman, T. Haut, Jozsef Bakosi, et al. Modeling of additive manufacturing processes for metals: Challenges and opportunities. *Current Opinion in Solid State & Materials Science*, 21(4):198–206, 2017.

[221] Iman Javaheri, Jiangyi Luo, Aaditya Lakshmanan, and Veera Sundararaghavan. Higher-order approximations for stabilizing zero-energy modes in non-ordinary state-based peridynamics models. *AIAA Journal*, 60(8), 2022.

[222] Cole Britt, Colt J. Montgomery, Michael J. Brand, Zi-Kui Liu, John S. Carpenter, and Allison M. Beese. Effect of processing parameters and strut dimensions on the microstructures and hardness of stainless steel 316L lattice-emulating structures made by powder-bed fusion. *Additive Manufacturing*, 40:101943, 2021.

[223] A. R. Shiveley, Paul A. Shade, Adam L. Pilchak, Jay S. Tiley, and R. Kerns. A novel method for acquiring large-scale automated scanning electron microscope data. *Journal of Microscopy*, 244(2):181–186, 2011.

[224] Thomas R. Bieler and Sheldon L. Semiatin. The origins of heterogeneous deformation during primary hot working of Ti–6Al–4V. *International Journal of Plasticity*, 18(9):1165–1189, 2002.

[225] Dhriti Bhattacharyya, Babu Viswanathan, Robb F. Denkenberger, David Furrer, and Hamish L. Fraser. The role of crystallographic and geometrical relationships between α and β phases in an α/β titanium alloy. *Acta materialia*, 51(16):4679–4691, 2003.

[226] Ralf Kohler. A segmentation system based on thresholding. *Computer Graphics and Image Processing*, 15(4):319–338, 1981.

[227] Zheng Lin, Jesse Jin, and Hugues Talbot. Unseeded region growing for 3d image segmentation. In *ACM International Conference Proceeding Series*, volume 9, pages 31–37. Citeseer, 2000.

[228] SA Hojjatoleslami and Josef Kittler. Region growing: a new approach. *IEEE Transactions on Image processing*, 7(7):1079–1084, 1998.

[229] Yian-Leng Chang and Xiaobo Li. Adaptive image region-growing. *IEEE transactions on image processing*, 3(6):868–872, 1994.

[230] Soumen Biswas and Ranjay Hazra. Robust edge detection based on modified moore-neighbor. *Optik*, 168:931–943, 2018.

[231] Ratika Pradhan, Shikhar Kumar, Ruchika Agarwal, Mohan P Pradhan, MK Ghose, et al. Contour line tracing algorithm for digital topographic maps. *International Journal of Image Processing (IJIP)*, 4(2):156–163, 2010.

[232] Luis A. Santaló and Mark Kac. *Crofton's Formulas and the Kinematic Fundamental Formula in Noneuclidean Spaces*, page 316–329. Cambridge Mathematical Library. Cambridge University Press, 2 edition, 2004.

[233] Manfredo P. Do Carmo. *Differential geometry of curves and surfaces: revised and updated second edition*. Courier Dover Publications, 2016.

[234] Elizabeth A. Holm and Corbett C. Battaile. The computer simulation of microstructural evolution. *JOM*, 53(9):20–23, 2001.

[235] Hiroshi Itahara, Hiroshi Nomura, Toshihiko Tani, and Hideaki Matsubara. Design of grain oriented microstructure by the Monte Carlo simulation of sintering and isotropic grain growth. *Journal of the Ceramic Society of Japan*, 111(1296):548–554, 2003.

[236] Daniel Pino Muñoz, Julien Bruchon, Sylvain Drapier, and François Valdivieso. Direct 3D simulation of powder sintering by surface and volume diffusion. In *Key Engineering Materials*, volume 554, pages 714–723. Trans Tech Publ, 2013.

[237] Yu U. Wang. Computer modeling and simulation of solid-state sintering: A phase field approach. *Acta Materialia*, 54(4):953–961, 2006.

[238] Zhenyu Wu and Richard Leahy. An optimal graph theoretic approach to data clustering: Theory and its application to image segmentation. *IEEE Transactions on Pattern Analysis and Machine Intelligence*, 15(11):1101–1113, 1993.

[239] Hiroshi Ishikawa. Exact optimization for Markov random fields with convex priors. *IEEE Transactions on Pattern Analysis and Machine Intelligence*, 25(10):1333–1336, 2003.

[240] Dorothy M. Greig, Bruce T. Porteous, and Allan H. Seheult. Exact maximum a posteriori estimation for binary images. *Journal of the Royal Statistical Society: Series B (Methodological)*, 51(2):271–279, 1989.

[241] Yuri Boykov, Olga Veksler, and Ramin Zabih. Fast approximate energy minimization via graph cuts. *IEEE Transactions on Pattern Analysis and Machine Intelligence*, 23(11):1222–1239, 2001.

[242] Siddhartha Srivastava and Veera Sundararaghavan. Graph coloring approach to mesh generation in multiphase media with smooth boundaries. *AIAA Journal*, 58(1):198–205, 2020.

[243] Siddhartha Srivastava, Mohammadreza Yaghoobi, and Veera Sundararaghavan. A graph-theoretic approach for multiscale modeling and prediction of crack propagation in polycrystalline materials. *Engineering Fracture Mechanics*, 241:107406, 2021.

[244] Siddhartha Srivastava. *Graph Theoretic Algorithms Adaptable to Quantum Computing*. PhD thesis, 2021.

[245] Hong-Kai Zhao, Tony Chan, Barry Merriman, and Stanley Osher. A variational level set approach to multiphase motion. *Journal of Computational Physics*, 127(1):179–195, 1996.

[246] Yuri Boykov, Vladimir Kolmogorov, Daniel Cremers, and Andrew Delong. An integral solution to surface evolution PDEs via geo-cuts. In *European Conference on Computer Vision*, pages 409–422. Springer, 2006.

[247] James D. Powers and Andreas M. Glaeser. Grain boundary migration in ceramics. *Interface Science*, 6(1):23–39, 1998.

[248] Paul Sweeney Jr. *Crofton Formulæ*. Senior thesis. 2018.

[249] Joachim Ohser and Frank Mücklich. *Statistical Analysis of Microstructures in Materials Science*. Wiley, 2000.

[250] Gaëtan Lehmann and David Legland. Efficient N-dimensional surface estimation using Crofton formula and run-length encoding. *Insight Journal*, 2012.

[251] Riyadh Al-Raoush, Karsten Thompson, and Clinton S Willson. Comparison of network generation techniques for unconsolidated porous media. *Soil Science Society of America Journal*, 67(6):1687–1700, 2003.

[252] Arash Rabbani, Shahab Ayatollahi, Riyaz Kharrat, and Nader Dashti. Estimation of 3-D pore network coordination number of rocks from watershed segmentation of a single 2-D image. *Advances in Water Resources*, 94:264–277, 2016.

[253] Mohammad M. Roozbahani, Rodrigo Borela, and David J. Frost. Pore size distribution in granular material microstructure. *Materials*, 10(11):1237, 2017.

[254] Frederick F. Lange. Sinterability of agglomerated powders. *Journal of the American Ceramic Society*, 67(2):83–89, 1984.

[255] Tsang-Tse Fang and Hayne Palmour. Useful extensions of the statistical theory of sintering. *Ceramics International*, 15(6):329–335, 1989.

[256] George C. Kuczynski. Statistical approach to the theory of sintering. In *Sintering and Catalysis*, pages 325–337. Springer, 1975.

[257] Jan Ma and Leongchew Lim. Effect of particle size distribution on sintering of agglomerate-free submicron alumina powder compacts. *Journal of the European Ceramic Society*, 22(13):2197–2208, 2002.

[258] Jyh-Ming M. Ting and Ray Y. Lin. Effect of particle-size distribution on sintering. *Journal of Materials Science*, 29(7):1867–1872, 1994.

[259] Jeremiah P. MacSleyne, Jeff P. Simmons, and Marc De Graef. On the use of moment invariants for the automated analysis of 3D particle shapes. *Modelling and Simulation in Materials Science and Engineering*, 16(4):045008, 2008.

[260] Kimiya Miyake, Yoshihiro Hirata, Taro Shimonosono, and Soichiro Sameshima. The effect of particle shape on sintering behavior and compressive strength of porous alumina. *Materials*, 11(7):1137, 2018.

[261] Ellen L.S. Solomon, Anirudh Raju Natarajan, Arunabha Mohan Roy, Veera Sundararaghavan, Anton Van der Ven, and Emmanuelle A Marquis. Stability and strain-driven evolution of β precipitate in Mg-Y alloys. *Acta Materialia*, 166:148–157, 2019.

[262] Michael L. Parks, Pabio Seleson, Steven J. Plimpton, Stewart A. Silling, and Richard B. Lehoucq. Peridynamics with LAMMPS: A user guide, v. 0.3 Beta. *Sandia Report (2011–8253)*, 2011.

[263] Stewart A. Silling and Ebrahim Askari. A meshfree method based on the peridynamic model of solid mechanics. *Computers and Structures*, 83(17-18):1526–1535, 2005.

[264] Mohammadreza Yaghoobi, John E Allison, and Veera Sundararaghavan. Prisms-plasticity tm: An open-source rapid texture evolution analysis pipeline. *Integrating Materials and Manufacturing Innovation*, 11(4):479–496, 2022.

[265] Randall J. LeVeque. *Finite difference methods for ordinary and partial differential equations: Steady-state and time-dependent problems.* SIAM, 2007.

[266] Dennis P. Flanagan and Ted B. Belytschko. A uniform strain hexahedron and quadrilateral with orthogonal hourglass control. *International Journal for Numerical Methods in Engineering*, 17(5):679–706, 1981.

[267] Richard W. Macek and Stewart A. Silling. Peridynamics via finite element analysis. *Finite Elements in Analysis and Design*, 43(15):1169–1178, 2007.

[268] Wenyang Liu, Gang Yang, and Yong Cai. Modeling of failure mode switching and shear band propagation using the correspondence framework of peridynamics. *Computers & Structures*, 209:150–162, 2018.

[269] Mohammadreza Yaghoobi, George Z Voyiadjis, and Veera Sundararaghavan. Crystal plasticity simulation of magnesium and its alloys: A review of recent advances. *Crystals*, 11(4):435, 2021.

[270] Sriram Ganesan, Mohammadreza Yaghoobi, Alan Githens, Zhe Chen, Samantha Daly, John Allison, and Veera Sundararaghavan. The effects of heat treatment on the response of we43 mg alloy: crystal plasticity finite element simulation and sem-dic experiment. *International Journal of Plasticity*, page 102917, 2020.

[271] Mohammadreza Yaghoobi, John E Allison, and Veera Sundararaghavan. Multiscale modeling of twinning and detwinning behavior of hcp polycrystals. *International Journal of Plasticity*, 127:102653, 2020.

[272] Alan Githens, Sriram Ganesan, Zhe Chen, John E. Allison, Veera Sundararaghavan, and Samantha H. Daly. Characterizing microscale deformation mechanisms and macroscopic tensile properties of a high strength magnesium rare-earth alloy: A combined experimental and crystal plasticity approach. *Acta Materialia*, 186:77–94, 2020.

[273] S. Ganesan. *Microstructural response of magnesium alloys: 3D crystal plasticity and experimental validationk*. PhD thesis, University of Michigan, Ann Arbor, 2017.

[274] Mohammadreza Yaghoobi, Zhe Chen, Veera Sundararaghavan, Samantha Daly, and John E Allison. Crystal plasticity finite element modeling of extension twinning in we43 mg alloys: calibration and validation. *Integrating Materials and Manufacturing Innovation*, 10:488–507, 2021.

[275] Mohammadreza Yaghoobi, Zhe Chen, Aeriel D Murphy-Leonard, Veera Sundararaghavan, Samantha Daly, and John E Allison. Deformation twinning and detwinning in extruded mg-4al: In-situ experiment and crystal plasticity simulation. *International Journal of Plasticity*, 155:103345, 2022.

[276] Zhe Chen, Mohammadreza Yaghoobi, Veera Sundararaghavan, John Allison, and Samantha Daly. The effects of microstructure on deformation twinning in mg we43. *Materials Science and Engineering: A*, 859:144189, 2022.

[277] Aaditya Lakshmanan, Mohsen Taheri Andani, Mohammadreza Yaghoobi, John Allison, Amit Misra, and Veera Sundararaghavan. A combined experimental and crystal plasticity study of grain size effects in magnesium alloys. *Journal of Magnesium and Alloys*, 2023.

[278] Aaditya Lakshmanan, Mohammadreza Yaghoobi, Krzysztof S Stopka, and Veera Sundararaghavan. Crystal plasticity finite element modeling of grain size and morphology effects on yield strength and extreme value fatigue response. *journal of materials research and technology*, 19:3337–3354, 2022.

[279] Veera Sundararaghavan and Siddhartha Srivastava. Microfract: An image based code for microstructural crack path prediction. *SoftwareX*, 6:94–97, 2017.

[280] Marco A. Lopez-Sanchez and Sergio Llana-Fúnez. An extension of the Saltykov method to quantify 3D grain size distributions in mylonites. *Journal of Structural Geology*, 93:149–161, 2016.

[281] Bahattin Kilic and Erdogan Madenci. An adaptive dynamic relaxation method for quasi-static simulations using the peridynamic theory. *Theoretical and Applied Fracture Mechanics*, 53(3):194–204, 2010.